1-1-2012

Microscale Measurements of Cell and Tissue Mechanics in Three Dimensions

Wesley Legant
University of Pennsylvania, wrlegant@gmail.com

Microscale Measurements of Cell and Tissue Mechanics in Three Dimensions

Abstract
Two-dimensional (2D) studies have revealed that mechanical forces drive cell migration and can feedback to regulate proliferation, differentiation and the synthesis/remodeling of extracellular matrix (ECM) proteins. Whether these observations can be translated to clinical settings or be utilized for tissue engineering will depend critically on our ability to translate these findings into physiologically relevant three-dimensional (3D) environments. The general goal of this dissertation has been to develop and apply new technologies capable of extending studies of cell and tissue mechanics into 3D environments.

In the first project, we measured both shear and normal traction forces exerted by cells cultured on planar substrates. We observed that focal adhesions serve as pivots about which cells generate rotational moments.

In the second project, we combined enzymatically degradable synthetic hydrogels with finite element models to measure the mechanical tractions exerted by cells fully encapsulated within 3D matrices. We found that cells reach out thin protrusions and pull back inward towards the cell body with the highest forces at the tip. Cellular extensions that were invading into the surrounding matrix displayed a strong inward force 10-15 microns behind the leading tip, suggesting that growing extensions may establish a "contractile waypoint," before invading further.

To study the forces cells exert during tissue remodeling, we utilized photolithograpy to generate arrays of microtissues consisting of cells encapsulated in 3D collagen matrices. Microcantilevers were used to constrain the remodeling of the collagen gel and to report the forces generated during this process. We used this technique to explore the effects of boundary stiffness and matrix density within model tendon and cardiac tissues. Finally, we combined this system with a Foerster radius energy transfer (FRET) based biosensor of fibronectin conformation to reveal how tissue geometry and cell-genereated tractions cooperate to pattern matrix conformation during tissue remodeling.

Together, these studies highlight novel approaches to understand the nature of cell-ECM interactions in 3D matrices. Such mechanical insights will help us to understand how physical forces drive cell migration and behavior within physiologically relevant environments.

Degree Type
Dissertation

Degree Name
Doctor of Philosophy (PhD)

Graduate Group
Bioengineering

First Advisor
Christopher S. Chen

Keywords
Cell Mechanics, Fibronectin, Focal Adhesion, Mechanotransduction, Tissue Engineering, Traction Force Microscopy

Subject Categories
Biomechanics | Biomedical | Biophysics

MICROSCALE MEASUREMENTS OF CELL AND TISSUE MECHANICS IN THREE DIMENSIONS

Wesley R. Legant

A DISSERTATION in Bioengineering

Presented to the Faculties of the University of Pennsylvania

in Partial Fulfillment of the Requirements for the Degree of Doctor of Philosophy

2012

Christopher S. Chen, MD, PhD, Professor, Department of Bioengineering
Supervisor of Dissertation

Beth Winkelstein, PhD, Professor, Department of Bioengineering
Graduate Group Chairperson

Dissertation Committee

Daniel A. Hammer, PhD, Professor, Department of Bioengineering

Paul A. Janmey, PhD, Professor, Institute for Medicine and Engineering

Rebecca G. Wells, MD, Associate Professor, Department of Medicine

MICROSCALE MEASUREMENTS OF CELL AND TISSUE MECHANICS IN THREE DIMENSIONS

ACKNOWLEDGEMENTS

This work would never have been possible without the support and guidance of many people. I would first like to thank my advisor, Dr. Christopher Chen, whose mentorship has been critical not only to the work presented here, but also for advising me in the vast array of activities required to fund and manage a research lab. Your perspective and encouragement over the past 5 years has shaped how I view science and was critical for my decision to pursue a career in academia. I would also like to thank my committee members Drs. Daniel Hammer, Paul Janmey, and Rebecca Wells, for their insightful questions and comments that have provided me with a broader scientific perspective of this work.

Thanks to all the former members of the Chen lab, epecially Nate, Sami, Sri, Wendy and Ravi for providing an exceptional atmosphere to start my endeavor. And, thank you to all the current members of the Chen lab for putting up with me constantly saying that experiments won't work, hypotheses are undefined and that that powerpoint slide is pretty much "the worst thing imaginable." I could never joke with everyone if I wasn't sure that your passion, hard work, and motivation for science will most certainly prove me wrong. I especially thank Jeroen (The Foreigner), Thomas (Frenchy), Brandon (you'll always be the New Guy), Brendon, Ritu, Jordan, Jan, Colin and Michelle for reminding me that life does indeed exist outside science and that it can actually be pretty sweet. Colin, you were my equal coauthor in crime for the work presented in chapter 3, but my shoes will always be brighter and cooler.

I would like to thank Drs. Howard Hu and Pedro Ponte-Castaneda in the mechanical engineering department at Penn for helpful discussions and ideas and Peter Rocket for always having a better idea of what I really want than what I had actually asked for. Thank you so much to Dr. Guy Genin in the mechanical engineering department at Washington University in St. Louis. Your passion for science and teaching is unparalleled and your advice has been invaluable. I truly look forward to working with you in the future.

Thank you to Dr. Viola Vogel for casually mentioning that we should work on a collaborative project after we had just met at a conference in my 3rd year of graduate school. And thank you even more for remembering that conversation when I approached you again 2 years later with the crazy idea to come out to Zurich for a year. The work performed in chapter 7 would never have existed without your openness and enthusiasm. Thank you to Norma at ETH, for coordinating everything Swiss. My time in Zurich was an exceptional experience and is one that I'll always remember.

I am immensely grateful to my family for their love and encouragement. Thank you to my brothers, Brad and Andy, for convincing me that I was the nerd of the family and for fully supporting my efforts to prove you right. I owe an endless debt of gratitude to my parents for all their efforts throughout the past 28 years. I never could have accomplished any of this without your help. Thank you so much and I love you both.

Finally, Colette, being able to share this experience with you has been amazing. You always have a laugh and a positive outlook for every one of my grumpy complaints. Some things just seem to fit. I can't wait to plan the rest of our lives together.

ABSTRACT

MICROSCALE MEASUREMENTS OF CELL AND TISSUE MECHANICS IN THREE DIMENSIONS

Wesley R. Legant

Christopher S. Chen

Two-dimensional (2D) studies have revealed that mechanical forces drive cell migration, and can feedback to regulate proliferation, differentiation and the synthesis/remodeling of extracellular matrix (ECM) proteins. Whether these observations can be translated to clinical settings or be utilized for tissue engineering will depend critically on our ability to translate these findings into physiologically relevant three-dimensional (3D) environments. The general goal of this dissertation has been to develop and apply new technologies capable of extending studies of cell and tissue mechanics into 3D environments.

In the first project, we measured both shear and normal traction forces exerted by cells cultured on planar substrates. We observed that focal adhesions serve as pivots about which cells generate rotational moments.

In the second project, we combined enzymatically degradable synthetic hydrogels with finite element models to measure the mechanical tractions exerted by cells fully encapsulated within 3D matrices. We found that cells reach out thin protrusions and pull back inward towards the cell body with the highest forces at the tip. Cellular extensions that were invading into the surrounding matrix displayed a strong inward force 10-15 μm behind the leading tip, suggesting that growing extensions may establish a "contractile waypoint," before invading further.

To study the forces cells exert during tissue remodeling, we utilized photolithograpy to generate arrays of microtissues consisting of cells encapsulated in 3D collagen matrices. Microcantilevers were used to constrain the remodeling of the collagen gel and to report the forces generated during this process. We used this technique to explore the effects of boundary stiffness and matrix density within model tendon and cardiac tissues. Finally, we combined this system with a Foerster radius energy transfer (FRET) based biosensor of fibronectin conformation to reveal how tissue geometry and cell-genereated tractions cooperate to pattern matrix conformation during tissue remodeling.

Together, these studies highlight novel approaches to understand the nature of cell-ECM interactions in 3D matrices. Such mechanical insights will help us to understand how physical forces drive cell migration and behavior within physiologically relevant environments.

TABLE OF CONTENTS

LIST OF TABLES

LIST OF FIGURES

CHAPTER 1: INTRODUCTION

All cells interact mechanically with the surrounding extracellular environment. Blood cells experience shear stresses from the surrounding fluid; cells in the musculoskeletal system drive the active contraction, and bear the passive compression that permits motion of the limbs. During development, the forces generated by individual cells are transmitted through tissues to drive morphogenesis and these same forces maintain tissue tone and homeostasis in adult organisms (Fung 1993; Keller, Davidson et al. 2003). At the cellular level, the interaction between cytoskeletal actin filaments and myosin motors creates contractile forces that are coupled to the extracellular matrix (ECM) at mechano-sensitive sites in the cell membrane called focal adhesions (FAs). During wound healing and tissue remodeling, the tractions generated by cells are transmitted through the ECM over length scales that are much larger than the individual cells themselves to drive the contraction of granulation tissue and scar formation. Importantly, forces generated by cells not only drive the physical changes, but also can feedback through FAs to affect cellular events such, proliferation and differentiation (Huang, Chen et al. 1998; Fu, Wang et al. 2010), and this mechano-coupling between cells and the ECM is altered in diseases such as osteoporosis, hypertension and muscular dystrophy (Cain and Khalil 2002; Tatsumi, Ishii et al. 2007; Jaalouk and Lammerding 2009). However, despite the importance of cellular forces and mechanical tractions in many physiological and pathological phenomena, the exact nature of when, where and how cells exert forces, and further, how these forces are transmitted through the ECM is still poorly understood. A key limiting factor to studies thus far is that relatively few techniques exist to measure cellular forces, which are in the micro- to nano-Newton range. The techniques that are currently available typically require that cells be cultured on two-dimensional (2D) planar surfaces even though many cellular processes are altered or lost completely when cells are removed from a three-dimensional (3D) ECM. The focus of this dissertation is to develop novel methods to measure the forces exerted by cells and tissues at multiple length scales. The development and application of these techniques will help elucidate the complex role that cell generated forces play in biology and lend insight into the engineering of regenerative therapies. The following section provides a short summary of the work conducted.

Develop computational and experimental methods to measure the 3D mechanical tractions exerted by cells cultured on planer elastic substrates (2.5D Traction Force Microscopy).

Recent methods have revealed that cells on cultured on planar substrates exert both shear and normal tractions against the ECM. However, the location and origin of the normal tractions with respect to the adhesive and structural elements of cells have not been elucidated. We

developed a high spatio-temporal resolution, multi-dimensional traction force microscopy (2.5D TFM) to measure and model the full nature of cellular forces applied on a planar substrates. We show that cells cultured on planer surfaces exert pushing and pulling normal traction stresses in addition to previously reported shear stresses. Shear tractions are localized under elongated FAs while upward normal tractions are detected in front of (toward the leading edge) and downward normal tractions behind (toward the cell nucleus) adhesions and the termini of linked actin stress fibers. The net effect of these forces at the cell-ECM interface produces significant rotational moments about FAs, which form in protruding and retracting peripheral regions. The moments are also highly dynamic. Temporal 2.5D TFM analysis of migrating and spreading cells shows that the locations of rotational moments shift outward as the leading edge extends. Compiling these findings, we developed a finite element model that clarifies the mechanical relationship between actomyosin contractile force, FAs, and a pliable ECM.

Develop an approach to measure the 3D mechanical tractions exerted by cells fully encapsulated within 3D hydrogel matrices (fully 3D Traction Force Microscopy).

Quantitative measurements of cell-generated forces have heretofore required that cells be cultured on two-dimensional substrates. We describe a technique to quantitatively measure three-dimensional traction forces exerted by cells fully encapsulated within well-defined elastic hydrogel matrices. We apply this approach to measure tractions from a variety of cell types and contexts, and reveal patterns of force generation attributable to morphologically distinct regions of cells as they extend into the surrounding matrix.

Create and characterize a platform to quantitatively assess the sensitivity and resolution of cellular traction measurements in both 2.5D and fully 3D settings.

Measurements of cell generated tractions, collectively termed traction force microscopy, have emerged as an indispensible tool to study cell mechanics, migration and mechanotransduction. To date, there have been numerous advances and alternative techniques presented to convert a measured displacement field within an elastic media to surface tractions exerted by cells. However, the variety of different measurement techniques and experimental parameters utilized can make it difficult to compare traction maps computed with different methods or across different studies. We present a general approach utilizing simulated data and Fourier decomposition of surface tractions to fully probe the spatial resolution and traction sensitivity of TFM measurements. This approach is readily compatible with all current methods

of TFM and should serve as a useful metric for characterizing and comparing future measurements of cell generated traction forces. As a demonstration, we apply this method to characterize both the 3D tractions exerted by cells cultured on top of planer half-spaces (pseudo-3D TFM) and the 3D tractions exerted by cells fully surrounded by a 3D matrix (fully-3D TFM). Within these contexts, we assess the effects of finite displacement sampling (bead density), measurement noise, and regularization on the recovered surface tractions.

Utilize micro-electro-mechanical (MEMS) based approaches to measure the forces and stresses present in micropatterned, multicellular tissue constructs.

Physical forces generated by cells drive morphologic changes during development and can feedback to regulate cellular phenotype. Because these phenomena typically occur within a 3D matrix *in vivo,* we utilized MEMS technology to generate arrays of microtissues consisting of cells encapsulated within 3D micropatterned matrices. Microcantilevers were used to simultaneously constrain the remodeling of a collagen gel and to report forces generated during this process. By concurrently measuring forces and observing matrix remodeling at cellular length scales, we report an initial correlation and later decoupling between cellular contractile forces and changes in tissue morphology. Independently varying the mechanical stiffness of the cantilevers and collagen matrix revealed that cellular forces increased with boundary or matrix rigidity while levels of cytoskeletal and ECM proteins correlated with levels of mechanical stress. By mapping these relationships between cellular and matrix mechanics, cellular forces, and protein expression onto a novel bio-chemo-mechanical model of microtissue contractility, we demonstrate how intratissue gradients of mechanical stress can emerge from collective cellular contractility and finally, how such gradients can be used to engineer protein composition and organization within a 3D tissue. Together, these findings highlight a complex and dynamic relationship between cellular forces, ECM remodeling, and cellular phenotype and describe a novel system to study and apply this relationship within engineered 3D microtissues.

Investigate the interplay between cell generated forces, tissue stresses, and fibronectin conformation within 3D matrices.

Encapsulations of cells in type-I collagen matrices are widely used 3D *in vitro* models of wound healing and tissue morphogenesis and are common constructs for tissue engineering, drug delivery, and for *in vivo* implantation. As cells remodel the exogenous collagen scaffold, they also assemble a dense fibronectin (Fn) matrix that aids in tissue compaction; however, the spatio-

temporal (re)organization of Fn and collagen in this setting has yet to be quantitatively investigated. Here, we utilized microfabricated tissue gauges (μTUGs) to guide the contraction of microscale encapsulations of fibroblasts within collagen gels. We combined this system with a Foerster Radius Energy Transfer (FRET) labeled biosensor of Fn conformation to probe the organization, conformation and remodeling of both the exogenous collagen and the cell-assembled Fn matrices. We show that within hours, compact Fn from culture media absorbed to the collagen scaffold. Over the course of tissue remodeling, this Fn-coated collagen scaffold was compacted into a thin, sparsely populated core around which cells assembled a dense fibrillar Fn shell. This resulted in two separate Fn populations (compact/absorbed and extended/fibrillar) that may have different downstream signaling properties. Cell contractility and microtissue geometry cooperated to remodel these two populations, resulting in spatial gradients in Fn conformation. Together, these results highlight an important spatio-temporal interplay between two prominent ECM molecules (Fn and collagen) and cellular traction forces, and will have implications for future studies of the force-mediated remodeling events that occur within collagen scaffolds either in 3D *in vitro* models or within surgical implants *in vivo*.

CHAPTER 2: BACKGROUND/SIGNIFICANCE

2.1 Physiological motivation: mechanical forces in biology

Mechanical stresses are present in all facets of physiology. The coordinated contraction and extension of the musculoskeletal system drives locomotion. Red blood cells and vessel walls endure complementary shear stresses as blood is pumped throughout the body. Pulmonary cells in the lungs are stretched and compressed with each breath. To cope with this, cells have developed specialized systems that allow them to generate and sense mechanical stress (Vogel and Sheetz 2006; Geiger, Spatz et al. 2009), and aberrations to these systems often result in disease pathologies (Ingber 2003; Jaalouk and Lammerding 2009) and developmental abnormalities (Wozniak and Chen 2009). Indeed, nearly all cells in the body possess the ability to contract and generate force through actin/myosin interactions. The coordinated contraction of these proteins drives cell migration and morphogenesis, both in physiological settings such as development and wound healing (Taber 1995; Hinz, Mastrangelo et al. 2001; Keller, Davidson et al. 2003) and in pathological settings such as tumor metastasis (Paszek, Zahir et al. 2005; Pathak and Kumar 2011; Wirtz, Konstantopoulos et al. 2011). However, while much progress has been made on elucidating the individual components (proteins and molecules) that are necessary for cells to sense and generate force, it is still unclear how the spatial and temporal organization of cell generated forces themselves cooperate on a physical level to drive cell migration and tissue morphogenesis, especially when these events occur in three-dimensional settings.

2.2 Myosin II initiated contraction of actin fibers: the engine of cell contractility

Cellular contraction arises from the motor activity of myosin II molecules acting against actin filaments (Huxley 1969; Rayment, Holden et al. 1993). ATP hydrolysis drives conformational changes in the myosin molecules, resulting in cross-bridge cycling and ratcheting of myosin along actin. This ratcheting combines with actin polymerization to drive the retrograde flow and disassembly of actin networks within the cell (Theriot and Mitchison 1991; Wilson, Tsuchida et al. 2010). When cells are cultured on relatively rigid substrates, myosin II molecules are capable of arranging into minifilaments which can then crosslink and bundle adjacent actin fibers into larger structures termed stress fibers (Burridge and Chrzanowska-Wodnicka 1996). The collective motor activity of myosin II in minifilaments causes actin filaments to slide relative to one another which, at a larger length scale (several microns), results in the net contraction of actin stress fibers (Isenberg, Rathke et al. 1976). Both the motor and crosslinking ability of myosin II has been shown to be critical for maintaining cytoskeletal integrity and driving migration (Laevsky and Knecht 2003; Cai, Rossier et al. 2010). The ATPase activity of myosin

II can be modulated intracellularly by phosphorylation and de-phosphorylation of residues on the myosin regulatory light chains by myosin light chain kinase (MLCK) and myosin light chain phosphatase (mPP), respectively (Sellers 1991; Tan, Ravid et al. 1992). MLCK and mPP are in turn regulated by numerous pathways within the cell to spatially and temporally control myosin activation and thereby link cellular contraction to biochemical signaling (Burridge and Chrzanowska-Wodnicka 1996).

2.3 Cell-ECM adhesions: linking the cytoskeleton to the extracellular matrix

Contracting stress fibers do not interact directly with the substrate, but rather terminate into dense protein plaques termed focal adhesions (FAs) that span the plasma membrane and serve as a link between the cytoskeleton and the ECM (Abercrombie, Heaysman et al. 1971). In addition to a variety of adhesive and structural molecules, FAs also contain a vast array of different signaling molecules, thus positioning them as a major sensory complex in cells (Geiger, Spatz et al. 2009). Traction stresses applied to the intracellular surface of the adhesion either via retrograde actin flow or contracting actin stress fibers are transmitted to the ECM via transmembrane integrin receptors. Integrins are a heterodimeric family of proteins that serve as the primary adhesive molecules in anchorage dependent cells (Hynes 1992; Hynes 2002). Upon engagement to the ECM, contraction of the cell causes clustering and activation of integrins. Downstream of force-dependent integrin activation, additional molecules are recruited to the cytoplasmic side of the FA, thus reinforcing the linkage between the cytoskeleton and the ECM (Parsons, Horwitz et al. 2010). Interestingly, many of these molecules have biochemical signaling properties in addition to serving as a structural linkage. To date, more than 90 different components have been identified to reside within FAs, with another 66 more thought to be peripherally associated under certain conditions (Zaidel-Bar, Itzkovitz et al. 2007). Despite the ever increasing "parts list" of FA proteins, several common trends have emerged that govern how mechanical stresses at FAs are converted into downstream biochemical signals. Forces within adhesions are transmitted down to the nanoscale where they effect conformational changes of the constituent molecules (Sawada, Tamada et al. 2006; Lee, Kamm et al. 2007). These conformational changes could alter the rates of biochemical reactions, change binding affinity (Kong, Garcia et al. 2009), and alter kinase signaling activity (Mitra, Hanson et al. 2005; Kuo, Han et al. 2010). This molecular-scale force propagation was recently measured by using a novel Foerster resonance energy transfer (FRET) vinculin sensor (Grashoff, Hoffman et al. 2010). Vinculin is a key structural element of FAs and is thought to help link integrins to the actin

cytoskeleton (Burridge and Chrzanowska-Wodnicka 1996). Interestingly, the amount of force that was propagated across vinculin molecules in adhesions was context dependent, suggesting that alterations in how mechanical loads are distributed between adhesion molecules may be a key regulatory mechanism. In support of this idea, the molecular composition of adhesions is both spatially and temporally regulated (Zamir, Katz et al. 2000; Wozniak, Modzelewska et al. 2004; Shroff, Galbraith et al. 2007). Moreover, recent advances in super-resolution 3D imaging has revealed a stratified organization within the axial dimension of FAs, with signaling molecules clustering in between the integrins and the actin binding proteins (Kanchanawong, Shtengel et al. 2010). Finally, it is important to note the presence of multiple positive and negative feedback loops connecting force-mediated FA signaling pathways and myosin II-induced contractility (Parsons, Horwitz et al. 2010). Together, these pathways allow cells to dynamically sense, exert, and respond to mechanical forces within their surroundings.

2.4 Traction stress as a regulator of cell phenotype

Cells have evolved numerous mechanisms to adapt and respond to their physical environment. It is not surprising then, that alterations in the mechanical properties of the environment surrounding cells can in turn alter cellular behavior. It was hypothesized early on that mechanical forces were critical in guiding the development of embryos and in maintaining the mass and integrity of connective tissues (Wolff 1892; Beloussov, Dorfman et al. 1975). Advances in chemistry and materials science have enabled highly controlled *in vitro* studies of how cells sense changes in ECM mechanics. Seminal studies in the field have utilized mechanically tunable polyacrylamide hydrogels coupled to different ECM ligands to show that cell morphology, contractility, migration and FA formation are increased on more rigid surfaces (Pelham and Wang 1997; Lo, Wang et al. 2000; Discher, Janmey et al. 2005). More recent experiments have utilized these hydrogels to show that stem cell differentiation and self-renewal can all be modulated by the rigidity of the extracellular environment. Mesenchymal stem cells cultured on polyacrylamide hydrogels that mimic the rigidity of brain, muscle or bone tended to express markers specific to those lineages (Engler, Sen et al. 2006), and the self-renewal of skeletal muscle stem cells was found to be optimal on hydrogels that mimic the rigidity of muscle tissue (Gilbert, Havenstrite et al. 2010). Tumor cells are also responsive to the extracellular environment. The progressive stiffening of the stromal tissue surrounding the primary tumor can feedback to affect tumor cell malignancy (Paszek, Zahir et al. 2005; Levental, Yu et al. 2009). While representing only a small subset of the cell functions that can be regulated by the

mechanics of surrounding tissue, these highlight a clear link between ECM mechanics and cell phenotype.

It is important to note that in each of the examples presented above, the ability for cells to respond to the mechanics of their environment was critically dependent on myosin II-induced contractility and cell-generated tractions. Much as the stiffness of a spring can only be determined upon stretching, cells must probe and deform the surrounding matrix in order to assess its mechanical properties. This suggests that it is not necessarily the inherent rigidity of the ECM that affects cell function, but rather the ability of the ECM to transmit mechanical stresses which in turn feed into downstream cellular pathways. In support of this hypothesis, studies which combined measurements of cell-generated traction stresses, modulations of substrate rigidity, and pharmaceutical manipulation of cytoskeletal contractility revealed that increasing or decreasing the contractility of cells and thereby the stresses generated at FAs could override rigidity or geometry dependent effects. Mesenchymal stem cells cultured on islands of adhesive proteins that either restrict or permit spreading will tend to differentiate more favorably toward adipogenesis or osteogenesis respectively (McBeath, Pirone et al. 2004; Fu, Wang et al. 2010). Cells on smaller islands generate lower traction stresses than those on larger islands, which is thought to be a key factor in the differentiation switch. In support of this, increasing cellular contractility on small islands led to increased osteogenesis, while inhibiting contractility on large islands suppressed both adipogenesis and osteogenesis. Moreover, gradients in traction stresses have been shown to correlate with gradients in proliferation in multicellular sheets of epithelial cells (Nelson, Jean et al. 2005). These data reveal a central role for cell tractions in regulating numerous cell behaviors.

2.5 Cellular tractions: measurements from single isolated cells

In 1980, Albert Harris pioneered the technique of using elastic substrata to visualize the tractions of individual cells. In this method, cells are cultured on a thin film of crosslinked silicon on top of a lubricating fluid (Harris, Wild et al. 1980). As the cell spreads and migrates, it exerts forces on the substrate, which generates wrinkles within the film. By knowing the mechanical properties of the film, the wrinkles may be correlated to the forces exerted by the cell (**Figure 2.1**). Improvements to this technique have resulted from incorporating fiduciary markers into the substrate and by replacing the silicon film with a polyacrylamide gel that permits experimental control over mechanical characteristics. These advances have developed into the technique of traction force microscopy (TFM), which permits the visualization of traction fields with

subcellular resolution (Dembo and Wang 1999; Balaban, Schwarz et al. 2001; Butler, Tolic-Norrelykke et al. 2002) (**Figure 2.2**). However, while tracking discrete markers greatly enhanced the resolution of observed traction fields, there are inherent disadvantages to measuring forces on continuous elastic substrata where the displacement at one point in space is affected by the convolution of all forces. Additional techniques have been developed which permit independent measurement of cellular force at discrete points along the cell surface. Cantilever arrays consist of vertically mounted beams spaced at regular intervals. Cells spread across the tops of these beams and exert tractions which can be observed by recording the bending of each individual beam (Tan, Tien et al. 2003) (**Figure 2.3**). More recently, FRET across integrin/ligand bonds at FAs has been utilized to report the magnitude of tractions exerted by cells on 2D and in 3D matrices (Kong, Polte et al. 2005; Huebsch, Arany et al. 2010). It should be noted, though, that this method provides only a scalar quantification of the tractions applied by cells and lacks any directional information. Finally, the finite element method has recently been used to extend traditional TFM techniques into the measurement of both tangential and normal forces exerted by cells on top of 2D planar substrates (Hur, Zhao et al. 2009; Maskarinec, Franck et al. 2009; Delanoe-Ayari, Rieu et al. 2010). Notably, the studies reported large downward displacements around the central regions of spreading cells, hypothesized to be caused by the nucleus pushing down as the cell cortex compresses it (Hersen and Ladoux 2011). The downward push is theorized to balance out the pulling force that is detected near the cell periphery, for the overall force has to be zero. In another study, the push and pull forces are found at the leading edge, trailing back, and the central areas of migrating cells at various times, suggesting a more dynamic distribution of cellular forces (Maskarinec, Franck et al. 2009). Taken together, these TFM methods show that cells generate mechanical forces in all three dimensions. However, assessing the resolution of the traction mappings in these systems has been challenging, and there is no clear agreement on the location of the normal or shear forces relative to key subcellular structures, such as adhesions and actin. The relationship between 3D cell traction forces and cytoskeletal structures will be addressed in Chapter 3 of this thesis – "Develop computational and experimental methods to measure the 3D mechanical tractions exerted by cells cultured on planer elastic substrates (2.5D TFM)."

While recent studies have extended traditional 2D TFM to allow detection of 3D forces exerted by cells cultured on top of 2D planar substrates, several recent high visibility studies have found that cellular differentiation and migration are altered when cells are fully encapsulated within a 3D hydrogel matrix as compared to cultured on a 2D surface. Importantly, while the

presence of cellular traction has been shown to be critical for cellular differentiation and migration in 3D matrices (Fraley, Feng et al. 2010; Huebsch, Arany et al. 2010), directly measuring these cellular tractions in 3D remains challenging. The computational and experimental methods necessary to extend 2.5D TFM into fully 3D matrices will be addressed in Chapter 4 of this thesis – "Develop an approach to measure the 3D mechanical tractions exerted by cells fully encapsulated within 3D hydrogel matrices (fully 3D TFM)."

Commensurate with the increasing appreciation for the role of mechanical forces in biology, numerous methods have been developed to measure the forces generated by cells with sub-cellular accuracy. The majority of such techniques utilize continuous elastic substrates to report cell traction forces. However, converting a measured displacement field within the substrate to the source tractions exerted by cells requires inversion of an ill-posed mathematical problem. These classes of problems are often unstable and typically require regularization to generate a reasonable solution. Due to this fact, the accuracy of the traction recovery depends on several factors including accuracy and density of displacement measurements, an accurate choice of the regularization parameter (or optimal smoothing of the displacement field), as well as the magnitude and spatial frequency of the loadings themselves (since the displacement field will decay more rapidly for smaller or more rapidly varying tractions). While improvements have been made to optimize each of these parameters, there has thus far been lacking a quantitative metric to assess the accuracy and potential improvements offered by a given modification. This discrepancy has made it difficult to compare cell traction measurements obtained with different techniques and makes it challenging to verify the biological conclusions drawn from a given measurement. A simple method to fully characterize the resolution and sensitivity of traction force measurements obtained using different methods and under a variety of experimental conditions could provide a standard metric to assess TFM data. In Chapter 5 of this thesis, I will utilize Fourier decomposition of simulated traction fields to present– "A quantitative platform to characterize the resolution and sensitivity of cellular traction measurements."

2.6 Cellular tractions: measurements from muscles and multicellular constructs

The first studies of mechanotransduction stemmed from experiments performed not on single cells, but on isolated muscle tissue. In the 1920's and 1930's A.V. Hill and others pioneered many of the experiments that defined the central dogma of biological force production

when they recorded the generation of millinewton scale forces by isolated amphibian muscles (Hill 1922; Hill 1938; Fung 1967). Indeed, analysis of length-tension and force-velocity curves was a critical complement to biochemical studies performed at the same time in leading to the discovery of the actin-myosin contractile element. Importantly, these same relations (i.e. the myosin driven sliding of cross-linked actin filaments) apply for non-muscle cells as well (Vicente-Manzanares, Ma et al. 2009). However, while measurements of forces from isolated tissues are physiologically relevant, they represent a combination of both cell generated and ECM dissipated loads and are limited in the number of experimental manipulations that can be performed. To address these concerns while still maintaining a physiologically relevant 3D environment, researchers have focused primarily on studies of cells seeded in hydrogel matrices such as collagen or fibrin (Kolodney and Wysolmerski 1992; Wozniak, Desai et al. 2003; Sieminski, Hebbel et al. 2004). Centimeter scale constructs recapitulate many of the properties of *in vivo* tissues (Eschenhagen, Fink et al. 1997; Asnes, Marquez et al. 2006), and the mechanical contributions from the constituent cells can be inferred from changes in the properties of the bulk gel (Grinnell 1994) or from the force generated by the construct against an isometric strain gauge (Wakatsuki, Kolodney et al. 2000) (**Figure 2.4**). Contractility antagonists can be used to decouple the active contractile element of the cells from the passive mechanical properties of the matrix which itself can be tuned in rigidity and composition (Wakatsuki, Kolodney et al. 2000; Zahalak, Wagenseil et al. 2000; Marquez, Genin et al. 2005). Useful insights have been gained with these systems, including the role of myosin light chain phosphorylation and Rho kinase in regulating *in vivo* cellular contractility (Kolodney and Elson 1993; Kolodney and Elson 1995; Wozniak, Desai et al. 2003). However, because the forces generated by centimeter-scale constructs are integrated over a large number of cells, these studies may be insensitive to local heterogeneities in cell forces or signaling. Additionally, while hydrogels more closely approximate the stiffness and chemical composition of the 3D microenvironment than do 2D substrates, force measurements are obscured by the complex properties of the matrix. While less complex than *in vivo* tissues, the mechanical properties of reconstituted collagen gels for example are heterogeneous, viscoelastic, non-affine, anisotropic and time varying. This implies that force measurements at the cellular level will be spatially and temporally dependent as well as influenced by the prior history of stress and strain. These characteristics make the high-resolution determination of cell traction forces within these constructs difficult if not impossible. Finally, due to the size of previously engineered constructs, heterogeneous oxygen concentrations and transport limitations may further confound results. I will develop a microfabricated platform to

measure forces from microscale encapsulations of cells in collagen gels in Chapter 6 of this thesis – "Utilize micro-electro-mechanical (MEMS) based approaches to measure the forces and stresses present in micropatterned, multicellular tissue constructs." By dramatically reducing the size of traditional collagen-based tissue constructs, I hope to minimize issues of heterogeneity and reduce diffusion limitations while still maintaining a physiologically relevant 3D environment.

2.7 Stresses in the ECM: how are cellular tractions propagated?

As individual cells contract, these forces are transmitted through integrins to the surrounding ECM. While much work has previously focused on the stresses present at the integrin/ECM interface (i.e. at FAs), the transmission of cell-generated tractions may also cause alterations to the structure and composition of the ECM molecules themselves. By using a FRET based biosensor of Fn conformation, cell generated tractions have been shown to unfold polymerized Fn fibrils at the molecular level, thus uncovering cryptic binding sites that may in turn alter cell function (Baneyx, Baugh et al. 2002). In addition, these tractions can trigger the release of growth factor stores in the ECM (Wipff, Rifkin et al. 2007), thereby providing a link between mechanical and soluble stimuli. Fibronectin (Fn) is a major component of the ECM that is critical for survival (George, Georges-Labouesse et al. 1993) and is up-regulated in morphogenetic events such as embryogenesis, wound healing and angiogenesis (Grinnell, Billingham et al. 1981; Boucaut and Darribere 1983; Khan, Chan et al. 2005). It is secreted by cells as a dimer that is composed of 230-270 kDa subunits. Each subunit consists of three types of repeating units (type I, II, and III) that contain sites for interaction with receptors at the cell surface, with other ECM molecules and for self assembly (i.e. interaction with other Fn molecules) (Mao and Schwarzbauer 2005). Fn is encoded by a single gene that can be alternatively spliced at three sites to generate the two forms found *in vivo*: an inactive plasma-soluble dimer that is secreted by hepatocytes (plasma Fn) and in a form secreted by fibroblasts and other cells that is incorporated into a fibrillar matrix at the cell surface (cellular Fn). Plasma and cellular Fn are differentiated by the presence of alternative splice isoforms incorporating extra type III domains which are labeled EIIIA and EIIIB and are present in varying concentrations in cellular, but not in plasma Fn (Schwarzbauer, Patel et al. 1987). Importantly, both cellular and plasma Fn can be assembled into insoluble fibrils by cells. The mechanisms governing this assembly are an active area of investigation, but it is known that fibril assembly proceeds through dimer binding to $\alpha 5\beta 1$ integrins at the cell surface (Mosher, Fogerty et al. 1991) and that fibril growth often proceeds in a coordinated manner with growth of actin stress

fibers (Sechler and Schwarzbauer 1997). Once assembled into fibrils, the conformation of the Fn polymers can be altered by cell-generated tractions to expose cryptic binding sites and thereby change the affinity for binding to integrins or to other ECM proteins (Smith, Gourdon et al. 2007). Interestingly, the assembly and persistence of a stressed Fn matrix has been shown to be essential for the assembly of other ECM matrices such as collagen I and thrombospondin-I (Sottile, Shi et al. 2007) and FA structure and composition are altered on 3D fibrillar Fn when compared to cells cultured on Fn adsorbed to glass (Cukierman, Pankov et al. 2001). These results suggest the presence of a feedback loop between cell-generated tractions and ECM structure and composition. In chapter 7 of this thesis, I will combine micropatterned tissue samples with a FRET based biosensor of Fn conformation to – "Investigate the interplay between cell generated forces, tissue stresses, and fibronectin conformation within 3D matrices."

2.8 Summary

All cells possess the necessary machinery to generate mechanical force. The presence of these forces drives morphogenetic events and can feedback through stresses at FAs and through changes in ECM conformation to alter cell phenotype. However, studies of the role of these forces have been hindered by a lack of methods to measure cell-generated forces in physiologically relevant 3D settings. It is the goal of this work to develop and characterize new methods that will allow accurate measurement of cell-generated forces and matrix remodeling both from single isolated cells and from microscale collagen-based tissue constructs. It is my hope that both the methods and the results uncovered through their implementation will represent a significant contribution to the field of mechanotransduction.

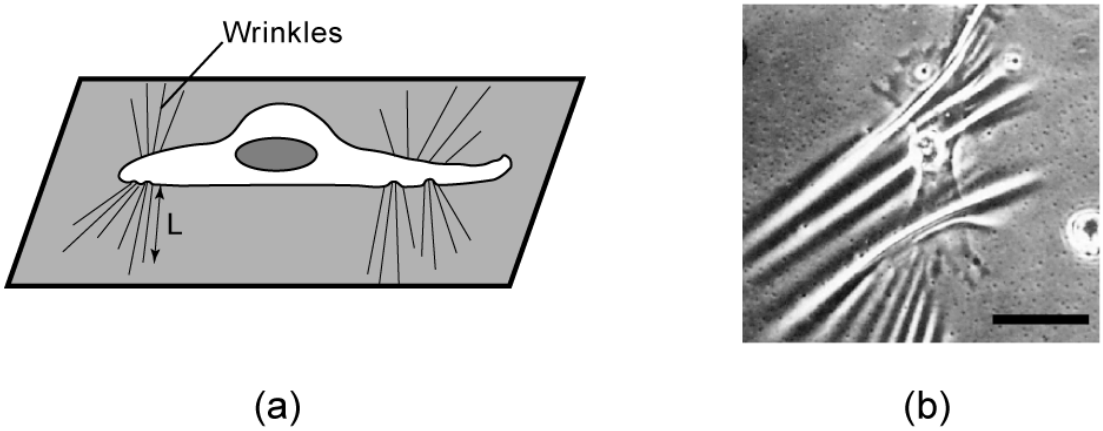

Figure 2.1: Wrinkling silicone membranes for measuring traction forces. (**a**) Cells plated onto a thin film of silicone exert traction forces that wrinkle the membrane. Measurement of cellular tension is inferred qualitatively by the length (L) and number of wrinkles in the silicone film. (**b**) Phase contrast micrograph of a cell on a wrinkling silicone membrane. Adapted from (Kelley, D'Amore et al. 1987). Scale bar: 50 μm.

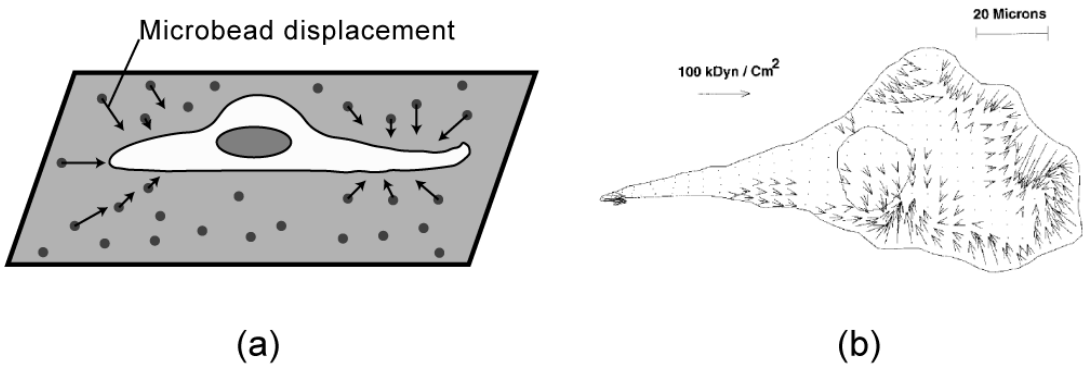

Figure 2.2: Traction force microscopy. (**a**) Cells exert traction forces that deform the elastic substrate and displace the microbeads that are embedded within it. (**b**) Example of the spatial traction force vector maps that are inferred from the displacement field. The scale arrow denotes the range of traction forces measured. Adapted from (Dembo, Oliver et al. 1996).

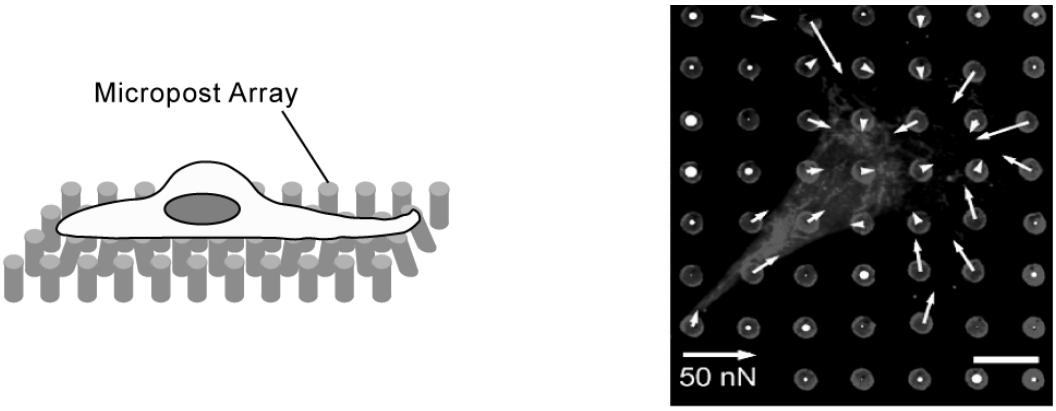

Figure 2.3: Micropost array for force measurements. (**a**) Microfabricated array of vertical microposts deflect and report the local traction force of the adherent cell on the tops of the microposts. (**b**) Representative micrograph of the measured displacements of the microposts tips and the corresponding traction forces. Scale arrow indicates the range of traction forces. Adapted from (Tan, Tien et al. 2003). Scale bar: 10 μm.

CHAPTER 3: CELLS ON PLANAR SURFACES EXERT ROTATIONAL MOMENTS ABOUT FOCAL ADHESIONS*

***The work in this chapter was performed in collaboration with Colin K. Choi.**

3.1 RATIONALE

Understanding how cells generate and respond to mechanical forces is critical in cell biology. In anchorage-dependent cells, myosin-II cross-links and contracts actin filaments to generate tension, which is transmitted to the ECM via integrin-mediated adhesions (Balaban, Schwarz et al. 2001; Beningo, Dembo et al. 2001; Vicente-Manzanares, Ma et al. 2009). The traction stresses (force per area) exerted between these adhesions and the extracellular matrix (ECM) drive cell spreading and migration in critical events such as tissue morphogenesis (Gumbiner 1996; Discher, Janmey et al. 2005), wound healing (Hinz, Mastrangelo et al. 2001) and tumor metastasis (Munevar, Wang et al. 2001; Friedl and Gilmour 2009). In addition, these stresses have been shown induce changes in adhesion signaling, cytoskeletal reorganization, and gene expression (Ingber 1991; Vogel and Sheetz 2006; Geiger, Spatz et al. 2009; Parsons, Horwitz et al. 2010; Schwartz 2010), thereby regulating numerous cell functions, such as proliferation (Chen, Mrksich et al. 1997; Nelson, Jean et al. 2005) and differentiation (Engler, Sen et al. 2006; Fu, Wang et al. 2010).

Sub-cellular resolution measurements of traction stresses have advanced our understanding of mechanotransduction and enabled quantitative modeling of cellular interactions with the ECM (Sabass, Gardel et al. 2008; Aratyn-Schaus and Gardel 2010; Hoffman, Grashoff et al. 2011). One consistent trend these measurements reveal is that cells exert inwardly oriented tractions at their periphery, where focal adhesions (FAs)grow centripetally (Geiger, Spatz et al. 2009; Gardel, Schneider et al. 2010; Parsons, Horwitz et al. 2010). However, the vast majority of the methods (collectively termed traction force microscopy, TFM) have assumed that cells exert only shear forces (parallel to the plane of the substrate). Interestingly, recent TFM studies have demonstrated that cells on planar substrata induce significant vertical deformations which are due to out of plane, normal tractions, indicating that cellular forces are much more complex than previously thought (Hur, Zhao et al. 2009; Maskarinec, Franck et al. 2009; Delanoe-Ayari, Rieu et al. 2010; Franck, Maskarinec et al. 2011). However, generating a high spatiotemporal resolution of the traction mappings in these systems has been challenging, and there is no clear agreement on the dynamics and the location of the normal forces. Thus, how normal and shear traction stresses are integrated and what type of net forces is produced relative to FAs and the actin cytoskeleton remains poorly understood.

In this study, we developed a high-resolution 2.5D TFM (measurement of 3D forces exerted by cells on 2D planar surfaces as opposed to cells fully encapsulated within a 3D matrix

(Legant, Miller et al. 2010)) to explore the precise nature of cellular forces applied to the ECM. After fully characterizing the resolution of both the shear and normal forces using numerical simulations, we applied this approach to fibroblasts expressing GFP-tagged paxillin, actin, or farnesyl (membrane marker) to measure the full multi-dimensional traction stresses relative to FAs and the actin cytoskeleton. We find that cells exert shear and normal tractions around the termini of actin stress fibers and under FAs at the cell periphery. In the nuclear and peri-nuclear regions where FAs are not highly present, both shear and normal tractions are low. When these traction components are integrated, the measurements show significant rotational moments exerted about FAs. Furthermore, the moments are highly dynamic as their wave-like profiles translate spatially and temporally with protruding and retracting cell edges during cell spreading and migration. Finally, we generated a finite element (FE) model of the FA and pliable substrate and combined this model with 3D super resolution imaging to explore the most plausible means by which such moments may be generated subject to geometrical constraints within a very thin (200-300 nm) cellular lamella.

3.2 MATERIALS AND METHODS

3.2.1 Cell culture and plasmids

Spontaneously immortalized mouse embryonic fibroblasts (MEFs) were cultured in DMEM (Cellgro by Mediatech, Inc.) with 5 % fetal bovine serum (Klein, Yung et al. 2007) (Richard Assoian, University of Pennsylvania, Philadelphia, PA). MEFs were transfected transiently with paxillin-EGFP, EGFP-actin, and mEGFP-farnesyl-5 (Clare Waterman, National Institutes of Health, Bethesda, MD) using Lipofectamine 2000 (Invitrogen) or TransIT-LT1 (Mirus). Transfected cells were plated on hydrogels for at least 3 hours to allow spread fully before image acquisition.

3.2.2 Preparation of polyethylene glycol substrates and mechanical characterization

Polyethylene glycol (PEG)-based hydrogels with Arginine-Glycine-Aspartic (RGD) were synthesized as described previously (Miller, Shen et al. 2010). Briefly, dry PEG (MW 6000; Sigma-Aldrich, St. Louis, MO) was acrylated to generate PEG-diacrylate (PEGDA) by reaction with triethylamine (TEA) and acryloyl chloride in anhydrous dichloromethane under argon. Separate PEG-RGD macromers were generated by reacting PEGDA with monocystein CGRGDS peptides by dissolution in 100mM sodium phosphate, pH 8.0, followed by filtration through a 0.22 μm PVDF membrane (Millipore, Billerica, MA), dialysis, and lyophilization. To make flexible 2D substrates for TFM experiments, PEGDA and PEG-RGD macromers were dissolved in phosphate buffered saline (PBS) pH 7.4, and these prepolymer solutions were mixed with 0.2 mm diameter, nonfunctionalized fluorescent beads (suncoast yellow; Bangs Labs, Fishers, IN). The final concentrations for PEG and RGD were 5.5 wt % and 10 mM, respectively. The mixture was pipette onto coverslips that were functionalized with 3-(trimethoxysilyl)propyl methacrylate (Sigma-Aldrich) and flattened by top coverslips, treated with SurfaSil (Thermo Scientific, Waltham, MA) per the manufactuere's instructions. For polymerization, the prepolymer mixture between the coverslips was exposed to 100 mW / cm^2 UV light for 30 sec using Omnicure S2000 (Lumen Dynamics, Mississauga, Canada). Next, the top coverslips were removed from the 2D hydrogel substrates that were covalently linked the bottom coverslips. The substrates were incubated in PBS at 37 °C for at least 24 hours to allow swelling, and PBS was replaced with cell culture media prior to cell plating.

The shear modulus of PEG hydrogels was measured using an AR 2000 rheometer (TA Instruments, New Castle, DE), equipped with a temperature-controlled Peltier plate at 37 °C and

a 20 mm stainless steel plate geometry. Hydrogel samples were prepared and swollen using identical reagents and methods as the substrates for the 2.5D TFM experiments. With the geometry head in contact with the hydrogel, strain sweeps of 1 % and 5 % at 0.25 Hz were performed, followed by frequency sweeps from 0.1 – 10 Hz at 1 % strain. Data were collected from multiple measurements of three independent samples. The Young's modulus was calculated from the shear modulus using the Poisson ration of 0.34.

3.2.3 Image acquisition

All cells were imaged with a 60x, 1.2 numerical aperture (N.A.), water immersion objective (UPLSAPO 60XW, Olympus, Tokyo, Japan.) attached to an Olympus IX71 inverted microscope equipped with a CSU10 spinning disc confocal scan head (Yokogawa Electric Corporation, Tokyo, Japan), live cell incubator (Pathology Devices) and the ImagEM 16-bit EMCCD camera (Hamamatsu Photonics, Hamamatsu City, Japan). A 98 x 98 x 15 μm volume was imaged around each cell to incorporate the entire cell volume and approximately 15 microns of hydrogel below the cell. These parameters corresponded to voxel dimensions of 0.1917 x 0.1917 x 0.5 μm in the horizontal and axial planes, respectively. After the stressed image was acquired, the cells were treated with 0.5% Sodium dodecyl sulfate (SDS) detergent (JT Baker, Center Valley, PA), re-equilibrated for 10 min, and then re-imaged to acquire a reference image of the non-stressed hydrogel. Timelapse datasets were acquired at time intervals ranging from 30 sec to 3 min. Super-resolution structured illumination images were acquired as described previously (Shao, Kner et al. 2011).

3.2.4 Calculation of bead displacements

Multipage TIFF images of the hydrogel exterior to the cell were imported into Matlab (The Mathworks, Inc., Natick, MA) and bead centroids were identified as described previously (Legant, Miller et al. 2010). Once bead centroids were identified, beads in the stressed (subject to cell generated tractions) dataset were matched to beads in the relaxed (after cell lysis) dataset using a previously described feature vector-based algorithm relating the relative position of each bead to its local neighbors (Legant, Miller et al. 2010). To correct for mechanical drift, regions of the hydrogel that were significantly far from the cell were indicated by the user in each dataset. The displacement of these beads should be only affected by mechanical drift and not by cell generated tractions, thus the mean displacement of beads in these regions was used to correct for

drift in the rest of the dataset. Bead displacements were then interpolated onto a uniform grid within the hydrogel top 5 μm of the hydrogel. In this manner, the set of reference locations of the displacements are constant for all time points and datasets. This fact allows the use of a single singular value decomposition of the Green's matrix for all datasets as described below and dramatically decreases the computational expense of computing cell tractions.

3.2.5 Generation of a discretized Green's function and calculation of cellular tractions

We generated a discretized Green's function relating tractions on the cell surface to displacements within the gel using the finite element method. To approximate a semi-infinite halfspace, we generated a 3D tetrahedral mesh of a 300 μm wide by 300 μm long by 60 μm tall volume using Abaqus CAE. A 100 μm square central portion of the top surface corresponding to the region at which cell tractions are exerted was discretized separately to have 6080 triangular elements, corresponding to an average element area of approximately 1.64 μm^2. We then solved the forward finite element solution under the linear small strain approximation to relate the nodal displacements in the gel to unit tractions applied to each facet on the aforementioned surface in each of the three Cartesian directions (18,240 total solutions). From each of these solutions, the displacement grid locations were queried for the computed displacements. Because both the bead coordinates and the location of applied tractions are at discrete locations, the relation between bead displacements within the gel $\bar{\boldsymbol{u}}$ and tractions on the surface of the cell $\bar{\boldsymbol{T}}$ is now transformed into a set of linear equations

$$\bar{\boldsymbol{u}} = \Gamma \bar{\boldsymbol{T}} \quad (1)$$

where we have adopted the notation used in (Schwarz, Balaban et al. 2002) in which

$$\bar{\boldsymbol{u}} = [u_1(\bar{\boldsymbol{r}}_1); u_2(\bar{\boldsymbol{r}}_1); u_3(\bar{\boldsymbol{r}}_1); u_1(\bar{\boldsymbol{r}}_2); u_2(\bar{\boldsymbol{r}}_2); u_3(\bar{\boldsymbol{r}}_2); \dots; u_1(\bar{\boldsymbol{r}}_m); u_2(\bar{\boldsymbol{r}}_m); u_3(\bar{\boldsymbol{r}}_m)]$$

is a 3m column vector, where m is the number of tracked beads and $\bar{\boldsymbol{r}}$ is the position vector of each bead.

$$\bar{\boldsymbol{T}} = [T_1(\bar{\boldsymbol{r}}'_1); T_2(\bar{\boldsymbol{r}}'_1); T_3(\bar{\boldsymbol{r}}'_1); T_1(\bar{\boldsymbol{r}}'_2); T_2(\bar{\boldsymbol{r}}'_2); T_3(\bar{\boldsymbol{r}}'_2); \dots; T_1(\bar{\boldsymbol{r}}'_n); T_2(\bar{\boldsymbol{r}}'_n); T_3(\bar{\boldsymbol{r}}'_n)]$$

is a 3n column vector, where n is the number of discretized facets on the surface of the cell and $\bar{\boldsymbol{r}}'$ is the position vector of each facet. Subscripts for both *u* and *T* in these definitions represent displacements and tractions respectively along each Cartesian axis.

$\boldsymbol{\Gamma}$ is an m x n matrix of the following form:

$$\boldsymbol{\Gamma}_{ij}^{mn} = \begin{bmatrix} G_{ij}^{11} & \cdots & G_{ij}^{1n} \\ \vdots & \ddots & \vdots \\ G_{ij}^{m1} & \cdots & G_{ij}^{mn} \end{bmatrix} \quad (2)$$

Each element of $\boldsymbol{\Gamma}$ is a 3 x 3 submatrix relating the displacement of bead m in direction i in response to a load on facet n in direction j:

$$\boldsymbol{G}_{ij} = \begin{bmatrix} g_{11} & g_{12} & g_{13} \\ g_{21} & g_{22} & g_{23} \\ g_{31} & g_{32} & g_{33} \end{bmatrix} \quad (3)$$

We used 0[th] order Tikhonov regularization together with the L-curve criterion(Hansen 2001) for implementing and choosing the correct value for the Lagrange parameter, λ resulting in the following optimization:

$$min\{|\boldsymbol{\Gamma}\bar{\boldsymbol{T}} - \bar{\boldsymbol{u}}|^2 + \lambda^2|\bar{\boldsymbol{T}}|^2\} \quad (4)$$

This optimization problem was solved by singular value decomposition using the suite of Matlab routines "*Regularization tools*" by PC Hansen (Hansen 2007). As the reference bead centroids were identical between all time points, only a single decomposition $\boldsymbol{\Gamma}$ is required to solve for the tractions at each time point. Renderings of cellular tractions were computed in Tecplot 360 (Tecplot Inc., Bellevue, WA), and contour plots were scaled such that approximately 1% of all elements on the cell were saturated.

3.2.6 Measurement of TFM sensitivity and resolution

In order to fully characterize the sensitivity and resolution of our traction measurements, we adopted a technique similar to that described in (Legant, Miller et al. 2010). Briefly, we

generated sinusoidally varying load distributions across the surface of the hydrogel with progressively decreasing wavelength (increasing spatial frequency). The vector valued traction distribution can be decomposed into scalar valued function multiplied by basis vectors. We chose the traditional basis vectors to be aligned with the Cartesian axis except that we rotated them such that the in-plane basis vectors were aligned parallel and perpendicular with the direction of wave propagation. In order to fully characterize the TFM response, we applied loadings at the hydrogel surface as transverse sinusoidal waves of three types: 1) Shear loads in which the direction of force application was orientated perpendicular to the direction of wave propagation, 2) shear loads in which the direction of force application was oriented parallel to the direction of wave propagation, and 3) normal tractions with the forces oriented into and out of the planar halfspace (**Figure 3.1**). For each loading, we solved the forward finite element problem to compute the displacement field within the surrounding hydrogel at the afformentioned grid locations. Experimentally measured levels of noise (taken by measuring bead displacements before and after treatments with SDS in cell-free regions of the hydrogel) were then superimposed onto these displacements. Tractions were then recovered as described above compared to the initial loadings (**Figure 3.1**).

3.2.7 Finite element modeling

Finite element simulations of adhesions were carried out in Abaqus utilizing the finite strain option (NLGEOM). The PEG hydrogel was modeled as a 200 x 200 x 60 μm cube with *ENCASTRE boundary conditions along the bottom surface. The material was treated as a NeoHookean solid according to

$$U = C_{10}(\bar{I}_1 - 3) + \frac{1}{D_1}\left(J^{el} - 1\right)^2 \quad (5)$$

where U is the strain energy per unit of reference volume, C_{10} and D_1 are material parameters, $\bar{I}_1 = \bar{\lambda}_1^2 + \bar{\lambda}_2^2 + \bar{\lambda}_2^2$ is the first deviatoric strain invariant. The deviatoric stretches are defined as $\bar{\lambda}_i = J^{-\frac{1}{3}}\lambda_i$ where λ_i are the principal stretches and J is the total volume ratio. $J^{el} = J$ for isothermal conditions. The initial shear modulus and bulk modulus and bulk modulus are given by $\mu_0 = 2C_{10}$ and $\kappa_0 = \frac{2}{D_1}$ respectively. Values of C_{10} and D_1 were computed using the measured shear modulus of 2431 Pa. The bulk modulus was computed based on a measured Poisson ratio

for the PEG hydrogels of 0.34 via $\kappa_0 = \frac{2\mu_0(1+\nu)}{3(1-2\nu)}$ as 6787 Pa. The FA was modeled as a 150 nm tall elliptical plate with major and minor axis of 6 and 2 μm respectively. The FA material was treated as linearly elastic with a Young's modulus of 2.431 MPa (373 times more rigid than the initial modulus of the PEG hydrogel) and a Poisson ratio of 0.49. The bottom surface of the adhesion was tied to the PEG hydrogel using the surface to surface *TIE constraint in Abaqus. A shear load was applied to the upper surface of the adhesion using *DSLOAD in Abaqus. The magnitude of this load was increased until the horizontal displacements of the hydrogel matched those observed experimentally. An optimal match for the horizontal displacements was observed for a shear load of approximately 2.917 kPa.

For studies simulating the effect of a ventral cortex, the FA was contiguous with a 150 nm tall surrounding sheet anchored at the opposite end (approximately 50 μm behind the edge of the adhesion) using the *ENCASTRE boundary conditions. The interaction between the cortex and the PEG hydrogel was treated as either frictionless or tied in the tangential or normal directions to the interface respectively. The material properties of the cortex were treated as linearly elastic. The Young's modulus of the cortex and the applied shear load were calibrated to generate horizontal and vertical deformations that closely matched our experimental observations. Optimal matches were found for a cortex stiffness of 1.2155 MPa and a shear load of 10.9 kPa. All simulations were modeled utilizing a symmetry boundary condition cutting vertically through the center plane of the adhesion.

3.3 RESULTS

To determine precise cellular traction fields relative to cytoskeletal structures, we first investigated MEFs expressing EGFP-actin. We plated cells on RGD-conjugated PEG hydrogels containing fluorescent beads and allowed them to spread before acquiring volumetric images (**Figure 3.2a**). Comparable to spreading on traditional cell culture substrata (e.g. glass, plastic) coated with natural ECMs, MEFs on PEG hydrogels spread initially in an isotropic manner, followed by anisotropic protrusions and polarization (Dubin-Thaler, Giannone et al. 2004). Once fully spread, cells were relatively flat, and high-resolution structured illumination microscopy (SIM) showed that lamella are approximately 200-300 nanometers tall, whereas the primary increase in height (up to 2-3 microns) occurs only near the nucleus. The 3D displacement field within the substrate was determined by tracking beads before and after lysing the cell with detergent. With this method, we found that the shear components of the displacements are present only at the cell periphery, which agrees with previous implementations of 2D TFM (Beningo, Dembo et al. 2001; Munevar, Wang et al. 2001; Aratyn-Schaus and Gardel 2010). For the vertical components, however, we found significant in plane and out of plane displacements underneath the thin cell periphery, while no displacements (neither in plane nor out of plane) could be detected under the cell nucleus (**Figure 3.2b and c)**. Closer inspection of the vertical displacements revealed that cells deform the hydrogel upwards under the leading edge and then downward approximately 20 μm behind the leading edge (**Figure 3.2d**). To quantify the traction stress from the displacement field, we followed a procedure similar to that outlined in (Legant, Miller et al. 2010). Briefly, we generated a tetrahedral mesh of the hydrogel volume under the cell. Unit tractions were then applied in each of the Cartesian directions at each facet on the surface, and the induced displacement fields were recorded after solving the forward problem for stress equilibrium. These traction-displacement mappings were used then to generate a discretized Green's function for the hydrogel volume, replacing the Boussinesq solution commonly used in 2D TFM. Before applying our 2.5D TFM method to cells, we sought to fully characterize the resolution limits of both the shear and normal traction reconstructions under experimentally relevant levels of noise and bead density. We determined the average spatial resolution of the tractions to be between 5 and 15 microns (for traction magnitudes that are between 5 and 20% of the hydrogel elastic modulus, or between approximately 325-1300 Pa). It is important to note that the traction resolution is inherently anisotropic, with normal tractions and shear tractions that are directed orthogonal to the spatial axis of variation having approximately 2

fold higher spatial resolutions than shear tractions directed parallel to the axis of spatial variation (**Figure 3.1**).

In agreement with the displacement field, we found that both shear and normal cellular traction stresses were limited to the cell periphery; negligible tractions were detected in the peri-nuclear and nuclear regions (**Figure 3.3a and b**). Interestingly, maximum shear tractions occurred at the termini of stress fibers (**Figure 3.3c**), whereas maximal upward and downward normal tractions were concentrated approximately 5 μm distal (toward cell periphery) and 5 μm proximal (towards cell center) to the stress fiber ends, respectively (**Figure 3.3d**). These differential tractions suggest that FAs, which grow at the ends of stress fibers and serve as the primary force-applying structure to the ECM, mediate localized torque in addition to shearing tractions (Chrzanowska-Wodnicka and Burridge 1996; Ponti, Machacek et al. 2004; Choi, Vicente-Manzanares et al. 2008; Kanchanawong, Shtengel et al. 2010). To determine the location of multi-dimensional tractions relative to FAs, we transfected MEFs with paxillin-EGFP, an adapter protein that localizes to integrin-mediated adhesions (Deakin and Turner 2008). As expected, the application of maximal shear traction occurred directly under the EGFP-paxillin decorated FAs near cell periphery (**Figure 3.3e and g**). Moreover, we detected upward and downward traction stresses distal and proximal of the adhesions, respectively, indicating that FAs serve as pivot points for rotational moments (**Figure 3.3f and h**). These moments were present in both the leading lamella and in retracting extensions of cells (**Fig. 3.3e and f**), and their magnitudes mirrored FA growth and disassembly. Taken together, these results reveal that shear tractions and rotational moments are generated under and around FAs, respectively, which establishes a more complex and intrinsic force distribution than previously described.

To examine whether rotational moments around FAs are present during dynamic cellular processes, we analyzed traction stresses of migrating or spreading MEFs. Cells were transfected with EGFP-farnesyl (a membrane localized GFP-tagged protein), and time-lapse volumetric stacks were acquired to follow and correlate the dynamic changes in cell shape to traction forces. Similar to fully spread and relatively stationary cells, both migrating and spreading cells generated rotating moments localized to protruding and retracting regions with maximum stress reaching ~500 Pa. In migrating cells, we found that shear and vertical tractions are highly dynamic, as their application sites progressed forward with the extending leading edge during migration (**Figure 3.4a and b**). Such discrete force distributions were also observed during initial cell spreading. As described previously, cells (including MEFs on PEG hydrogels) spread

initially in an isotropic manner and flatten against the substrate out as they become polarized. As the cell appears to compress itself against the substrate during spreading, we were curious whether out-of-plane tractions may also be present in this setting. We observed the emergence of both shear and normal forces shortly (approximately 20 minutes) after the cell adhered to the substrate (**Figure 3.4c and d**). Both the shear and normal forces were restricted to the leading lamella and both grew substantially during the first hour of spreading. In contrast to previous studies which showed substantial downward compression under the nucleus, we found no tractions under the cell nucleus, but observed instead the presence of outwardly propagating "waves" of rotational tractions that emerged in the perinuclear region and propagated outward with the leading edge of the extending lamella (**Figure 3.4d**).

3.4 DISCUSSION

In this study, we developed a high-resolution 2.5D TFM to investigate the generation of multi-dimensional cellular tractions at the cytoskeletal level. To our knowledge, these data are the first to show that cells exert discrete shear and normal tractions that produce dynamic rotational moments at FAs and associated actin stress fibers. Previous studies have reported the presence of normal forces exerted by cells in planar substrates (26-29), yet their specific location relative to the cytoskeletal structures was unknown. Here, we reveal that cells on planar substrates exert upward and downward forces near the distal and ventral ends of FAs, respectively, with a characteristic radius of approximately 20 μm. This demonstrates that the adhesions serve as pivots to mediate a torque on the ECM. The shear and normal traction stresses were localized in cell peripheries (e.g. protrusions, retracting tails), where FAs formed. The locations, magnitude, and dynamics of these tractions were characteristically consistent in polarized cells, migrating cells, as well as initially spreading cells, indicating that the rotational moment about adhesions is an intrinsic physical phenomenon coupled to cellular interactions with the ECM.

To examine how FAs in a thin cellular body, such as the ~200 nm tall lamellum, mediate a substantial out of plane moment, we generated a finite element model with assumptions derived from our current knowledge of cell adhesions. The model incorporates both the PEG hydrogel and a FA plaque and is solved for stress-equilibrium under the full non-linear stress-strain relationship. Based on a recent interferometric photoactivated localization microscopy (iPALM) study (Kanchanawong, Shtengel et al. 2010) and our SIM data, the FA in our working model is designed as a rigid plate 150 nm in height coupled to an elastic hydrogel substratum which was modeled as a Neo-Hookean solid. We assumed that the force transmitted on the ECM substrate is generated by myosin II, which cross-links and contracts actin filaments to pull on the physically linked adhesions (Chrzanowska-Wodnicka and Burridge 1996; Choquet, Felsenfeld et al. 1997; Geiger, Spatz et al. 2009; Vicente-Manzanares, Ma et al. 2009; Gardel, Schneider et al. 2010; Parsons, Horwitz et al. 2010) (**Figure 3.5a**). To mimic this mechanism, we applied a shear load to the top surface of the adhesion plate. The magnitude of this load was then scaled to induce a lateral ECM displacement of similar magnitude (~1 μm) to what was observed experimentally. As the material adjacent to the adhesion is compressed, shear lag from the top of the adhesion to the substrate causes the plate to rotate, thereby generating a moment (**Figure 3.5b**). In this setting, we find that a lateral ECM displacement of 1 μm corresponds to approximately 150 nm

vertical displacements generated at the distal and ventral ends of the adhesion (**Figure 3.5c and d**). However, as the experimentally measured vertical displacements exerted under FAs appeared to be significantly larger (~300 nm), we sought to determine means by which the rotation could be increased.

One possibility involves changing the location of the shear force exerted on FAs by actin stress fibers. By restricting the shear traction onto the leading 1/3 of the adhesion, our model produced significantly more rotation, although still slightly below what we measured experimentally (**Figure 3.6**). However, the increased vertical displacements were still slightly below what we measured in cells. In addition, our super-resolution SIM imaging revealed that actin fibers generally formed behind the leading edge of FAs, making this model scenario unlikely. Because FAs do not exist in isolation, but rather reside within a dense actin cortex, we were curious what would happen if we incorporated a rigid ventral actin cortex surrounding the FA plate into our model. The presence of separate dorsal and ventral actin layers in the cell has known for some time (Ponti, Machacek et al. 2004; Giannone, Dubin-Thaler et al. 2007; Svitkina 2007; Urban, Jacob et al. 2010), and more recently, 3D super-resolution, stochastic optical reconstruction microscopy (STORM) showed directly that the dorsal and ventral actin layers have dramatically different architectures in the vicinity of FAs (Xu, Babcock et al. 2012). In this model, the 150 nm tall adhesion plate resides within a 150 nm tall ventral cortex, and we applied a uniformly distributed shear load to the top surface of the adhesion. As the adhesion translates laterally, it compresses the cortex, which in turn applies a reactive force on the edge of the adhesion. This leads to increased rotation of the adhesion such that the experimentally measured vertical displacements could be recapitulated (**Figure 3.5d**). Interestingly, because the adhesion is now acting against the resistance of the ventral cortex in addition to the substrate, this model predicts that the shear load at the surface of the adhesion plate needs to be approximately 5 times larger than if we assume an isolated adhesion with no cortex. Thus, with ventral cortex in the model, only 20% of the total force generated by myosin II-mediated contraction is transmitted to the substrate by FAs, while the remaining 80% acts against the actin cytoskeleton. In support of this, the ventral actin cortex, as visualized in the aforementioned STORM study, appeared to be buckled as a series of arches with bases tethered to the substrate at FAs. Such buckling was not apparent in the dorsal actin layers. Together, these findings are strongly reminiscent of ventral buckling under compressive loading due to a dorsal contractile element and lend indirect support for our cytoskeletal model.

Our data and model show that all the forces (both shear and normal) are transmitted at the periphery of the cell. We find minimal forces exerted in the nuclear or peri-nuclear regions, whereas previous studies (Hur, Zhao et al. 2009; Delanoe-Ayari, Rieu et al. 2010) suggested a role for nuclear compression in causing a downward pushing force into the substrate. This discrepancy may be due to differences in cell type (fibroblasts vs. endothelial cells or *Dictyostelium*), cell shape (spread vs. round), or hydrogel rigidity (~6.5 kPa in this study vs. 400 Pa, ~4kPa for previous studies). Indeed, we observed that downward tractions are localized in the nuclear region in cells that are in the early phase of spreading (**Figure 3.4c and d**) or when we apply our method to cells on more flexible substrates (~1 kPa). However, even on flexible substrates once cells began to polarize, the normal tractions spread to the cell periphery (**Figure 3.7**).

The measurements of a discrete rotational moment around FAs demonstrate a more complex nature of cellular forces at the cell-ECM interface than the current model in the field. Cell-generated tension at adhesions has been depicted largely in 2D, as studies showed that adhesion growth, actin flow, and traction stresses are coupled and exhibit correlated planar dynamics (Balaban, Schwarz et al. 2001; Beningo, Dembo et al. 2001; Gardel, Sabass et al. 2008; Aratyn-Schaus and Gardel 2010). Via this relationship, mechanotransduction processes at adhesions are proposed to be regulated predominantly by shear forces that stretch adhesion proteins to induce signaling activity or conformation changes (Bershadsky, Kozlov et al. 2006; Hoffman, Grashoff et al. 2011). Our findings of rotational moment introduce additional factors to consider, including molecular compression, integrin engagement with the ECM via downward forces, and a balance between contractility and torque that may regulate adhesion-mediated signaling differentially. In addition, the mappings of multi-dimensional cellular forces and cytoskeletal structures presented here should find use in current models of cell migration and adhesion mechanobiology (Lauffenburger and Horwitz 1996; Pelham and Wang 1999; Chen 2008; Gardel, Schneider et al. 2010; Schwartz 2010; Barnhart, Lee et al. 2011). Future improvements to the spatial and temporal resolution of cell traction measurements in 2.5D and fully 3D (Legant, Miller et al. 2010) settings, combined with sub-diffraction limit imaging of the 3D cytoskeletal and adhesion architecture (Kanchanawong, Shtengel et al. 2010; Xu, Babcock et al. 2012) and dynamics within the lamella will be critical fully understanding how cells generate, sense and respond to mechanical forces in a variety of physiological settings.

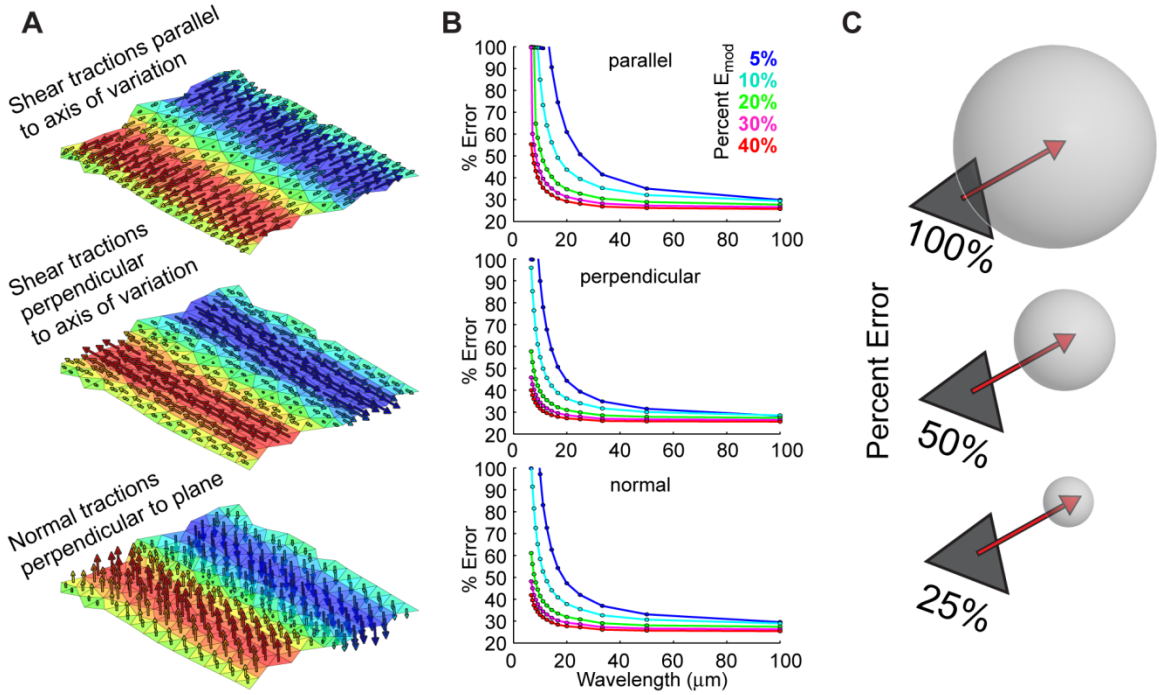

Figure 3.1: Numerical characterization of the sensitivity and spatial resolution of traction measurements. (**a**) Vector renderings of representative loadings displaying the orientation of the shear tractions and normal tractions used for TFM characterization. (**b**) Percent error of the recovered tractions is plotted as a function of wavelength of the applied loadings for each of the orientations shown in (**a**). All values were computed for experimentally relevant levels of bead density and displacement measurement error. (**c**) Graphical representation of the percent error (as expressed in (b). The recovered traction vector will be predicted to lie within a sphere centered at the tip of the true applied traction vector with a radius equal to the percentage error scaled by the magnitude of the applied traction vector.

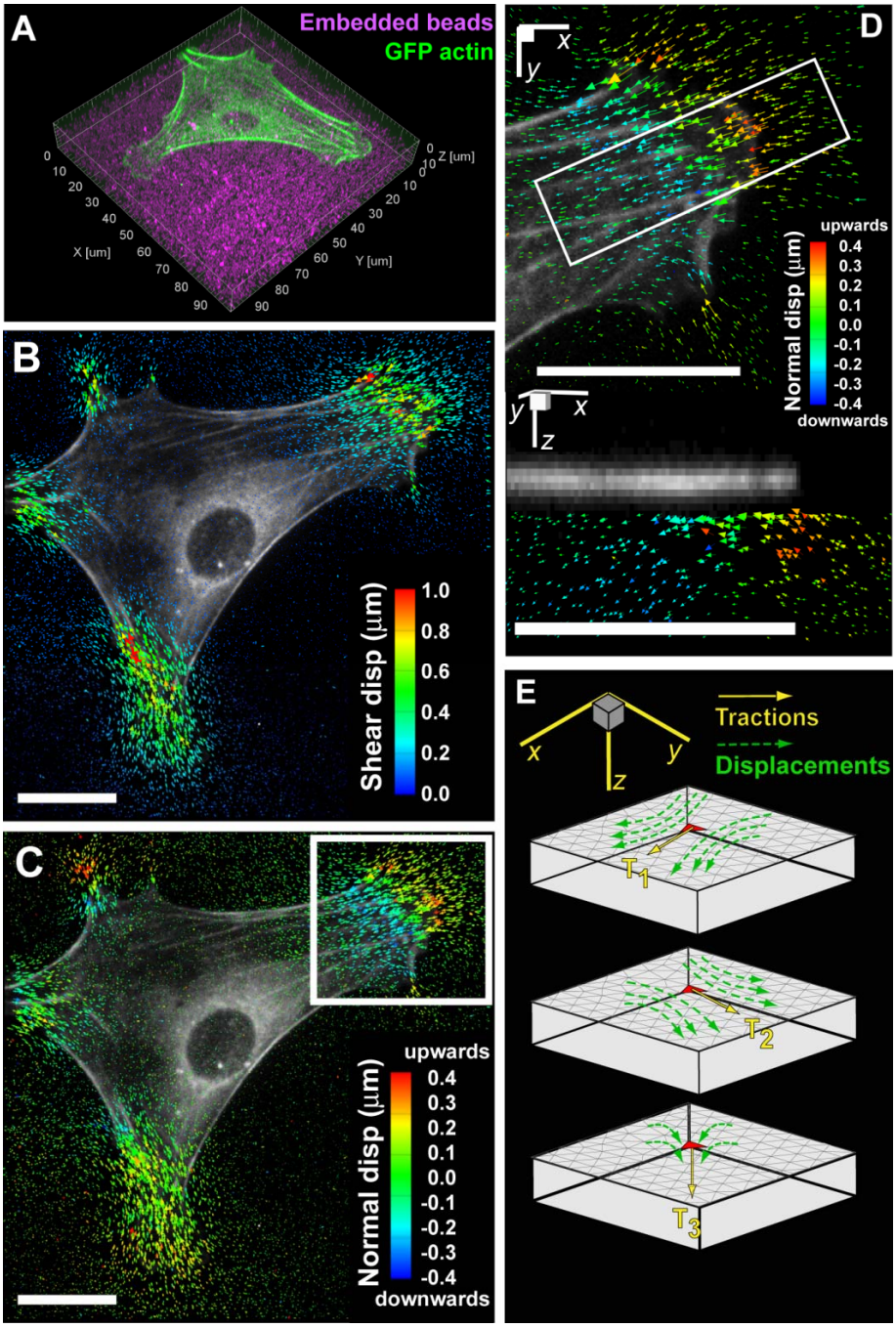

Figure 3.2: Experimental setup and computational methods. (**a**) Volume rendering of an EGFP-actin expressing mouse embryonic fibroblast (MEF) fully spread and polarized on a 2D PEG hydrogel with fluorescent beads imbedded (magenta). (**b**)-(**c**) Shear and normal components of bead displacement trajectories color-coded by magnitude. Scale bar, 20 μm. (**d**) Inset outlined in (**c**) magnified showing the normal component of bead displacement trajectories. Scale bar, 20 μm. The bottom figure is the cross-sectional view of the inset outlined above showing the multi-dimensional bead displacement trajectories. Scale bar, 20 μm. (**e**) Schematic of the finite element model to reconstruct the Green's function.

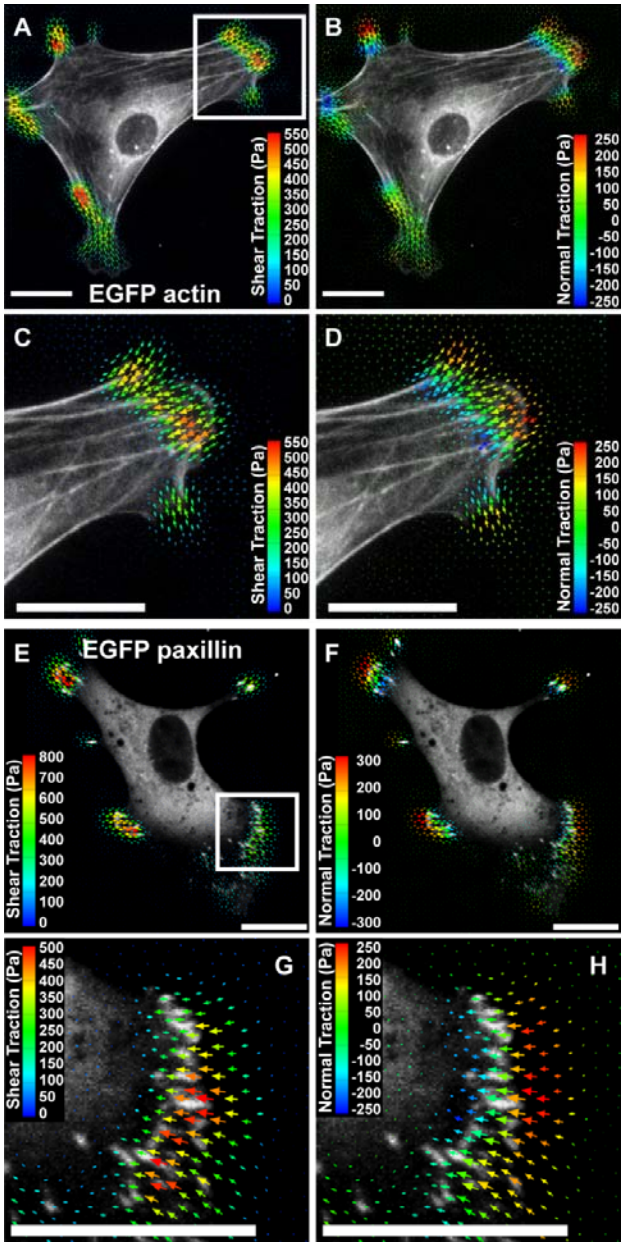

Figure 3.3: 2.5D Traction stress and cytoskeletal localization. (**a**)-(**b**) Shear and vertical traction stress vectors generated by a MEF expressing EGFP-actin. The vectors are color-coded by magnitude. Both components of traction stresses are localized to the cell periphery. (**c**)-(**d**) Inset outlined in (**a**) magnified showing shear and vertical traction stress vectors. Maximum shear stresses are detected at the termini of actin stress fibers, whereas the upward and downward normal stresses are applied in front and behind of the fiber ends, respectively. (**e**)-(**f**) Shear and normal traction stress vectors generated by a MEF expressing paxillin-EGFP are localized to focal adhesions in broad peripheral regions and a narrow retracting tail. (**g**)-(**h**) Inset outlined in (**e**) magnified showing shear and normal traction stress vectors relative to focal adhesions. Maximum shear stresses are detected directly over elongated focal adhesions, whereas the upward-to-downward gradient of normal stresses forms rotational moment around the adhesions.

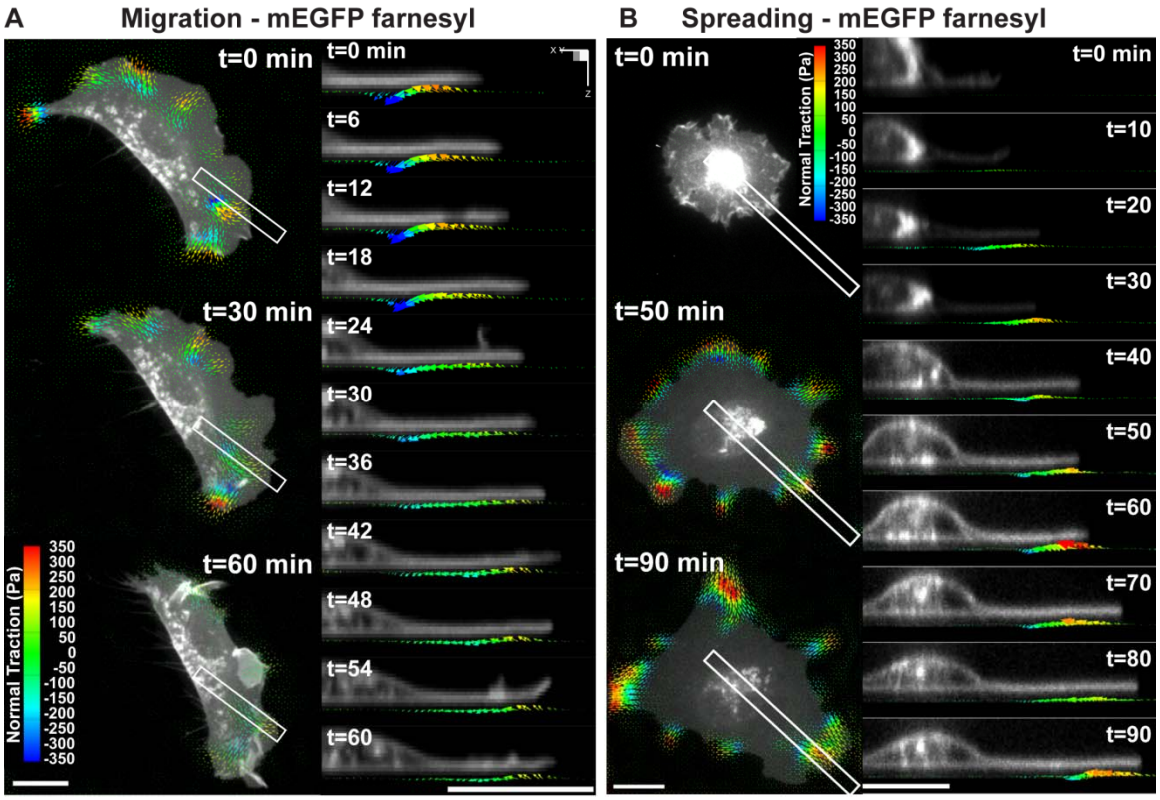

Figure 3.4: Dynamic measurements of 2.5D traction stress. (**a**) Time-lapse images depicting normal traction stress vectors generated by a migrating MEF expressing mEGFP-farnesyl. As the cell moves (towards right), rotational moments are applied continuously in the protruding front as well as the sides. Scale bar, 20 µm. (**b**) Time-lapse cross-sectional views of the inset outlined in (**a**) showing dynamic rotational moments that move with the thin protruding cellular body during cell migration. Scale bar, 20 µm. (**c**) Time-lapse images of mEGFP-farnesyl expressing MEF undergoing spreading. No significant vertical traction stresses are detected until the cell extends thin protrusions and flattens against the substratum. No forces are detected under the nucleus at any time. Scale bar, 20 µm. (**d**) Time-lapse cross-sectional views of the inset outlined in (**c**). Comparable to migrating cells, rotating moments progress outward with the leading edge and remain localized to cell periphery. Scale bar, 20 µm.

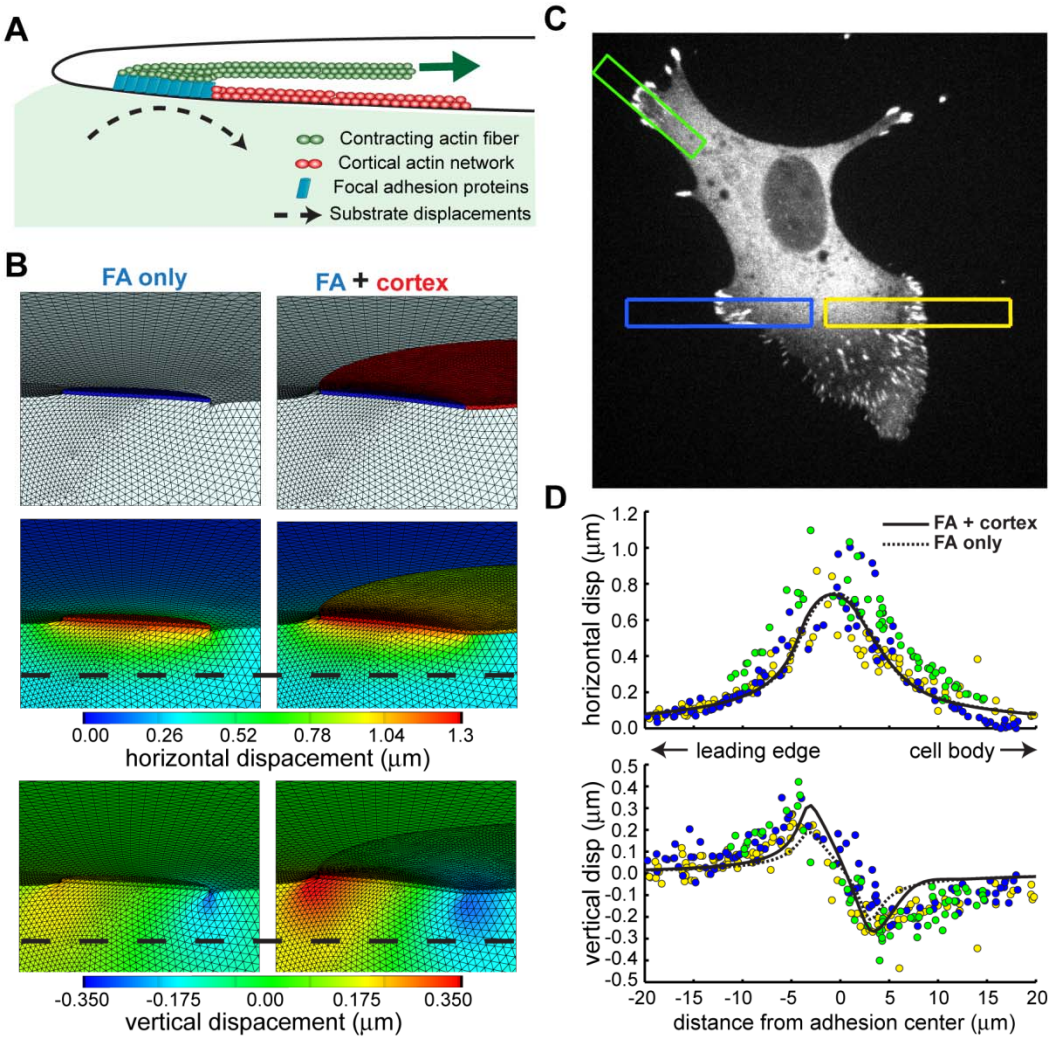

Figure 3.5: Finite element models of focal adhesion rotations. (**a**) Cartoon depicting the key elements in the FEM model. A contracting actin fiber generates a shear traction on the upper surface of a focal adhesion (FA) which is modeled as a rigid plate connected to the PEG hydrogel. To increase the amount of FA rotation, we also tested the contribution of a rigid cortical actin network on the ventral surface of the cell. (**b**) Finite element renderings showing deformed configurations of the PEG hydrogel, focal adhesion and ventral cortex. Contour maps along the symmetry plane show both horizontal and vertical displacements within the hydrogel. Displacements were sampled at 1 μm below the hydrogel surface (dashed black lines) and compared to those produced by cells. (**c**) Maximum intensity projection of a GFP-paxillin expressing MEF. Colored boxes indicate regions beneath focal adhesion from which displacements were sampled. (**d**) Scatter plots of the measured hydrogel displacements from the regions indicated in (**c**). Only beads residing within the first 0-2 μm of the hydrogel are shown. The simulated hydrogel displacements 1 μm from the hydrogel surface are shown for both the FA only and the FA + cortex models.

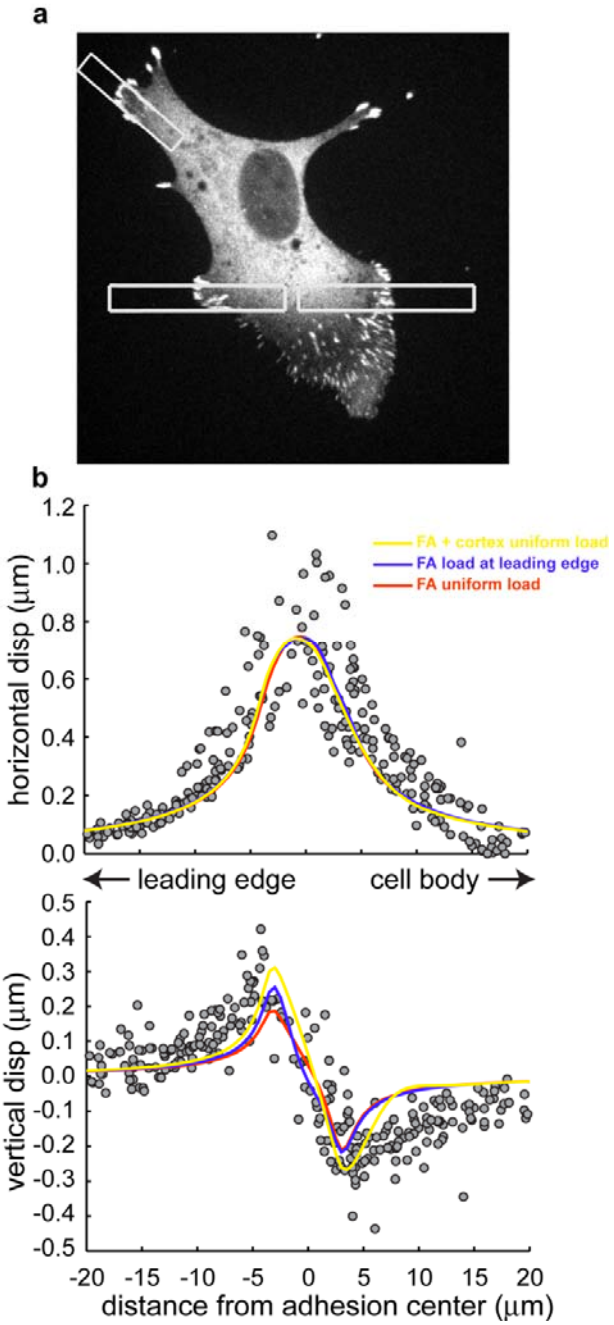

Figure 3.6: Non-uniform distributions of shear loadings on focal adhesions could lead to increased rotation. (**a**) Maximum intensity projection of a GFP-paxillin expressing MEF. White boxes indicate regions beneath focal adhesion from which displacements were sampled. (**b**) Scatter plots of the measured hydrogel displacements from the regions indicated in (**c**). Only beads residing within the first 0-2 μm of the hydrogel are shown. The simulated hydrogel displacements 1 μm from the hydrogel surface are shown for the FA with a uniform shear load, the FA with the shear load concentrated to the front (toward the cell periphery) 30% of the adhesion and the FA + cortex models.

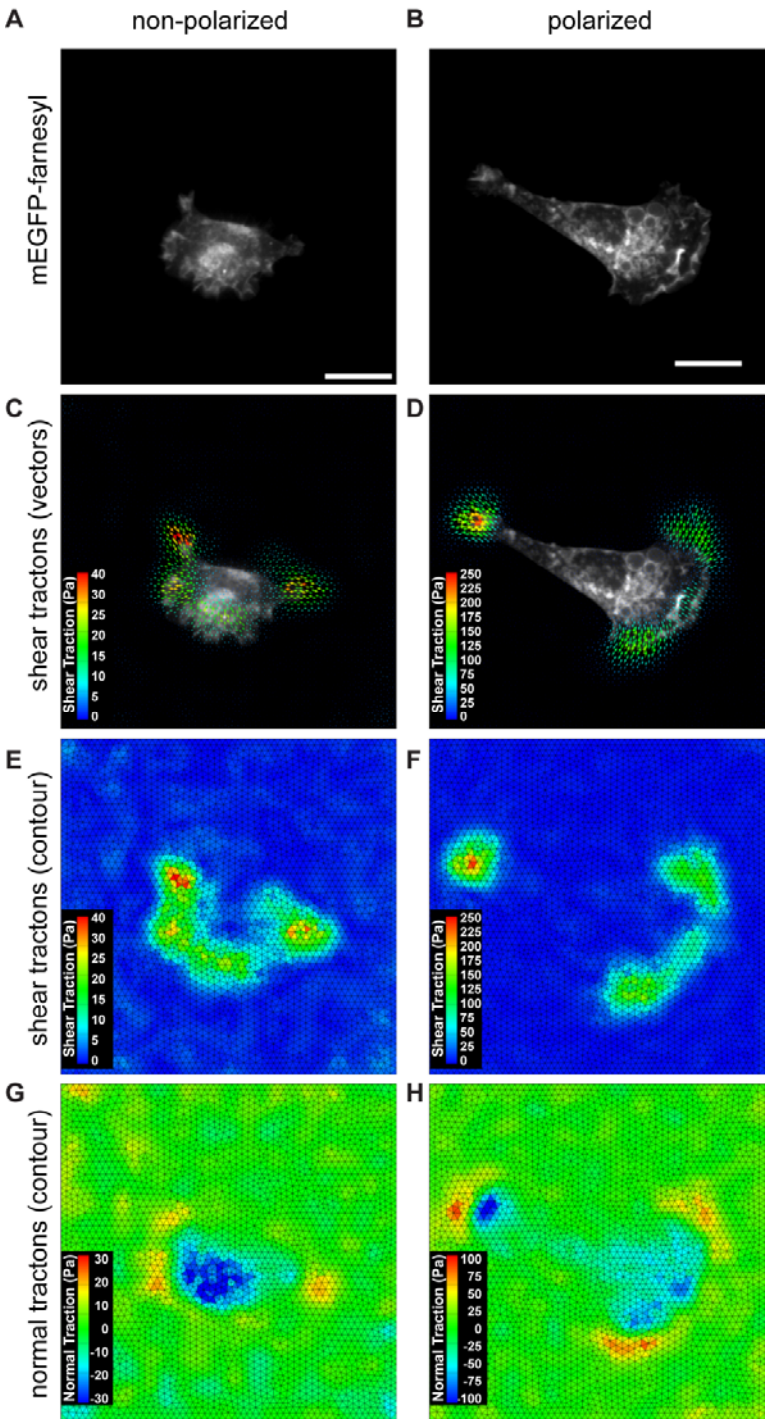

Figure 3.7: 2.5D TFM measurements of cells on soft substrates (**a, b**) Maximum intensity projections of mEGFP-farnesyl expressing MEFs cultured on soft (~1kPa) PEG hydrogels depicting either unpolarized or polarized cells. (**c, d**) Vector renderings of the tractions exerted by cells. Vectors are color coded according to the magnitude of the shear tractions. (**e, f**) Contour plots of the shear tractions exerted by cells. (**g, h**) Contour plots of the normal tractions exerted by cells.

CHAPTER 4: MEASUREMENT OF MECHANICAL TRACTIONS EXERTED BY CELLS IN THREE-DIMENSIONAL MATRICES

4.1 RATIONALE

Cells are constantly probing, pushing and pulling on the surrounding extracellular matrix (ECM). These cell-generated forces drive cell migration and tissue morphogenesis and maintain the intrinsic mechanical tone of tissues (Dembo and Wang 1999; Keller, Davidson et al. 2003). Such forces not only guide mechanical and structural events, but also trigger signaling pathways that promote functions ranging from proliferation to stem cell differentiation (Huang, Chen et al. 1998; McBeath, Pirone et al. 2004). Therefore, precise measurements of the spatial and temporal nature of these forces are essential to understanding when and where mechanical events are invoked in both physiological and pathological settings.

Methods employing planar elastic surfaces or arrays of flexible cantilevers have mapped, with subcellular resolution, the forces that cells generate against their substrates (Dembo and Wang 1999; Balaban, Schwarz et al. 2001; Butler, Tolic-Norrelykke et al. 2002; Tan, Tien et al. 2003). However, many processes are altered when cells are removed from native 3D environments and cultured on 2D substrates. At a structural level, cells encapsulated within a 3D matrix exhibit dramatically different morphology, cytoskeletal organization, and focal adhesion (FA) structure from those on 2D substrates (Cukierman, Pankov et al. 2001). Even the initial means by which cells attach and spread against a 2D substrate are quite different from the invasive process required for cells to extend inside a 3D matrix. These differences suggest that dimensionality alone may significantly impact how cellular forces are generated and transduced into biochemical or structural changes. Yet, although the mechanical properties of 3D ECMs and the cellular forces generated therein have been shown to regulate many cellular functions (Pampaloni, Reynaud et al. 2007), the quantitative measurement of cellular forces within a 3D context has yet to be demonstrated. Here, we quantitatively measure the traction stresses (force per area), or hereafter tractions, exerted by cells embedded within a hydrogel matrix.

4.2 MATERIALS AND METHODS

4.2.1 Hydrogel synthesis, cell encapsulation

Polyethylene glycol diacrylate (PEGDA) was synthesized from polyethylene glycol (PEG, MW 3400, Sigma) and then modified with the collagenase-sensitive peptide CGPQGIWGQGCR to make degradable photoactive hydrogel precursors as described previously (Miller, Shen et al. 2010). Polyethylene glycol diacrylamide (PEGDAAm, MW 3400) was synthesized from PEG by forming the dimesylate, then the diamine, and finally the diacrylamide as described previously (Elbert and Hubbell 2001). PEGDAAm was then reacted with the collagenase-sensitive peptide in sodium borate (100 mM, pH 9.0) until the product polydispersity matched that for PEGDA-peptide precursors. For encapsulation, NIH 3T3 cells were resuspended to a final concentration of 60,000 cells/ml in a 10 or 11% w/v solution of degradable PEGDA-peptide macromer in PBS containing 1 μmol/ml acrylate-PEG-CGRGDS, 0.5 mg/ml Irgacure 2959 (I2959, Ciba) and two types of fluorescent beads (0.2 μm diameter, non-functionalized, yellow green dyed, Polysciences, and 0.2 μm diameter, non-functionalized, suncoast yellow dyed, Bangs Labs) at approximately $3.75x10^{10}$ beads/ml each. Note that the pore size of the PEG gels is an order of magnitude smaller than the diameter of the beads used in this study (Raeber, Lutolf et al. 2005). Therefore, the beads are physically encapsulated within the hydrogel and do not diffuse. Bovine pulmonary artery smooth muscle cells, human mesenchymal stem cells and Lewis lung carcinoma cells were encapsulated in a 7% w/w solution of PEGDAAm-peptide macromer in PBS containing 5 μmol/ml acrylate-PEG-CGRGDS, 5 μmol/ml acrylate-PEG-CGRGES, 0.5 mg/ml Irgacure 2959 (I2959, Ciba) and two types of fluorescent beads. 20 μl of cell-laden prepolymer solution was pipetted onto coverslips (#0 thickness, Fisher Scientific) that were functionalized with 3-(trimethoxysilyl)propyl methacrylate (Sigma) as per the manufacturer's instructions. The solution was contained in annular molds made from poly(dimethyl siloxane) (PDMS, Dow corning) and exposed to 200 mW/cm^2 (measured for 365 nm) UV light from an Omnicure S2000 (320-500 nm, EXFO) for a total of 3,000 mJ. After removing the PDMS mold, polymerized hydrogels, which now formed a cylindrical disc approximately 4 mm diameter and 500 μm tall that was covalently linked to the coverslip along the bottom surface, were immersed in cell culture media and incubated under standard growth conditions (37 ºC, 5% CO_2) for 72 hrs.

4.2.2 Microscopy, image segmentation, finite element mesh generation, and computational resources

Encapsulated cells were imaged with a 40x, 1.1 NA, water immersion objective (LD C-Apochromat, Carl Zeiss Microimaging Inc.) attached to an Olympus IX71 inverted microscope equipped with a CSU10 spinning disc confocal scan head (Yokogawa Electric Corporation), live cell incubator (Pathology Devices) and an ImagEM 16-bit EMCCD camera (Hamamatsu Photonics). A 147 x 147 x 200 μm volume was imaged around each cell, which corresponded to voxel dimensions of 0.2841 x 0.2841 x 0.8 μm in the horizontal and axial planes, respectively. After the stressed image was acquired, the cells were treated with 0.5% Sodium dodecyl sulfate (SDS) detergent (JT Baker), re-equilibrated for 45 min, and then re-imaged to acquire a reference image of the non-stressed hydrogel. This detergent was chosen so as to completely denature all cellular proteins, although in practice, more mild detergents or specific inhibitors of cytoskeletal contractility could be used as well. Timelapse datasets were acquired at 30 minute intervals and 1 μm spacing in the axial plane. This temporal and spatial resolution was chosen so as to increase the image acquisition speed, (approximately 3 minutes of exposure per volume per cell) and to reduce phototoxicity. Images were saved in multipage TIFF format, imported into Amira (Visage Imaging), and manually segmented to identify the cell and the surrounding hydrogel. A 2D surface mesh of the cell was generated from the segmented image, simplified to the desired number of elements, and smoothed using built in functions. This mesh was then imported into Hypermesh (Altair) as a stereolithography file. To approximate an infinite medium, we generated a 400 μm cube centered on the cell, seeded the edges with 9 nodes (element size of 50 μm), and generated a 2D quadrilateral surface mesh. Using these two surface meshes as a template, we then generated a 3D tetrahedral mesh (4 node linear tetrahedron elements "C3D4" in Abaqus) of the enclosed volume. These meshes were then imported into Abaqus (Dassault Systèmes) for finite element analysis with the bottom surface of the cube fixed as a boundary constraint. Validity of the finite element approximation of an infinite medium was verified by fixing the top surface of the cube as an additional boundary constraint and showed no substantial difference in the recovered tractions. Unless otherwise mentioned, for all measurements, the cells were discretized using 2,000 linear elements. The center of mass of the cell was computed using the area weighted centroids of each element on the 2D surface mesh of the cell. Renderings of cellular tractions were computed in Tecplot 360 (Tecplot Inc.), and contour plots were scaled such that approximately 1% of all elements on the cell were saturated. The deviation of the

tractions fields from static equilibrium was assessed by summing the projection of the forces (tractions multiplied by facet area) on each facet of the cell along each Cartesian direction. All data presented in the manuscript were calculated using a Dell Precision T7400 workstation equipped with dual quad core Intel Xeon processors and 16 GB of RAM.

4.2.3 Mechanical characterization of hydrogel substrates

The shear modulus of swollen gels was obtained using an AR 2000 oscillating rheometer on a temperature controlled Peltier plate at 37ºC and a 20 mm stainless steel plate with solvent trap geometry (TA Instruments). Cylindrical gel samples were created from 125 μL of identical precursor solution to that used for traction measurements, covalently linked to 3-(trimethoxysilyl)propyl methacrylate (Sigma) treated glass microscope slides and then swollen in growth media at 37 ºC and 5% CO_2 for 72 hours. Immediately prior to testing, the slides were removed from media and carefully blotted dry with laboratory wipes. The heights and diameter of the swollen gels were measured with calipers and were typically ~0.5 mm thick and ~19 mm diameter. To prevent slipping, 400 grit, wet/dry sandpaper was sectioned to fully cover the geometry and attached with double-stick tape. The head was lowered to a gap corresponding to approximately 0.2 N of normal force. Three consecutive controlled oscillatory strain sweeps were performed from 0.1% to 50% radial strain with 30 linearly spaced measurements at 0.25 Hz (**Figure 4.1a**). Following the strain sweeps, frequency sweeps were performed from 0.1 to 10 Hz, 10 measurements per decade on a log scale, at 1% controlled strain (**Figure 4.1b**). These data were acquired for six independent samples from multiple experiments. The data from the strain sweeps were averaged to yield a shear modulus of 196 ± 66, 328 ± 76 and 267 ± 34 Pa (± s.d.) for 10% w/v and 11% w/v PEGDA and 7% w/w PEGDAam hydrogels respectively. These values were used to calculate Young's moduli of 585 ± 196, 978 ± 228 and 796 ± 102 Pa (± s.d., assuming a Poisson's ratio of 0.49) (**Figure 4.1c**).

4.2.4 Assessment of local hydrogel mechanics and sensitivity analysis of the recovered tractions

Because cell spreading and invasion require the use of degradable hydrogels, it is possible that the local mechanics near the cell membrane may weaken relative to the bulk hydrogel properties. To test this possibility, we measured the hydrogel deformation near and far from the voids where cells were previously located (i.e. after treatment with SDS) in response to a

well defined compressive load in both degradable and non-degradable PEG gels. Cell-laden degradable matrices were prepared as described above, cultured for 72 hrs, labeled with Cell Tracker Red (Invitrogen) as per the manufacture's instructions and then treated with 0.5% SDS. Non-degradable matrices were prepared in an identical manner using PEGDA (MW 6000, Sigma) in absence of degradable peptides and measured after 48 hrs. These matrices were imaged before and after applying a uniform compression of approximately 5% strain using a microscope mounted micromanipulator pressed against a coverslip laid over the gel (**Figure 4.2a**) and bead displacements throughout the volume were computed between the unstressed and compressed images. A 3D tetrahedral mesh was constructed in the vicinity of a cell as described above, and nodal displacements of the boundary nodes were interpolated from the experimentally observed bead displacements. The forward finite element solution was then solved for static equilibrium under homogeneous or heterogeneous (i.e., weakening near the cell) material assumptions, and predicted bead displacements within the simulated volume were compared to experimental observations. We compared displacement fields obtained experimentally versus those generated by finite element simulations using homogeneous material properties (reported as error in **Figure 4.2b**), and found no significant difference between the degradable and non-degradable materials, suggesting that local degradation exterior to the cell is not occurring in the degradable gels or not to an extent that contributes to alterations in bead displacements. Further supporting this conclusion, finite element simulations that incorporate local weakening of the hydrogel near the cell boundary diverge to a greater extent from the observed experimental displacements than do those using a homogeneous material assumption (**Figure 4.2c**). Importantly, because our method calculates a numerical Green's function, we are able to use all bead measurements with suitable signal to noise (often up to 20 μm or greater from the cell surface), and as a result, traction recovery is relatively insensitive to small local changes in material properties. This can be illustrated by setting all finite elements near the cell surface to be locally weaker than the surrounding hydrogel and then computing the tractions based on experimentally observed bead displacements. For example, a 50% decrease in local modulus within 5 μm of the cell changed the calculated tractions in by approximately 15% when compared to homogeneous conditions, whereas a 50% decrease in local modulus within 10 μm of the cell changed the tractions by approximately 30% (**Figure 4.2d, e**). Even under these conditions (i.e. a 50% decrease at 10 μm from the cell), the computed tractions were still qualitatively similar to those under the homogeneous assumption (**Figure 4.2f**).

4.2.5 Calculation of bead displacements and hydrogel strain

Multipage TIFF images of the hydrogel exterior to the cell were imported into Matlab (The Mathworks) and bead centroids were identified as described previously (Gao and Kilfoil 2009). Once bead centroids were identified, beads in the stressed (subject to cell generated tractions) dataset were matched to beads in the relaxed (after cell lysis) dataset using a feature vector-based algorithm relating the relative position of each bead to its local neighbors (**Figure 4.3**). For each target bead to be matched in the stressed dataset, feature vectors were generated to its nearest neighbors, measured by the Euclidian distance between bead centroids (**Figure 4.3a**). Candidate matches for the target bead in the relaxed dataset were identified as those beads nearest to the spatial coordinates of the target bead in the stressed dataset (**Figure 4.3b**). For each of these candidate matches, feature vectors were generated to the nearest neighbors in the relaxed dataset and compared to the target feature vectors (**Figure 4.3c**). The candidate bead with feature vectors most closely matching the target bead was identified as being the same bead in the stressed and relaxed datasets, and the displacement recorded (**Figure 4.3d**). The number of target feature vectors, candidate matches, and candidate feature vectors can be optimized for a given displacement field; however, it is in general necessary to include a greater number of candidate feature vectors than target feature vectors as the relationship between nearest neighbors can change between the stressed and relaxed datasets. In these cases, the best matching candidate feature vectors are used.

To compute the bead displacements used for calculating cellular tractions, we implemented two rounds of bead tracking as follows. A preliminary round of bead tracking was performed to identify initial bead displacements. To correct for temperature-dependent swelling and mechanical drift in the gel, we applied a quadratic correction to the displacement of all beads, computed by minimizing the total bead displacement as follows. We defined the objective function as:

$$\min\left|\mathbf{C}_{\text{stressed}} - \mathcal{F}\left\{\mathbf{C}_{\text{relaxed}}\right\}^{\text{T}}\right|^2 \quad (1)$$

Unless otherwise designated, all norm symbols signify the Frobenious norm. $\mathbf{C}_{\text{stressed}}$ and $\mathbf{C}_{\text{relaxed}}$ are m x 3 matrices in which each row is the position vector of a bead centroid in the stressed or relaxed dataset and m is the total number of beads tracked. The function $\mathcal{F}$ accepts the centroids

of the beads in the relaxed dataset and shifts the x, y, and z components according to a quadratic correction.

$$\mathcal{F}_{ij}\{\mathbf{C}\} = \sum_{k=1}^{3}\left(Q_{jk}(C_{ik})^2 + A_{jk}C_{ik} + d_j + M_{jk}C_{ik}\sum_{l=1}^{3} C_{il}P_{kl}\right) \quad (2)$$

where Q and M are matrices containing coefficients of quadratic terms of single and mixed variables respectively, A and d contain affine terms, $(C_{ik})^2$ represents the square of component *ik* of C, and P is the following permutation matrix: [0,1,0;0,0,1;1,0,0]. Together, Q, M, A, and d comprise 30 terms over which the optimization of equation (2) was carried out using built-in functions for constrained non-linear optimization in Matlab. After applying this correction, a second round of bead tracking was performed to compute the final displacement field, which was then processed using a running average filter to remove misidentified beads.

To compute the strain in the hydrogel surrounding the cells, bead displacements were interpolated onto a uniform 4 μm cubic grid using Matlab. This grid size was chosen to be just greater than the average distance between beads. The Green-St. Venant (Lagrangian) strain tensor, $\mathbf{E}=(\mathbf{F}^T\mathbf{F}-\mathbf{1})/2$, was estimated at the center of each element, where **1** is the identity tensor and the deformation gradient **F** was estimated using standard tri-linear interpolation shape functions.

4.2.6 Generation of a discretized Green's function and calculation of cellular tractions

We generated a discretized Green's function relating tractions on the cell surface to displacements within the gel using the finite element method. 3D tetrahedral meshes were obtained as described above, and used to generate the forward solution relating bead displacements in the gel to unit tractions applied to each facet on the surface of the cell in each of the three Cartesian directions. From each of these solutions, the experimentally measured bead coordinates were queried for the computed displacements. Because both the bead coordinates and the location of applied tractions are at discrete locations, the relation between bead displacements within the gel $\mathbf{u}$ and tractions on the surface of the cell $\mathbf{T}$ is now transformed into a set of linear equations

$$\mathbf{u} = \Gamma\mathbf{T} \quad (3)$$

where we have adopted the notation used in ref (Schwarz, Balaban et al. 2002) in which

$$\mathbf{u} = [u_1^1(\mathbf{r}); u_2^1(\mathbf{r}); u_3^1(\mathbf{r}); u_1^2(\mathbf{r}); u_2^2(\mathbf{r}); u_3^2(\mathbf{r}); \dots; u_1^m(\mathbf{r}); u_2^m(\mathbf{r}); u_3^m(\mathbf{r})]$$

is a 3m column vector, where m is the number of tracked beads and $\mathbf{r}$ is the position vector of each bead.

$$\mathbf{T} = [T_1^1(\mathbf{r}'); T_2^1(\mathbf{r}'); T_3^1(\mathbf{r}'); T_1^2(\mathbf{r}'); T_2^2(\mathbf{r}'); T_3^2(\mathbf{r}'); \dots; T_1^n(\mathbf{r}'); T_2^n(\mathbf{r}'); T_3^n(\mathbf{r}')]$$

is a 3n column vector, where n is the number of discretized facets on the surface of the cell and $\mathbf{r}'$ is the position vector of each facet. Subscripts for both *u* and *T* in these definitions represent displacements and tractions respectively along each Cartesian axis.

$\mathbf{\Gamma}$ is an m x n matrix of the following form:

$$\Gamma_{ij}^{mn} = \begin{bmatrix} G_{ij}^{11} & \cdots & G_{ij}^{1n} \\ \vdots & \ddots & \vdots \\ G_{ij}^{m1} & \cdots & G_{ij}^{mn} \end{bmatrix} \quad (4)$$

Each element of $\mathbf{\Gamma}$ is a 3 x 3 submatrix relating the displacement of bead m in direction i in response to a load on facet n in direction j:

$$G_{ij} = \begin{bmatrix} g_{11} & g_{12} & g_{13} \\ g_{21} & g_{22} & g_{23} \\ g_{31} & g_{32} & g_{33} \end{bmatrix} \quad (5)$$

We used 0th order Tikhonov regularization together with the L-curve criterion(Hansen 2001) for implementing and choosing the correct value for the Lagrange parameter, λ, resulting in the following optimization:

$$\min\{|\mathbf{\Gamma T} - \mathbf{u}|^2 + \lambda^2|\mathbf{T}|^2\} \quad (6)$$

This optimization problem was solved by singular value decomposition using the suite of Matlab routines "*Regularization tools*" by PC Hansen (Hansen 2007). To save computational resources,

only the displacements of beads within 20 μm from the cell surface were used to calculate cellular tractions. Incorporating measurements of beads greater than 20 μm from the cell surface did not substantially change the recovered tractions.

4.2.7 Measurement of uncertainties in the displacement field and discretized cell surface and validation using simulated data

The errors of the displacement measurements were measured from bead displacements before and after treatment with 0.5% SDS in six separate regions of the gel that contained no cells from multiple experiments. These six datasets were used to accurately reflect our experimental bead distribution and displacement resolution in all numerical simulations. To determine the uncertainty in our discretization of the cell surface, two separate surfaces were generated (starting with raw confocal data, proceeding through manual image segmentation and finally to surface reconstruction) of seven cells from multiple experiments. The differences between the two surface meshes for each cell were computed by finding the minimal distance between the nodes of one surface and the closest plane of the alternate surface. To model the cell in our numerical analysis, we used a simplified geometry of a 50 μm diameter sphere meshed using 2,000 triangular elements and generated a 3D tetrahedral mesh as described above. We first tested our ability to recover a uniform traction of 183 Pa oriented in the outward normal direction on each facet. The forward solution for this loading was solved and measurements of bead displacements were computed at the centroid locations of each bead for each of the six fields measured above, thus giving six separate datasets of simulated bead displacements.

The tractions were recovered, as described in section above, for each of these simulated displacement fields and compared to the applied loading, thus giving a measurement of the mean error and deviation of the recovered tractions. To simulate the effect of bead displacement noise on the recovered tractions, the experimentally measured displacements from each of the six noise fields was superimposed on the displacement due to the simulated loadings, and the tractions recomputed. To simulate the effect of surface discretization error, for each node of our spherical surface mesh, we randomly sampled measurements of the surface discretization error (computed as described above). As the most accurate discretization can be expected to lie in between the two experimentally generated surfaces, the spatial coordinates of each node from our spherical mesh were shifted either in the inward or outward normal direction (chosen randomly) by one half the magnitude of the experimentally measured noise. The restriction of the noise to the

normal directions was necessary to avoid element intersections. This procedure was repeated to generate six independent samples of the surface discretization noise (ie we generated six independent "noisy" spherical surfaces) on which to recover tractions.

To test the spatial resolution of the recovery, we applied oscillatory loadings normal to the cell surface (**Figure 4.4a**). The magnitudes of these loadings varied sinusoidally with respect to the spherical coordinate θ and ranged from ± 183, ± 743 and ± 1467 Pa. The frequency of these loadings was then increased progressively from two to ten oscillations per 360 degrees, and six separate measurements of the recovered tractions were obtained for each loading. The characteristic length of the simulated loadings was calculated as the average period of oscillation on the surface of the sphere. The relative error between the simulated and recovered loadings was computed by summing over all elements as:

$$\text{Relative Error} = \frac{\left|\mathbf{T}_{\text{recovered}} - \mathbf{T}_{\text{simulated}}\right|^2}{\left|\mathbf{T}_{\text{simulated}}\right|^2} \qquad (7)$$

where $\mathbf{T}_{\text{recovered}}$ and $\mathbf{T}_{\text{simulated}}$ are n x 3 matrices containing the recovered and simulated tractions respectively, n is the number of facets used to discretize the cell, and each row contains the Cartesian components of the traction computed at a given facet. In this manner, a value of 0 indicates perfectly recovered tractions, 1 indicates that the errors are of equal magnitude to the simulated loadings, and a value of greater than 1 indicates that the errors are larger than the simulated loadings. For cases in which this value lies between 0 and 1, it is possible to express a percent traction recovery as (1-Relative Error) x 100. Bead displacements were then solved using the forward finite element solution. Experimentally measured noise was then superimposed onto these displacements and the corresponding loadings were recovered. In this setting, there are two primary sources of experimental noise: 1) uncertainty of the bead displacements, and 2) uncertainty in the discretization of the cell surface. Our bead tracking resolution was approximately ± 0.075 μm and ± 0.210 μm (standard deviation) in the horizontal and axial planes respectively (**Figure 4.4b**), whereas the uncertainty of the discretized cell surface was non-normally distributed with a median magnitude of 0.176 μm (**Figure 4.4c**). In absence of noise, the accuracy of the recovered tractions decreased with the characteristic length of the simulated loadings, but generally matched to within 20% for all original loadings measured. Addition of bead displacement error or surface discretization error, either alone or in combination, reduced

accuracy of the recovered loadings by an additional 10-30% (**Figure 4.4d**). The reconstruction was also sensitive to the magnitude of the applied loadings, since these determined the magnitude of the bead displacements and consequently the signal to noise ratio for any given measurement. Oscillating loadings with amplitudes of either ± 1467 or ± 734 Pa showed little difference in the accuracy of the recovered tractions. However, loadings with an amplitude of ± 183 Pa were more sensitive to experimental noise, with the L-curve method failing for loadings with a characteristic length of 10 μm (**Figure 4.4e**). However, despite these limitations, the general periodic features of even the more complex simulated loadings were still captured (**Figure 4.4f, g**).

4.2.8 Measurement of contractile moments

A useful metric for quantifying cellular tractions is the "contractile moment" (Butler, Tolic-Norrelykke et al. 2002), defined here as $M_{ij} = \int r_i F_j(\mathbf{r}) d\mathbf{r}$ where r_i are the Cartesian components of the position vector for a given cell facet with respect to the center of mass of the cell, and F_j are the Cartesian components of the force (traction multiplied by facet area) exerted at the corresponding facet (**Figure 4.5 a-d**). The diagonal terms of this matrix are associated with dilatational or contractile tractions, while the off diagonal terms are associated with tractions that exert torques about the center of mass of the cell. The near symmetric nature of these matrices (before any correction) is indicative of torque equilibrium. After symmetrization (by taking the mean of the off-diagonal terms), the contractile moment matrix can be diagonalized by eigenvalue decomposition ($\mathbf{M}_{eig}$) to reveal the principal contractile (or dilatational) terms (**Figure 4.5e**). We found that the contractile moments of the cells in this study were of similar order to those presented in ref (Butler, Tolic-Norrelykke et al. 2002) for cells cultured on top of a planar fibronectin (Fn) coated polyacrylamide gel with Young's modulus of ~1,200 Pa, which suggests that a change in dimensionality alone (i.e. cells fully encapsulated within a 3D matrix as opposed cultured on top of a 2D planar surface) does not dramatically alter the total contractile potential of a cell. This is further quantified by the trace of the contractile moment matrix which gives the net contractile moment of the cell. This scalar invariant can be used as a metric for total cellular contractility. All single cells measured demonstrated a negative net moment (indicating net inward contraction), whereas the multicellular tumor spheroids demonstrated a positive net moment (indicating expansion or dilation) (**Figure 4.5f**).

4.2.9 Bootstrap analysis

Bootstrap analysis is a useful method to determine the effects of bead displacement uncertainty on the traction measurements for actual cells (Dembo and Wang 1999; Schwarz, Balaban et al. 2002). Briefly, after computation of the tractions for a given cellular geometry, the forward solution is solved to record the best fit bead displacements (i.e. the bead displacements that would be predicted from the computed tractions). Experimental noise, measured as described above, was then randomly sampled and superimposed onto these displacements and the inverse problem was solved to recover a new traction field. The difference between the original tractions and the recovered bootstrap tractions gives a measurement of the possible variation in tractions that could be attributed to noise (**Figure 4.6a**). We computed the mean bootstrap error for each traction measurement from 100 bootstrap iterations (ie 100 independent, random samples of experimental noise) and compiled measurements of the mean bootstrap error from traction measurements of 12 total cells (encapsulated in 978 Pa hydrogels and meshed with 2,000 facets each to yield 24,000 traction measurements). Bootstrap errors were predominantly in the range of 25-75 Pa, which gives a lower bound on the sensitivity of the traction measurements. In contrast, traction magnitudes were substantially higher (**Figure 4.6b**). Box and whiskers plots of the relative magnitude of bootstrap error compared to the traction magnitudes reveal that bead displacement uncertainty contributes roughly 10 percent uncertainty to the reported tractions (based on median values) (**Figure 4.6c, d**). This contribution is higher for smaller tractions (e.g. below 50 Pa), but substantially reduced for larger tractions.

4.2.10 Computational resources and finite element accuracy

To illustrate the computational requirements necessary for the calculation of cellular tractions, we performed timing analysis of the various steps. The main computational steps in our analysis are 1) bead tracking, 2) finite element computation of a numerically generated Green's function, and 3) singular value decomposition of the discretized Green's matrix. The computational expense of each of these steps depends on the complexity and resolution of the finite element mesh used to discretize the cell and surrounding hydrogel, and the number of beads tracked in each measurement. As stated in above, all data presented in the manuscript were calculated using a Dell Precision T7400 workstation equipped with dual quad core Intel Xeon processors and 16 GB of RAM. Because many of the algorithms in each step can take advantage of parallel processing, we compared the time required using two, four and eight CPU's (**Figure 4.7a**). The total time required to calculate cellular tractions was approximately 4.5 hours per dataset with the majority of this time spent on computing the bead displacements. Additionally,

we report the time required to compute tractions on a simplified finite element mesh. These simplified meshes dramatically reduce the computational requirements and time (down to 3.3 hrs per dataset), yet still capture the fundamental aspects of the cellular tractions. To determine the error introduced by using these finite element meshes, we compared the computed tractions obtained with linear elements versus quadratic elements. The tractions computed using 2,000 linear elements to discretize the cell surface differed by approximately 30% from those using quadratic elements while tractions computed using a simplified mesh of 1,000 linear elements differed by approximately 45% (**Figure 4.7b**). Nonetheless, in each of these cases, the qualitative differences between the tractions computed using linear or quadratic elements were nearly indistinguishable (**Figure 4.7c**). It should be noted, however, that coarser discretizations of the cell surface may introduce additional error due to the inability of highly simplified meshes to accurately capture complex cellular morphologies.

4.2.11 Cell culture

NIH 3T3 cells obtained from ATCC were cultured in high glucose DMEM containing 10% bovine serum, 2mM L-glutamine, 100 units/ml penicillin, and 100 mg/ml streptomycin (all from Invitrogen). Cell culture media was changed every 3 days. EGFP-lentiviral infection was carried out as described previously (Gao, McBeath et al. 2010). Human mesenchymal stem cells from Lonza and Lewis lung carcinoma (LLC) cells from ATCC were cultured in growth medium (low glucose DMEM containing 10% fetal bovine serum, 0.3 mg/ml glutamine, 100 units/ml streptomycin and 100 units/ml penicillin). Immediately upon encapsulation of single LLC cells, the medium was supplemented with 50 ng/ml of recombinant human hepatocyte growth factor (R & D systems) to drive proliferation and spheroid formation.

4.3 RESULTS

GFP-expressing fibroblasts were encapsulated within mechanically well-defined polyethylene glycol (PEG) hydrogels that incorporate proteolytically degradable domains in the polymer backbone and pendant adhesive ligands (Miller, Shen et al. 2010). The incorporation of adhesive and degradable domains permits the cells to invade, spread, and adopt physiologically relevant morphologies (**Figure 4.8a**). The hydrogels used in this study had a Young's modulus of 600 to 1,000 Pa (**Figure 4.1c**), a range similar to commonly used ECMs such as reconstituted collagen or Matrigel and to *in vivo* tissues such as mammary and brain tissue (Discher, Janmey et al. 2005; Paszek, Zahir et al. 2005). Cells in 3D PEG gels deformed the surrounding matrix, which was visualized by tracking the displacements of 60,000-80,000 fluorescent beads in the vicinity of each cell (**Figure 4.8b, Figure 4.3**). Bead displacements were determined relative to a reference, stress-free, state of the gel after lysing the cell with detergent. We typically observed deformations of 20-30% peak principal strain in much of the surrounding hydrogel (**Figure 4.8c, d).** The largest strains, up to 50%, occurred in the vicinity of long slender extensions, which is consistent with observations of strong forces exerted by these regions on 2D substrates (Chan and Odde 2008). Because the mechanics of the PEG hydrogels showed no substantial dependence on strain or frequency (**Figure 4.1a,b**), we used linear elasticity theory and the finite element method to determine the cellular tractions that would give rise to the measured bead displacements. Briefly, we generated a finite element mesh of the hydrogel surrounding the cell from confocal images. A discretized Green's function was constructed by applying unit tractions to each facet on the surface of the cell mesh and solving the finite element equations to calculate the induced bead displacements (**Figure 4.8e**). Standard regularization methods for ill-posed, over-determined linear systems of equations were then used to compute the tractions exerted by the cell (see **Materials and Methods**). The time required for the calculation of a single data set is approximately 4.5 hours using readily available computational equipment. However, this can be reduced dramatically by using a simplified finite element mesh of the cell and hydrogel. These lower resolution datasets still capture the fundamental character of higher resolution measurements (**Figure 4.7**).

We used simulated traction fields to validate the approach and to characterize its spatial resolution (**Figure 4.4**). Experimental noise from the bead displacements was measured from cell-free regions of the hydrogel before and after detergent treatment, and surface discretization noise was measured from multiple discretizations of the same cells. These datasets then were superimposed onto the displacements generated by simulated loadings prior to traction

reconstruction. In this setting, the percent of traction recovered was proportional to the magnitude and characteristic length of the simulated loadings (defined as the average period of spatial oscillation). For all cases, the presence of noise reduced recovery accuracy by approximately 20-30%. Despite these limitations, the recovered tractions still captured the essential periodic features of even the most spatially complex simulated loadings with characteristic lengths of spatial variation down to 10 μm.

We next calculated the tractions from live cells encapsulated within 3D hydrogels and found that cells exerted tractions in the range of 100-5000 Pa, with strong forces located predominantly near the tips of long slender extensions (**Figure 4.9a, b**). For all measurements, forces were in static equilibrium with a typical error of approximately 1-5% of the total force applied by the cell. Further analysis revealed that these tractions were minimally impacted by possible variations in local hydrogel mechanics or by uncertainty in the measured bead displacements (**Figure 4.2** and **4.6**). Previous measurements of cellular forces on 2D surfaces have generally been limited to shear loadings, although recent studies have measured small forces exerted normal to the planar surface as well (Hur, Zhao et al. 2009; Maskarinec, Franck et al. 2009). However, it is unclear whether these relationships might be altered for cells inside a 3D matrix. Here, we found that cells encapsulated within a 3D matrix predominantly exerted shear tractions; although, small normal tractions were also present near the cell body. To determine if patterns of force might be associated with specific regions of cells, we quantified the magnitude and angle of tractions with respect the center of mass of the cell. Generally, tractions increased as a function of distance from the center of mass (**Figure 4.9c**). Interestingly, cells encapsulated in hydrogels with a Young's modulus of ~1,000 Pa generated stronger tractions than those in ~600 Pa hydrogels. However, the observed differences in tractions were not due to an overall increase in total cellular contractility, as measured by the net contractile moment (**Figure 4.5**), but rather, were most apparent in strong inward tractions near the tips of long slender extensions (**Figure 4.9c**). This reveals a local and non-linear reinforcement of cellular contractility in response to substrate rigidity and suggests that such regions may be hubs for force-mediated mechanotransduction in 3D settings. The cell bodies showed no bias in traction angle; however, strong tractions became progressively aligned back toward the center of mass in more well spread regions of the cell (e.g. near the tips of long slender extensions) (**Figure 4.9d**). In general, these patterns of force were reflected in multiple cell types, but could be altered by cell-cell proximity or culture as a multicellular aggregate. Neighboring 3T3 cells preferentially extended away from

each other, whereas proliferating multicellular tumor spheroids exerted outward normal tractions on the matrix (**Figure 4.10** and **4.11**).

Upon closer inspection, we found a subset of extensions that displayed strong tractions several microns behind the leading tip, while the tractions at the tip itself were substantially lower. As such traction profiles are similar to those observed behind the leading edge of a lamellipodia for a migrating cell on a 2D substrate (Dembo and Wang 1999), we hypothesized that such regions may represent invading or growing cellular extensions in 3D. To test this possibility, we measured the tractions from time-lapse images of cells as they invaded into the surrounding hydrogel (**Figure 4.12a**). Indeed, tractions at the tips of growing extensions were notably lower than the strong tractions exerted by proximal regions of the same extension (**Figure 4.12b** and **Figure 4.13**). However, we did not observe normal forces pushing into the ECM in these extensions. Moreover, we also detected strong tractions from small extensions on the cell face opposite the invading extensions. Such stable extensions exhibited very different force distributions than the growing extensions, often lacking the characteristic drop in force near the leading edge, and may correspond to an anterior-posterior polarity axis formed in the cell.

4.4 DISCUSSION

In this work, we build upon recent advances in materials science, particle tracking and continuum mechanics to quantitatively measure the tractions exerted by cells encapsulated within 3D matrices. Using this method, we observed that cells in 3D matrices probe the surrounding ECM primarily through strong inward tractions near the tips of long slender extensions. Interestingly, invading extensions suppressed these inward forces at the most distal tip which suggests that a local inhibition of myosin generated contractility allows tip advancement. Importantly, we demonstrate that this technique is generalizable to different cell types, cell-cell interactions and even to multicellular tumor structures where both tumor growth and invasion have been previously shown to be mechanoresponsive (Paszek, Zahir et al. 2005). Because the synthetic hydrogels used in this study are of similar elastic moduli to *in vivo* tissues (Discher, Janmey et al. 2005; Paszek, Zahir et al. 2005) and can support a wide range of cellular functions (Lutolf and Hubbell 2005), we anticipate that this approach will enable investigations into the role of cellular forces in a variety of biological settings.

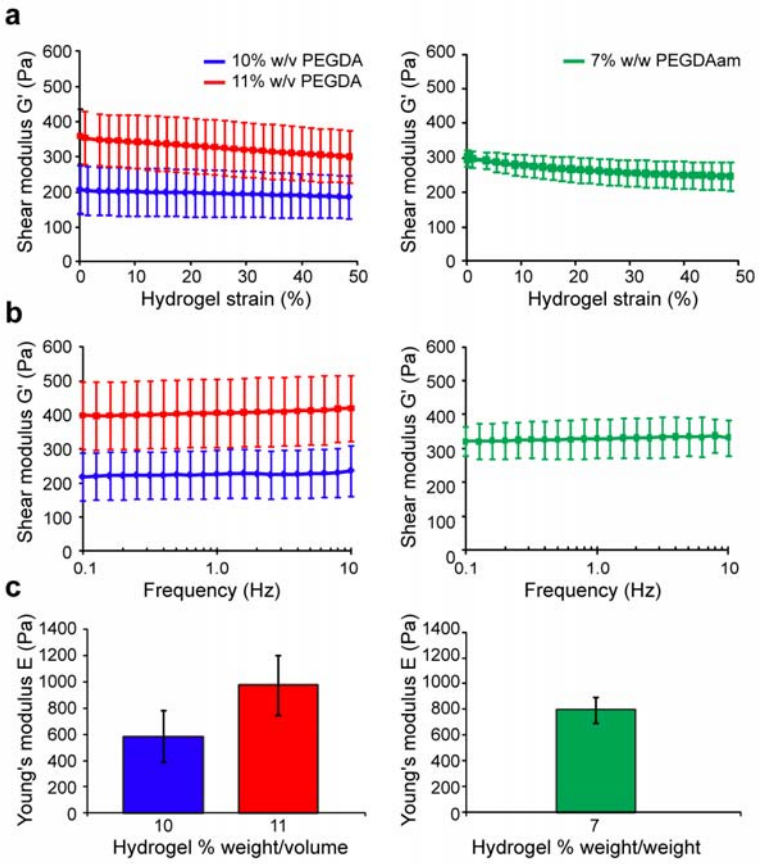

Figure 4.1: Mechanical characterization of hydrogel matrices. Hydrogel mechanics were determined using shear rheology. Swollen, cell-laden hydrogels were measured after three days of culture in growth medium (identical conditions to the measurement of cellular tractions). Samples were compressed to 0.2 N normal force to ensure good contact between the hydrogel and geometry. (**a**) Plot of the shear modulus (G′) as a function of applied radial strain for polyethelyne diacrylate based (PEGDA) and polyethylene diacrylamide-based (PEGDAam) hydrogels. All hydrogels were linear over the ranges of strain measured. Average shear moduli obtained from these plots were 196 ± 66, 328 ± 76 and 267 ± 34 Pa for 10% w/v and 11% w/v PEGDA and 7% w/w PEGDAam hydrogels respectively. (**b**) Plot of the shear modulus (G′) as a function of frequency for PEGDA and PEGDAam hydrogels. Measurements were obtained at 1% radial strain at frequencies varying from 0.1 to 10 Hz. Hydrogel moduli showed no substantial dependence on frequency over the range of applied loadings. (**c**) Young's moduli of PEGDA and PEGDAam hydrogel matrices. Hydrogels were assumed to be nearly incompressible with a Poisson's ratio of 0.49 leading to predicted Young's moduli of 585 ± 196 and 978 ± 228 Pa for 10% w/v and 11% w/v PEGDA and 796 ± 102 Pa for 7% w/w PEGDAam hydrogels respectively. For all plots, errors bars are ± standard deviation from $n = 6$ samples.

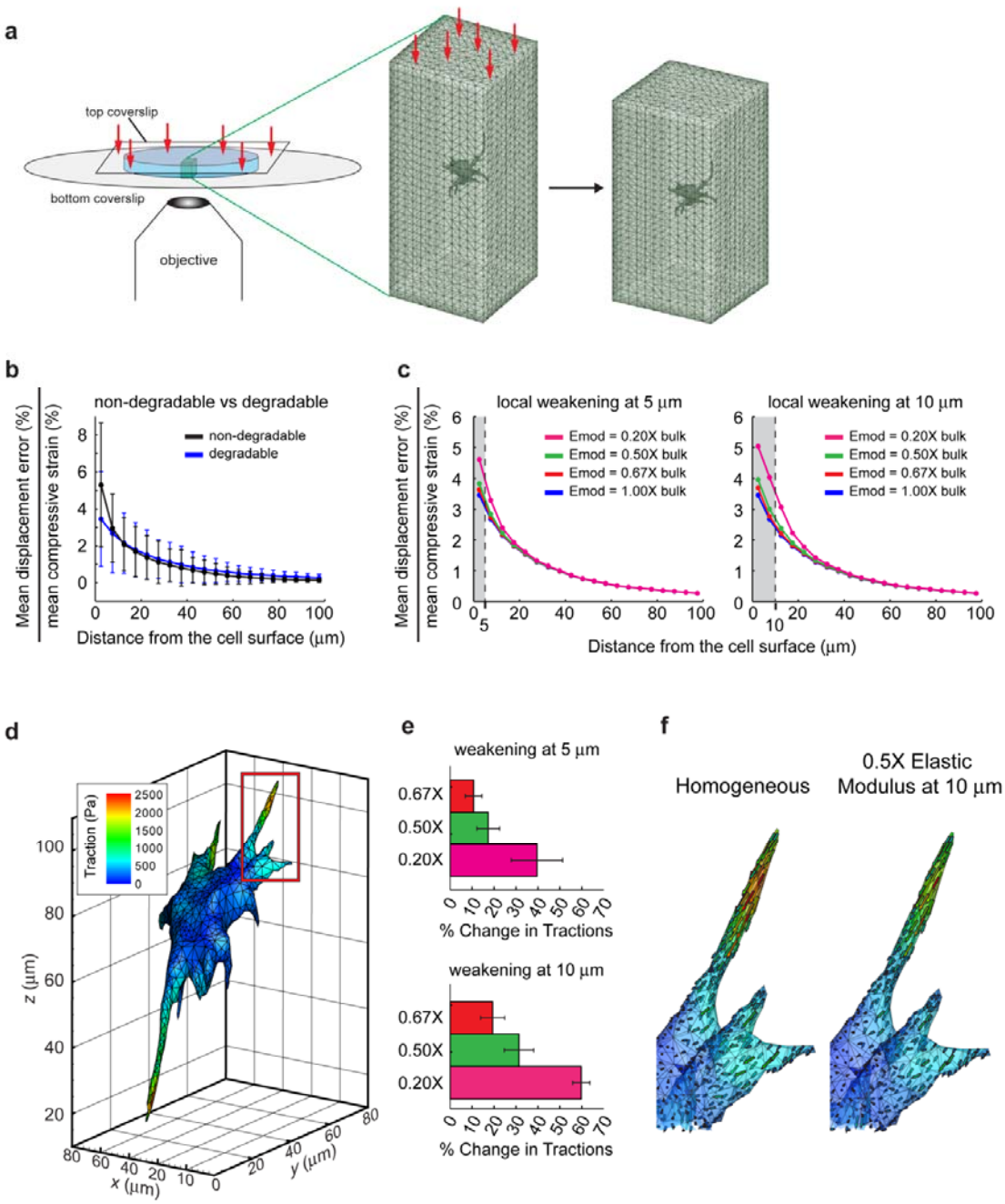

Figure 4.2: Sensitivity analysis of tractions to local hydrogel mechanics. (**a**) Schematic of the experimental setup used to compress hydrogel samples. For a given measurement, the sample was compressed to between 5-7% strain. (**b**) Plot of the errors between the experimental

displacements, and those computed using a finite element simulation defined as: $\frac{|\mathbf{d}_{\text{experimental}}-\mathbf{d}_{\text{FEM}}|^2}{|\mathbf{d}_{\text{experimental}}|^2}$, where **d** is the displacement vector relating the positions of a given bead before and after hydrogel compression. Data were binned into 5 μm increments based on the vicinity of a given bead to the cell boundary and the mean value of each bin was used to generate a single curve for each cell. Because the error is expected to scale with strain (given the small strain approximation), these values were normalized by the mean compressive strain for a given sample (which typically varied by ~1-2% between samples). No significant difference was observed between the errors in the degradable and non-degradable hydrogels ($P = 0.5$ by student t-test on the mean error of the points within 0-20 μm of the void surface). (**c**) Plot of the errors between the experimental and finite element displacements for cells in degradable hydrogels. Finite element models incorporating local heterogeneities were created by setting the modulus of all elements within either 5 or 10 μm of the cell boundary to 0.67X, 0.5X, or 0.2X that of the surrounding material. All heterogeneous models diverged more significantly from the experimental displacements than did the homogeneous model (P = [0.021, 0.020, 0.019] and P = [0.038, 0.016, 0.009] for 0.67X, 0.5X and 0.2X curves at 5 μm and 10 μm respectively by paired student t-test on the mean error of points within 0-20 μm of the void surface). (**d**) Contour plot of the tractions exerted by an NIH 3T3 fibroblast encapsulated in a 978 Pa degradable hydrogel. (**e**) Sensitivity analysis of the computed tractions under heterogeneous mechanical assumptions. Percent change in tractions was calculated as $\frac{|\mathbf{T}_{\text{homogeneous}}-\mathbf{T}_{\text{heterogeneous}}|^2}{|\mathbf{T}_{\text{homogeneous}}|^2}$ x 100 for each of the six heterogeneities tested above. (**f**) Expanded views show the tractions from **d** computed under homogeneous material assumptions, and those computed under the assumption that the Young's modulus of the hydrogel within 10 μm of the cell boundary is 0.5X that of the bulk (i.e. within 10 μm of the cell is 489 Pa). Data from **b**, **c**, and **e** are from $n = 3$ cells per condition. Error bars in **b** and **e** are ± standard deviation on the mean.

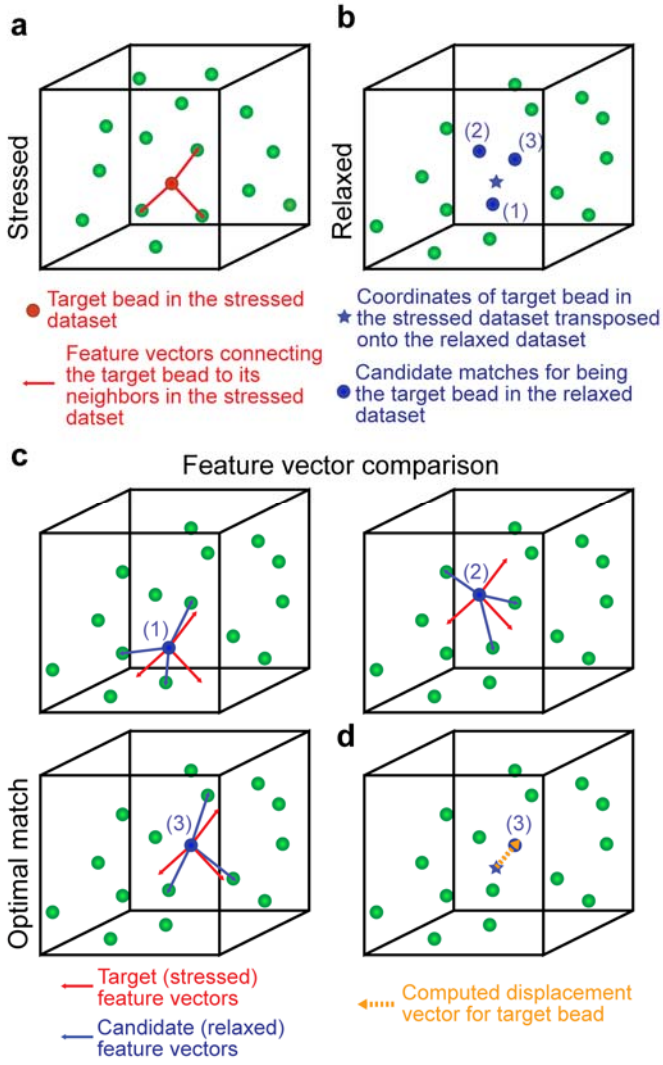

Figure 4.3: Algorithm for tracking bead displacements in 3D. The key challenge to determine the displacement field within the hydrogel is to identify matching beads within the stressed (i.e., subjected to cell generated tractions) and relaxed (after cell lysis) datasets. (**a**) For each bead in the stressed dataset (target beads), feature vectors are drawn to the nearest neighboring beads (target feature vectors). These vectors provide a unique "signature" for each bead. (**b**) The spatial coordinates of a target bead within the stressed dataset are transposed onto the relaxed dataset and neighboring beads within this relaxed dataset are identified as candidate matches. (**c**) For each candidate match in the relaxed dataset, feature vectors are drawn to the nearest neighboring beads. The most closely matching candidate and target feature vectors identify the optimal match (i.e., the same bead has been located in the stressed and relaxed datasets). (**d**) Once a match is made, the displacement is calculated from the spatial coordinates of the matched beads in the stressed and relaxed datasets.

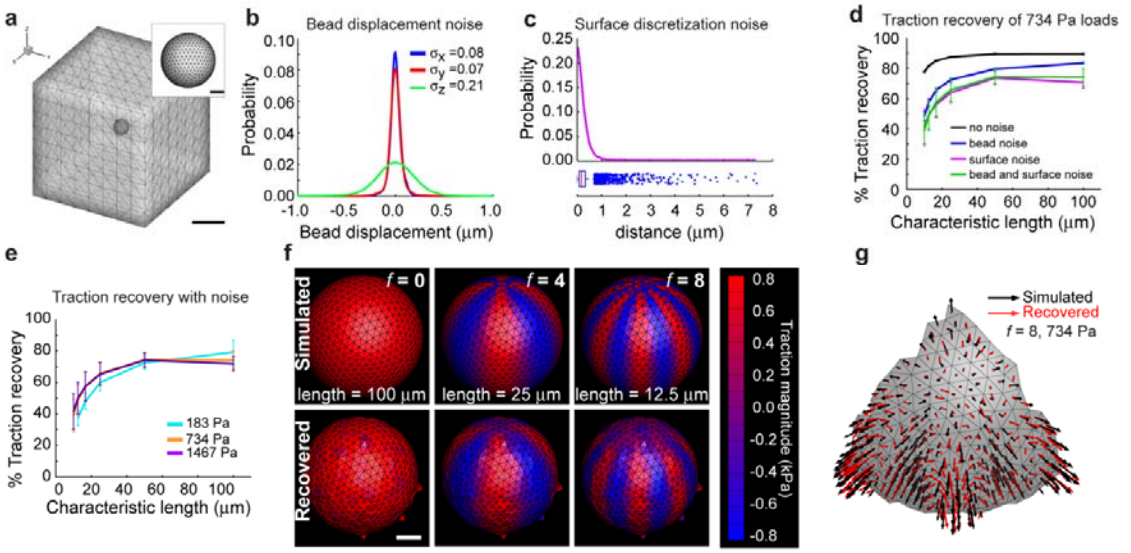

Figure 4.4: Validation using simulated tractions on a spherical cell. (**a**) Computational domain showing surface meshes on the inner cellular sphere (50 μm diameter) and outer cube of matrix (400 μm per side). Scale bar = 100 μm, 10 μm (inset). (**b**) Probability densities of experimentally measured bead displacements (noise) in absence of cells. Measurements are compiled from six separate locations within the gel from several experiments. (**c**) Boxplot and probability density of surface discretization error measured from two independent meshings of seven different cells from multiple experiments. (**d**) Percent of traction recovery summed over all facets, defined as: $\left(1-\frac{|\mathbf{T}_{\text{recovered}}-\mathbf{T}_{\text{simulated}}|^2}{|\mathbf{T}_{\text{simulated}}|^2}\right)$ x 100, as a function of characteristic length of the simulated loadings (defined as the average period of oscillation on the surface of the sphere). Plotted recoveries are in the presence of no noise, bead noise alone, surface noise alone, and bead and surface noise combined. Error bars are standard deviation on the mean. **e**) Percent of traction recovery as a function of characteristic length in the presence of surface and bead noise for loadings of three different magnitudes that span the range of tractions exerted by cells. Note that the 10 μm, 183 Pa data point is omitted because the L-curve method fails to find an appropriate corner for this loading. **f**) Contour plots showing the magnitude of simulated and recovered tractions on a representative surface in the presence of both bead displacement and surface discretization noise. **g**) Magnified plot of the simulated and recovered tractions on each facet of the cell for one of the most rapidly varying traction fields (f = 8, characteristic length = 12.5 μm).

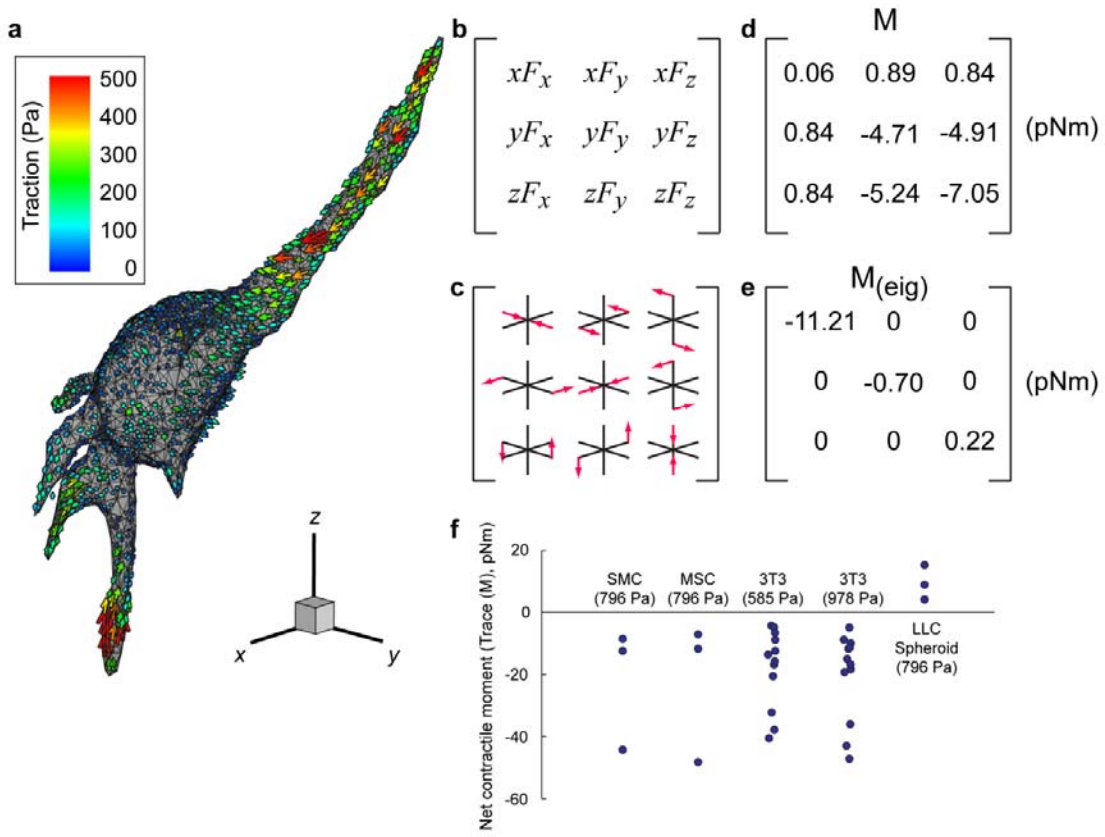

Figure 4.5: Measurement of contractile moments. (**a**) Tractions exerted by a human mesenchymal stem cell encapsulated in a 7% w/w PEGDAam based hydrogel. For clarity, only one half of all vectors are shown. (**b**) Component representation of the contractile moment matrix. The Cartesian coordinates x, y, and z represent the distance of the centroid of a given surface facet from the center of mass of the cell and the forces F_x, F_y, and F_z are the Cartesian components of the force (traction multiplied by facet area) exerted at the corresponding facet. Summation over all facets gives the appropriate term of the moment matrix. (**c**) Schematic of the contractile moment matrix showing the orientation of the terms with respect to the Cartesian axis. (**d**) Contractile moment matrix of the cell in **a**. (**e**) Diagonalized (via eigenvalue decomposition) contractile moment matrix. (**f**) Plot of the net contractile moments of cells and multicellular spheroids.

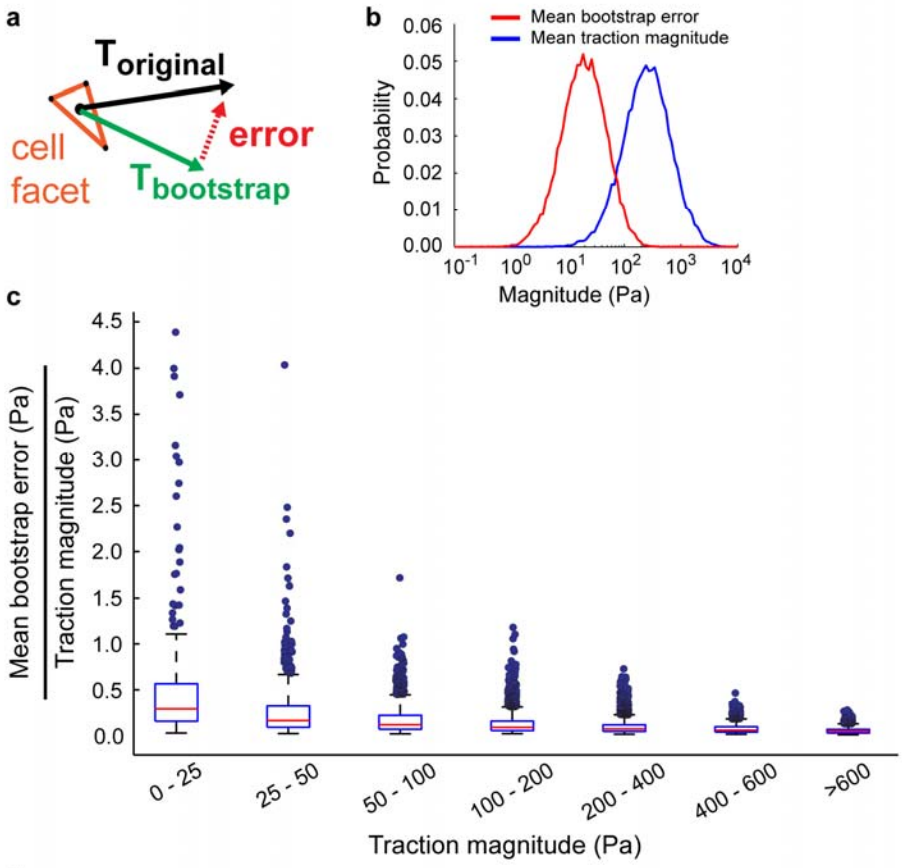

d

Bin Edges (Pa)	Median	25th Percentile	75th Percentile	Number of Observations	Number of Outliers
0 - 25	0.29	0.16	0.57	325	24
25 - 50	0.16	0.09	0.32	1081	51
50 - 100	0.12	0.07	0.22	3091	143
100 - 200	0.09	0.05	0.16	5784	265
200 - 400	0.07	0.04	0.12	6773	332
400 - 600	0.06	0.04	0.09	3076	135
>600	0.04	0.03	0.07	3870	131

Figure 4.6: Bootstrap analysis of tractions. (**a**) Schematic for the computation of bootstrap errors. Experimental noise is superimposed onto best fit displacements (as computed using the L-curve) given by a known traction field ($\mathbf{T}_{original}$) and a new traction field is recovered ($\mathbf{T}_{bootstrap}$). The Euclidian distance between the original and bootstrapped tractions is recorded as the bootstrap error. (**b**) Probability densities of the mean bootstrap error, computed from 100 iterations on the tractions from 12 cells (meshed with 2,000 facets each, yielding 24,000 total measurements of the mean error) and of the original traction magnitudes computed from 12 cells as above. (**c**) Box and whiskers plot of the mean bootstrap error normalized by the original traction magnitude, giving a fold error due to bead displacement uncertainty. (**d**) Table listing the median values, 25th percentile, 75th percentile, number of observations and number of outliers for each bin of **c**.

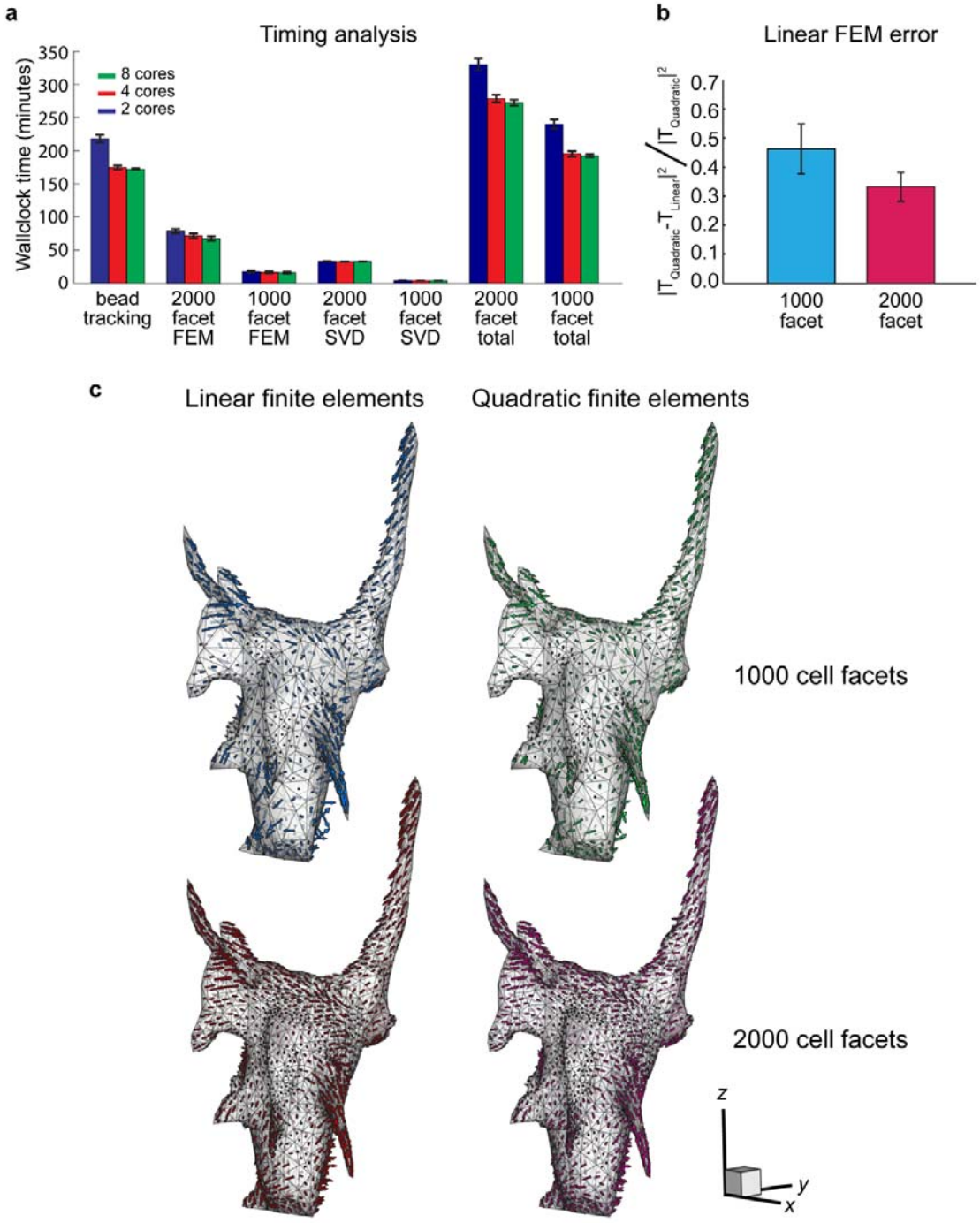

Figure 4.7: Computational requirements and FEM accuracy. (**a**) Plot of the times required for the various steps in the computation of 3D cellular tractions using linear finite elements: bead tracking, finite element computation of the discretized Green's function (FEM), and singular value decomposition (SVD). Data are shown for both simplified (1,000 cellular facets) and

complex (2,000 cellular facets) meshes. (**b**) Plot of the error introduced by the complex and simplified meshes used to discretize the cell surface and surrounding hydrogel. The solutions obtained using quadratic elements were used to approximate the exact solution when compared to those obtained with linear elements. (**c**) Vector plots of the tractions computed using the simplified (1,000 cellular facets with linear (blue), or quadratic (green) elements) and complex (2,000 cellular facets with linear (red) or quadratic (magenta) elements) finite element meshes.

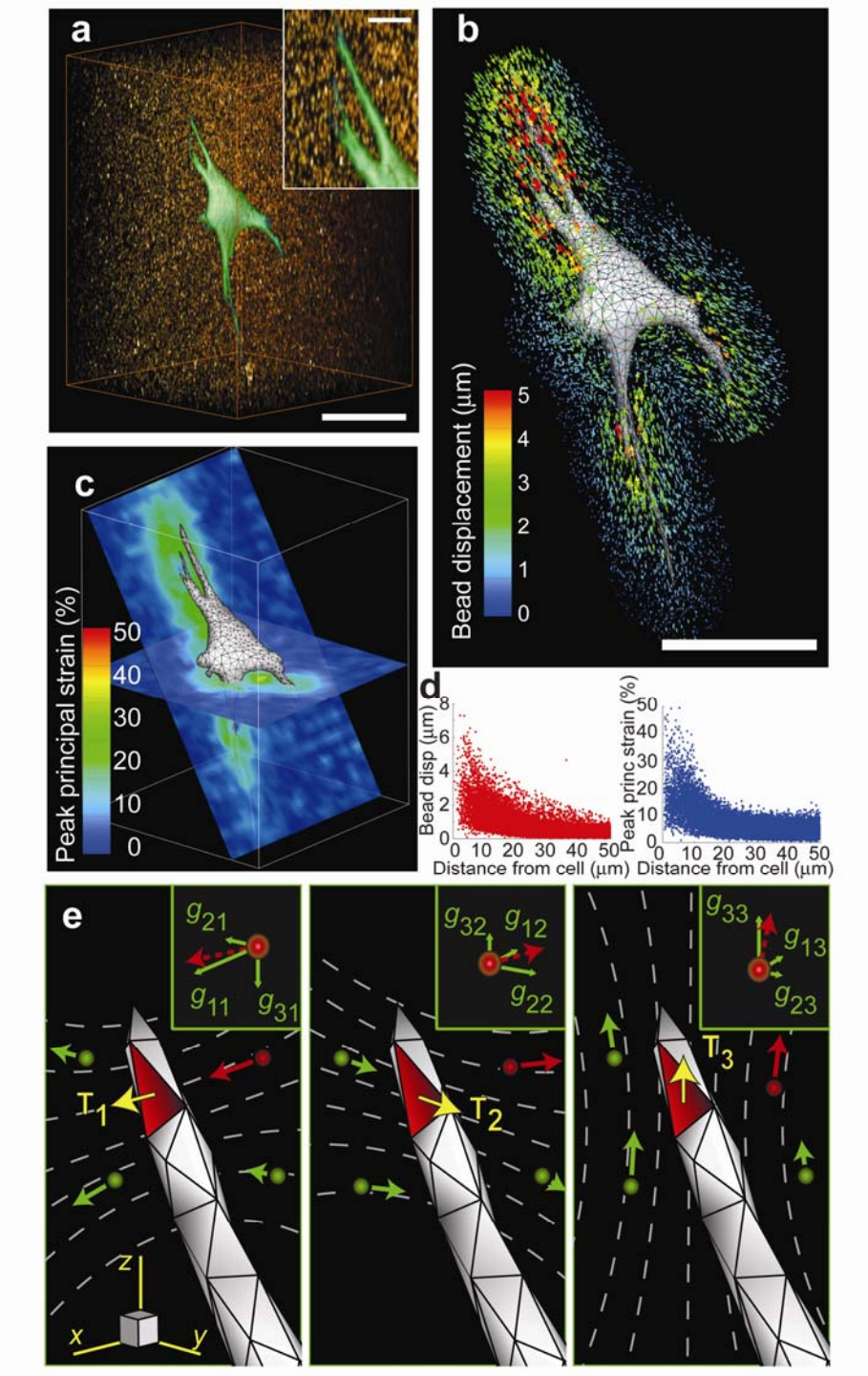

Figure 4.8: Cell-induced hydrogel deformations and construction of a discretized Green's function. (**a**) Volume rendering of a GFP-expressing NIH 3T3 fibroblast (green) spreading into a 3D hydrogel containing fluorescent beads (red). Scale bar = 50 μm, 10 μm (inset). (**b**) Surface mesh of the cell. Scale bar = 50 μm. Bead displacement trajectories are mapped and color coded by magnitude. (**c**) 2D slices through the volume showing the magnitude of the peak principal

strain in the hydrogel surrounding the cell. (**d**) Plots of bead displacements and hydrogel strain as a function of distance from the cell surface. (**e**) Schematic outlining the use of the finite element method to reconstruct the Green's function. From linear elasticity theory, the displacement field within the gel $\mathbf{u}(\mathbf{r})$ and the tractions on the surface of the cell $\mathbf{T}(\mathbf{r}')$ are related by a Fredholm integral equation of the first kind

$$\mathbf{u}(\mathbf{r}) = \int \boldsymbol{\Gamma}(\mathbf{r}, \mathbf{r}')\, \mathbf{T}(\mathbf{r}') d\mathbf{r}' \qquad (1)$$

where $\mathbf{r}$ and $\mathbf{r}'$ are the position vectors of the beads and cell facets, respectively. The finite element method was used to discretize the Green's function $\boldsymbol{\Gamma}$ into

$$\Gamma_{ij}^{mn} = \begin{bmatrix} G_{ij}^{11} & \cdots & G_{ij}^{1n} \\ \vdots & \ddots & \vdots \\ G_{ij}^{m1} & \cdots & G_{ij}^{mn} \end{bmatrix} \qquad (2)$$

where m is the number of tracked beads and n is the number of facets used to discretize the cell. Each element of $\boldsymbol{\Gamma}$ is a 3 x 3 submatrix relating the displacement of bead m in direction i in response to a load on facet n in direction j (inset, green arrows):

$$G_{ij} = \begin{bmatrix} g_{11} & g_{12} & g_{13} \\ g_{21} & g_{22} & g_{23} \\ g_{31} & g_{32} & g_{33} \end{bmatrix} \qquad (3)$$

Equation (1) is now discretized into $\mathbf{u} = \boldsymbol{\Gamma}\mathbf{T}$ (4) and can be inverted using least squares minimization routines for ill-posed, over-determined systems.

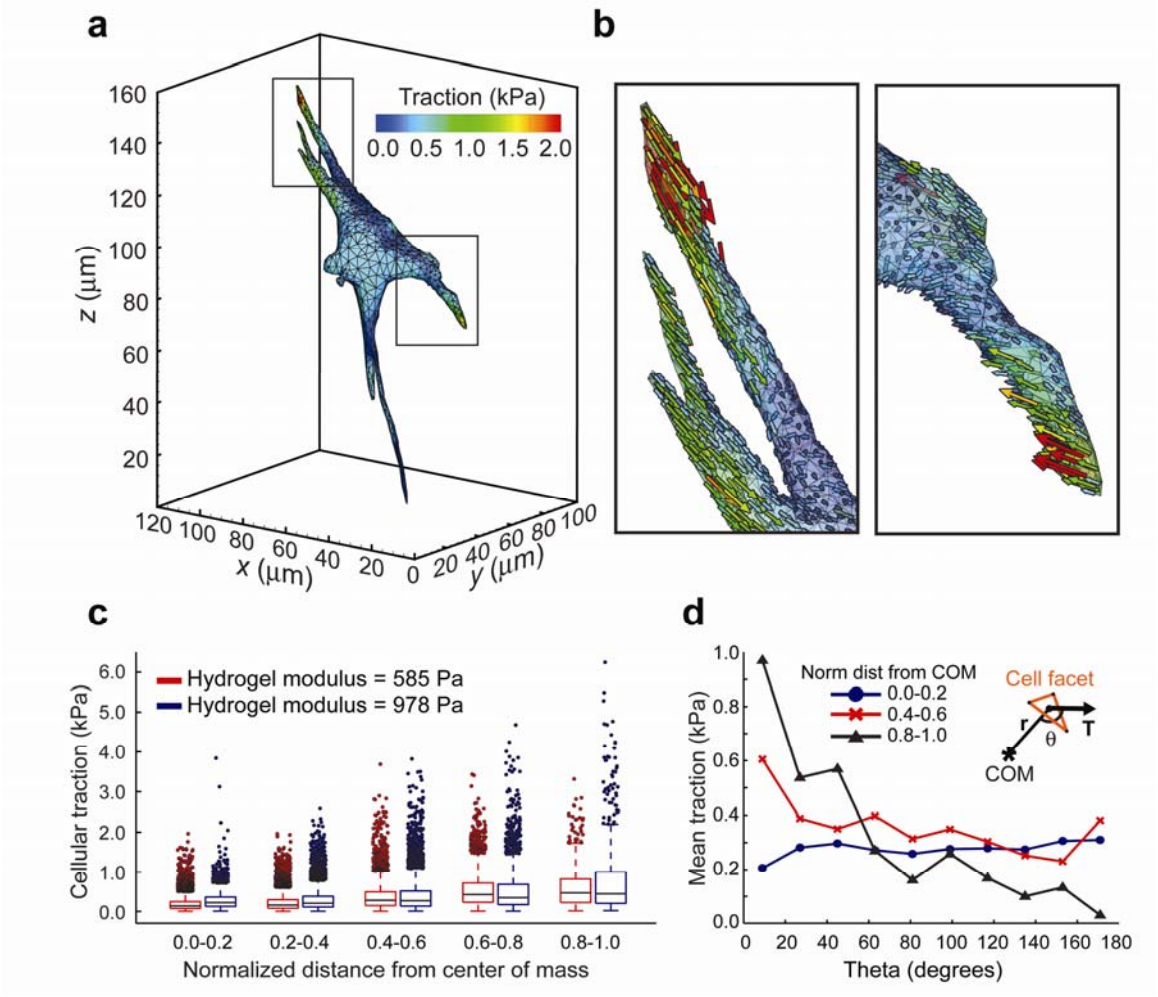

Figure 4.9: Measurement of tractions exerted by live cells. (**a**) Contour plot of the tractions (magnitude) exerted by the cell. (**b**) Magnified sections outlined in **a** showing the individual traction vectors on each facet. (**c**) Plot of the traction magnitudes as a function of the normalized distance from the center of mass (COM) of the cell. Most spread regions (e.g. tips of long slender extensions) are approximately 1 whereas the cell body is approximately 0. Tractions from cells encapsulated in 585 ± 196 and 978 ± 228 Pa (Young's modulus, ± s.d.) hydrogels are shown. (**d**) Mean traction at a given angle with respect to the center of mass for cells encapsulated in 978 ± 228 Pa hydrogels. Plots shown are for least spread (0.0-0.2), moderately spread (0.4-0.6) and most spread (0.8-1.0) regions of cells. Data from **c** and **d** are from n = 12 cells from each condition.

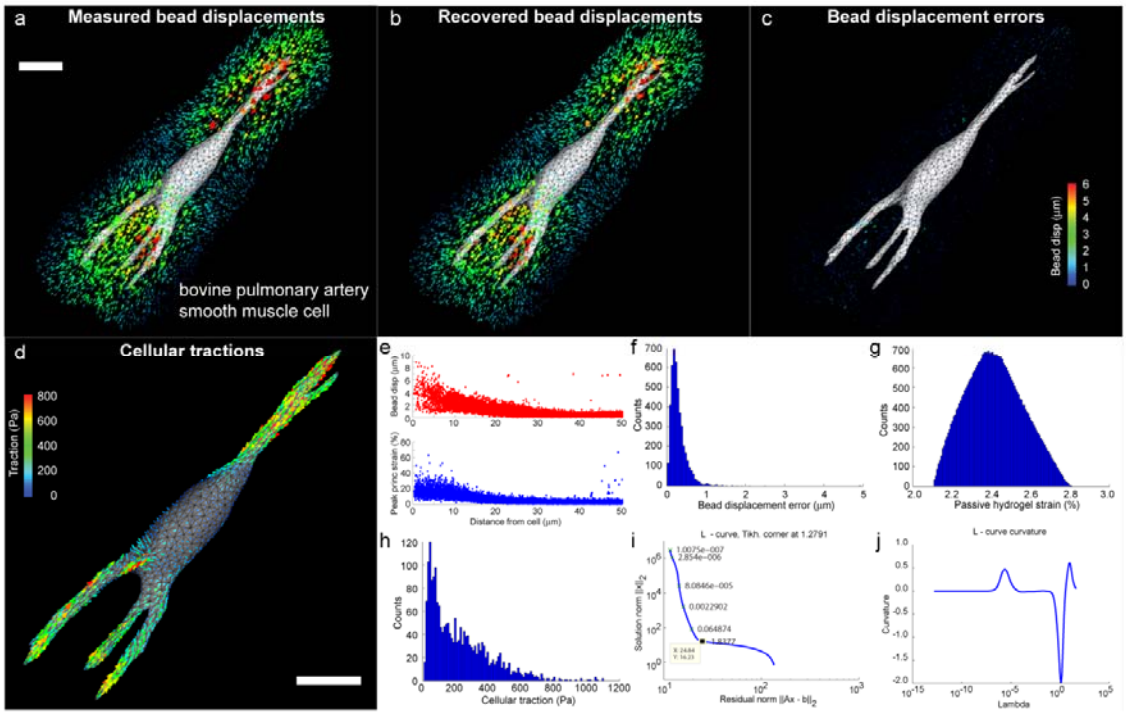

Figure 4.10: 3D traction datasheet. Bovine pulmonary artery smooth muscle cells were encapsulated in a 7% w/w PEGDAam based hydrogel and allowed to spread over 72 hours. To measure the tractions exerted by the cell, volumetric images were acquired before and after treatment with 0.5% SDS. In order to verify the accuracy of the reconstructed tractions, it is useful to generate a datasheet displaying all relevant data for a given cell. (**a**) Surface mesh of the cell showing measured bead displacements in the hydrogel. Scale bar = 20 μm. (**b**) Plot of the "best fit" bead displacements that would be predicted based on the recovered cellular tractions. (**c**) Plot of the errors in bead displacements between the experimentally measured and best fit fields. (**d**) Plot of the tractions exerted by the cell. Scale bar = 20 μm. (**e**) Plots of the bead displacement and peak (maximum magnitude) principal hydrogel strain as a function of distance from the surface of the cell. (**f**) Histogram of the errors between the measured and best fit bead displacements. (**g**) Histogram of the peak principal strains induced by correction for passive hydrogel drift and swelling. (**h**) Histogram of the cellular tractions. (**i**) Plot of the L-curve (log-log plot of the solution norm vs. the residual norm as a function of lambda) used to calculate the correct amount of regularization. The corner of the L-curve indicates the optimal amount of regularization. (**j**) Plot of the curvature of the L-curve showing a distinct minimum in curvature at the optimal value of lambda.

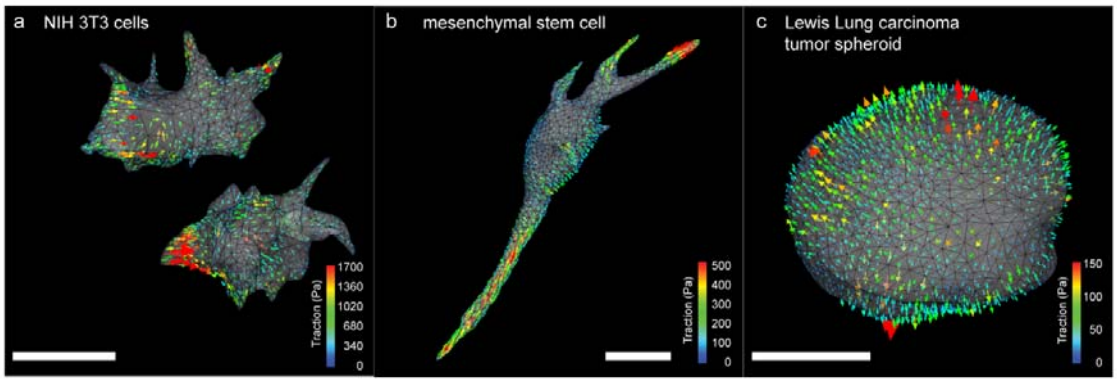

Figure 4.11: Measurement of cellular tractions in different contexts. (**a**) NIH 3T3 fibroblasts were encapsulated in an 11% w/v PEGDA based hydrogel and allowed to spread for 72 hrs. Two cells in the vicinity of each other extend processes preferentially away from the neighboring cell and pull back inward towards their respective centers of mass. These data demonstrate that the more complex configuration of two neighboring cells does not limit the algorithm in its ability to reconstruct tractions. (**b**) Human mesenchymal stem cells were encapsulated in a 7% w/w PEGDAam based hydrogel and allowed to spread over 72 hours. These cells invaded into the surrounding hydrogel with long slender and occasionally branched extensions. Strong forces were located predominantly near the tips of these extensions and pulled inward back toward the center of mass of the cell. (**c**) Lewis lung carcinoma cells were encapsulated in a 7% w/w PEGDAam based hydrogel and cultured for 72 hrs. During this time, the cells did not invade into the surrounding hydrogel as did the other cell types measured, but rather rapidly proliferated forming a multicellular spheroid. The expanding spheroid deformed the surrounding hydrogel and exerted predominantly outward normally directed tractions that were distributed over the surface of the multicellular structure. Such 'pressures' have been observed in large tumor masses, but not previously appreciated in small spheroids. All scale bars = 20 μm.

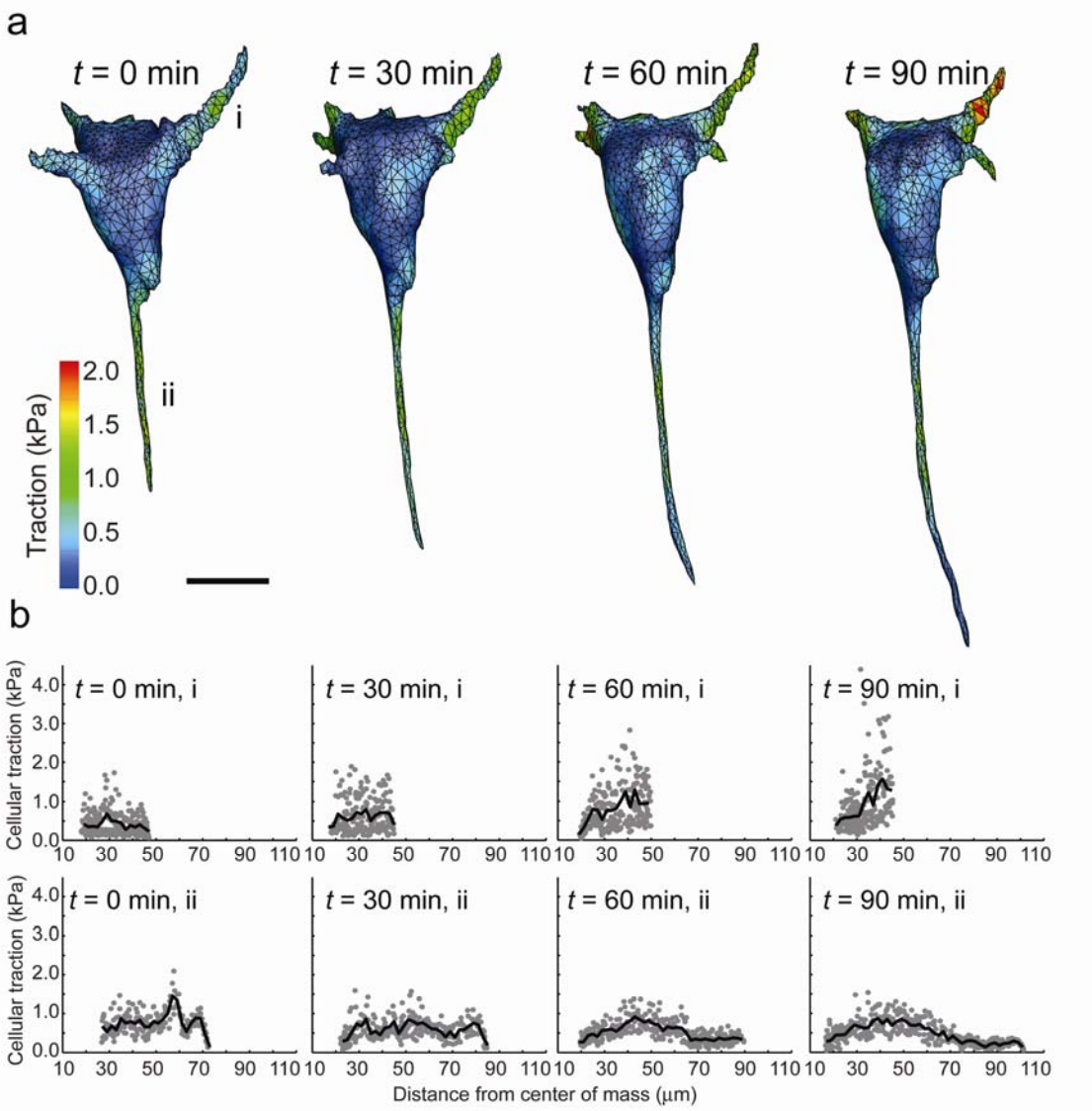

Figure 4.12: Measurement of dynamic tractions exerted by spreading cells. (**a**) Contour plot of the tractions (magnitude) exerted by a cell as it invades into the surrounding hydrogel. Stabile and invading extensions are labeled i and ii, respectively. Scale bar = 20 μm. (**b**) Tractions exerted by extensions labeled in **a** as a function of distance from the center of mass of the cell.

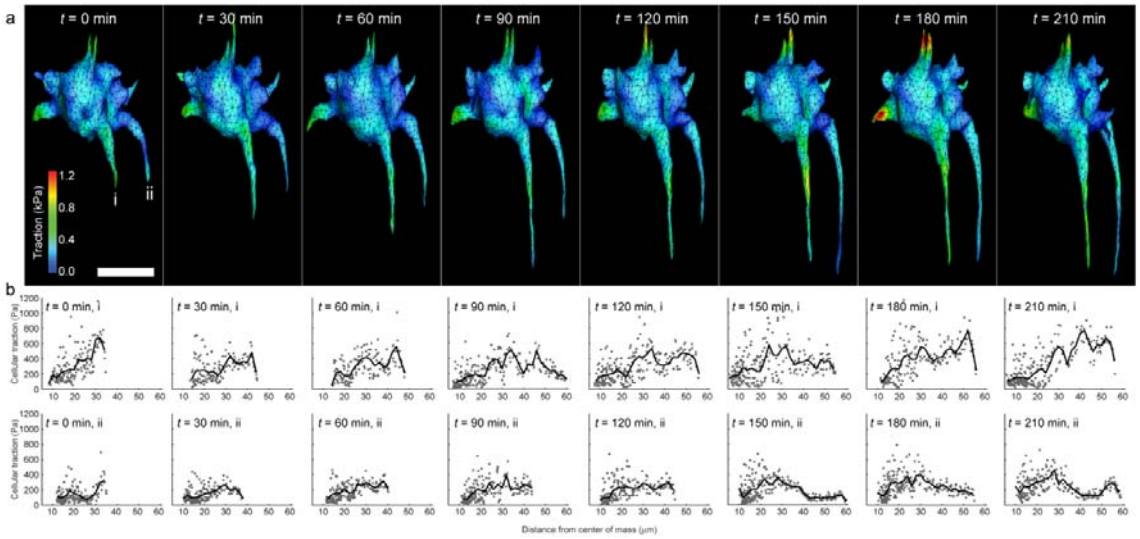

Figure 4.13: Measurement of dynamic tractions exerted by spreading cells. NIH 3T3 fibroblasts were encapsulated in an 11% w/v PEGDA based hydrogel and allowed to begin spreading. The cell and surrounding hydrogel were then imaged for 3.5 hours in 30 minute intervals. (**a**) During this time, the labeled extensions (i and ii) exerted tractions as they extended into the matrix. Interestingly, this spreading seemed to be biased, occurring only on one face of the cell. In contrast, strong forces were also exerted by small dynamic protrusions on the face of the cell opposite these spreading extensions. Scale bar = 20 μm. (**b**) Tractions exerted by the extensions labeled in **a** are plotted as a function of the distance from the center of mass of the cell. Consistent with our observations from other cells, these invading structures showed strong forces proximal to the leading edge, with a drop in traction near the tip.

CHAPTER 5: A QUANTITATIVE PLATFORM TO CHARACTERIZE THE RESOLUTION AND SENSITIVITY OF CELLULAR TRACTION MEASUREMENTS

5.1 RATIONALE

Cells migrate by exerting spatially and temporally coordinated traction forces on their surroundings (Lauffenburger and Horwitz 1996; Dembo and Wang 1999; Beningo, Dembo et al. 2001; Fournier, Sauser et al. 2010; Jannat, Dembo et al. 2011). When inside a multicellular tissue, the collective action of these forces by many cells leads to morphogenetic events and maintains tissue homeostasis (Wolff 1892; Stopak and Harris 1982; Stopak, Wessells et al. 1985). Recent work has revealed that the forces exerted by cells against the extracellular matrix (ECM) can also feedback through integrins and FA proteins to regulate a diverse array of cellular functions including proliferation and differentiation (Huang, Chen et al. 1998; McBeath, Pirone et al. 2004; Engler, Sen et al. 2006; Geiger, Spatz et al. 2009). Commensurate with the increasing appreciation for the role of mechanical forces in biology, there now exist numerous methods to measure the forces generated by cells with sub-cellular accuracy, including measuring the deformations underlying cells grown on elastic substrates (continuum approaches - collectively termed traction force microscopy (TFM)) (Harris, Wild et al. 1980; Dembo and Wang 1999; Balaban, Schwarz et al. 2001; Butler, Tolic-Norrelykke et al. 2002) and on arrays of microfabricated elastic pillars (discrete approaches) (Tan, Tien et al. 2003; du Roure, Saez et al. 2005; Fu, Wang et al. 2010). In discrete systems, cell generated tractions act on the tips of deformable pillars which have been functionalized and an adhesive protein. Individual pillars will then bend in response to the applied loads. In this setting, the resolution of the force reconstruction is given explicitly by the spacing of the pillars, and the accuracy of a given traction measurement depends only on the ability to precisely determine both the amount of pillar bending and the mechanical properties of each pillar. This straightforward calculation allows maps of cell tractions to be computed simply and with minimal computation. However, such systems constrain cell adhesions to discrete and punctuate locations and require microfabrication tools which may not be readily available. In contrast, continuous substrates are often generated from linearly elastic hydrogels such as polyacrylamide or polyethylene glycol which are then functionalized with an adhesive peptide or protein. These substrates do not constrain the locations or growth of adhesions, but suffer from the fact that the displacements measured at a given location on the substrate are influenced by all tractions exerted on the surface. Thus, reconstructing the cellular tractions from a measured displacement field traditionally requires inversion of an ill-posed mathematical problem and regularization to obtain a stable solution (Dembo, Oliver et al. 1996). Nevertheless, due to the minimal experimental resources required, continuous methods remain the most widely used techniques to measure cell generated tractions.

There now exists a multitude of different approaches to convert a measured displacement field into a cellular traction field, including the boundary element method (BEM) (Dembo, Oliver et al. 1996), Fourier transform traction cytometry (FTCC) (Butler, Tolic-Norrelykke et al. 2002), traction reconstruction from point sources (Balaban, Schwarz et al. 2001) and finite element methods (FEM) (Yang, Lin et al. 2006). A full description of these techniques can be found in (Wang and Lin 2007) and several quantitative comparisons can be found in (Sabass, Gardel et al. 2008). Moreover, recent approaches have extended the measurement of cellular tractions on continuous substrates into pseudo-3D (cells exerting 3D tractions on top of a planar half space) (Hur, Zhao et al. 2009; Maskarinec, Franck et al. 2009; Delanoe-Ayari, Rieu et al. 2010) and fully-3D (cells fully encapsulated within a 3D matrix) settings by utilizing a discretized Green's function (DGF) approach (Legant, Miller et al. 2010).

In part, the large diversity of approaches reflects the complexity of solving mathematically ill-posed problems. Comparing the measurements from different techniques and even from different experimental implementations of the same technique is challenging because the accuracy of the traction recovery will depend on several factors including the accuracy and density of displacement measurements, an accurate choice of the regularization parameter (or optimal smoothing of the displacement field for FTCC and FEM methods), as well as the magnitude and spatial frequency of the loadings themselves (since the displacement field will decay more rapidly for smaller or more rapidly varying tractions). While improvements have been made to optimize each of these parameters, there has thus far been lacking a quantitative metric to assess the accuracy and potential improvements offered by a given modification. A full characterization of the spatial resolution and traction sensitivity afforded by a given measurement is essential when attempting to draw biological conclusions from experimentally measured traction data; however, such measurements are rarely included when presenting TFM data. Here, we present a general approach to quantify the spatial resolution and sensitivity of cellular traction measurements in both pseudo-3D (**Part A**) and fully-3D (**Part B**) settings. Using computational simulations, we investigate the relative contributions and ultimate limits of traction reconstruction due to 1) noise on the displacement measurements, 2) density of displacement measurements, and 3) the choice of the regularization parameter. It is our hope that the data and methods presented here will serve as a benchmark for future studies of cellular tractions in pseudo-3D and fully-3D settings and provide a framework to determine whether biological conclusions drawn from computed traction fields are reasonable given the constraints of the traction reconstruction algorithms.

5.2 METHODS

5.2.1 Finite element modeling

Finite element models were constructed in Abaqus Standard (Dassault Systèmes). All models were constructed from 4 node tetrahedral elements using standard tri-linear shape functions ("C3D4" in Abaqus). Loads were applied as surface tractions using the distributed load ("DSLOAD – TRVEC" in Abaqus). For both the pseudo-3D and fully 3D geometries, the bottom surface of the hydrogel was fixed using the "ENCASTRE" boundary condition. Fixing the side boundaries in addition to the bottom surface had little effect on the recovered tractions, thus confirming the approximation of a semi-infinite or infinite medium for the pseudo-3D and fully 3D cases respectively. All solutions were acquired under the linear small strain approximation using a direct solver. All data presented in the manuscript were calculated using a Dell Precision T7400 workstation equipped with dual quad core Intel Xeon processors and 16 GB of RAM.

5.2.2 Computation of surface tractions from volume displacement fields

From linear elasticity, the displacement field $\bar{\boldsymbol{u}}(\bar{\boldsymbol{r}})$ within a continuum is related to the traction field $\bar{\boldsymbol{T}}(\bar{\boldsymbol{r}}')$ at a point via a Green's function $\boldsymbol{\Gamma}(\bar{\boldsymbol{r}}, \bar{\boldsymbol{r}}')$ and a Fredholm integral of the first kind:

$$\bar{\boldsymbol{u}}(\bar{\boldsymbol{r}}) = \int \boldsymbol{\Gamma}(\bar{\boldsymbol{r}}, \bar{\boldsymbol{r}}')\ \bar{\boldsymbol{T}}(\bar{\boldsymbol{r}}')\ \mathrm{d}\bar{\mathbf{r}} \qquad (1)$$

For 2D planar elastic halfspaces, this relationship has been solved analytically by Boussinesq (Boussinesq 1885) for point shear forces parallel to the surface of the half space

$$\boldsymbol{u_i} = \frac{\boldsymbol{P(1+\nu)}}{\boldsymbol{2\pi ER}}\left\{\boldsymbol{\delta_{i1}} + \frac{\boldsymbol{x_1 x_i}}{\boldsymbol{R^2}} + \boldsymbol{(1-2\nu)}\left(\frac{\boldsymbol{R\delta_{i1}}}{\boldsymbol{R+x_3}} - \frac{\boldsymbol{Rx_1\delta_{i3}}}{\boldsymbol{(R+x_3)^2}} - \frac{\boldsymbol{x_1 x_i}}{\boldsymbol{(R+x_3)^2}}\right)\right\} \textbf{(2)}$$

and by Cerruti (Cerruti 1882) for point forces acting normal to the surface of the half space

$$\boldsymbol{u_i} = \frac{\boldsymbol{P(1+\nu)}}{\boldsymbol{2\pi E}}\left\{\frac{\boldsymbol{x_3 x_i}}{\boldsymbol{R^3}} + \boldsymbol{(3-4\nu)}\frac{\boldsymbol{\delta_{i3}}}{\boldsymbol{R}} - \frac{\boldsymbol{(1-2\nu)}}{\boldsymbol{R+x_3}}\left(\boldsymbol{\delta_{3i}} + \frac{\boldsymbol{x_i}}{\boldsymbol{R}}\right)\right\} \qquad \textbf{(3)}$$

Where the basis vectors are oriented such that e_1 and e_2 are parallel to the surface of the halfspace and e_3 projects into the depth of the volume. P is the magnitude of the applied force

and E and v are the Young's modulus and Poisson ratio of the material respectively. $R = \sqrt{x_1^2 + x_2^2 + x_3^2}$ is the geometric distance from the location of force application and the location of displacement measurement. Thus the displacements induced any combination of surface loadings on a halfspace can be computed via linear superposition of these solutions and integration over the surface of load application. For the fully 3D case, the displacement field within the volume due to a point force was determined by Lord Kelvin (Thompson 1848):

$$\boldsymbol{u_i} = \frac{(1+v)}{8\pi E(1-v)R}\left\{\frac{P_k x_k x_i}{R^2} + (3-4v)P_i\right\} \quad (4)$$

where 2-4 have been reproduced from (Bower 2009). While these formulas are important when considering the behavior of the physical system, experimentally implementing them requires discretization of the surface and numerical integration. Moreover, in the fully 3D case, the cell-ECM interface will be of arbitrary geometry and there does not exist an analytical solution to relate the displacement within the hydrogel to the tractions on the surface of this interface. To address these limitations and to maintain generality between the pseudo-3D and fully 3D settings, we generated a discretized approximation of $\boldsymbol{\Gamma}$ using the finite element method as described previously (Legant, Miller et al. 2010). This approach, termed the discretized Green's function (DGF) approach, allows for the finite thickness of the hydrogel to be explicitly incorporated in the pseudo-3D setting and permits $\boldsymbol{\Gamma}$ to be defined on the complex surface of an encapsulated cell in the fully 3D setting. Because both the tractions, and displacements are measured at discrete locations, equation 1 can be represented in matrix form as:

$$\mathbf{u} = \boldsymbol{\Gamma}\mathbf{T} \quad (5)$$

where we have adopted the notation used in Schwartz et al. 2002 in which

$$\mathbf{u} = [u_1^1(\mathbf{r}); u_2^1(\mathbf{r}); u_3^1(\mathbf{r}); u_1^2(\mathbf{r}); u_2^2(\mathbf{r}); u_3^2(\mathbf{r}); \ldots; u_1^m(\mathbf{r}); u_2^m(\mathbf{r}); u_3^m(\mathbf{r})]$$

is a 3m column vector, where m is the number of points at which the displacement is known and $\mathbf{r}$ is the position vector describing the location of each point.

$$\mathbf{T} = [T_1^1(\mathbf{r}'); T_2^1(\mathbf{r}'); T_3^1(\mathbf{r}'); T_1^2(\mathbf{r}'); T_2^2(\mathbf{r}'); T_3^2(\mathbf{r}'); \ldots; T_1^n(\mathbf{r}'); T_2^n(\mathbf{r}'); T_3^n(\mathbf{r}')]$$

is a 3n column vector, where n is the number of discretized facets on the surface of the cell or hydrogel and $\mathbf{r}'$ is the position vector of each facet. Subscripts for both *u* and *T* in these definitions represent displacements and tractions respectively along each Cartesian axis.

$\mathbf{\Gamma}$ is an m x n matrix of the following form:

$$\Gamma_{ij}^{mn} = \begin{bmatrix} G_{ij}^{11} & \cdots & G_{ij}^{1n} \\ \vdots & \ddots & \vdots \\ G_{ij}^{m1} & \cdots & G_{ij}^{mn} \end{bmatrix} \quad (6)$$

Each element of $\mathbf{\Gamma}$ is a 3 x 3 submatrix relating the displacement of bead m in direction I in response to a load on facet n in direction j:

$$G_{ij} = \begin{bmatrix} g_{11} & g_{12} & g_{13} \\ g_{21} & g_{22} & g_{23} \\ g_{31} & g_{32} & g_{33} \end{bmatrix} \quad (7)$$

We used 0^{th} order Tikhonov regularization together with either the L-curve criterion(Hansen 2001) or the discrepancy principal for implementing and choosing the correct value for the Lagrange parameter, λ, resulting in the following optimization:

$$\min\{|\mathbf{\Gamma T} - \mathbf{u}|^2 + \gamma^2|\mathbf{T}|^2\} \quad (8)$$

This optimization problem was solved by singular value decomposition using the suite of Matlab routines "*Regularization tools*" by PC Hansen (Hansen 2007). All error computations were computed in Matlab and figures prepared in Adobe Illustrator. Volume renderings were prepared in either Abaqus or Tecplot.

5.3 RESULTS

5.3.1 Part A: Pseudo-3D traction force microscopy

While 2D TFM has been a mainstay of the mechanotransduction field for nearly two decades, only recently have investigators extended these methods to measure the normal forces exerted by cells on top of planar substrates in addition to shear forces (Hur, Zhao et al. 2009; Maskarinec, Franck et al. 2009; Delanoe-Ayari, Rieu et al. 2010). The origin and consequence of these out of plane forces has yet to be elucidated; however, they have been shown to be of comparable magnitude to the previously observed shear forces and thus may contribute significantly to cell migration and mechanotransduction on 2D substrates. To date, different methods for computing the normal force have yielded varying results as to the location and direction of these forces with some studies demonstrating a pulling (upward) force at the cell perimeter and a pushing (downward force) at the cell interior (Hur, Zhao et al. 2009; Delanoe-Ayari, Rieu et al. 2010). While other methods report a more context dependent force profile with a possibility of forces that appear significantly out of equilibrium or are pushing and pulling in different areas of the cell at different stages of migration (Maskarinec, Franck et al. 2009). While these varying reports may likely be due to differences in cell type or cell stage, there has yet to be an in depth analysis of the resolution of the traction reconstruction afforded by these methods, and thus it is not clear to what extent they can be directly compared. Here, we utilize simulated datasets to provide a platform for measurement of the resolution of both shear and normal forces. We quantitatively characterize the accuracy and sensitivity of the computed tractions to changes in bead density, localization precision and choice of regularization parameter.

5.3.1.1 Spatially defined simulated traction fields to characterize the limits of traction reconstruction

We modeled the hydrogel substrate as a semi-infinite half-space 300 μm x 300 μm x 60 μm with the bottom surface fixed (**Figure 5.1a**). The 100 μm x 100 μm region immediately below the cell was meshed using 4056 triangular elements with an average area of 2.5 μm^2 (**Figure 5.1b**). Each of these elements represents a discrete region upon which a constant surface traction may be computed. Thus the element area determines an absolute lower bound for the spatial resolution of the recovered tractions (much like the pixel size of a CCD chip represents a lower bound for image resolution). When characterizing the resolution of any measurement

system, it is important to assess its performance for all possible loading configurations. While the tractions exerted by polarized cells have been roughly approximated using a force dipole (Butler, Tolic-Norrelykke et al. 2002), this simplification fails to capture many complexities in the traction fields exerted by cells under actual experimental conditions including spreading and migrating cells. Here, we depart from previous characterizations of TFM which seek to compute the recovery from idealized cellular loadings (Butler, Tolic-Norrelykke et al. 2002; Schwarz, Balaban et al. 2002; Sabass, Gardel et al. 2008), and instead draw analogy to how the frequency responses of signal amplifiers are characterized. Using Fourier theory, any 2D distribution of traction forces on the surface of the hydrogel can be represented by a weighted summation of sinusoidal functions. Therefore, by characterizing the response of our TFM measurements to sinusoidally oscillating traction forces of varying wavelengths (or spatial frequencies) and amplitudes, and making use of the linearity of the small strain approximation, we are able to completely characterize the resolution and sensitivity limits for any combination of applied loadings. To implement this, we generated sinusoidally varying load distributions across the surface of the hydrogel with progressively decreasing wavelength (increasing spatial frequency) (**Figure 5.1c**). However, in contrast to an electrical signal which is a 1D scalar function, cell traction forces are 3D vector valued functions. This vector valued traction distribution can be decomposed into scalar valued function multiplied by basis vectors. We chose the traditional basis vectors to be aligned with the Cartesian axis except that we rotated them such that the in-plane basis vectors were aligned parallel and perpendicular with the direction of wave propagation. In order to fully characterize the TFM response, we applied loadings at the hydrogel surface as transverse sinusoidal waves of three types: 1) Shear loads in which the direction of force application was orientated perpendicular to the direction of wave propagation, 2) shear loads in which the direction of force application was oriented parallel to the direction of wave propagation, and 3) normal tractions with the forces oriented into and out of the planar halfspace (**Figure 5.1d**). For each loading, we solved the forward finite element problem to compute the displacement field within the surrounding hydrogel. We then simulated beads at random locations and at varying densities within the 10 μm depth of hydrogel immediately below the 100 μm x 100 μm region of load application. Simulated bead displacements were interpolated from the nodal displacements using standard tri-linear shape functions and varying levels of Gaussian noise were superimposed onto these displacements. Tractions were then recovered as described in **Methods** and compared to the initial loadings (**Figure 5.1e**).

The magnitude of the displacements within the hydrogel will determine the signal to noise and thus strongly affect the accuracy of the recovered tractions. Under the small strain approximation, the magnitude of the displacement fields will scale linearly with the magnitude of the applied loadings. Thus, stronger tractions will result in larger displacements with higher signal to noise and will be more easily recovered. Additionally, tractions oscillating with progressively higher spatial frequencies will produce smaller displacements than those generated by tractions oscillating with lower spatial frequencies (**Figure 5.2a-c**). Moreover, because the displacements decay more slowly along the direction of the force application (~1/r, when r is the parallel distance from a point source) than perpendicular to the direction of force (~$1/r^3$, when r is the perpendicular distance from a point source), we found that shear tractions oriented perpendicular to the axis of spatial variation generated significantly larger displacements than shear tractions which were oriented parallel to the axis of spatial variation. Normal tractions generated maximal displacements of an intermediate magnitude; however, decayed more slowly as a function of distance from the surface than did either of the shear loadings (**Figure 5.2a-c**). Thus, the ultimate signal to noise will be determined not only by the bead localization precision, but also by the magnitude, orientation, and characteristic length of the applied traction field.

5.3.1.2 Resolution limits as a function of measurement noise and bead density

We calculated the percent error for each traction reconstruction as $\frac{|\mathbf{T}_{\text{applied}}-\mathbf{T}_{\text{recovered}}|^2}{|\mathbf{T}_{\text{applied}}|^2} * 100$. As stated previously, this reconstruction is ill-posed, but can be solved by use of 0^{th} order Tikhonov regularization**,** where the optimal recovery depends on the choice the regularization parameter lambda (**Figure 5.3a**). Note that even under optimal values of regularization and no measurement noise, the ability to accurately recover tractions decreases as the magnitude or wavelength of the tractions decrease due to finite sampling of the displacement field. At each surface facet, we computed the difference between the recovered traction vector and the true applied traction vector as a fraction of the true traction vector length. As a visual representation, an error of 10% indicates that the recovered traction vector was computed to lie within a sphere that is centered at the tip of the true traction vector and has a radius of 10% of the length of the true traction vector (**Figure 5.3b**). Thus, significant information about the direction and magnitude can be obtained even with a reported error of 50%.

For each of the simulated loadings, we tested our ability to recover the tractions as a function of traction amplitude, number of displacement measurements, and displacement

measurement noise, all under optimal values of regularization (**Figure 5.4**). The relative magnitudes (scaled by the Young's modulus of the hydrogel) of the applied loadings and bead densities were chosen to be in the range of values previously reported for cells on 2D hydrogels (Sabass, Gardel et al. 2008). In absence of any displacement measurement noise, all loadings were readily recovered with errors of 15% or less. The residual errors in these instances can be attributed to errors in the interpolation of the finite element nodes onto the randomly chosen bead coordinates and the finite sampling of the displacement field. The addition of Gaussian noise to the displacements measurements lead to reductions of recovery efficiency. Loadings with smaller wavelengths were dramatically more sensitive to displacement measurement noise than loadings with larger wavelengths. Increasing bead density modestly decreased the sensitivity of a given traction reconstruction to measurement noise. An improvement of approximately 10-20% resulted from a 4 fold increase in bead density. All other parameters being equal, shear forces directed perpendicular to the axis of wave propagation were more accurately recovered and at higher spatial frequencies than shear forces directed parallel to the axis of wave propagation (**Figure 5.4a,b**). Normal forces directed perpendicular to the planer half-space were recovered with accuracy in between that of the two types of shear loadings (**Figure 5.4c**).

5.3.1.3 Traction reconstruction under optimal and estimated regularization parameters

In practice, an optimal value for the regularization parameter γ is not able to be computed for an experimental dataset. Instead, this value must be estimated either from knowledge of the source data or estimates of the measurement noise. The two most popular methods for choosing a value for γ are the discrepancy principle (Dembo, Oliver et al. 1996) and the L-curve (Schwarz, Balaban et al. 2002). A full description of the different methods for choosing γ can be found in (Hansen 2007), with different implementations in the context of TFM investigated in (REF Sabass). Here, we focus on finding γ through the use of the L-curve criterion, which acquires its name because a plot of log $|\mathbf{T}|^2$ vs. log $|\boldsymbol{\Gamma}\mathbf{T} - \mathbf{u}|^2$ as a function of γ often has an "L" shape. The corner of the L-curve corresponds to an optimal balance between matching the experimental displacement data and regularizing to remove high frequency noise (Hansen 2001). This value is dependent only on the experimental data and mathematical character of $\mathbf{T}$ and requires no a priori assumptions.

To determine the effect of estimating γ on the resolution of the TFM measuremnts, we fixed the bead density at 20E10 beads/cm3 and computed the reconstruction errors under optimal

and L-curve selected regularization. For high signal to noise displacements (i.e. under low noise, long wavelengths, or high traction magnitudes), the traction reconstructions computed using the L-curve gave a near optimal match to the applied loadings (**Figure 5.5**). However, as the signal to noise of the displacement measurements decreased (i.e. under higher noise, more rapidly varying loadings, or smaller magnitude tractions), the L-curve method can fail completely (vertical black lines in **Figure 5.5**). In these cases, the L-curve algorithm either failed to find, or found an incorrect corner. As the signal to noise of the displacement measurements decreases, the distinct corner of the L-curve becomes less apparent (**Figure 5.6a-c**). As this occurs, secondary corners may arise and cause an incorrect value of γ to be chosen. Care should be taken when using the L-curve with experimental data to verify that a distinct corner in fact exists. As a general practice, a of plot log $|\mathbf{T}|^2$ vs. log $|\Gamma\mathbf{T} - \mathbf{u}|^2$ as a function of γ should be generated for any experimental TFM measurement to investigate the sensitivity of the solution in the vicinity of a chosen value for γ.

5.3.2 Part B: Fully-3D traction force microscopy

While 2D and recently developed pseudo-3D TFM methods have contributed immensely to our understanding of cellular processes, many cellular behaviors are altered or lost completely when cells are removed from a 3D matrix and cultured on a 2D substrate. In this section, we investigate the tractions exerted by cells that are fully surrounded by a 3D hydrogel matrix. Similar to the pseudo-3D case, this system utilizes linearly elastic hydrogels that are functionalized with adhesive proteins; however, MMP degradable domains are also incorporated into the polymer backbone to permit cells to spread and invade the surrounding matrix. These synthetic hydrogels have been shown to recapitulate many mechanically mediated 3D cell behaviors including migration (Gobin and West 2002; Miller, Shen et al. 2010) proliferation (Patel, Gobin et al. 2005) and differentiation (Hwang, Varghese et al. 2011). Moreover, such matrices are leading candidates for tissue engineered substrates, where the aforementioned behaviors are essential to tissue integration and function. While natural matrices such as collagen or fibrin are commonly used cell culture platforms, such matrices are mechanically nonlinear, viscoelastic, non-affine, and can be dramatically altered by cells which bundle and crosslink surrounding fibers. They are therefore unsuitable for quantitative measurements of cellular tractions under homogeneous and isotropic continuum assumptions. In contrast, we have previously shown that degradable polyethylene glycol hydrogels remain largely inert to these

structural changes (Legant, Miller et al. 2010). Methods to measure the mechanical tractions exerted by cells encapsulated within synthetic hydrogel matrices are therefore poised to significantly contribute to studies of 3D cell behavior. Here, we demonstrate that simulated datasets can be used to quantify the spatial resolution and sensitivity of traction measurements as a function of noise on the displacement measurements, density of displacement measurements, and the choice of the regularization parameter.

5.3.2.1 Spatially defined simulated traction fields to characterize the limits of traction reconstruction

In order to generate spatially well defined loadings in a 3D setting, we modeled the cell as a 50 μm diameter sphere composed of 2000 triangular facets with an average element area of 3.7 μm^2. This sphere was centered within a 400 μm cube representing our computational domain (**Figure 5.7a, b**). Although this geometry is dramatically simplified from that of an actual cell in 3D, it allows the definition of loadings with wavelengths that are a function only of the spherical coordinate ϕ. Such loadings can be quantified by their average characteristic length of spatial variation, defined as the average wavelength of the loading on the surface of the sphere. As for the pseudo-3D case, for each loading, we solved the forward finite element problem to compute the displacement field within the surrounding hydrogel. We then simulated beads at random locations and at varying densities and interpolated from the computed nodal displacements. Varying levels of Gaussian noise were superimposed onto these displacements, and the tractions recovered as described in **Methods**. We generated 5 sinusoidal loadings with average wavelengths that varied from 50 to 10 μm (**Figure 5.7c**). All simulated loadings were in static equilibrium, thus avoiding the superposition of any low frequency offset in the displacements. In theory, it is possible to compare the recovery of both shear and normal tractions in the fully 3D setting; however, given that the curvature of the surface of an encapsulated cell vary at each location and may be dramatically different depending on direction, the translation of these comparisons into experimentally relevant settings is challenging. We thus only investigated loadings oriented normal to the surface of the sphere. Such a comparison still provides a general description for the resolution of a TFM measurement and allows for comparison of experimental parameters. However, the true resolution of an experimental measurement will be dependent on the local geometry of the cell-ECM interface.

The surface deformations induced by the simulated loadings are shown in **Figure 5.7d**. Similar to the pseudo-3D case, the magnitude of the displacements measured at a given distance from the cell surface will scale linearly with the magnitude of the applied loadings (assuming the use of the small strain approximation) and will decrease for loadings of smaller wavelength (**Figure 5.8a**).

5.3.2.2 Resolution limits as a function of measurement noise and bead density and regularization parameter

For each of the simulated loadings, we tested our ability to recover the tractions as a function of traction amplitude, number of displacement measurements, and displacement measurement noise, all under optimal values of regularization (**Figure 5.8b**). The relative magnitudes (scaled by the Young's modulus of the hydrogel) of the applied loadings and bead densities were chosen to be in the range of values previously reported for cells in 3D hydrogels (Legant, Miller et al. 2010). In absence of any displacement measurement noise, all loadings were readily recovered to approximately 80% or greater, with more slowly varying loadings with a characteristic length of 100 μm reaching as high as 99% recovery. The presence of Gaussian measurement noise to the displacements lead to reductions of recovery accuracy. Similar to the pseudo-3D case, loadings with smaller wavelengths were dramatically more sensitive to displacement measurement noise in comparison to loadings with longer wavelengths. Increasing bead density had a relatively modest effect on the recovery of large characteristic lengths, but had a stronger effect on the ability to recover more rapidly varying loadings, especially with increasing levels of displacement measurement noise. To determine the effect of estimating γ, we fixed the bead density at 89E9 beads/cm^3 and computed the reconstruction errors under optimal, L-curve methods for each loading. Under low noise or slowly varying loadings, we found each of these methods to provide a reasonable estimate of the regularization parameter for most of the loadings applied (**Figure 5.8c**). However, under higher noise, or more rapidly varying loadings, the L-curve method can fail completely (vertical black lines in **Figure 5.8c**).

5.4 DISCUSSION

Measurements of cell generated tractions have enabled the field of mechanotransduction and revealed the fundamental mechanical principles by which cells interact with their surroundings. Continuous methods utilizing linearly elastic hydrogels are the most widely used approaches to measure cell traction forces and are currently the only methods capable of measuring forces in pseudo-3D and fully 3D settings. However, these data are sensitive to experimental and computational parameters resulting in measurements that can vary widely in their sensitivity and resolution. It is thus often difficult the compare results between different studies and to assess the validity of biological conclusions drawn from reported traction datasets. Here, we present a general approach to fully calibrate the resolution and sensitivity of TFM measurements utilizing Fourier decomposition of surface tractions and simulated datasets. This approach is compatible with implementations that utilize the inverse method to relate substrate displacements to surface tractions (BEM, FTTC, DGF), as well as direct and FEM based approaches. Further, with relatively few modifications, it can be used to characterize traditional 2D TFM methods as well as pseudo-3D and fully 3D techniques.

To illustrate the validity of our technique, we fully characterized the effects of bead density, measurement noise and regularization utilizing a DGF approach and the L-curve in both pseudo-3D and fully 3D settings. This approach was chosen because the L-curve requires no a priori assumptions about the measurement errors and because DGF is the only approach to date that has been used to measure mechanical tractions exerted by cells fully surrounded by a 3D matrix (Legant, Miller et al. 2010). Direct approaches have recently been used to perform pseudo-3D TFM measurements, but such techniques have not yet been applied to cells in a fully 3D setting. A recent work by Hur et al. (Hur, Zhao et al. 2009) demonstrated that cells on elastic half-spaces generated significant out of plane tractions. In this work, the authors expanded on the method introduced by (Yang, Lin et al. 2006) by computing 3D bead displacements near the surface of the hydrogel and then extrapolating this displacement field onto the surface. They then generated a finite element model of the hydrogel and applied the surface displacements as a boundary condition prior to solving the forward problem for stress equilibrium. Another work by Maskarinec et al. (Maskarinec, Franck et al. 2009) revealed the 3D forces generated by migrating cells by solving for the surface tractions by directly computing the material strains via differentiation of the displacement field. Material stresses were computed via an appropriate constitutive relationship and then extrapolated onto the surface of the hydrogel by taking the dot product of the surface normal vector and the local stress tensor. These approaches appear to be a

promising way to measure cell traction forces in pseudo-3D settings and do not require solving the inverse problem. However, each of these approaches requires extrapolation (either of the displacement field or the stress tensor) onto the surface of the hydrogel. As such, these approaches will only utilize displacements very near the surface. In contrast, Green's function approaches are capable of utilizing all displacement measurements with a suitable signal to noise, which as illustrated in Figs 2 and 8, can propagate a significant distance into the hydrogel. A full characterization of these direct techniques using simulated datasets similar to those presented here will more clearly reveal the advantages and disadvantages of both direct and inverse approaches.

Several important findings emerged from our investigations. First, it is essential to acknowledge that the force sensitivity and spatial resolution of any TFM measurement are interdependent. Larger tractions will be able to be recovered at higher spatial frequencies than smaller tractions. Thus, one can not report the sensitivity (e.g. Pascals) without specifying the spatial frequency at which such tractions can be recovered. Further, one can not report the resolution (e.g. μm) without specifying the magnitude of the tractions at which this resolution is achieved. We also found that the resolution of a TFM measurement is inherently anisotropic. Shear tractions varying perpendicular to the axis of spatial variation and normal tractions exerted perpendicular to the hydrogel surface will be more readily recovered than shear tractions varying parallel to the axis of spatial variation. Finally, the accuracy of the displacement measurements is critical for an accurate determination of the source tractions. For inverse methods, this is reflected by the need to accurately choose an optimal amount of regularization. This effect will also be manifest for direct methods that smooth the displacement measurements prior to computing the tractions. These limitations should be kept in mind for future implementations of TFM. Ideally, a full Fourier characterization should be performed under experimentally relevant levels of bead density (or displacement measurements) and measurement noise to completely characterize the resolution of future traction measurements.

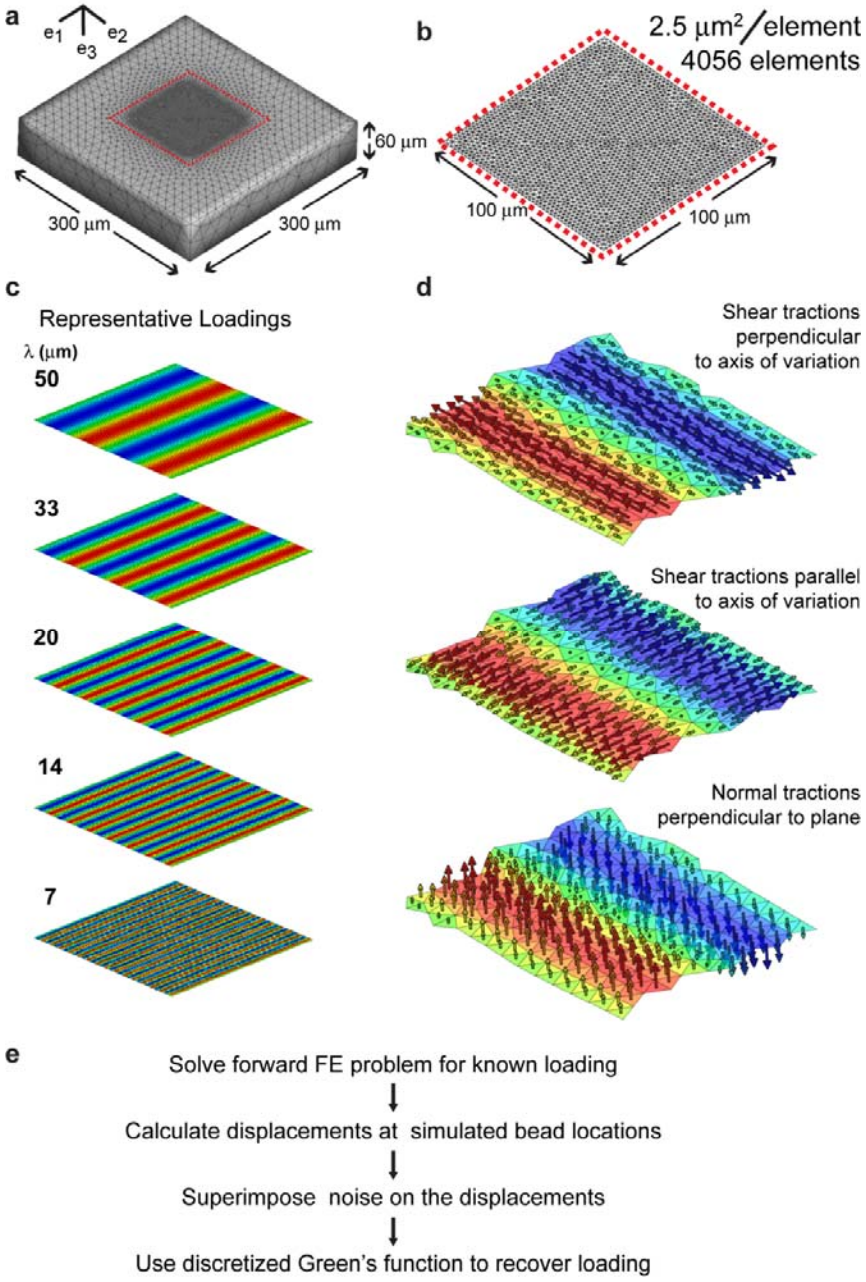

Figure 5.1: Description of computational domain and simulated loadings for pseudo-3D geometries. **a)** Finite element mesh utilized for traction calculations. The central region represents the location of load application. **b)** Expanded view of the central region in (**a**). **c)** Contour maps of representative loadings scaled by the projection of the traction vector along the e_2 (perpendicular), e_1 (parallel) or e_3 (normal) axis. **d)** Vector renderings of representative loadings displaying the orientation of the shear tractions and normal tractions used for TFM characterization. **e)** Process flow diagram illustrating the steps used to characterize the resolution and sensitivity of TFM measurements.

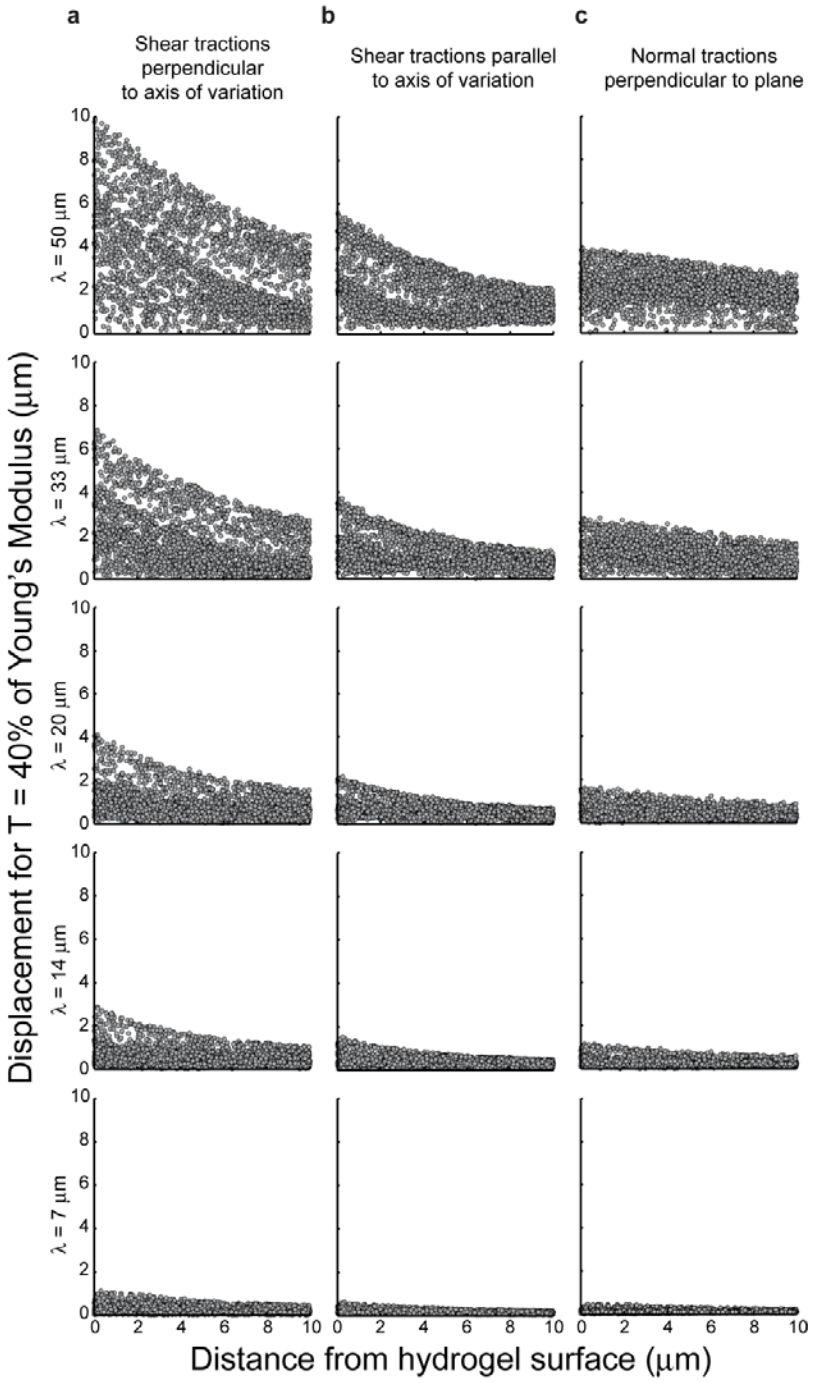

Figure 5.2: Displacements induced by simulated loadings. **a-c)** Displacements within the depth of the hydrogel plotted as a function of the distance from the surface at which the simulated loadings are applied. Representative plots are shown for loadings scaled such that the maximum amplitude is 40% of the hydrogel Young's modulus. Under the small strain approximation, all displacements should scale linearly with the traction amplitude. Rows are sorted by the wavelength of the applied loadings. Columns are sorted by the orientation of the applied traction vectors within each loading.

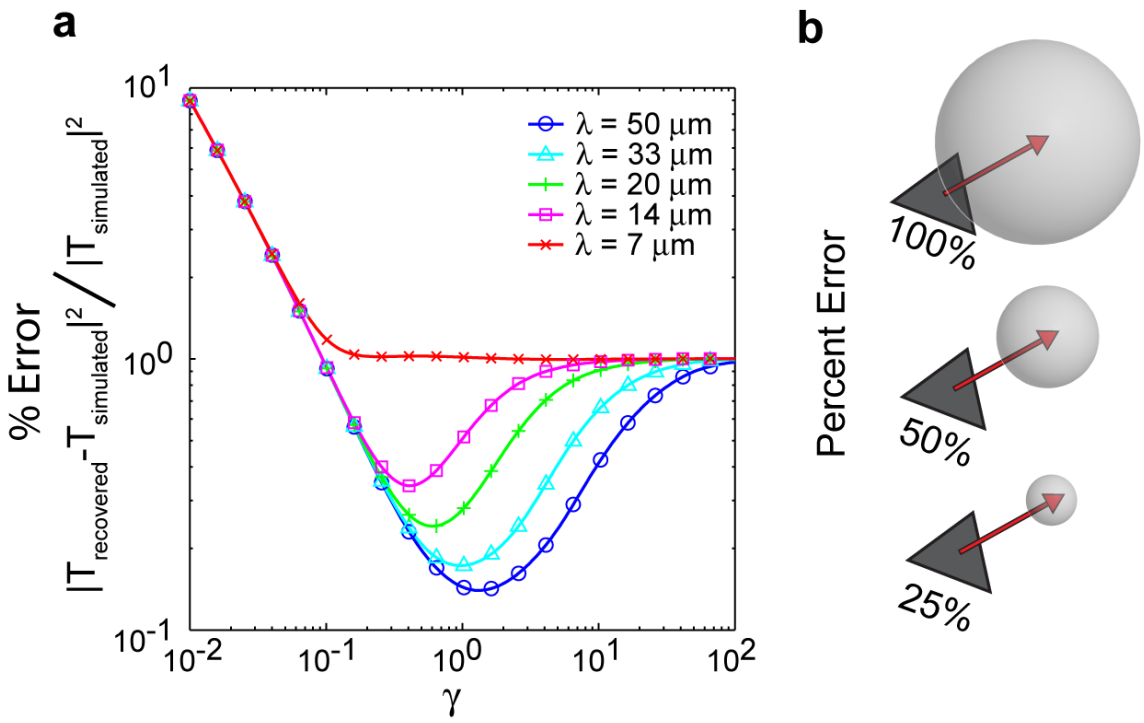

Figure 5.3: Effect of regularization and graphical error representation. **a)** Log-log plot of the percent error in the recover loadings (as compared to the original simulated loadings) as a function of the regularization parameter γ. A representative plot is shown for applied loadings with a maximum amplitude of 40% of the hydrogel Young's modulus, measured at a bead spacing of 1.22 μm with a measurement noise of 50 nm. Optimal values of γ will give the best traction recovery possible for a given combination of bead density and measurement noise. As the wavelength of the simulated tractions decrease, the errors in the recovered tractions will increase even under optimal regularization. **b)** Graphical representation of the percent error (as expressed in (**a**). The recovered traction vector will be predicted to lie within a sphere centered at the tip of the true applied traction vector with a radius equal to the percentage error scaled by the magnitude of the applied traction vector.

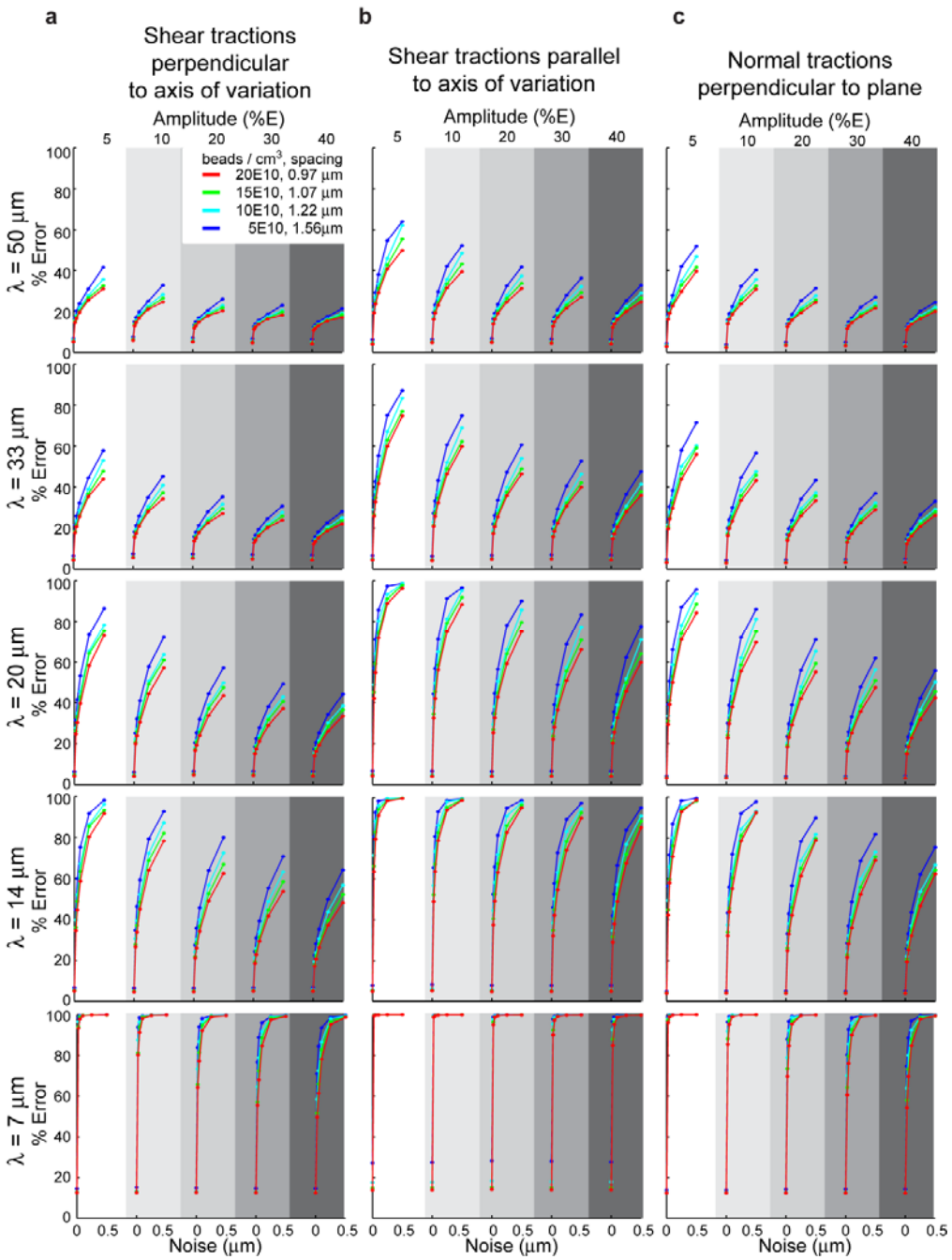

Figure 5.4: Traction recovery under optimal regularization. a-c) Percent error of the recovered tractions is plotted as a function of bead density and measurement noise under optimal regularization. Both the wavelength and magnitudes of the simulated loadings were varied in order to probe the resolution and sensitivity of the recovered tractions. Rows are sorted by the wavelength of the applied loadings. Columns are sorted by the orientation of the applied traction vectors within each loading. Within each plot, differences in bead density are indicated by the transition in color from red to blue. Progressively darker shades of grey indicate simulations performed with applied loadings of increasing magnitude. Increasing levels of noise are plotted within each condition ranging from 0 to 0.5 µm.

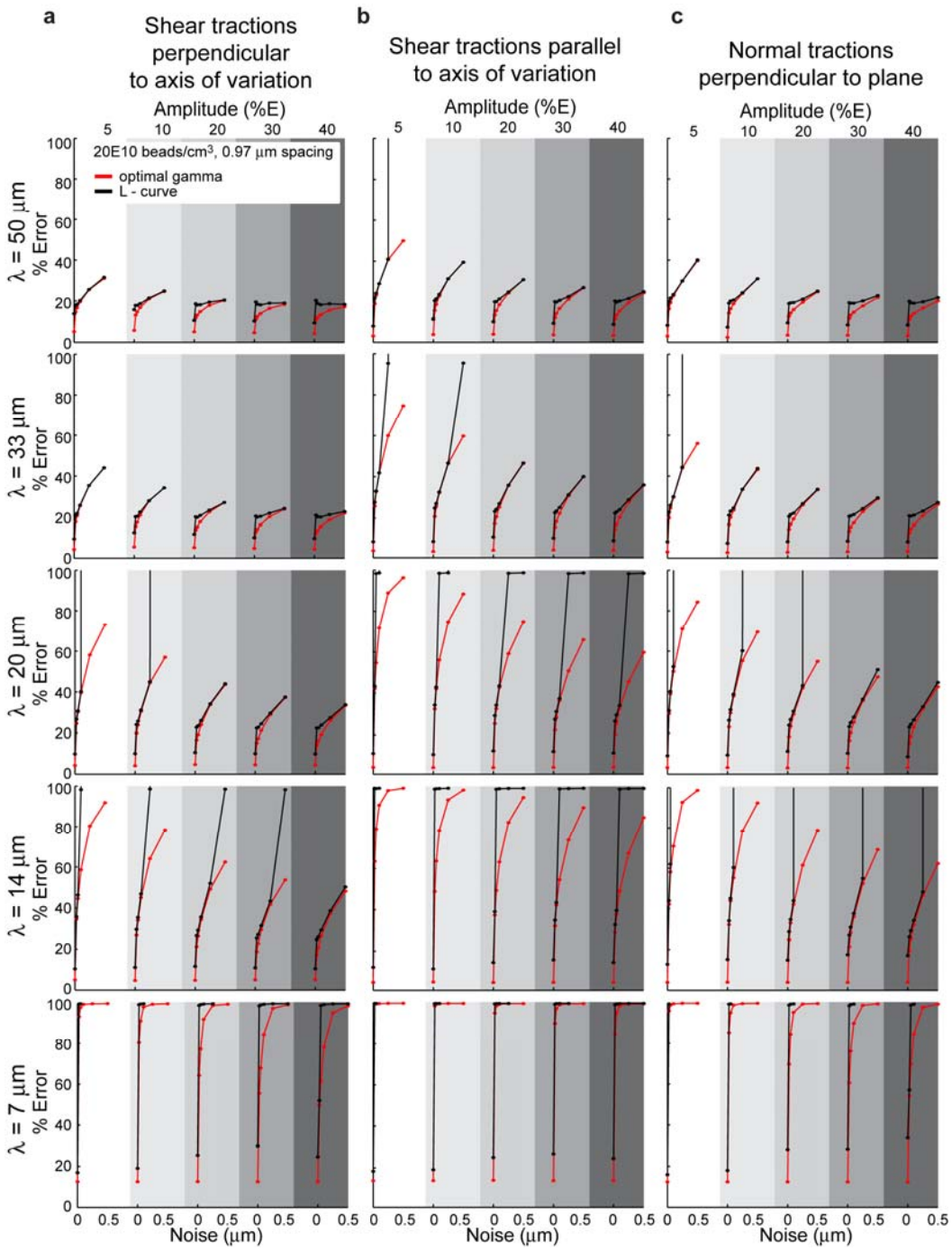

Figure 5.5: Traction recovery under regularization estimated via the L-curve. a-c) Percent error of the recovered tractions is plotted as a function of bead density and measurement noise. Traction recoveries are compared under optimal regularization (red) and regularization estimated using the L-curve method (black). All plots are organized as in Figure 5.4; however, for clarity, only curves utilizing a bead spacing of 0.97 μm are shown. The large errors in the L-curve plots (indicated by the diverging black lines) demonstrate measurements for which the L-curve method failed to find an appropriate value of γ.

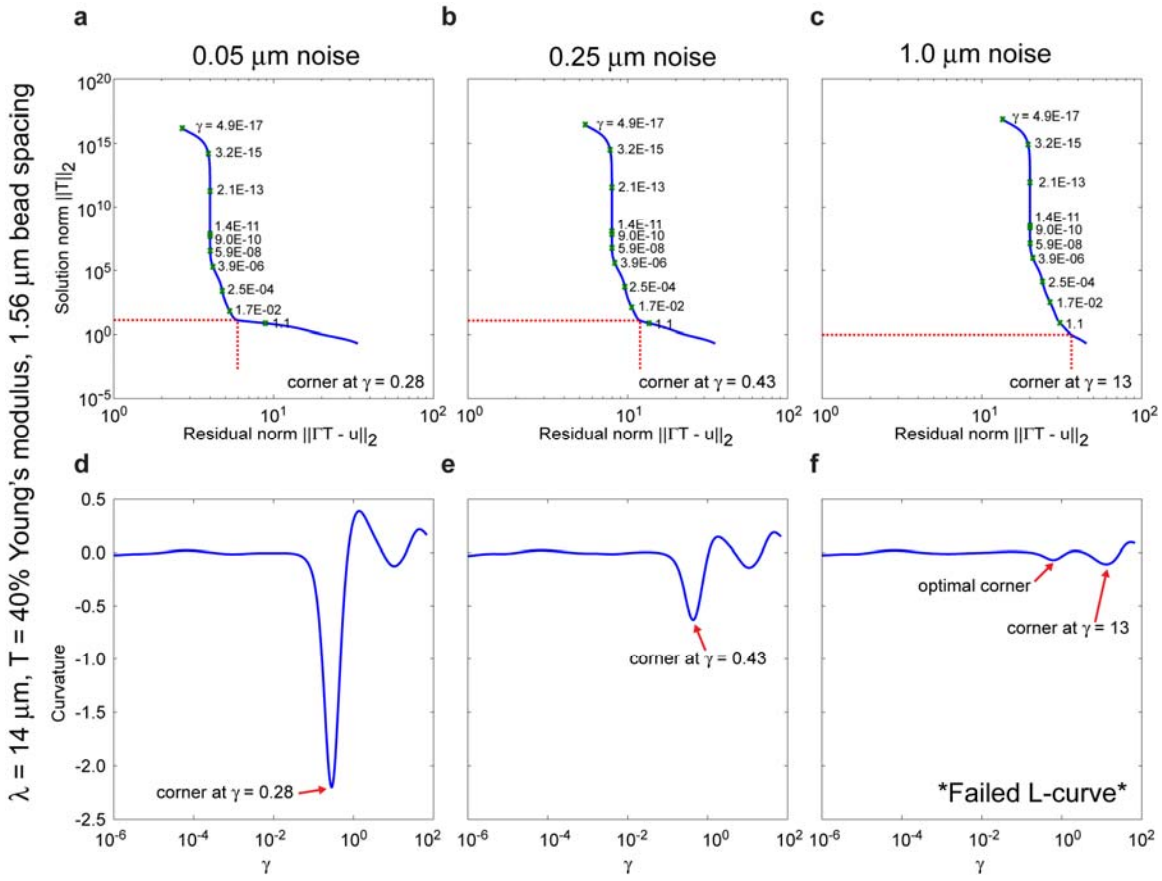

Figure 5.6: Use of the L-curve to find an optimal value of γ. a-c) Representative log-log plots of the solution norm ($|\mathbf{\Gamma T}|^2$) vs. the residual norm ($|\mathbf{\Gamma T - u}|^2$) as a function of γ for a simulated loading with wavelength of 14 μm, magnitude of 40% of the hydrogel Young's modulus and a bead spacing of 1.56 μm. The corners of these curves indicate the estimated value of optimal regularization for each condition. **d-e)** Plots of the second derivative (curvature) of the data displayed in (**a-c**) as a function of γ. The value of minimum curvature indicates the corner of the L-curve. As noise on the displacement measurements was increased from 50 nm to 1 μm, the corner became less prominent eventually leading to a misidentification and non-optimal value of γ.

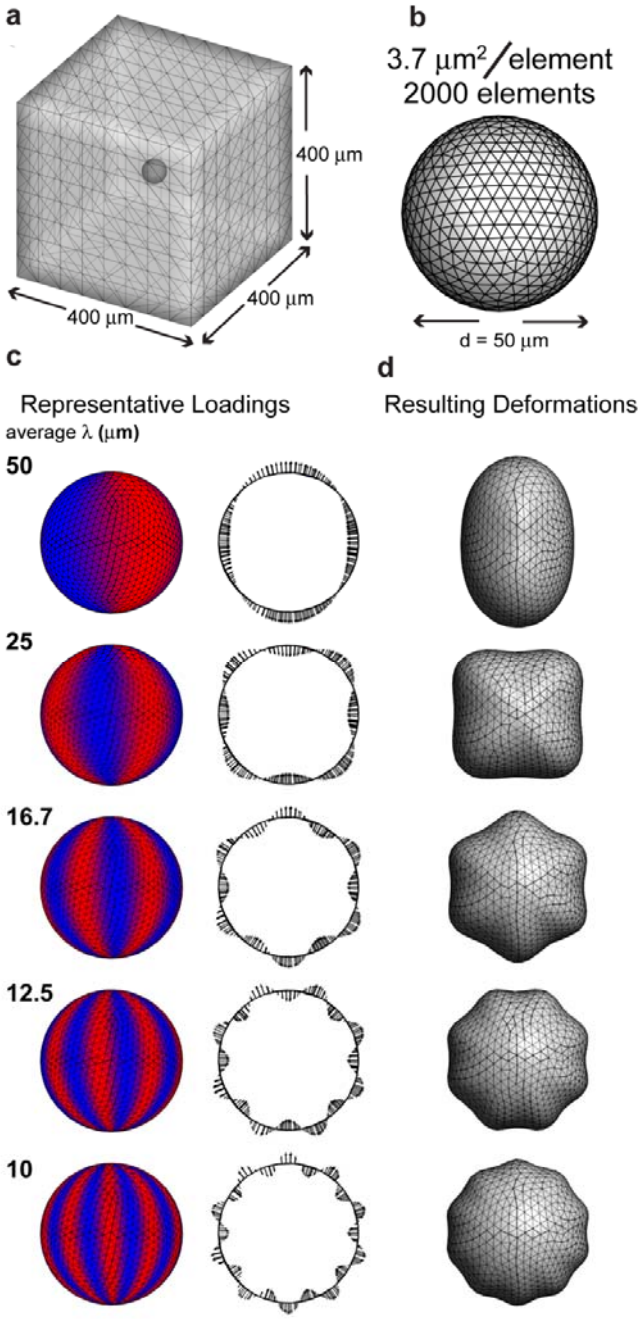

Figure 5.7: Description of computational domain and simulated loadings for fully 3D geometries. **a)** Finite element mesh utilized for traction calculations. The hydrogel was modeled as a 400 μm cube with a 50 μm diameter spherical void at the center. Simulated tractions were applied to the surface of this void. **b)** Expanded view of the void in (**a**). **c)** Contour maps of representative loadings scaled by the magnitude of the traction vector. Only tractions oriented normal to surface were considered. For these loadings, λ represents the average wavelength of the loading on the surface of the sphere. Vector renderings of representative loadings are shown to the right by taking the horizontal cross-section of the sphere. **d)** Resulting deformations of the void surface caused by the loadings presented in (**c**).

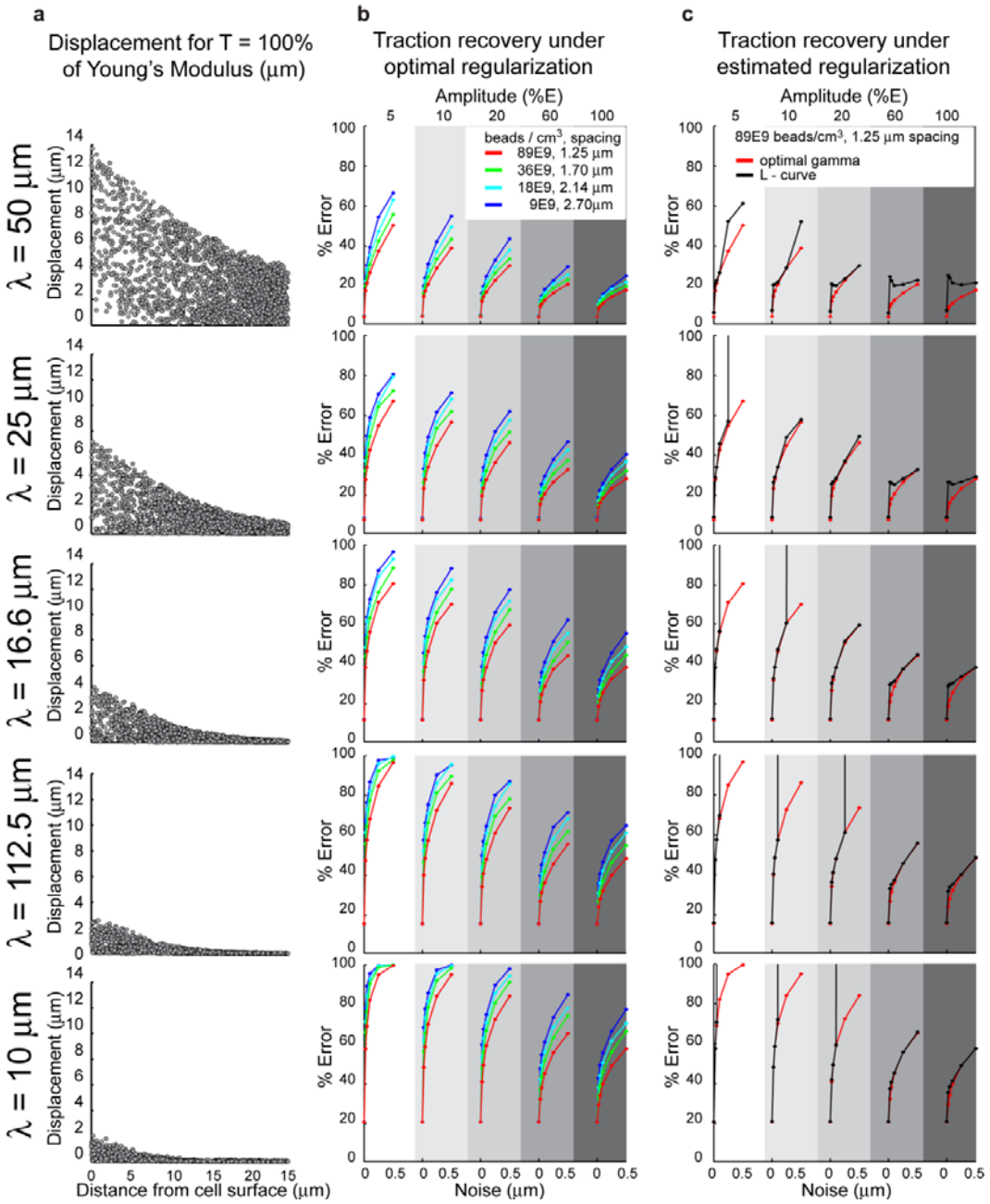

Figure 5.8: Displacements and traction recovery in fully 3D geometries. a) Displacements within the hydrogel plotted as a function of the distance from the spherical surface at which the simulated loadings are applied. Representative plots are shown for loadings scaled such that the maximum amplitude is 100% of the hydrogel Young's modulus. Rows are sorted by the wavelength of the applied loadings. **b)** Percent error of the recovered tractions is plotted as a function of bead density and measurement noise under optimal regularization. **c)** Percent error of the recovered tractions is plotted as a function of bead density and measurement noise for tractions recovered using the L-curve method (red) and under optimal regularization (black). Only curves utilizing a bead spacing of 1.25 μm are shown. Plots in (**b**) and (**c**) are organized in an identical manner to those in Figure 5.4.

CHAPTER 6: MICROFABRICATED TISSUE GAUGES TO MEASURE AND MANIPULATE FORCES FROM 3D MICROTISSUES

6.1 RATIONALE

It has long been appreciated that the generation and transduction of mechanical force by cells can drive the buckling, extension, or contraction of multicellular tissues during development (Beloussov, Dorfman et al. 1975; Taber 1995; Keller, Davidson et al. 2003) and is essential for wound healing and tissue homeostasis in adult organisms (Wolff 1892; Tomasek, Gabbiani et al. 2002). In addition to physically driving tissue assembly, these forces also regulate cell signaling and gene expression, thereby coordinating tissue morphogenesis with cellular differentiation (Farge 2003; Somogyi and Rorth 2004). Yet, although cellular forces are known to contribute to tissue morphogenesis and tissue repair, a more detailed picture of how tissue mechanics link to morphogenetic phenomena has been hindered by a lack of model systems in which both mechanics and remodeling can be simultaneously examined.

Centimeter scale encapsulations of cells in ECM analogues are widely used as model systems for many morphogenetic processes (Bell, Ivarsson et al. 1979; Stopak and Harris 1982; O'Brien, Zegers et al. 2002; Yamada and Cukierman 2007). However, while such systems can recapitulate many developmental processes, the cellular forces within these encapsulations are typically inferred only indirectly by measuring the volumetric contraction of free-floating constructs, or from the population average of constructs pulling against rigid strain gauges (Kolodney and Wysolmerski 1992; Lee, Tsai et al. 1998). Moreover, the scale of these encapsulations often necessitates histological sectioning to visualize fine scale cellular structures and protein distributions within the construct. Because such sections are incompatible with live cell microscopy and provide information about only a small region of a much larger construct, it has been difficult to fully map cellular contractility, tissue mechanics and cellular phenotype simultaneously within a 3D encapsulation.

To obtain quantitative, spatially resolved measurements of cellular traction forces, investigators have cultured cells on the surface of specially engineered 2D substrates including elastic hydrogels and arrays of microfabricated pillars (Dembo and Wang 1999; Tan, Tien et al. 2003). These methods have been instrumental in defining the soluble and mechanical regulators of myosin generated contractility (Dembo and Wang 1999; Tan, Tien et al. 2003; Paszek, Zahir et al. 2005). Moreover, the amount of cytoskeletal tension generated against these substrates has been shown to modulate numerous cellular functions such as proliferation and differentiation (McBeath, Pirone et al. 2004; Nelson, Jean et al. 2005; Engler, Sen et al. 2006). However, while these approaches have highlighted an important connection between cell mechanics and cell

phenotype, the 2D nature of such techniques inherently limits the extent to which 3D morphogenetic phenomena can be described.

Here, we present an approach to measure forces from microscale constructs of cells embedded within 3D matrices. These microfabricated tissue gauges (μTUGs) incorporate MEMS cantilevers which simultaneously constrain and report forces generated by micropatterned 3D constructs in real time. Using this system, we simultaneously monitored matrix remodeling events and microtissue force generation, as well as reported rapid changes in microtissue force in response to soluble stimuli. We demonstrated that both the mechanical stiffness of the cantilevers and collagen matrix influence tissue remodeling by altering cellular contractile forces and matrix protein deposition. Using these findings, we generated a computational model of multicellular contractility that predicted that fine scale gradients of mechanical stress could be used to engineer patterned protein levels within microtissues of controlled geometry. Together, these studies highlight a novel approach to examine an important mechanical interplay between cellular contractility, ECM mechanics, and tissue organization within 3D matrices.

6.2 MATERIALS AND METHODS

6.2.1 Device fabrication and microtissue seeding

Single layer and multilayer templates were created by photopatterning SU-8 photoresist (Microchem, Newton, MA) on silicon wafers. Multilayer SU-8 masters were created using successive spin coat, alignment, exposure and baking steps. All exposure steps were performed on a Karl Suss MJB3 mask aligner (Suss Microtec, Waterbury Center, VT) using a U-360 band pass filter (HOYA, Freemont, CA). In order to prevent bleed through of the top cantilever lip into the lower segments, we used a modified version of the technique described in (Foulds IG 2006). We spun a thin interstitial layer consisting of 15% S1813 (Shipley, Marlborough, MA) and 85% SU-8 which strongly absorbed UV light. This served as a lithographic-stop layer and prevented unwanted crosslinking of the underlying SU-8 layers. All masters were developed in a single step in propylene glycol methyl ether acetate (PGMEA, Sigma, St. Louis, MO) followed by hard bake. A full listing of fabrication parameters is available in the supplementary materials (**Table 6.1**). To generate substrates for the microtissues, SU-8 masters were cast with a prepolymer of poly(dimethylsiloxane) (PDMS; (Sylgard 184; Dow-Corning, Midland, MI) as described previously (Tan, Tien et al. 2003). Prior to cell seeding, the PDMS templates were sterilized in 70% ethanol followed by UV irradiation for 15 minutes and treated with 0.2% Pluronic F127 (BASF, Ludwigshafen, Germany) to reduce cell adhesion. Liquid neutralized collagen (BD Biosciences, San Jose, CA) was then added to the surface of the substrates on ice and templates were degassed under vacuum to remove bubbles in the liquid. A cooled suspension of cell laden neutralized collagen was then added to the substrate and the entire assembly was centrifuged to drive the cells into the micropatterned wells. Excess collagen and cells were removed by dewetting the surface of the substrate prior to incubating at 37 ºC to induce collagen polymerization. The appropriate media was then added to each substrate.

6.2.2 Device characterization

Cantilever dimensions were measured for 40 cantilevers (20 each from 2 independent substrates) for each geometry under differential interference contrast (DIC) microscopy using a 20X Plan-Apochromat objective on a Zeiss Axiovert 200M (Carl Zeiss MicroImaging, Inc.). The elastic modulus of the PDMS was measured via uniaxial tensile testing on an Instron 5848 Microtester equipped with a 50 N load cell (Instron, Canton, MA). 3 strips each from 3 independent preparations were measured using digital calipers, preloaded to 0.5 N and then

stretched at a strain rate of 1%/second. The elastic modulus was calculated via a linear fit of the stress vs. strain curves over the region of 10-20% strain. These measurements were then used to numerically estimate cantilever spring constants and variability under linear bending assumptions (**Figure 6.1a,b**). To confirm our numerical estimations, we experimentally measured the spring constants from 3 sequential deflections of 20 cantilevers of each geometry (10 each from 2 separate substrates) using calibrated glass micropipettes (see below for micropipette calibration). Our experimental measurements fell within the range of values predicted by linear beam bending with an average spring constant of 0.098 ±0.017 μN/μm for the flexible geometry and of 0.397 ± 0.039 μN/μm for the rigid geometry (**Figure 6.1c**). For deformations spanning the range of those exerted by microtissues, all plots were linear with an average R^2 value of 0.96 and 0.99 for the flexible and rigid geometries respectively. Spring constant estimates from sequential deflections of individual cantilevers had an average repeatability of 5% (standard deviation). The inherent uncertainty of each force measurement was incorporated into all statistical comparisons using standard propagation of error formulas.

6.2.3 Microneedle calibration

Glass micropipettes (World Precision Instruments, Sarasota, FL) were calibrated by hanging thin wire weights (0.538-6.000 mg) from the needle tip. Needles were mounted horizontally with a micromanipulator on a microscope stage. A second micromanipulator was used to position the weights on the end of the needle tip. The needle tip was imaged with and without the weights in place. The difference in focal planes between the images of the loaded and unloaded tip was used to determine the amount of needle bending. All measurements were repeated a minimum of three times and the average values were used to generate load vs. displacement curves, which were then fit using linear regression. Two separate needles (k=0.3474 μN/μm, R^2=0.996 and k=0.0609 μN/μm, R^2=0.999) were calibrated in order to measure the stiffness of PDMS cantilevers with different geometries.

6.2.4 Force quantification

For quantifying microtissue forces, microtissues were cultured for 24 hours before brightfield images were taken of the cantilevers within each template (15 total, 5 each from 3 independent experiments) using an A-Plan10X objective on a Zeiss Axiovert 200M (Carl Zeiss MicroImaging, Inc.) with live cell incubator. Only tissues which were uniformly anchored to the

tips of the cantilevers were included in the analysis. Masks were generated in Adobe Photoshop (Adobe Systems Incorporated, San Jose, CA) outlining the base and cap regions of each cantilever and analyzed in MATLAB (The MathWorks, Natick, MA) to compute the cantilever deflection. To account for errors in microfabrication, which may cause the cantilevers to deviate from perfectly vertical positions in absence of loading, baseline cantilever deflections were calibrated for cell free collagen gels. Cantilevers with a spring constant of 0.098 μN/μm had an inward baseline deflection of 1.19 ± 1.36 μm. Cantilevers with a spring constant of 0.397 μN/μm had an inward baseline deflection of 3.17 ± .38 μm. These baseline deflections were subtracted from the computed displacement of the cantilevers with attached microtissues for all force measurements.

To measure dynamic changes in contractility between microtissues and single cells, microtissues and cells on mPADs were cultured for 24 hours in standard growth media, starved for 24 hours in media containing 0.1% bovine serum, and then treated with 10 μg/ml LPA followed by 50 μM blebbistatin.

6.2.5 Bio-chemo-mechanical model of microtissue contractility

We envisage a two-dimensional tissue, thickness b, lying in the $x_1 - x_2$ plane on top of cantilever posts with its normal along the x_3-direction (**Figure 6.2**). A bio-chemo-mechanical model has been devised that captures the formation and dissociation of stress fibers, as well as the associated generation of tension and contractility (Deshpande, McMeeking et al. 2006). The stress fiber formation is initiated by a nervous impulse or a biochemical or mechanical perturbation that triggers a signaling cascade within the tissue. We model this signal as an exponentially decaying pulse having level C (which may be thought of as the concentration of Ca^{2+} or Rho) given by

$$C = \exp(-t_i / \theta), \qquad (1)$$

where θ is the decay constant and t_i is the time after the onset of the most recent activation signal. The formation of stress fibers is parameterized by an activation level, designated η ($0 \le \eta \le 1$), defined as the ratio of the concentration of the polymerized actin and phosphorylated myosin within a stress fiber bundle to the maximum concentrations permitted by the bio-

chemistry. The evolution of the stress fibers at an angle ϕ with respect to the x_1 axis (**Figure 6.2**) is characterized by a first-order kinetic equation

$$\dot{\eta}(\phi) = \left[1-\eta(\phi)\right]\frac{C\bar{k}_f}{\theta} - \left(1-\frac{\sigma(\phi)}{\sigma_0(\phi)}\right)\eta(\phi)\frac{\bar{k}_b}{\theta}, \tag{2}$$

where the overdot denotes time-differentiation. In this formula, $\sigma(\phi)$ is the tension in the fiber bundle at orientation ϕ, while $\sigma_0(\phi) \equiv \eta\sigma_{\max}$ is the corresponding isometric stress at activation level η, with $\sigma_{\max}$ being the tensile stress at full activation ($\eta = 1$). The dimensionless constants $\bar{k}_f$ and $\bar{k}_b$ govern the rates of stress fiber formation and dissociation, respectively. In turn, the stress σ is related to the fiber contraction/extension rate $\dot{\varepsilon}$ by the cross-bridge cycling between the actin and myosin filaments. The simplified version of the Hill-like equation (Hill 1938) employed to model these dynamics is specified as

$$\frac{\sigma}{\sigma_0} = \begin{cases} 0 & \dfrac{\dot{\varepsilon}}{\dot{\varepsilon}_0} < -\dfrac{\eta}{\bar{k}_v} \\ 1+\dfrac{\bar{k}_v}{\eta}\left(\dfrac{\dot{\varepsilon}}{\dot{\varepsilon}_0}\right) & -\dfrac{\eta}{\bar{k}_v} \le \dfrac{\dot{\varepsilon}}{\dot{\varepsilon}_0} \le 0 \\ 1 & \dfrac{\dot{\varepsilon}}{\dot{\varepsilon}_0} > 0 \end{cases} \tag{3}$$

where the rate sensitivity coefficient, $\bar{k}_v$, is the fractional reduction in fiber stress upon increasing the shortening rate by $\dot{\varepsilon}_0$.

A two-dimensional constitutive description for the stress fiber assembly has been derived by noting that the axial fiber strain rate $\dot{\varepsilon}$ at angle ϕ is related to the material strain rate $\dot{\varepsilon}_{ij}$ by

$$\dot{\varepsilon} \equiv \dot{\varepsilon}_{11}\cos^2\phi + \dot{\varepsilon}_{22}\sin^2\phi + \dot{\varepsilon}_{12}\sin 2\phi, \tag{4}$$

The average stress generated by the fibers follows from a homogenization analysis as

$$S_{ij} = \frac{1}{\pi}\int_{-\pi/2}^{\pi/2}\begin{pmatrix} \sigma(\phi)\cos^2\phi & \dfrac{\sigma(\phi)}{2}\sin 2\phi \\ \dfrac{\sigma(\phi)}{2}\sin 2\phi & \sigma(\phi)\sin^2\phi \end{pmatrix} d\phi. \tag{5}$$

The constitutive description for the tissue is completed by including contributions from passive elasticity, attributed mainly to the collagen matrix. The passive stresses act in parallel with the active cellular response, whereupon additive decomposition gives the total stress:

$$\Sigma_{ij} = S_{ij} + \left(\frac{E\nu}{(1-2\nu)(1+\nu)} \varepsilon_{kk}\delta_{ij} + \frac{E}{(1+\nu)} \varepsilon_{ij} \right), \tag{6}$$

where δ_{ij} is the Kronecker delta and (for a linear response) E is the effective Young's modulus and ν the Poisson ratio.

The corresponding characterizing parameter for the *actin* (or stress-fiber) orientation imaged in the experiments is not straightforward. Most techniques only image the dominant stress-fibers. The very fine mesh-work of actin filaments is not visible when standard epifluorescence or confocal microscopes are used. Thus, to correlate the observations with the predictions we define a circular variance $\Gamma = 1 - (\overline{\eta} / \eta_{\max})$, used by (Pathak, Deshpande et al. 2008) that provides an estimate of how tightly the stress-fibers are clustered around a particular orientation ϕ. Here $\eta_{\max}$ is the maximum polymerization level, which occurs at orientation ϕ_S while $\overline{\eta}$ is an average value defined as $\overline{\eta} \equiv 1/\pi \int_{-\pi/2}^{\pi/2} \eta \mathrm{d}\phi$. The value of Γ varies from 0 to 1, corresponding to perfectly distributed and totally aligned distributions, respectively.

6.2.6 Finite element method simulations of microtissue contractility

The microtissue contractility model was implemented in ABAQUS (Dassault Systemes) as a user-defined material as described previously (1, 3). The tissue was modeled using membrane elements (M3D4 in ABAQUS) of unit thickness and the response solved for in a finite strain setting. Solutions are presented using an average element size of 1 μm. Mesh sensitivity studies confirmed that reducing the mesh size further did not significantly change the results. Cantilevers were modeled as rigid plates constrained to move in the $x_1 - x_2$ plane. Dimensions of these 2D plates were same as the top face of the cantilevers used in the experiments. The displacement d_i of the plates within the $x_1 - x_2$ plane is constrained by a spring of stiffness k such that the force F_i applied by the tissue is related to d_i via the relation $F_i = kd_i$. Spring elements are modeled using the SPRING1 option in ABAQUS. The values of spring constant k were chosen to match with the cantilever stiffness used in the experiments. The contact between

the tissue and the 2D plate, representing the top face of the cantilever, is implemented by employing the TIE CONSTRAINT option between the tissue and the periphery of the rigid plate in ABAQUS.

Unless otherwise specified, the reference material parameters used in this study were the same as those previously published in (Deshpande, McMeeking et al. 2006). To capture the effects of the collagen matrix density and cantilever stiffness as well as variance in tissue type specific contractility, parametric analysis was conducted for the passive Young's modulus (*E*) and the maximum tension capable of being exerted by the stress fibers ($\sigma_{\max}$); refer to (1)for further details about these parameters. Suitable agreement to experimental results was found using E=5 kPa, 15 kPa, and 25 kPa for microtissues constructed from 1.0, 1.75, and 2.5 mg/ml collagen respectively (**Table 6.2**). These values gave very close agreement with experimental measurements of microtissue forces under each condition and are in the range of previously published values for tissue-populated collagen matrices (Wakatsuki, Kolodney et al. 2000). Maximum isometric stress, $\sigma_{\max}$, was determined to be 250 kPa. The non-dimensional reaction rate constants are $\bar{k}_f = 10$, $\bar{k}_b = 1$, $\bar{k}_v = 2$ with $\dot{\varepsilon}_o = 3.0\times10^{-3}\ \mathrm{s}^{-1}$ and the Poisson ratio $\nu = 0.3$. Maximum isometric stress, was determined to be 250 kPa. To correlate observations of protein alignment with model predictions, we used the circular variance (Γ) described in (Pathak, Deshpande et al. 2008) that provides an estimate of how tightly simulated stress fibers are clustered around a particular orientation. The value of Γ varies from 0 to 1, corresponding to uniformly distributed and totally aligned distributions respectively.

6.2.7 Immunofluorescence, quantitative immunofluorescent microscopy and image analysis

Microtissues were fixed with 4% paraformaldehyde in PBS, permeabilized with 0.2% Triton X-100 in PBS, incubated with antibodies against fibronectin (MP Biomedicals, Solon, OH) or tenascin C (Millipore/Chemicon, Billerica, MA) and detected with fluorophore-conjugated, isotype-specific, anti-IgG antibodies and counterstained with DAPI (Invitrogen, Carlsbad, CA). Filamentous actin was visualized by incubating samples with fluorophore conjugated phalloidin (Invitrogen, Carlsbad, CA). To quantify average protein composition, microtissues were cultured for 3 days, fixed and imaged with an A-Plan10X objective. Protein density was quantified by measuring the average fluorophore intensity within the microtissue (40 tissues total, 10 each from 4 independent experiments) for a 30 μm wide segment at the tissue midpoint using distinct

fluorphores for each protein, dividing by the volume of the tissue defined by this region and normalizing by DAPI staining intensity. Heat maps of protein expression were created within individual microtissues created from 1.75 mg/ml collagen and tethered to rigid cylindrical cantilevers. Microtissues were cultured for 5 days, fixed and optically sectioned under high magnification with a Plan-Neofluar 40X objective in 6 μm slices using an Apotome structured illumination unit (Carl Zeiss MicroImaging, Inc.). Masks were generated in Adobe Photoshop labeling the positions of each cantilever and used to align and crop the z-stacks each microtissue. To determine cell density, DAPI images were binarized within MATLAB using a user determined threshold that was consistent between all conditions. Optical slices from each tissue (12 tissues total, 4 each from 3 independent experiments) were then averaged to quantify protein and cell distributions for each condition. All microtissues selected for protein analysis were randomly chosen from brightfield images of tissues which were uniformly anchored to the cantilever tips.

To quantify the alignment of cytoskeletal and matrix proteins, we implemented principal component analysis filtering on the image gradients as described in (Bazen and Gerez 2002). The alignment information from each optical slice was then compiled using a second implementation of principal component analysis to determine the dominant orientation.

6.2.8 Statistical comparisons

All reported statistical comparisons were performed by student t-test on the mean and verified with a Mann-Whitney U test (MWU) on the median with certainty of $p<0.05$ unless otherwise noted.

6.2.9 Cell culture and reagents

NIH 3T3 cells obtained from ATCC were cultured in high glucose DMEM containing 10% bovine serum, 2mM L-glutamine, 100 units/ml penicillin, and 100 mg/ml streptomycin (all from Invitrogen). Depending on experimental conditions, microtissues were incubated with ascorbic acid 50 μg/ml (Sigma, St. Louis, MO) with DMSO (control), blebbistatin 50 μM (EMD biosciences, Gibbstown, NJ) and/or aphidicolin 1 μg/ml (Sigma, St. Louis, MO). Cardiomyocyte cells were isolated from day 0 c57bl/6 mouse embryos (Harlan Laboratories) and cultured in DMEM:M199 (4:1) containing 10% horse serum, 1% (1M) HEPES buffer, 100 units/ml

penicillin, and 100 mg/ml streptomycin (all from Invitrogen), and 5% fetal bovine serum (Fisher Scientific). Cell culture media was changed every 3 days unless otherwise noted.

6.3 RESULTS

To miniaturize cultures of cells embedded within 3D collagen matrices, we microfabricated arrays of wells within a PDMS mold (**Figure 6.3a**). The mold was immersed in a suspension of cells and unpolymerized type I collagen and centrifuged to drive cells into the recessed wells. Excess solution was removed and the remaining constructs were polymerized. Within hours, we observed the spontaneous contraction of the collagen matrix by the cells. Raised cantilevers incorporated within each template spatially restricted the contraction of the collagen matrix and resulted in a large array of microtissues anchored to the tips of the cantilevers (**Figure 6.3b**). We used a novel multilayer photolithography process to generate wide heads at the tips of the cantilevers, which ensured that microtissues remained anchored even in highly deflected configurations (**Figure 6.3c**). Because adhesion of the tissue was limited to the upper cantilever section, the stiffness each cantilever could be controlled by altering the thickness of the lower sections. We used linear bending theory and experimental measurements using calibrated glass micropipettes to report the load-displacement relationship for two different cantilever geometries with measured spring constants of 0.098 ± 0.017 μN/μm and 0.397 ± 0.039 μN/μm (**Figure 6.1**). These spring constants were then used to link the measured cantilever deflections to the amount of force generated by microtissues under varying conditions.

Shortly after seeding, we observed that NIH 3T3 cells embedded within a collagen matrix extended and retracted thin protrusions and compacted the matrix around the cell periphery. Because cells were distributed throughout the tissue, the collective action of these local processes resulted in bulk contraction of the collagen gel (**Figure 6.3d**). This bulk contraction first became evident 3 hours after seeding and was nearly complete after 12 hrs. In that same time frame, microtissue tension increased nearly 8 fold and then continued to increase another 2 fold over the next 12 hours in absence of gross changes in bulk tissue morphology (**Figure 6.3e**).

In addition to driving long-term morphologic changes, more rapid dynamics in cellular contractility, which may be triggered in response to soluble factors, can play critical roles in settings such as vascular homeostasis (Furchgott and Vanhoutte 1989). However, diffusion limited concentration gradients may complicate the interpretation of such responses within traditional, centimeter-scale, 3D cultures (Ramanujan, Pluen et al. 2002; Griffith and Swartz 2006). For simple diffusion (i.e., that governed by Fick's 2nd Law) the time required for diffusion of soluble factors scales with the thickness of the construct squared; therefore, concentration gradients in microtissues (thickness ~100 μm) should equilibrate 100 times faster than those in

bulk gels (thickness ~1 mm). To illustrate the experimental relevance of this effect, we compared the dynamic contractile response of microtissues in response to a soluble factor stimulus to that of cells cultured on 2D microneedle arrays (mPADs) which lack any diffusion barrier (Tan, Tien et al. 2003) (**Figure 6.3f**). We found that both 3D microtissues and single cells in 2D increased or decreased contractile forces within 5-10 minutes of treatment with lysophosphatidic acid (LPA), a known stimulant for myosin activity, or with blebbistatin, a myosin ATPase inhibitor, respectively. In contrast, centimeter-scale constructs have been shown to require substantially longer (greater than 30 minutes) to reach equilibrium after a similar stimulus (Kolodney and Elson 1993).

While the contraction of a tissue arises from the actions of its constituent cells, it is currently unclear how tissue mechanics can feedback to affect cellular force generation. When we created microtissues with a range of cell densities, we observed an approximately linear relationship between microtissue tension and cell density (**Figure 6.4a**), which provided an estimate of the average force generated per cell within each construct. Interestingly, the stiffness of the cantilevers impacted the magnitude of force generated by cells. Cells within microtissues tethered to flexible cantilevers (k=0.098 μN/μm) generated approximately 14 nN/cell while cells within microtissues tethered to more rigid cantilevers (k=0.397 μN/μm) generated approximately 1.7 fold more force (**Figure 6.4a and b**). These values for cellular contractile forces are in the range of those measured previously (see compilation in (Wakatsuki, Kolodney et al. 2000)).

In addition to boundary mechanics, the bulk modulus of the matrix within which the cells are embedded may be another means by which tissue mechanics can feedback to influence cellular contractile forces. To compare the relative impact of these two effects, we independently varied collagen density (1.0 mg/ml vs. 2.5 mg/ml) and cantilever stiffness (0.098 μN/μm vs. k=0.397 μN/μm) while controlling for cell density (**Figure 6.4c-e**). We observed that microtissue tension increased both with increased cantilever stiffness and increased collagen density (**Figure 6.4c**). Normalizing the measured forces by the cross-sectional areas of the microtissues in these four conditions further revealed that mechanical stress increased with increased cantilever stiffness, but decreased with increased collagen density (**Figure 6.4d**). This decreased stress with collagen density may result from the decreased compaction of denser gels and provides an interesting divergence in the relative impact of boundary rigidity versus matrix stiffness.

Because specific cytoskeletal and ECM protein levels are altered in mechanically aberrant conditions such as wound healing and hypertension (Tomasek, Gabbiani et al. 2002;

Berk, Fujiwara et al. 2007), we investigated whether mechanical feedback may be a means to regulate such changes in protein expression in microtissues. Interestingly, using quantitative immunofluorescence, we found that changes in the amounts of fibrillar actin and ECM proteins fibronectin (Fn) and tenascin C qualitatively mirrored the changes in mechanical stress within microtissues under each condition (**Figure 6.4f-i**). These results suggest that multiple mechanical inputs (e.g. tissue boundary mechanics, matrix rigidity, and mechanical stress) can feedback to regulate cellular contractile forces and protein deposition, two key factors in maintaining tissue homeostasis.

While we observed that average protein levels in microtissues correlated with average mechanical stress, the emergence of complex tissue forms *in vivo* relies on intricately patterned ECMs and fine scale gradients of mechanical stresses to guide cell migration and differentiation (Thiery, Duband et al. 1985; Lee and Goldstein 2003; Krieg, Arboleda-Estudillo et al. 2008). To determine whether our microtissue approach could be used to study the effects of spatially patterned mechanical stresses, we developed a computational model to predict how such stresses may be distributed within individual microtissues. We adapted a bio-chemo-mechanical model based on actin/myosin force generation, which was originally used to describe the distribution of proteins and forces within single cells (Deshpande, McMeeking et al. 2006; Pathak, Deshpande et al. 2008). A full description of the equations and assumptions governing this model is provided in the supplementary materials. Briefly, the microtissue is modeled as a continuum in which actin fibers are free to polymerize in any direction. Once formed, actin fibers contract according to a modified version of the Hill equation (Hill 1938), which describes actin-myosin contractility in muscle. This contraction generates stresses within the tissue that then feedback to stabilize the actin fibers themselves and ultimately modulate tissue morphogenesis. Experimental measurements of the effects of cantilever and matrix stiffness were used to calibrate parameters for the initial mechanical properties of the collagen/cell composite and to set limits on the maximal stress capable of being generated by an actin/myosin element.

The model recapitulated the observed increase in microtissue tension in response to increased cantilever stiffness and matrix density (**Table 6.2**). We then applied the model to microtissues with 4 rigid cylindrical cantilevers forming a square tissue, in order to observe the effects of enhanced internal variations in stress (**Figure 6.5b**). For such geometries, the model predicted the generation of large gradients of intratissue stress and filamentous actin with peak levels that propagate away from the cantilevers (**Figure 6.5c and d**). Based on these computational results, we generated the same geometries in our microtissue platform (**Figure**

6.5a). In agreement with our predictions, we observed patterned levels of filamentous actin, Fn and tenascin C within the microtissue that correlated with the degree of predicted mechanical stress (**Figure 6.5e-g**). This effect was not due to heterogeneous cell density as cells were uniformly distributed throughout the tissue (**Figure 6.5h**). Moreover, when we reduced stress in pre-contracted microtissues by treatment with blebbistatin, the protein levels decreased and were concentrated mainly around the anchors rather than propagating inward (**Figure 6.5e-g**). To confirm that differences in protein expression between control and blebbistatin treated samples were not simply due to differences in cell proliferation, we inhibited proliferation in both conditions using aphidicolin and observed similar distributions of protein accumulation without altering cell density between the two conditions (**Figure 6.6**). We simulated the effect of blebbistatin in our model by reducing the parameter for actin/myosin contractility to 10% of maximal, and found reduced levels and more uniform patterns of mechanical stress and filamentous actin that correlated with the observed lower peak expression and more diffuse distributions of protein staining (**Figure 6.5c and d**).

Another prediction of our model was that actin fibers would preferentially form and orient at the periphery of microtissues and in the direction of high stress gradients (**Figure 6.7a**). Because patterned ECM alignment can play a critical and functional role in how forces and stresses are distributed within different tissues (Chen and Ingber 1999), we sought to investigate whether our model predictions would be confirmed experimentally. We found that actin was more fibrillar around the periphery of microtissues and was aligned in the direction of predicted principal stresses (**Figure 6.7b**). Inhibiting myosin activity in pre-contracted tissues with blebbistatin reduced the overall amount of fibrillar actin and shifted the orientation to qualitatively match that which would be predicted by limiting actin/myosin contractility to 10% in our model (**Figure 6.7a and b**). Interestingly, both tenascin C, and to a lesser extent Fn, demonstrated patterned fibrillar regions and alignment in parallel with actin (**Figure 6.7c and d**) suggesting that mechanical stress may be a potent modulator of the organization of both cytoskeletal and ECM proteins.

6.4 DISCUSSION

It has been suggested that a complex interplay between cellular contractile forces, matrix mechanics, and ECM remodeling contributes to developmental morphogenesis and tissue remodeling (Beloussov, Dorfman et al. 1975; Taber 1995; Keller, Davidson et al. 2003). Blocking myosin activity or surgically manipulating contractile cells via laser microdissection can alter or prevent morphogenesis at numerous stages of development (Edwards and Kiehart 1996; Hutson, Tokutake et al. 2003). Similarly, altering cellular forces or matrix mechanics *in vitro* has implicated a role for mechanics in model systems for development of tendons and muscles, as well as more intricate structures such as mammary ducts and vascular networks (Bell, Ivarsson et al. 1979; Stopak and Harris 1982; Montesano, Orci et al. 1983; Eschenhagen, Fink et al. 1997; O'Brien, Zegers et al. 2002). Here we provide a simple approach to measure these cellular forces and mechanical stresses during microtissue remodeling events.

Previous studies using 2D substrates have demonstrated that substrate stiffness can regulate cellular contractile forces (Paszek, Zahir et al. 2005; Saez, Buguin et al. 2005) and protein expression (Pelham and Wang 1997), among other effects (Engler, Sen et al. 2006; Engler, Carag-Krieger et al. 2008). Cells encapsulated in attached versus floating collagen gels also modulate expression of cytoskeletal and ECM proteins, illustrating the importance of mechanics in 3D settings (Chiquet-Ehrismann, Tannheimer et al. 1994; Halliday and Tomasek 1995; Grinnell 2003). Here, by constraining microtissues using flexible cantilevers, we simultaneously varied boundary and matrix stiffness with quantitative precision, and demonstrated that in 3D matrices, cellular contractility is regulated by overall stiffness while protein expression correlates with mechanical stress. The mechanical stiffness of the cantilevers that anchor the tissue may represent the rigidity of the external structure against which a tissue is contracting, such as the stiffness of bone against a ligament or blood pressure against smooth muscle in the vessel wall. In an analogous manner, collagen density may represent varying degrees of tissue fibrosis. These findings could have implications for the treatment of hypertensive and fibrotic disorders where elevated mechanical stress is associated with ECM stiffening (Berk, Fujiwara et al. 2007; Georges, Hui et al. 2007). Our study suggests that such stiffening may feedback to locally increase cellular contractility and matrix deposition, thereby creating a positive feedback loop between mechanical stress and disease progression. Molecules which target this feedback by modulating mechanotransduction pathways may hold promise as future therapeutics.

The ability of the μTUG system to generate large arrays of spatially isolated microtissues, each created from 80 nanoliters of starting material, may be readily extended to high throughput, low volume screening applications. While 2D assays still provide substantially higher spatial resolution of the forces generated by individual cells, our μTUG system together with our mathematical model of multicellular contractility present a technique to study such mappings when cells are embedded within 3D matrices. The small dimensions of the microtissue constructs allow for rapid penetration of soluble effectors into the constructs in absence of substantial diffusion barriers. While our initial studies focused on mesenchymal cell contractions which occur on the time scale of minutes, the measurement of 3D cellular forces over much faster time scales is an important functional readout for engineered physiologic or pathologic cardiac, skeletal, and smooth muscles. To illustrate that μTUGs could be used for such studies, we created microtissues of neonatal rat cardiomyocytes and observed periodic cantilever deflections in response to synchronous beating of the constituent cells.

By mapping the relationships between stress, cellular contractility and protein expression onto a novel bio-chemo-mechanical model of microtissue contractility, and coupling this model to finite element methods, we demonstrated how micropatterned gradients of mechanical stress can be used to generate patterned responses in a 3D tissue *in vitro*. Thus, while similar mechanical gradients have been shown to effect gene expression and contribute to tissue formation *in vivo* (Farge 2003; Somogyi and Rorth 2004), our studies highlight the possibility of exploiting mechanical patterning for the *in vitro* engineering of complex tissues. Future studies which compare the extent to which data from 2D and 3D systems correlate as well as advancements in the spatial resolution of 3D force mapping will be instrumental in linking changes in cellular and matrix mechanics to *in vivo* phenomena. Such methods will hopefully lead not only to more effective approaches to engineer replacement organs and tissues, but also to a more complete understanding of the role of mechanical equilibrium in tissue homeostasis and disease.

Table 6.1: μTUG fabrication parameters

Step	Procedure	Specifications	Time	Notes
1)	Spin SU8-2050	500 RPM	90 s	84 RPM/S acceleration
		2200 RPM	60 s	336 RPM/S acceleration
2)	Soft Bake	65 degrees C	10 min	
		95 degrees C	30 min	
3)	Cool to 25 degrees C			
4)	Expose Lower Section	200 mJ		*Through U-360 filter (HOYA)*
5)	Spin SU8-2100	500 RPM	120 s	84 RPM/S acceleration
		1500 RPM	90 s	336 RPM/S acceleration
6)	Soft Bake	65 degrees C	10 min	
		95 degrees C	30 min	
7)	Cool to 25 degrees C			
8)	Spin dSU8-2007-15%	500 RPM	10 s	resist=15% S-1813, 85% SU8-2007
		1000 RPM	30 s	
9)	Soft Bake	65 degrees C	2 min	
		95 degrees C	5 min	
10)	Cool to 25 degrees C			
11)	Expose Center Section	500 mJ		*Through U-360 filter (HOYA)*
12)	Spin SU8-2050	500 RPM		84 RPM/S acceleration
		2200 RPM		336 RPM/S acceleration
13)	Soft Bake	65 degrees C	10 min	
		95 degrees C	30 min	
14)	Cool to 25 degrees C			
15)	Expose Top Section	175 mJ		*Through U-360 filter (HOYA)*
16)	Post Exposure Bake	65 degrees C	10 min	
		95 degrees C	30 min	
17)	Cool to 25 degrees C			
18)	Develop in PGMEA	30 degrees C	30 min	with agitation
19)	Rinse in IPA		2 min	with agitation
20)	Hard Bake	175 degrees C	8 hrs	

Table 6.2: Simulation of microtissue forces

	Cantilever stiffness, k = 0.098 µN/µm		**Cantilever stiffness**, k = 0.397 µN/µm	
	Experiments	**Simulations**	**Experiments**	**Simulations**
E=5 kPa (CD=1.0mg/ml)	5.13 ± 0.25 µN	4.10 µN	7.92 ± 0.47 µN	8.30 µN
E=25 kPa (CD=2.5mg/ml)	5.77 ± 0.31 µN	4.45 µN	10.25 ± 0.44 µN	10.8 µN

CD: Collagen Density, σ_{max} = 250 kPa for all cases, experimental measurements are ± standard error on the mean

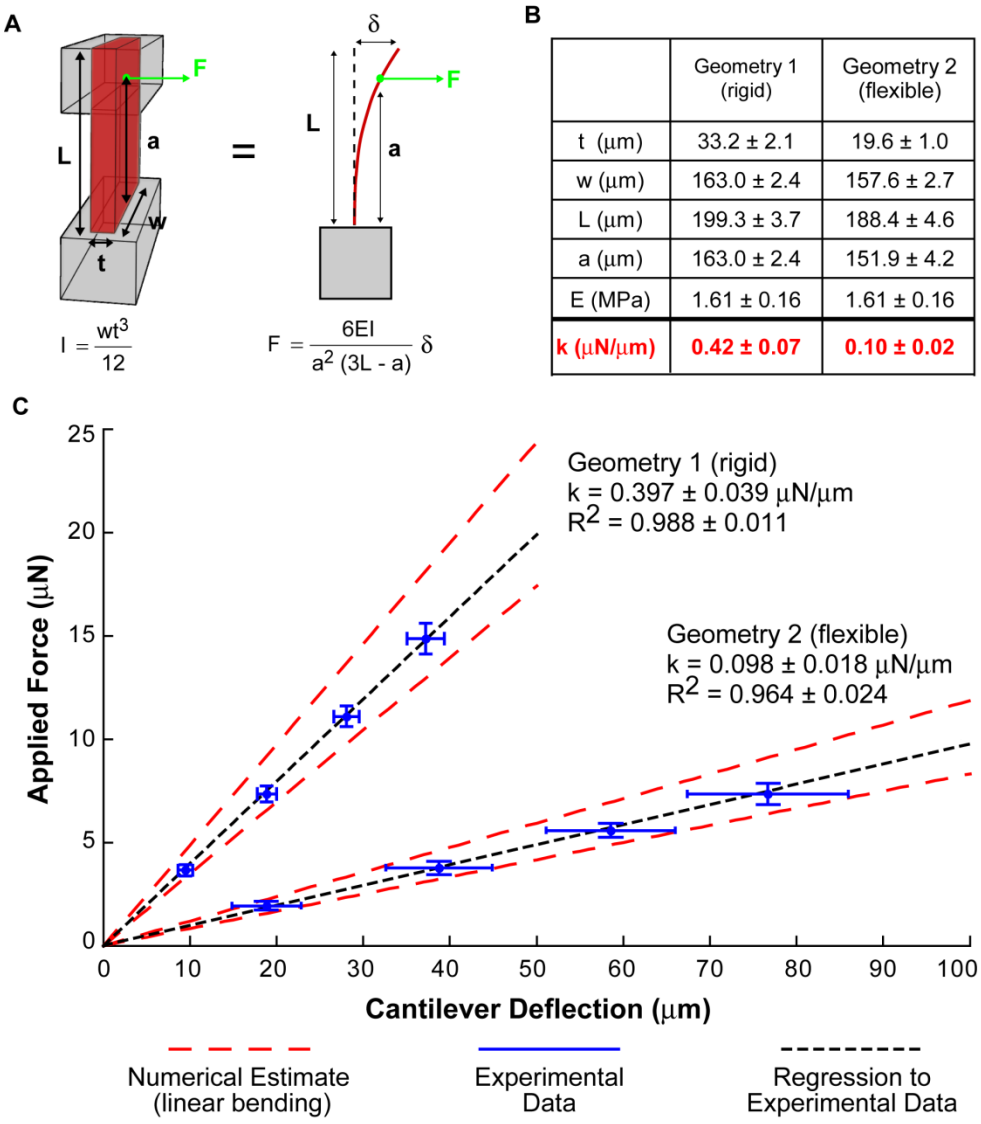

	Geometry 1 (rigid)	Geometry 2 (flexible)
t (μm)	33.2 ± 2.1	19.6 ± 1.0
w (μm)	163.0 ± 2.4	157.6 ± 2.7
L (μm)	199.3 ± 3.7	188.4 ± 4.6
a (μm)	163.0 ± 2.4	151.9 ± 4.2
E (MPa)	1.61 ± 0.16	1.61 ± 0.16
k (μN/μm)	**0.42 ± 0.07**	**0.10 ± 0.02**

Figure 6.1: Characterization of cantilever mechanics. (A) CAD images depicting linear modeling of cantilever deflections. Cantilever deflection is modeled as 1D beam bending due to a load applied at the centroid of the top cap. (B) Experimental measurements of cantilever dimensions. Spring constant (k) is calculated using the formulas presented in (A). (C) Plot of force vs. cantilever deflection showing the numerical estimates from (B, dashed red lines), the experimental data using calibrated micropipettes (blue crosshairs) and the average linear regression to the experimental data (dashed black lines). Data from (B) are the average ± standard deviation from 40 measurements (40 cantilevers of each geometry, 20 measurements each from 2 separate substrates). Data from (C) are the average of data points (blue crosshairs) ± standard deviation from 3 sequential deflections each of 20 cantilevers from each geometry (10 each form two separate substrates). Dashed black lines are linear plots of the average spring constant for each geometry based on linear regressions to the experimental data from each individual cantilever measurement.

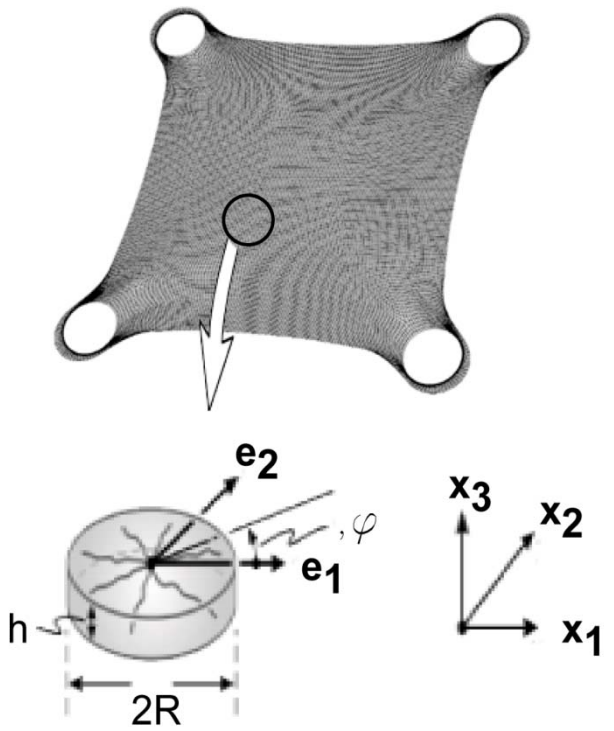

Figure 6.2: Finite element mesh and representative volume element for stress fiber formation used in a computational model of actin-myosin contraction.

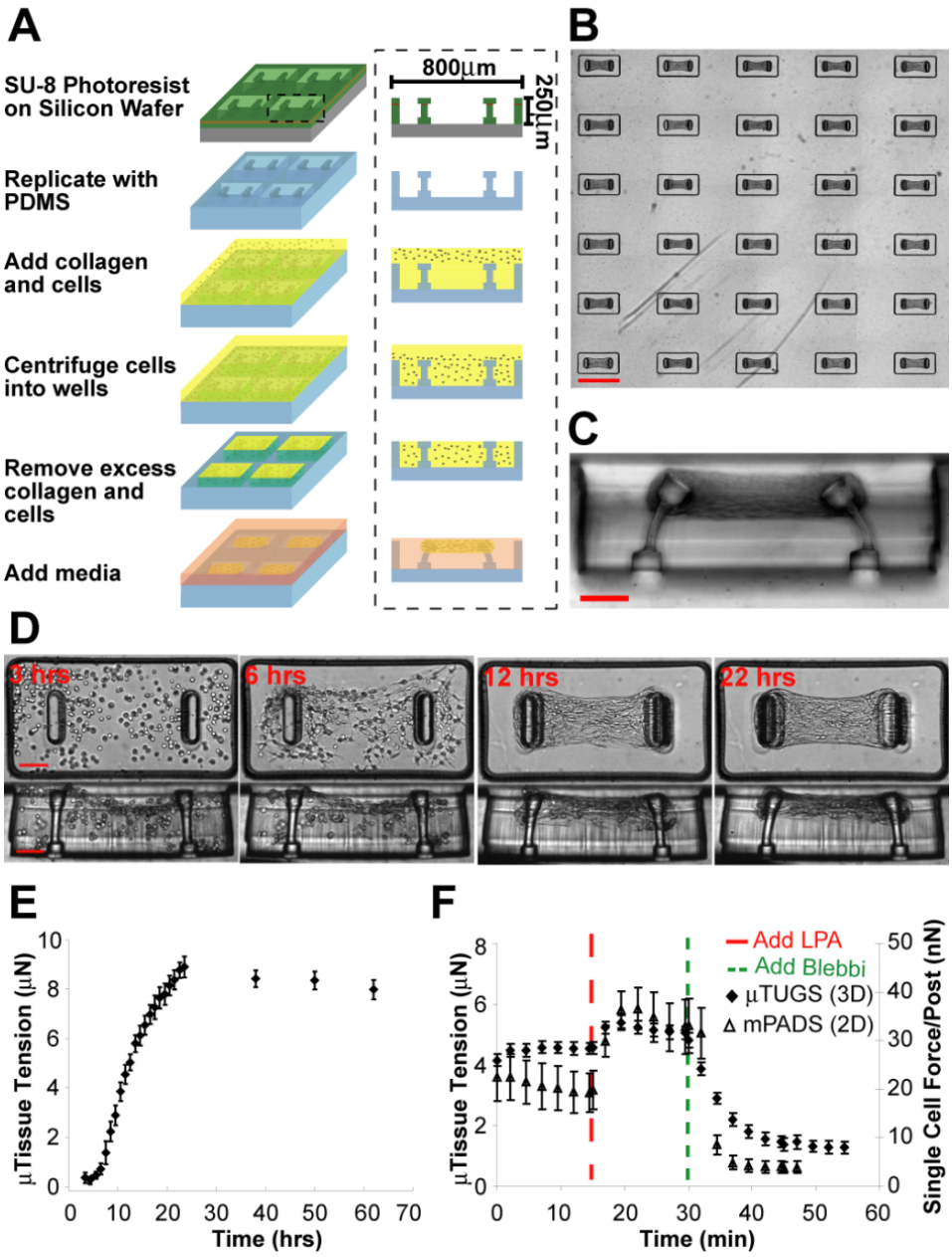

Figure 6.3: Fabrication method and temporal response of microtissues. (A) Process flow diagram for the creation of µTUG arrays. (B) Large arrays of microtissues are simultaneously generated on a substrate. (C) Cross section view of a single µTUG well. (D) Representative images depicting the time course of a contracting microtissue. (E) Time course of forces generated during microtissue contraction. Data points represent the average force for 5 microtissues ± standard error on the mean (SEM). (F) The temporal response of microtissues (closed diamonds) and single cells on mPADs (open triangles) in response to 10 µg/ml LPA and 50 µM blebbistatin. Data points represent the average force for 10 microtissues or 5 individual cells ± SEM. (scale bars, 800 µm-B, 100 µm-C,D)

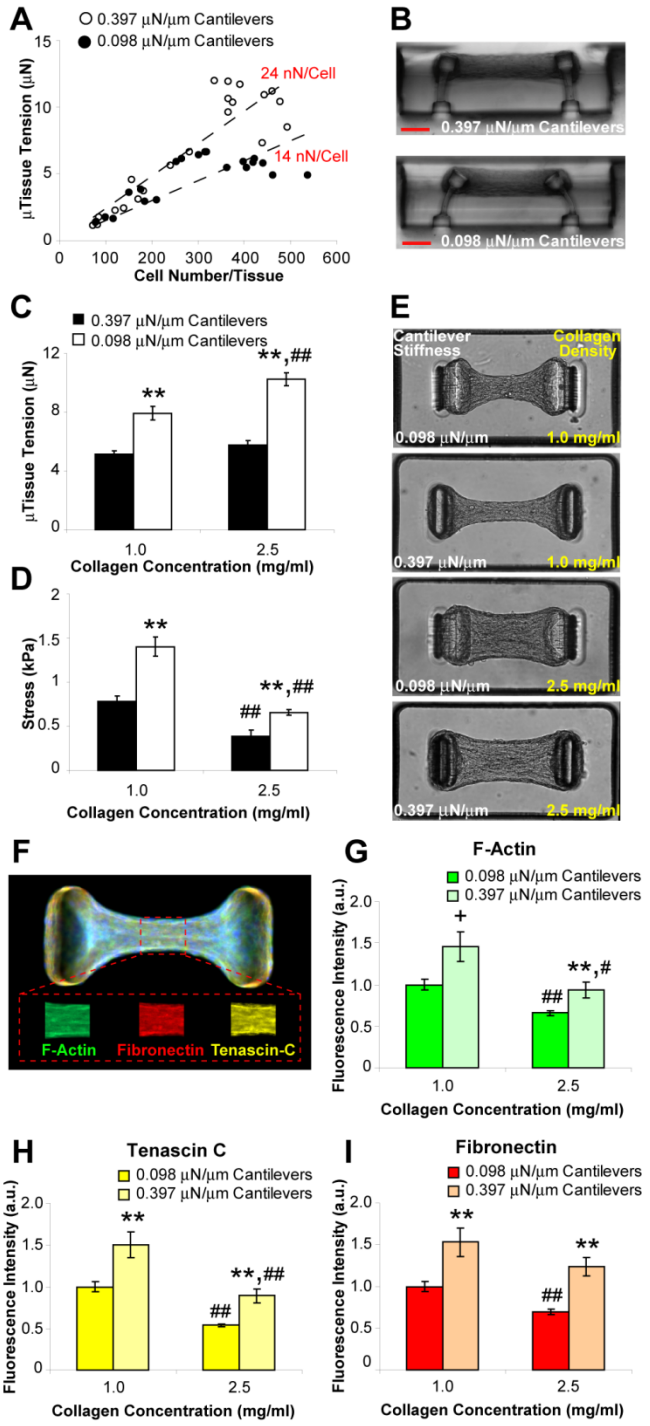

Figure 6.4: Boundary and matrix mechanics regulate cellular contractility and protein deposition. (A) Plot of microtissue tension vs. number of cells per tissue for constructs tethered to rigid (0.397 µN/µm, closed circles) or flexible (0.098 µN/µm, open circles) cantilevers. (B) Representative cross sections of microtissues tethered to rigid or flexible cantilevers. (C) Plot of average microtissue tension for tissues constructed from 1.0 mg/ml or 2.5 mg/ml collagen gels tethered to rigid or flexible cantilevers. (D) Plot of average midpoint stress for tissues

constructed from 1.0 mg/ml or 2.5 mg/ml collagen tethered to rigid or flexible cantilevers. (E) Phase contrast images of microtissues in each of the 4 combinations of collagen density and cantilever stiffness. (F) Representative immunofluorescence overlay of cytoskeletal and ECM proteins within microtissues. Mean fluorophore intensity was measured over a 30 μm long segment at the tissue midsection using distinct fluorphores for each protein (inset). (G-I). Plots of average relative fibrillar actin, fibronectin and tenascin C levels under each of the 4 combinations of collagen density and cantilever stiffness. Data from (C, D) are the average of 15 microtissues from each condition ± SEM. Data from (G-I) are the average of 40 microtissues for each condition ± SEM. (**, $p<0.01$ *, $p<0.05$ +, $p<.05$ (student T) and $p=0.15$ (MWU) for 0.098 vs. 0.397 μN/μm cantilevers. ##, $p<0.01$ #, $p<0.05$ for 2.5 vs. 1.0 mg/ml collagen) (scale bar, 100 μm)

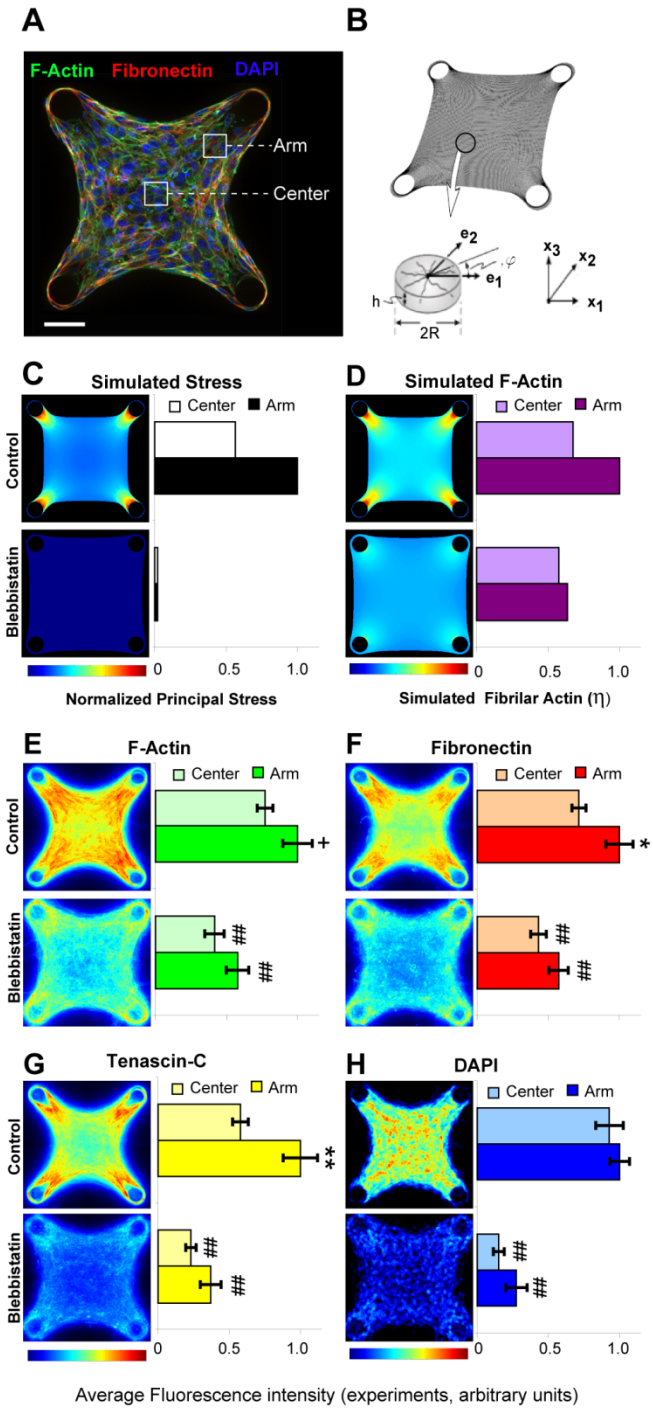

Figure 6.5: Predicted stress gradients within microtissues mirror patterned intratissue protein levels. (A) Immunofluorescence optical section of a microtissue tethered to 4 cylindrical posts showing: phalloidin-green, fibronectin-red, and DAPI-blue. Arm and center regions used for quantification are indicated. (B) Finite element mesh and representative volume element for stress fiber formation used in a computational model of actin-myosin contraction. (C) Simulated distribution of principal stresses within a microtissue under 100% (control) and 10% (blebbistatin) conditions for simulated stress fiber contraction. (D) Simulated distribution of

fibrillar actin within a microtissue under 100% (control) and 10% (blebbistatin) conditions for simulated stress fiber contraction. (E-G) Heat maps showing distribution of phalloidin, fibronectin and tenascin C constructed from optical sections of microtissues under control and blebbistatin (50 μM) conditions. (H) Heat map of DAPI staining within microtissues under control and blebbistatin (50 μM) conditions. Heat maps are 2D projections of immunofluorescence staining from 120 optical sections (approximately 10 sections per microtissue for 12 different microtissues in each condition). (**, $p<0.01$ *, $p<0.05$ +, $p=0.06$ (student T and MWU) for center vs. arm. ##, $p<0.01$, for control vs. blebbistatin) (scale bar, 50 μm)

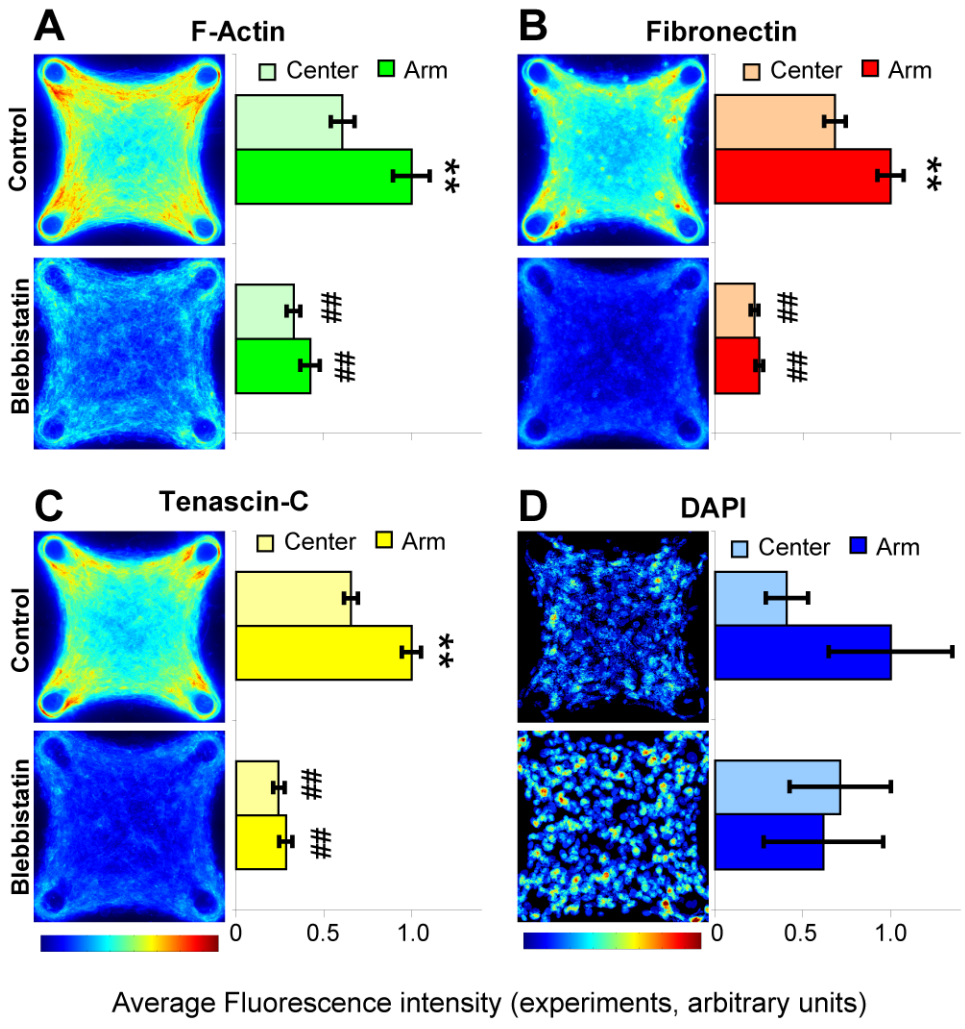

Figure 6.6: Patterned protein levels within aphidicolin treated microtissues. (A-D) Heat maps showing distribution of phalloidin, fibronectin, tenascin C and DAPI constructed from optical sections of microtissues under control and blebbistatin (50 μM) conditions. To normalize cell density between control and blebbistatin conditions, microtissues were cultured for 3 days after seeding in the presence of 1 μM aphidicolin before fixing. Experimental heat maps are 2D projections of immunofluorescence staining from 160 optical sections (approximately 10 sections per microtissue for 16 different microtissues in each condition). (**, $p<0.01$ for 0.16 vs. 1.0 μN/μm cantilevers. ##, $p<0.01$ for 2.5 vs. 1.0 mg/ml collagen)

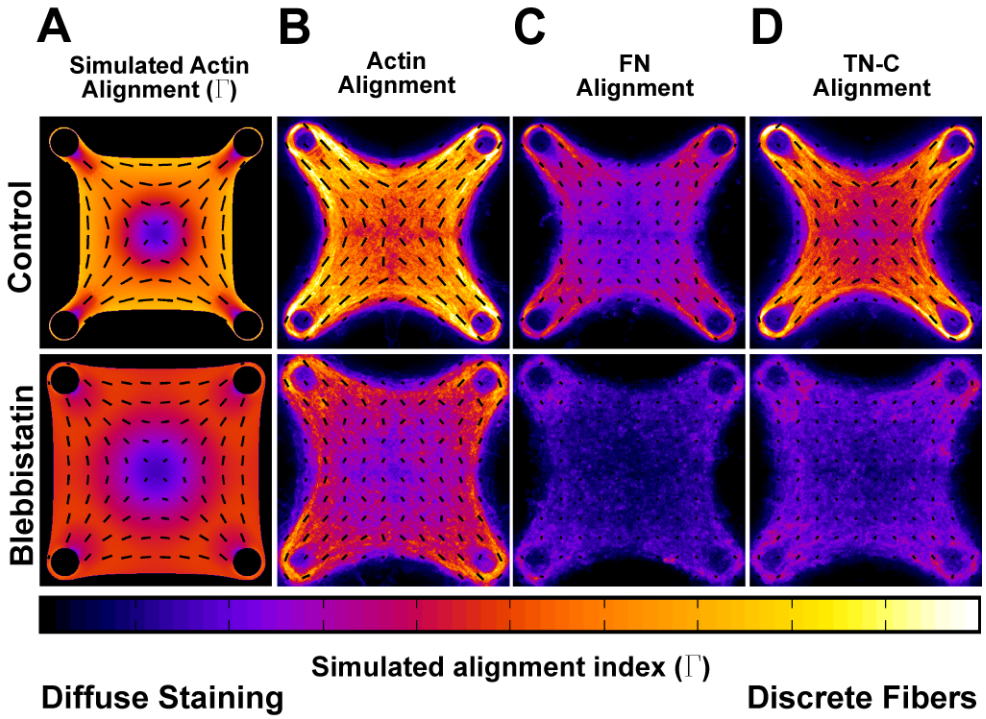

Figure 6.7: Tension induced alignment of cytoskeletal and ECM proteins within patterned microtissues. (A) Simulated bundling (Γ) and alignment of actin fibers within a microtissue under 100% (control) and 10% (blebbistatin) conditions for simulated stress fiber contraction. (B-D) Heat maps depicting degree of bundling and alignment of actin, fibronectin and tenascin C based on fluorescence images of microtissues under control and blebbistatin (50 μM) conditions. In all cases, quiver orientation indicates orientation of the simulated or observed fibrils. Quiver length and heat map colors depict how distinctly these proteins are bundled (clustered into discrete fibers). Alignment data for each protein was quantified from immunofluorescence staining of 120 optical sections (approximately 10 sections per microtissue for 12 different microtissues in each condition).

CHAPTER 7: FORCE-INDUCED FIBRONECTIN ASSEMBLY AND MATRIX REMODELING IN A 3D MICROTISSUE MODEL OF TISSUE MORPHOGENESIS

7.1 RATIONALE

3D encapsulations of cells in type-I collagen have served as *in vitro* models of tissue morphogenesis and wound healing for nearly thirty years (Stopak and Harris 1982; Stopak, Wessells et al. 1985; Nakagawa, Pawelek et al. 1989; Grinnell and Petroll 2010) and more recently as a strategy for tissue engineering, drug delivery, and *in vivo* implantation (Eschenhagen, Fink et al. 1997; Wallace and Rosenblatt 2003; Zimmermann, Melnychenko et al. 2006). Cells within these matrices exert contractile forces on the surrounding matrix fibers, resulting in a dramatic reorganization of the extracellular environment and the self-assembly of a coherent tissue-like structure. Concurrent with the modification of the exogenous collagen scaffold, cells also assemble a dense meshwork of additional extracellular matrices (ECMs) including fibronectin (Fn) (Adachi, Mio et al. 1998) and tenascins (Chiquet-Ehrismann, Tannheimer et al. 1994) as well as other proteins (Davenport and Nettesheim 1996). During morphogenetic events *in vivo*, a Fn matrix serves as a provisional template that directs the assembly of more permanent collagen fibers (Sottile and Hocking 2002; Midwood, Williams et al. 2004; Sottile, Shi et al. 2007; Kadler, Hill et al. 2008). However, it is not clear to what extent the inverse is true, namely, how or if an exogenous collagen scaffold can direct the formation of a cell-derived Fn matrix.

Given that the molecular conformation of Fn and indeed the physical assembly of a fibrillar Fn matrix are modulated by the same cell-generated forces that drive the reorganization of the collagen scaffold (Zhong, Chrzanowska-Wodnicka et al. 1998; Smith, Gourdon et al. 2007; Dzamba, Jakab et al. 2009; Lemmon, Chen et al. 2009), it seems likely that modifications to the structure of a provisional Fn matrix would occur concurrently with collagen compaction. On 2D surfaces, a mechanically extended conformation of Fn has been shown to impact matrix assembly (Kubow, Klotzsch et al. 2009) and the binding of proteins and bacterial adhesins (Little, Schwartlander et al. 2009; Chabria, Hertig et al. 2010). Understanding to what extent Fn is sensitive to mechanical forces when it is assembled within a composite 3D tissue in which other load bearing ECM proteins are present will be critical for translating insights from 2D studies into the more complex remodeling events that occur in 3D and *in vivo*.

A key limitation to these types of investigations has been that bulk encapsulations of cells in collagen matrices are typically millimeters to centimeters in scale (Stopak and Harris 1982; Stopak, Wessells et al. 1985; Nakagawa, Pawelek et al. 1989; Eschenhagen, Fink et al. 1997; Wallace and Rosenblatt 2003; Zimmermann, Melnychenko et al. 2006; Grinnell and Petroll 2010). The optics of such large structures and the massive movements occurring from gel

compaction preclude the application of traditional high resolution fluorescence microscopy. Furthermore, cells within such gels will experience heterogeneous mechanical and soluble conditions throughout the depth of the construct. *In situ* observation of Fn conformation has recently become feasible by utilizing a Foerster Radius Energy Transfer (FRET) labeled biosensor of Fn conformation (Baneyx, Baugh et al. 2002; Smith, Gourdon et al. 2007), but previous applications of this tool have been limited to 2D cultures or very thin (< 20 microns) cell derived matrices (Kubow, Klotzsch et al. 2009). To address the optical limitations of centimeter-scale constructs, we have recently established micro-electro-mechanical (MEMS) based microfabricated tissue gauges (uTUGs) in which one can observe compaction of nanoliter-scale 3D microtissues consisting of hundreds of cells encapsulated in type-I collagen gels (Legant, Pathak et al. 2009; Boudou, Legant et al. 2012).

Here, we combine uTUGs with a FRET biosensor of Fn conformation to probe the organization, conformation and remodeling of both the exogenous collagen scaffold and the cell assembled Fn matrices during force-mediated tissue condensation. We observe the presence of two separate Fn populations (compact/collagen-absorbed and extended/ fibrillar) that may have different downstream signaling properties. Cell contractility and tissue geometry cooperate to drive gradients in Fn conformation within 3D microtissues and we confirm that increases in tissue stress are accompanied by the assembly of a fibrillar Fn matrix. By understanding how Fn is organized during collagen compaction, these results will have important implications for future studies of the remodeling events that occur within collagen scaffolds either in 3D *in vitro* models or within surgical implants *in vivo*.

7.2 MATERIALS AND METHODS

7.2.1 Device fabrication and microtissue seeding

Single layer and multilayer templates were created as described previously(Legant, Pathak et al. 2009). SU-8 photoresist (Microchem) was spin coated onto silicon wafers. Multilayer SU-8 masters were created using successive spin coat and exposure steps. To generate substrates for microtissues, SU-8 masters were cast with a prepolymer of PDMS (sylgard 184; Dow-Corning). Before cell seeding, the PDMS templates were sterilized in 70% ethanol followed by UV irradiation for 15 minutes and treated with 0.5% Pluronic F127 (BASF) to reduce cell adhesion. Liquid neutralized collagen I from rat tail (BD biosciences) was then added to the substrates on ice and templates were degassed under vacuum. Additional collagen and cells were then added to the mold and the entire assembly was centrifuged to drive the cells in the micropatterned templates. Excess solution was removed by dewetting the surface of the substrate prior to incubating at 37 ˚C to induce collagen polymerization. Fn containing media was then added to each substrate. All constructs in this study were prepared using a final concentration of 1.75 mg/ml collagen.

7.2.2 Calculation of cantilever spring constant and microtissue force/stress

Cantilever spring constants were calculated utilizing a capacitive MEMS force sensor mounted on a micromanipulator as described previously (Klotzsch, Smith et al. 2009). Images of the sensor tip and cantilever head were acquired during each test using an Olympus FV1000 confocal microscope with an air immersion 0.4 NA 10x objective. To account for local deformation of the PDMS material around the sensor, the spring constant of the MEMS sensor was calibrated against the side of the PDMS well which can be viewed as an elastic half space of the same material modulus as the PDMS cantilevers and was found to be 104 nN/μm ± 1.9 nN/μm. This value was then used for the subsequent measurements of the force required for cantilever bending. For each measurement the sensor tip was placed 20 microns below the top of the post and the probe translated laterally against the outer edge of the cantilever using a custom written Lab View (National Instruments) script. The probe base was displaced approximately 150 microns for each measurement. The displacement of the probe tip (and thus of the cantilever head) was calculated from the spring constant measured above and the reported sensor force and was verified visually during the deformation. 5 cantilevers were measured across a substrate and measurements were repeated for three different substrates of each condition. Cantilevers were

found to have linear responses up to approximately 40 microns of deformation. As the majority of cantilever deformations observed in this paper were below 40 microns, this section was fit using a linear fit with a spring constant of 148 nN/μm ± 35nN/μm which was then used for calculation of microtissue forces. Only microtissues that were uniformly anchored to the tips of the cantilevers were included in the analysis. Microtissue stress was calculated by imaging the entire volume of the microtissue within a 30 μm wide strip (measured along the long axis of the tissue) at the tissue midpoint. The cross-sectional area of this region was then measured from the confocal z-stack data using custom written Matlab (The Mathworks) scripts.

7.2.3 Fibronectin isolation, fluorescent labeling and denaturation curves

Fn was isolated from human plasma (Zurcher Blutspendedienst SRK) by affinity chromatography as described previously(Smith, Gourdon et al. 2007). For cysteine (acceptor) labeling, Fn was denatured in 4M urea at a concentration of 1g/l and incubated with 40 fold molar excess of Alexa Fluor 546-maleimide (Invitrogen) for 3 hours at room temperature. Cysteine labeled Fn was separated from free dye using by size exclusion chromatography PD-10 column (Sephadex) equilibrated with PBS with 0.1M $NaHCO_3$ [pH 8.5]. Cysteine labeled Fn was then incubated with 60 fold molar excess Alexa Fluor 488-succinimidyl ester for 3 hours at room temperature to label amines (donors) before separating Fn-donor/acceptor (Fn-DA) from free dye with a second PD-10 column equilibrated in PBS. Fn-DA was then diluted to 0.3 g/l in PBS, aliquoted and stored at -80 ˚C until needed. A labeling ratio of 4 acceptors and ~7 donors per Fn dimer was determined by measuring the absorbances of Fn-DA at 280, 496 and 56 nm and using published extinction coefficients for dyes and Fn. Unlabeled Fn as isolated in a similar manner, dialyzed in PBS for 48 hrs (Slide-a-lyzer dialysis cassette, 10,000 MW cutoff, Pierce) and diluted to 1 g/l in PBS before aliquoting and storing at -80 ˚C. After thawing, all samples were stored at 4 ˚C and used within 72 hours. All cell culture experiments utilized unlabeled Fn in 10 fold excess to Fn-DA in order to avoid signal from intermolecular FRET. Denaturation curves were obtained by diluting Fn-DA to a final concentration of 0.1 g/l in specified concentration of GdnHCl, and imaging with confocal microscopy under identical parameters to those used for cell culture.

7.2.4 Confocal microscopy

Z-stack images were acquired with an Olympus FV1000 confocal microscope with a water immersion 0.9 NA 40X objective. Four post microtissue images were acquired at 512 x

512 pixels per slice with 2 μm slice spacing for voxel dimensions of 0.621 x 0.621 x 2.0 μm. The mid-sections of 2 post microtissue images were acquired at 256 x 256 pixels with 1.5X zoom factor per slice with 2 μm slice spacing for voxel dimensions of 0.828 x 0.828 x 2.0 μm. All images were acquired with 3X Kalman line averaging. FRET images were acquired using a single photo multiplier tube (PMT) by sequentially acquiring images through a diffraction grating and slit. Donor and acceptor intensities were detected using 20 nm bandwidths centered at 510-530 nm and 560-580 nm respectively. Serial imaging of the same volume confirmed that no photo bleaching was occurring. To ensure that no artifacts occurred due to the microscope setup, laser power, pixel dwell time and PMT voltage were kept constant between all conditions.

7.2.5 FRET calculation and colocalization analysis

FRET ratios are reported as the intensity of the acceptor (Ia) divided by the intensity of the donor (Id). All images were 12-bit (4096 relative intensity units) and were processed with custom written Matlab (The Mathworks) scripts. First, background values were determined from tissue-free regions of each image and subtracted from the raw images. Then, images of each channel were binary thresholded using a cutoff value of 2x background (Fn donor and acceptor), 1.75x background (collagen), and 1.5x background (DAPI). These settings were determined empirically based on the intensity of each fluorescence signal and then kept constant for all experiments. Prior to calculation of the FRET ratio, donor and acceptor images were smoothed using a 2 x 2 pixel local averaging filter. Donor bleed through was calculated from images of microtissues labeled with Alexa-488 Fn and was determined to be a linear function of donor intensity with a slope of 0.224 (i.e. approximately 20% of the donor intensity was present in the acceptor channel). Acceptor images were thus scaled appropriately prior to calculation of the FRET ratio. Any saturated pixels, or those below the threshold value were excluded from the FRET analysis. Median values were calculated for each tissue from all pixels above threshold with a single tissue considered as an independent observation. Colocalization analysis was performed on a voxel by voxel basis with Fn considered to be colocalized with collagen if each channel was above the aforementioned threshold values.

7.2.6 Immunofluorescent staining and protein density mapping

Microtissues were cultured for the indicated periods of time before fixation with 4% formaldehyde in PBS for 1 hr at 37 ˚C. Samples were subsequently rinsed for 30 minutes in PBS,

before blocking overnight in 10% donkey serum. The exogenous collagen scaffold was labeled using primary antibodies directed against type-I rat collagen (Chondrex) and detected using fluorophore conjugated, isotyp- specific, anti-IgG antibodies (Jackson ImmunoResearch). The use of primary antibodies specific for rat-tail collagen ensures that we only examine the localization of the original collagen scaffold and not collagen assembled *de novo* by the constituent NIH 3T3 cells (which are from mice). Cell nuclei were counter stained with DAPI. Density maps of protein and DAPI labeling were created by averaging the immunofluorescent (or FRET labeled Fn) data from individual microtissues. Masks were generated in Adobe Photoshop labeling the positions of each cantilever and used to align and crop the z-stacks each microtissue. Optical slices from each tissue (10 tissues total) were then averaged to quantify protein and cell distributions for each condition. Because microtissues displayed small variations in thickness and in the vertical position at which they were tethered to the pillars, protein density maps were normalized by the thickness of each microtissue prior to averaging (ie plotted from the uppermost to the lower most surface of the tissue at each x-y position). Volume renderings of microtissues were constructed from confocal image stacks using Fiji.

7.2.7 Cell culture and reagents

NIH 3T3 fibroblasts (American Type Culture Collection, ATCC) were cultured in 4.5 mg/ml glucose containing DMEM + L-glutamine (Gibco) supplemented with 10% bovine serum (Biowest). Cells were maintained at 37 ˚C and 5% CO2 for all experiments. When indicated, Fn was added to the cell culture media at a total concentration of 50 μg/ml (5 μg/ml Fn-DA and 45 μg/ml unlabeled Fn). Blebbistatin (Sigma, 50 μM) treatment was performed for 2 hrs at 37 ˚C and 5% CO2 prior to fixation.

7.3 RESULTS

7.3.1 Utilization of micropatterned tissue gauges to generate collagen based microtissues.

In order to micropattern encapsulations of cells in collagen matrices, we used SU-8 photolithography to generate arrays of wells (400 μm x 400 μm x 110 μm deep) on a silicon wafer (**Figure 7.1**). Within each well, we incorporated raised cantilevers that served to constrain the final tissue geometry. After replicating the rigid photoresist structures with poly-dimethylsiloxane (PDMS) elastomer, we immersed the mold within a prepolymer solution of NIH 3T3 cells and type-I collagen. The entire assembly was centrifuged to drive the cells into the templates before removing excess solution and polymerizing the matrix. Within hours, the encapsulated cells begin to remodel the adjacent matrix fibers. The collective matrix remodeling by all cells within the construct condenses the tissue into a coherent band that becomes anchored to the cantilevers. Within this system, we also observed that as cells remodel the collagen gel, they simultaneously assemble a dense Fn matrix. It has previously been shown that the assembly of Fn fibers is regulated by cell traction forces both *in vitro* (Zhong, Chrzanowska-Wodnicka et al. 1998; Lemmon, Chen et al. 2009) and *in vivo* (Dzamba, Jakab et al. 2009) and can be modulated by the amount of mechanical stress within microtissues (Legant, Pathak et al. 2009); however, the spatio-temporal relationship between the Fn matrix and the collagen scaffold during compaction has not been studied in detail. As the chemical and mechanical microenvironment within which Fn is assembled can impact its conformation (Baugh and Vogel 2004; Antia, Baneyx et al. 2008) and therefore the accessibility of cryptic binding sites, we sought to precisely map the spatial distributions of Fn and collagen within the microtissue system.

7.3.2 Cells condense the collagen matrix into a densely aligned core around which they form a highly cellularized shell containing fibrillar fibronectin.

Within 24 hours, cells contract the collagen scaffold into a coherent tissue that is tethered around the cantilevers. Over 72 hours, the collagen scaffold is compacted into a dense core from which the cells have mostly receded into a highly cellularized peripheral shell (**Figure 7.2**). The use of primary antibodies specific for rat-tail collagen ensures that we only examine the localization of the original collagen scaffold and not collagen assembled *de novo* by the constituent cells. DAPI staining is uniform throughout the horizontal plane of the tissue; however, 3D density mapping of tissue cross sections confirmed the presence of a cellularized shell about a sparsely populated collagen scaffold with the highest cell density on the top surface.

Within hours of encapsulation, plasma Fn in the culture media absorbed to the collagen scaffold and the distributions of the two matrices were nearly identical after 24 hours (**Figure 7.2a**); however, over the next several days, the matrices form distinct patterns (**Figure 7.2b, c**). The collagen is compacted and aligned within the interior of the tissue, with highest densities at the perimeter of this core. Fn in contrast is assembled in concentric shells around the collagen core and is up regulated in regions of the tissue that have previously been suggested to be under high mechanical tension (Legant, Pathak et al. 2009). Acute (2 hour incubation) treatment with blebbistatin did not dramatically alter the distributions of Fn, collagen or DAPI, but did cause a relaxation of the tissue as observed by a decrease in the radius of tissue curvature between the boundaries (**Figure 7.2d**). As the signaling from Fn is not only dependent on its presence or absence, but also on its physical and conformational presentation, we next sought to determine whether the changes in Fn distribution that occur during tissue remodeling also correlate with changes in the conformation of the Fn molecules presented to cells.

7.3.3 Fibronectin transitions from predominantly compact collagen-absorbed, to mechanically extended fibers that are assembled during the remodeling of a collagen scaffold.

We incubated 4-post microtissues with a FRET based biosensor of Fn conformation (Fibronectin-Donor/Acceptor labeled, Fn-DA) and fixed after 24, 48 or 72 hours of remodeling. By acquiring confocal sections, the FRET signal can be used to map 3D Fn conformation within the tissue. The Fn-DA probe reports the average distance between donor and acceptor fluorophores on the Fn molecule and can thus be used to report conformational changes; however, because the acceptors are labeled on the $FnIII_7$ and $FnIII_{15}$ modules, we are only probing structural changes within ~12 nm of these regions (yellow circles in **Figure 7.3a**). We report the FRET ratio as the acceptor intensity (Ia) divided by the donor intensity (Id) after correction for spectral bleed-through and acceptor cross-talk as detailed in Methods. In order to correlate the FRET ratio seen in microtissues to structural changes in the Fn molecule, we calibrated the FRET ratio to soluble Fn-DA in known concentrations of the denaturant guanidine hydrochloride (GdnHCl) (**Figure 7.3b, c**). Previous work has demonstrated that the transition from compact Fn to an extended molecule correlates with the drop FRET signal seen for Fn in solution between 0M and 1M GdnHcl. Moreoever, Fn in solution begins to lose its secondary structure at concentrations of denaturant GdnHCl approaching 1M (Ia/Id = 0.40), with complete denaturation at 4M GdnHCl (Ia/Id = 0.29) (Smith, Gourdon et al. 2007).

We found that after 24 hours, the Fn within microtissues exists predominantly in a compact conformation, but that there was a significant drop in the median FRET ratio of Fn-DA as the tissue remodeled from 0.62 to 0.57 and 0.51, after 24, 48 and 72 hours respectively (**Figure 7.4 a, b**). Acute treatment with blebbistatin at 72 hours revealed that approximately 40 percent of the decrease in FRET was due to active cellular contractility whereas the remaining 60 percent was unaffected. The unaffected portion likely represents a combination of the drop in FRET that occurs during the transition from a predominantly compact form of Fn to a fibrillar matrix, residual energy within the fibrillar matrix stored through inter-fiber crosslinks, or improper refolding of the molecules within stretched Fn fibers. By simultaneously imaging the FRET signal and the immunofluorescence staining of the collagen scaffold, we separated the Fn population within microtissues into collagen-colocalized Fn and non-collagen-colocalized Fn to determine if these two populations might respond differently. At each time point, we found that collagen-colocalized-Fn was more compact than non-collagen-colocalized Fn, but that to within our measurement resolution (0.621 x 0.621 x 2.0 μm), both populations appeared to be progressively unfolded over time (**Figure 7.4c, d**). The higher FRET signal seen from collagen-colocalized Fn (as compared to non-collagen-colocalized Fn) could be due to mechanical stabilization of the Fn fibers by the collagen scaffold, or due to residual non-fibrillar Fn present in our measurement volume.

Interestingly, there was a gradual shift from predominantly collagen-colocalized Fn (83% colocalized vs. 17% non-colocalized after 24 hours) to nearly equal amounts of colocalized and non-colocalized Fn after 72 hours (48% colocalized vs. 52% non-colocalized) (**Figure 7.4e**). These two factors combine to result in an increase in the amount of total Fn presented to cells that has a loss in secondary structure from 1%, 3% to 13% after 24, 48 and 72 hours respectively (**Figure 7.4f**). However, even when tethered to rigid boundaries, the relative loss in secondary structure of Fn assembled within microtissues is significantly less than what has been shown for Fn assembled by cells cultured on rigid glass coverslips (Kubow, Klotzsch et al. 2009). We hypothesize that this discrepancy may be due to the large presence of compact, collagen-absorbed Fn molecules, the reduced rigidity of the collagen matrix (as compared to glass), or due to a portion of the mechanical load in 3D microtissues being distributed though the exogenous collagen scaffold instead of being transferred directly to Fn fibers.

7.3.4 Cellular contractility and tissue geometry direct 3D gradients in fibronectin conformation

Average FRET values within a microtissue only represent a limited view of the story. In contrast to soluble factors which are capable of diffusing throughout the tissue, conformational changes in the structure of Fn will only signal to cells capable of physically interacting with the molecule (i.e. cells within tens of microns of a given the binding site). We thus sought to determine whether the gradients in Fn concentration we observed previously also correlated with gradients in the conformation of the Fn molecules by taking average density maps of the FRET signal within the microtissues. We found that after 24 hours, Fn appeared to primarily be adsorbed to the collagen gel with no clear gradients present in the tissue. However over the course of remodeling, Fn became progressively fibrillar and increasingly strained with clear gradients emerging in both the horizontal and vertical tissue planes (**Figure 7.4g**). The highest FRET ratios (compact Fn) occurred at the core of the constructs, in regions where dense collagen staining was also observed. In contrast, lowest FRET ratio (mechanically extended Fn) occurred predominantly near the surface of the microtissue, in regions that were spatially separated from the collagen scaffold. Acute treatment with blebbistatin did not shift the overall FRET distributions, but rather increased the FRET signal within both the core and periphery of the microtissue.

Within this geometry, we observed gradients in Fn conformation that appeared to be correlated with regions of the tissue that would be subject to high mechanical tension. Moreover, previous studies have shown that the presence of Fn can dramatically increase the ability of cells to compact a collagen scaffold (Hocking, Sottile et al. 2000; Liu, Yanai et al. 2006). We therefore wanted to measure whether increases in tissue stress occurred concurrently with the assembly of a fibrillar Fn matrix. However, as the cantilevers in the 4-post configuration are rigid, we could not directly measure the tissue stress. To address this, we next cultured microtissues within PDMS molds that contained 2 flexible cantilevers (400 μm x 800 μm x 150 μm deep) (**Figure 7.5a**). We utilized multilayer SU-8 photolithography to generate wide caps at the tips of the flexible cantilevers (Legant, Pathak et al. 2009) that serve to anchor the tissue even when the cantilever becomes highly deflected. By displacing the cantilever tip with a MEMS strain sensor, we determined the cantilever spring constant to be 148 ± 35 nN/μm which was linear over the range of displacements tested (**Figure 7.5b, c**). This spring constant was then used to relate cantilever bending to microtissue force.

7.3.5 Increases in microtissue stress occur concurrently with the peripheral assembly of a progressively unfolded fibrillar fibronectin matrix

In microtissues tethered to two flexible cantilevers, we found that tissue tension increased during the first 24 hours and then leveled off at approximately 5.5 μN before a moderate increase in force between 48 and 72 hours to 6.7 μN (**Figure 7.5d**). Cross-sectional area decreased dramatically between 24 and 48 hours, but then increased between 48 and 72 hours due to increased cell proliferation at the periphery of the tissue (**Figure 7.5e**). As a result, median cross-sectional tissue stress increased progressively from 740 to 970 to 1090 Pa at 24, 48 and 72 hours respectively (**Figure 7.5f**). Concurrent with these increases in stress, we found that the median FRET ratios of Fn within these tissues decreased from 0.66 to 0.61 to 0.53 at each of these time points (**Figure 7.5g**). Similar to the 4 post configuration, a portion of the Fn remodeling was actively mediated by cell contractile forces. Acute (2 hour incubation) blebbistatin treatment after 72 hours of remodeling led to a dramatic decrease in tissue stress to 620 Pa, but only a partial restoration of FRET signal at approximately 0.56. Thus the increased tissue stress that occurs during the remodeling of a collagen scaffold correlates with a progressively unfolded Fn matrix assembled at the periphery. However, we did not observe a relationship between tissue stress and Fn FRET *within* each time point despite nearly a 2 fold variation in stress between tissues, thus it seems unlikely that these two parameters are directly related (i.e. that tissue stress is transmitted directly to Fn fiber strains or vice-versa). In microtissues, it's possible that most of the tissue stress may be transmitted not through the Fn matrix, but instead through the exogenous collagen scaffold or through direct transmission via the actin cytoskeleton and cell-cell junctions.

7.3.6 Fibronectin that is initially adsorbed to the collagen scaffold is not incorporated into the fibrillar fibronectin matrix, nor is it progressively stretched by cells

In the previous section, we demonstrated that both collagen-colocalized Fn and non-collagen-colocalized Fn molecules became progressively extended as the microtissue remodeled. However, because Fn-DA was continually present in the culture medium throughout the experiment, it was not clear whether the decrease in FRET observed for these two populations was due to the gradual stretching of the original Fn molecules, or due to the absorption/assembly of new Fn molecules in a more unfolded state. To test the relative roles of these processes, we incubated microtissues with pulses of labeled Fn-DA from 0-24 hours, 24-48 hours, or 48-72 hrs

before fixing. This experiment, only labels Fn present in the system during a given window of time. We found that Fn present during the first 24 hours of remodeling existed predominantly in a compact conformation and was not progressively strained by cells (**Figure 7.6a**). Microtissues incubated with Fn-DA for the first 24 hours of remodeling displayed the same FRET ratios whether they were fixed at 24 hours, or whether the Fn-DA was replaced with unlabeled Fn and the labeled matrix was allowed to be remodeled for an additional 48 hours. This lack of molecular extension occurred for both collagen-colocalized and non-collagen-colocalized populations (**Figure 7.6b**). In contrast, both collagen-colocalized and non-collagen-colocalized Fn present at the latter stages of tissue remodeling (48-72 hours) displayed dramatically lower FRET ratios despite only being remodeled by cells for a period of 24 hours (**Figure 7.6a, b**).

To further investigate, we next examined the spatio-temporal organization of both the collagen scaffold and Fn molecules incorporated during given stages of microtissue remodeling. When microtissues are fixed after 24 hours, we found that 80% of the Fn was co-localized with the collagen scaffold (**Figure 7.4e**). If, instead of fixing the sample after 24 hours, we replaced the Fn-DA with unlabeled Fn and allowed the microtissue to continue remodeling for an additional 48 hours, we found that nearly all labeled Fn was still highly co-localized (85%) with the collagen scaffold (**Figure 7.6c**). Moreover, the non-collagen-colocalized Fn appeared immediately adjacent to the collagen scaffold. Thus, even after 72 hours, the Fn molecules incorporated into the construct during in the early stages of remodeling exist predominantly in a compact conformation that is either bound to or in very close proximity to the collagen scaffold. This interaction appears to stabilize the Fn molecules such that they are not progressively stretched by cells as the tissue remodels. In contrast, Fn present between 48 and 72 hours was only 15 percent co-localized with collagen (**Figure 7.6c**) and the non-collagen-colocalized population was physically separated from the collagen scaffold. Thus the Fn fibrils assembled at these later time points are less stabilized by the collagen scaffold and more highly stretched by cell generated forces. The decrease in FRET observed for the small amount of collagen-colocalized Fn present between 48 and 72 hrs is harder to explain, but may be due to the presence of mechanically stretched matrix fibers that we are unable to spatially resolve from the collagen scaffold or due to the absorption of Fn molecules to the collagen scaffold in a more mechanically unfolded conformation. These results reveal that in contrast to simplified 2D systems, many factors within a dynamic 3D collagen matrix will contribute to the molecular composition of the matrix sensed by cells.

7.4 DISCUSSION

ECM assembly often involves the deposition of both provisional and more permanent matrices. During normal wound healing and in tissue culture, a type-I collagen matrix is deposited along and highly co-localized with provisional Fn fibers (Midwood, Williams et al. 2004; Kadler, Hill et al. 2008). In collagen based surgical implants and in 3D *in vitro* cell culture, cells are frequently placed in the inverse scenario. Namely, cells are encapsulated into an initial collagen scaffold within which they then assemble a fibrillar Fn matrix. By combining MEMS based uTUGs with Fn FRET probes we directly measured the spatial distributions and molecular conformation of Fn within 3D, collagen-based microtissues. We show that compact Fn from media quickly absorbs to and is stabilized by the collagen scaffold, whereas fibrillar Fn was later assembled by cells predominantly at the tissue periphery. This new fibrillar ECM becomes spatially segregated from the collagen fibers which are compacted at the tissue core. The net result of this process is that cells are increasingly isolated from the initial Fn coated collagen scaffold and progressively immersed in the new cell assembled Fn-rich ECM that displays a rather different set of molecular conformations. These two populations (compact/ absorbed and extended/ fibrillar) may have dramatically different signaling implications given the fact that Fn has multiple cryptic and mechano-regulated binding sites (Vogel 2006).

Importantly, while the collagen fibers do not individually co-localize with fibrillar Fn (as is the case during normal wound healing), they collectively serve as a dynamic biomaterial substrate that governs overall tissue geometry and against which cells assemble fibrillar Fn. As matrix assembly and remodeling will accompany the implantation of any biomaterial, it will be important to understand further how the initial properties of a scaffold affect the assembly of the cell-derived ECM within which cells will ultimately reside. Indeed, such "material driven ECM assembly" has been used recently to engineer the conformation of Fn on polymer scaffolds leading to increased myogenic differentiation of adhered cells (Salmeron-Sanchez, Rico et al. 2011). 2D studies utilizing inert glass slides or polyacrylamide gels have found that 1) Fn matrix fibers are progressively unfolded by cell generated forces (Smith, Gourdon et al. 2007), 2) Fn fibers assembled on rigid substrates are more unfolded than those assembled on soft substrates (Antia, Baneyx et al. 2008), and 3) crosslinking of fibrillar Fn matrices increases their rigidity and prevents their unfolding (Kubow, Klotzsch et al. 2009). However, collagen gels and many biomaterial implants are not inert substrates, but can actively be remodeled by cells and all of the above processes likely contribute to the conformation of the assembled fibrillar Fn matrix.

Our studies also highlight how matrix remodeling can be spatially templated. Tissue geometry and cell forces appear to cooperate as central factors to spatially pattern both the collagen scaffold and the conformation of the Fn molecules in the system. As specific regions of the collagen scaffold are dynamically aligned and compacted over time, they present a locally stiffening substrate against which cells are assembling a fibrillar Fn matrix. We observed gradients in the amount and conformation of Fn within tissues, which we mapped in 3D using FRET. These gradients propagate from the anchor points in regions that have previously been shown to experience high tensile stress (Legant, Pathak et al. 2009). Given that the conformation of surface adsorbed Fn has been shown to impact cell proliferation and differentiation (Garcia, Vega et al. 1999; Lan, Gersbach et al. 2005), such gradients in Fn conformation may be another means to manipulate cell phenotype during tissue morphogenesis.

The physical conformation of Fn *in vivo* has been shown to regulate morphogenetic movements (Rozario, Dzamba et al. 2009), and cryptic binding sites exposed in mechanically extended Fn fibrils can regulate cell adhesion and matrix assembly (Smith, Gourdon et al. 2007; Kubow, Klotzsch et al. 2009), increase the nonspecific binding of albumin and casein (Little, Schwartlander et al. 2009), and destroy N-terminal bacterial binding sites (Chabria, Hertig et al. 2010). Here, the gradients in Fn conformation in our microtissue system appeared to serve as an "extracellular memory" whereby the mechanical signals experienced by cells are dependent not only on the current stresses, but also on the history of previous ECM remodeling events that are reflected in accumulated molecular strains. Thus, in contrast to focal adhesions (FAs), which respond quickly and directly to mechanical stress (Geiger, Spatz et al. 2009), the fibrillar Fn matrix could "lock in" a molecular conformation during matrix crosslinking and result in long term patterns that will continue to signal to cells at a significantly longer time scale than the transient fluctuations in cell traction forces. Given the importance of Fn conformation to cellular function, understanding how these patterns emerge and are maintained will be critical for dissecting the interplay between long-range morphogenetic movements and local microenvironmental manipulation of cell phenotype. Our studies show that FRET based readouts of molecular conformation combined with μTUGs provide one approach to quantify such relationships, and highlights a means to understand the complex interplay between cells and matrix in highly anisotropic microenvironmental niches.

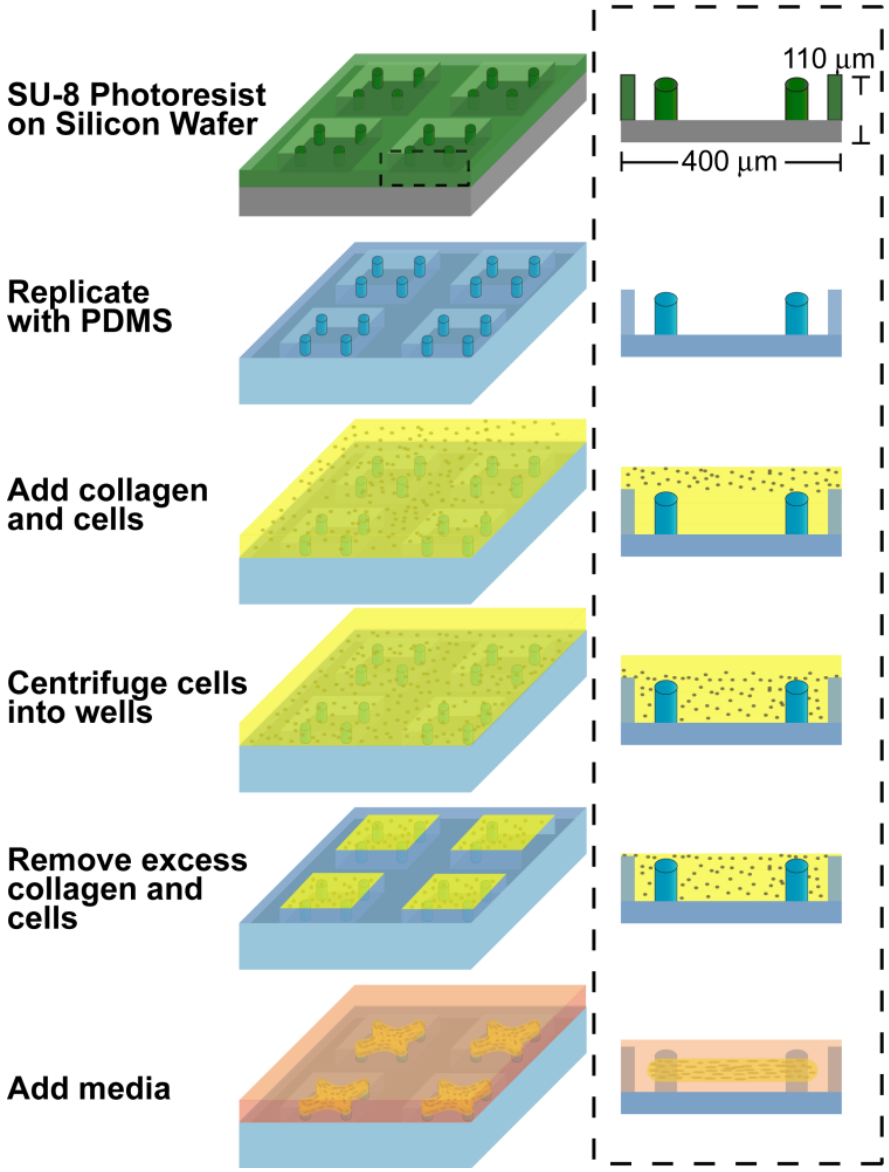

Figure 7.1: Fabrication and seeding of microfabricated tissue gauges (µTUG) molds. Process flow diagram for the creation of µTUG arrays. After replicating the rigid photoresist structures with PDMS elastomer, the mold is immersed within a prepolymer solution of cells and type-I collagen. The entire assembly is then centrifuged to drive the cells into the templates. Excess solution is removed and the matrix is polymerized (by increasing the temperature to 37 ˚C) prior to adding media.

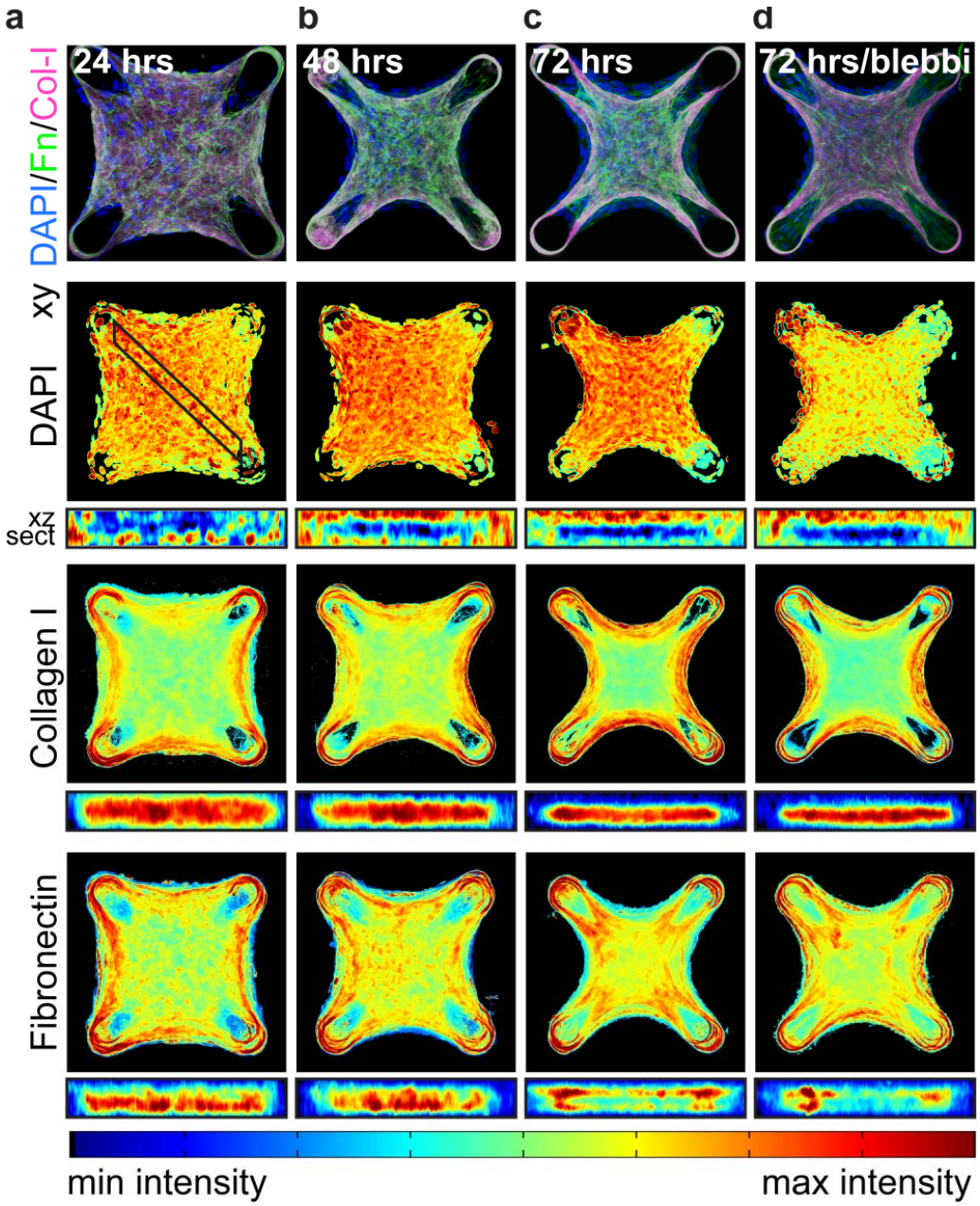

Figure 7.2: 3D averaged density maps of ECM protein in microtissues. a-d) Immunofluorescent images showing DAPI, collagen I and Fn within microtissues fixed after 24, 48 and 72 hours of remodeling, or after 72 hours of remodeling with acute (2 hours prior to fixing) incubation with 50 μM blebbistatin. Density maps represent the average protein density at a given location. In order to register images between tissues of different thickness, cross-sections (xz sect) are the plotted from the uppermost to the lower most surface of the tissues (ie normalized by tissue thickness). All density maps are the average of 10 individual microtissues from each condition. Color scales are normalized to depict the min and max values within each condition.

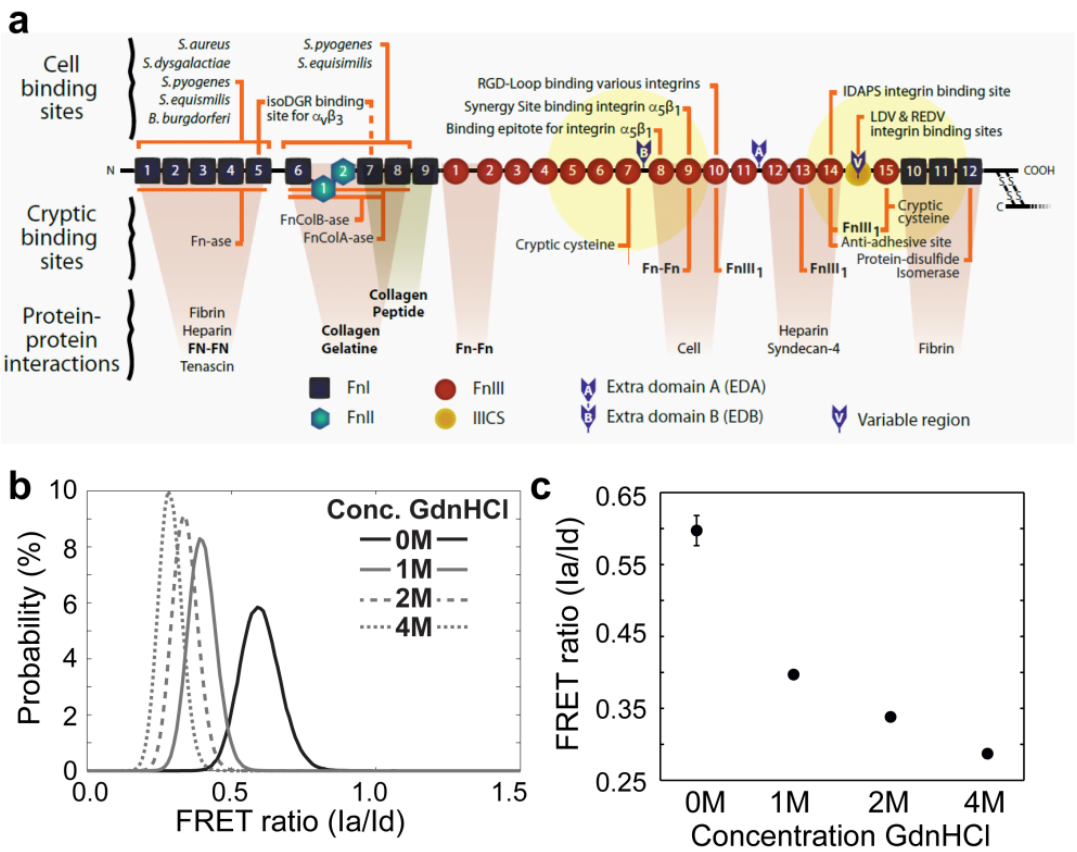

Figure 7.3: Fn structure and Fn-DA FRET labeling. **a)** Cartoon of Fn monomer depicting multiple cell and ECM binding sites (adapted from Vogel, Ann Rev 2006). Yellow spheres represent the 6 nm radius of energy transfer to acceptor labeled cysteines. Donors are randomly labeled at lysines at an average of 7 donors and 4 acceptors per molecule. **b)** Probability histograms of the FRET ratios from FN-DA in solution with increasing concentrations of the denaturant GdnHCl. **c)** Mean values for the histograms depicted in (**b**). Fn begins to lose its secondary structure at or below 1M GdnHCl (Ia/Id = 0.40) and is completely denatured at 4M GdnHCl (Ia/Id = 0.29). **b** and **c** are the average (± SD) of 5 fields of view under each condition.

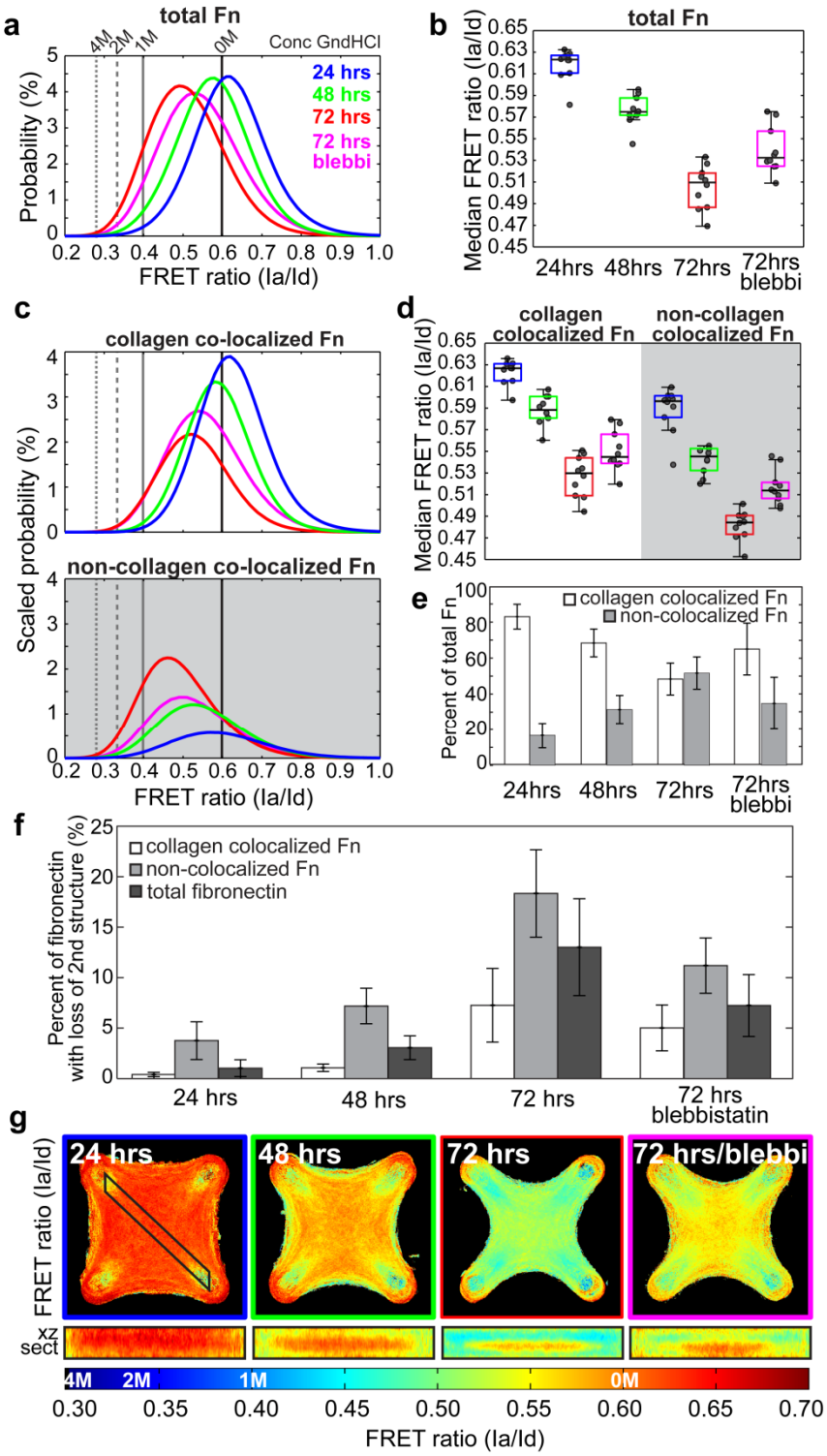

Figure 7.4: FRET measurement of Fn conformation in microtissues. a) Probability density functions (PDFs) of total Fn measured in microtissues fixed after 24, 48 or 72 hours of remodeling, or after 72 hours of remodeling with acute (2 hours prior to fixing) incubation with 50 μM blebbistatin. Corresponding values from Fn-DA in solutions of 0M, 1M, 2M and 4M

GdnHCl denaturant are indicated. **b)** Box and whiskers plot of the median FRET values within microtissues depicted in (**a**). **c)** Scaled PDFs showing separate populations of collagen-colocalized Fn and non-collagen-colocalized Fn. PDFs are scaled such that the areas under each curve equal the percent of either collagen-colocalized Fn or non-collagen-colocalized Fn at each time point. **d)** Box and whiskers plot of the median FRET values within microtissues depicted in (**c**) showing either collagen-colocalized Fn or non-collagen-colocalized Fn. **e)** Percent of Fn within microtissues fixed at each time point that is either colocalized with collagen, or non-colocalized with collagen. **f)** Percent of either collagen-colocalized, non-collagen-colocalized, or total Fn present in microtissues with a loss in secondary structure (FRET ratios below that of Fn in 1M GdnHCl). **g)** Average density maps of the FRET ratios (Ia/Id) within microtissues from (**a-f**). Corresponding denaturation points are indicated on the colorbar. All data and images were computed from 10 microtissues within each condition. Data in (**a-f**) was computed from the raw experimental data and not from the density maps. Data from (**a** and **c**) are the compiled PDFs for all microtissues within a given condition. Data from (**e**) are mean values ± SD.

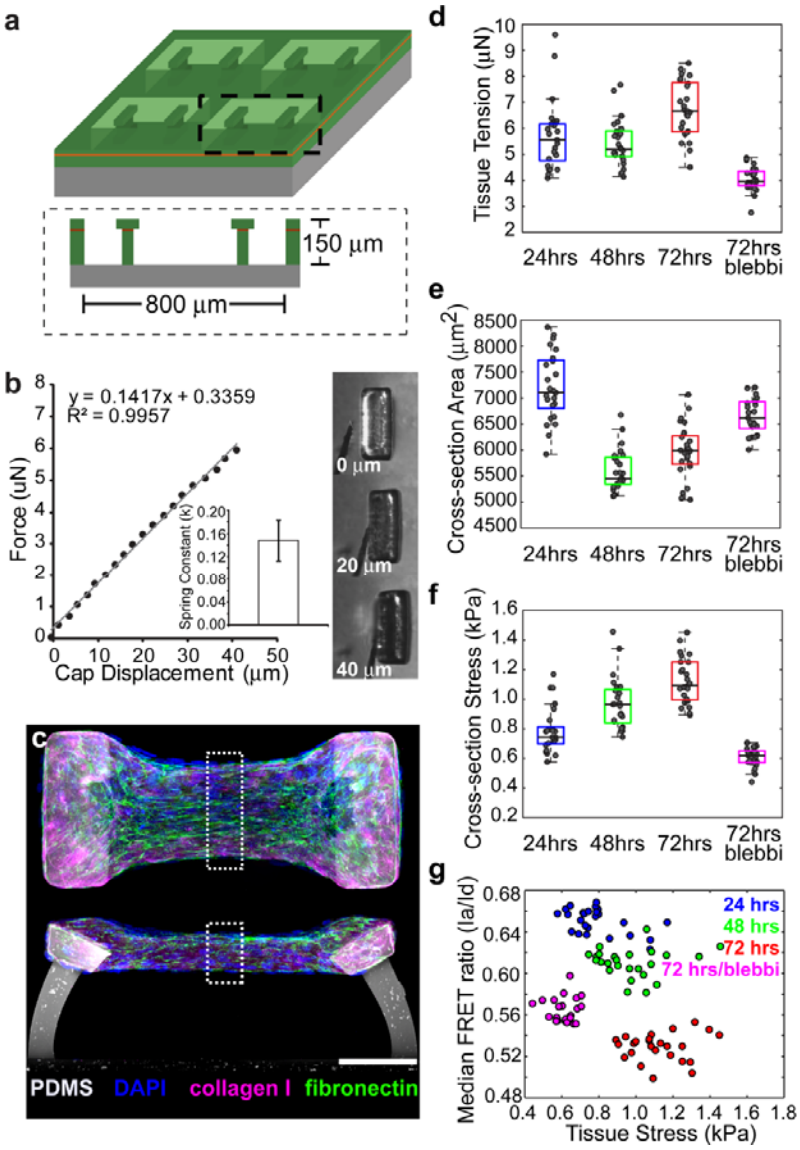

Figure 7.5: Increases in tissue stress occur concurrently with the assembly of a progressively unfolded fibrillar Fn matrix. **a)** Schematic of 2 post µTUG molds generated from multilayer SU-8 photolithography. **b)** Calibration of cantilever spring constants and corresponding transmitted light images of cap deflection. A representative plot of force vs. cap displacement is shown. Inset: Calculated spring constant (k = 148 ± 35 nN/µm (SD) for n = 15 measurements, 5 cantilevers each across 3 substrates). **c)** Representative top down and cross-section views for microtissues showing Fn (green), collagen (pink) and DAPI (blue) after 48 hours of remodeling. Dashed boxes indicate regions for calculation of cross-sectional area, cross-sectional stress and Fn-DA FRET. Scale bar = 100 µm. **d)** Box and whiskers plot of tissue tension for 2-post microtissues fixed after 24, 48 and 72 hours of remodeling, or after 72 hours of remodeling with acute (2 hours prior to fixing) incubation with 50 µM blebbistatin. **e)** Box and whiskers plot of cross-section area for tissues under the same conditions as (**d**). **f)** Box and whiskers plot of cross-section stress for tissues under the same conditions as (**d**). **g)** Scatter plot for the median FRET ratio (Ia/Id) vs. cross-section stress for tissues under the same conditions as (**d**). **d-g** are computed from 25 individual microtissues under each condition.

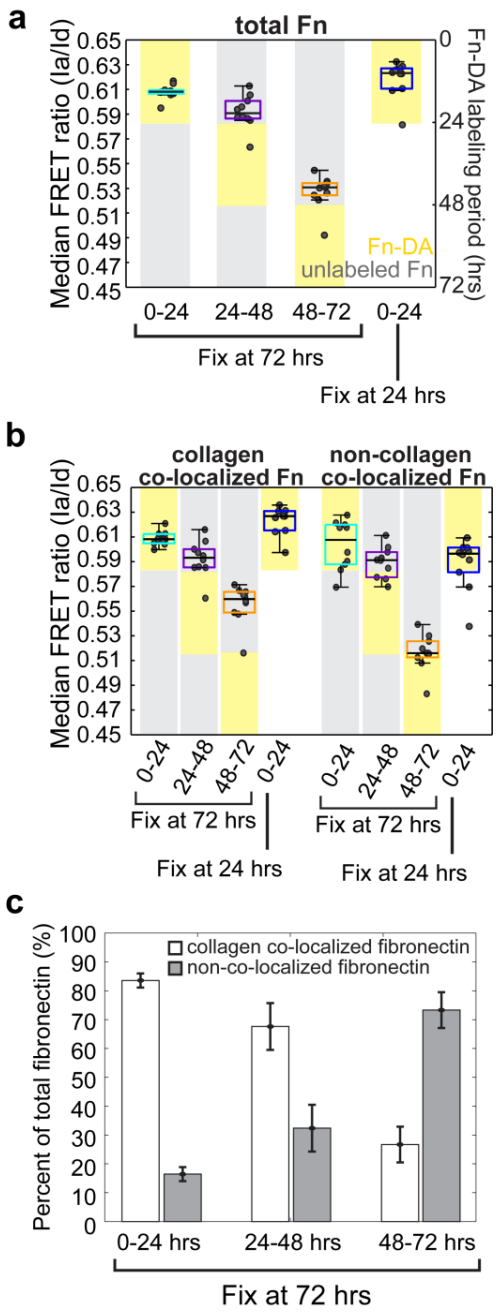

Figure 7.6: Fn-DA pulse-chase experiments and colocalization analysis. Fn-DA (yellow boxes) or unlabeled Fn (grey boxes) was present in culture for specified windows during tissue remodeling. Microtissues were then fixed at the indicated times and FRET signals recorded. **a)** Box and whiskers plot of the median FRET ratios (Ia/Id) for microtissues fixed after 72 hours in which Fn-DA was present between either 0-24, 24-48, or 48-72 hours or for microtissues fixed immediately after the first 24 hours of remodeling. **b)** Box and whiskers plot of the median FRET ratios (Ia/Id) showing either collagen-colocalized Fn or non-collagen-colocalized Fn for the same conditions as (**a**). **c)** Percent of Fn within microtissues assembled at the indicated increments that is either co-localized with collagen, or non-co-localized with collagen. Data from **a-c** are from 10 microtissues in each condition. Data from **b** are mean values ± SD.

CHAPTER 8: CONCLUSIONS AND FUTURE WORK

8.1 CONCLUSIONS

The mechanotransduction field has often been guided by the development of novel technologies. Optically transparent PA gels of tunable rigidity enabled researchers to study cells in highly controlled mechanical environments and revealed how substrate mechanics contribute to a diverse array of cell behaviors. Tracking the displacements of fiduciary markers within these hydrogels and converting these to mechanical stresses exerted by cells permitted the first "visualization" of cell-generated forces and permitted mathematical models of cell migration to be constructed (Carlsson and Sept 2008). However, to date, the vast majority of mechanotransduction studies have been restricted to investigating cells cultured on top of flat, planar substrates or within large-scale 3D systems utilizing mechanically complex, poorly defined ECMs. There is a quickly growing appreciation in many fields of biology, for the role of a 3D environment in maintaining cell phenotype and reproducing morphogenetic events (Debnath and Brugge 2005; Griffith and Swartz 2006; Pampaloni, Reynaud et al. 2007). As such, the general goal of this body of work was to generate novel tools to quantitatively study cell and tissue mechanics in 3D systems.

8.1.1 2.5D TFM reveals rotational moments about focal adhesions

In chapter 3 of this work, I extended traditional TFM approaches to measure the normal tractions exerted by cells (in addition to shear tractions) cultured on planar substrates. By developing a method with significantly improved spatial resolution and combining this method with live imaging of cytoskeletal and adhesion proteins, we demonstrated that cellular tractions are concentrated under the ends of actin stress fibers which terminate into focal adhesions (FAs). Importantly, we demonstrated that, in addition to shear loads, cells exert rotational moments about these adhesions, pulling vertically upward and pushing downward at the leading and trailing edges of the adhesion respectively. These moments are highly dynamic, shifting outward as the leading edge extends in migrating and spreading cells. In contrast to previous studies which hypothesized that the primary vertical forces exerted by cells were due to compression of the cell nucleus into the hydrogel (Hersen and Ladoux 2011), we found very little force exerted in these regions. We next developed several FEM models in order to explore how rotational moments can arise within the context of a very thin (~200 nm) cellular lamella. Our models suggested that a uniform shear load applied to the intracellular surface of a rigid adhesion (as could be applied by a contracting actin stress fiber) was insufficient to generate rotational moments of similar magnitude to what we observed experimentally. We hypothesized (and

confirmed using FEM), that increased rotation could be accomplished either by focusing the shear load to the leading edge of the adhesion or by incorporating a rigid ventral cortex into our models. These results are the first to highlight a characteristic, multi-dimensional force profile associated with adhesions. Our findings of a rotational moment introduces additional factors to consider when determining how forces could be propagated within an adhesion, including molecular compression of FA molecules at the trailing edge of the adhesion, integrin engagement with the ECM via downward forces, and a balance between contractility and torque that may regulate adhesion-mediated signaling differentially. In addition, the presence of rotational moments about adhesions should be of interested to future models of cell migration.

8.1.2 Synthetic hydrogels can be used to measure tractions exerted by cells fully encapsulated within a 3D matrix

While chapter 3 of this work revealed multidimensional tractions exerted about FAs, this method was still limited to measuring tractions exerted by cells cultured on planar surfaces. In chapter 4 of this work, I combined novel synthetic hydrogels developed within our lab (Miller, Shen et al. 2010) with finite element models to measure the mechanical tractions exerted by cells fully encapsulated within 3D matrices. Cells were encapsulated within photopolymerizable polyethylene glycol hydrogels that incorporate both MMP degradable domains and adhesive RGD sequences. Cells within these hydrogels adhered, spread and assumed similar morphologies to those observed in natural matrices such as collagen or fibrin. Because the hydrogels are linearly elastic and homogeneous, I was able to generate a finite element model of the hydrogel surrounding the cell at each time point. This model was then used to generate a discretized Green's function that related the displacement field within the hydrogel to tractions exerted at the cell-ECM interface. Using this method, we found that cells reach out thin protrusions, adhere to the surrounding matrix and pull back inward towards the cell body. The tips of these protrusions had higher tractions than the rest of the cell and were responsive to changes in the mechanics of the surrounding hydrogel. These results suggest then that the tips of these extensions might be hubs for FA based mechanosensitive signaling in 3D. Interestingly, when we combined this method with time-lapse, volumetric imaging of cells, we found that cellular extensions that were invading into the surrounding matrix still displayed a strong inward force, but that this force was concentrated 10-15 μm behind the leading tip. This suggests then that growing extensions must establish a "contractile waypoint," in front of which, they can then proceed to invade further. Importantly, this technique is not limited to measurements of single cells, but can be utilized to

measure the mechanical interactions of multiple neighboring cells as well as from multicellular structures such as tumor spheroids.

8.1.3 Fourier methods can be used to quantify the sensitivity and resolution of TFM measurements

Continuum based TFM approaches (i.e. those utilizing a continuous elastic substrate) are generally very difficult to characterize. This is because such techniques require relating an experimentally measured displacement field within the substrate to source tractions generated by the cell at the substrate boundary. This problem represents an ill-posed, inverse problem that is generally very sensitive to parameters such as the density and accuracy of the measured displacements. Even when these parameters are known, the recovery of source tractions will typically require regularization (or smoothing of the displacement field) to obtain a reasonable solution. As such, it is difficult to assess the ultimate accuracy of a given TFM measurement and thus have certainty in the biological conclusions drawn from such data. In chapter 5 of this work, I describe a simple, quantitative approach to fully characterize the sensitivity and spatial resolution of TFM measurements. By Fourier theory, any distribution of cellular tractions can be decomposed as an infinite superposition of sinusoidal functions with progressively increasing spatial frequency. Stated another way, by characterizing the response of a given TFM setup to sinusoidal loadings of progressively increasing frequency, we can gain insight into the resolution limits of the cellular tractions able to be recovered. As a proof of principle, we fully characterize the sensitivity and spatial resolution of both 2.5D and fully 3D TFM methods as a function of bead density and noise on the displacement measurements. We find that the resolution of traction measurements is inherently anisotropic. TFM measurements are roughly 2-fold less sensitive to shear tractions that are oriented parallel to the axis of spatial variation than to normal tractions or shear tractions oriented perpendicular to this axis. It is my hope that this simple approach will find use in future measurements of cell tractions and allow for complete reporting of the improvements or limitations afforded by new techniques.

8.1.4 Microfabricated tissue gauges can be used to measure tissue mechanics in 3D

While mechanically complex, encapsulations of cells in natural matrices such as fibrin, collagen, or Matrigel are widely used in biology. These matrices are able to be dynamically remodeled by cells and as such permit the *in vitro* recapitulation of morphogenetic and developmental phenomena. However, many implementations of these techniques utilize cultures

that are cm to mm in length scale, which introduces the possibility of diffusion limitations and can restrict the type of imaging that can be performed. Having worked with these larger constructs during my undergraduate studies, I was curious whether it would be possible to combine the microfabrication expertise and facilities available in our lab to miniaturize or even "micron"-ize encapsulations of cells in collagen gels. In chapter 6 of this work, I utilized multi-layer SU-8 photolithography to generate arrays of wells 800 x 400 x 250 μm deep. Within each well, we incorporated raised cantilevers that served to constrain the remodeling of the collagen matrix and report the forces generated by the microtissues. The entire chip was replicated out of a flexible, biocompatible PDMS using soft lithography, and a suspension of cells in type-I collagen was centrifuged into each well, thus generating large arrays of spatially isolated microtissues. By changing the mechanics of either the collagen matrix or the anchoring cantilevers, we found that we could alter cellular contractility and tissue stress. Interestingly, we found that levels of cytoskeletal proteins such as F-actin as well as ECM molecules such as Fn and tenascin correlated with the measured levels of mechanical stress in tissues. Finally, we combined our system with a bio-chemo-mechanical model of cellular contractility, pioneered by Vikram Deshpande and Bob McMeeking (Deshpande, McMeeking et al. 2006) to demonstrate how gradients in predicted levels of mechanical stress correlated with ECM patterning in microtissues of varying geometries. While initial studies focused primarily on fibroblast cells, we also demonstrated the possibility of utilizing cardiac cells to generate arrays of cardiac microtissues. By combining this approach with different matrices and cell types, it is my hope that this platform will enable studies of cell and tissue mechanics in a variety of biological contexts.

8.1.5 FRET-based biosensors can be combined with microfabricated tissue gauges to measure matrix conformation in 3D tissues

While much work has previously focused on how the stresses present at the integrin/ECM interface, and specifically at FAs alter cell phenotype, cell-generated tractions are also propagated throughout the surrounding ECM. In the extracellular environment, these forces can cause alterations to the structure and composition of the ECM molecules themselves. Viola Vogel's group has previously developed a FRET-based biosensor of Fn conformation that is capable of reporting these force induced structural changes; however, the majority of previous investigations utilizing this probe were restricted to cells on 2D surfaces. In chapter 7 of this work, I combined the microfabricated tissue gauges with a FRET-based biosensor of Fn

conformation. By utilizing these two approaches, we were able to spatially and temporally map Fn conformation during the remodeling of a collagen-based microtissue. We found that initially, Fn exists as a compact molecule that is adsorbed to the exogenous collagen scaffold. As the tissue remodels, fibrillar Fn is assembled at the tissue periphery where it is progressively unfolded by cell-generated forces. We found that two stable populations of Fn emerge within microtissues (compact/collagen adsorbed, and mechanically extended fibrillar) and that these populations could be spatially patterned in a manner that correlated with predicted levels of mechanical stress. In contrast to FAs, which are traditionally considered sensors of mechanical stress, the gradients in Fn matrix conformation present in our system appeared to serve as an "extracellular memory" whereby mechanical signals experienced by cells in a Fn matrix are dependent not only on the current stresses, but also on the history of previous ECM remodeling events that are reflected in accumulated molecular strains.

8.2 FUTURE DIRECTIONS

Many of the projects within this dissertation focused on developing new techniques capable of addressing long-standing challenges in the field of mechanotransduction. As such, the work performed in many sections represents a first step – development and characterization of a new technology. In addition to developing new methods, we also utilized these tools to perform new investigations into cell and tissue mechanics in 3D. However, these investigations represented only an initial starting point upon which future studies may build. Many intriguing findings arose from our initial implementations of the technologies developed here. Below, I will describe several avenues for future investigation that will harness the strengths of the methods developed above to significantly advance our understanding of cell and tissue mechanics.

8.2.1 Investigating the link between intracellular organization and 3D cell tractions

Our 2.5D TFM study revealed that even a relatively thin lamellar structure within cells was capable of generating significant torques against a planar ECM. Our FEM models suggest that such moments could be explained if a FA translates within a rigid ventral cortex. If this were true, then the ventral cortex should be under compression while the dorsal layers are under tension. All studies to date have suggested that cells exist in a state of pre-stressed tension (Shen, Datta et al. 2005; Kumar, Maxwell et al. 2006; Lu, Oswald et al. 2008). These studies utilized photoablation to sever individual stress fibers and demonstrated a viscoelastic retraction from the point of ablation. However, it is unclear whether these studies were ablating dorsal or ventral stress fibers, and further whether such a discrepancy could be made under current experimental setups. With future advances to laser photoablation systems, it may be possible to selectively ablate either the dorsal or ventral cortex within cells. Such studies could be combined with simultaneous measurements of 2.5D TFM to probe the 3D mechanics of cells. If the ventral cortex is under compression, then an increase or decrease in traction stress should accompany selective ablation of the ventral and dorsal cortex respectively. The presence of 3D forces at the cell-ECM interface suggests that these should arise from 3D stress distributions within the cells themselves. Actively measuring these distributions will require both careful experimental protocols and future technology development. Furthermore, the physiological implications of rotational moments existing about FAs have yet to be explored. The tension or compression experienced that the leading and trailing edges of adhesions could be a means to spatially control where new molecules add to or leave from adhesion plaques (Raz-Ben Aroush, Zaidel-Bar et al.

2008; Olberding, Thouless et al. 2010) or provide a spatially dependent signaling profile within an adhesion which has previously been assumed to be under uniform shear stress.

Even less is known about how the cytoskeleton and adhesions are organized to generate tractions in cells that are fully encapsulated within a 3D matrix. Recent studies have questioned the physical existence of FAs in 3D, suggesting instead that such molecules are distributed diffusely within the cytoplasm (Fraley, Feng et al. 2010). Although such findings may be due to over expression of fluorescently tagged molecules (Kubow and Horwitz 2010), the mechanisms that determine FA geometry, localization and dynamics within 3D settings remain largely unexplored. It is known for example that FA composition can vary dramatically between 2D and 3D settings (Cukierman, Pankov et al. 2001), but whether such compositional changes are triggered by dimensionality, topography or mechanical stresses is unknown. In 2D, it is thought that FA molecules serve as a type of clutch to transmit forces from retrograde actin flow to the substrate (Alexandrova, Arnold et al. 2008; Chan and Odde 2008; Aratyn-Schaus and Gardel 2010). However, it is unclear whether such a mechanism may exist in 3D. Nor is it known to what extent actin retrograde flow contributes to the traction profiles exerted by cells in 3D settings which often lack the typical lamellar architecture observed for cells on 2D substrates (Grinnell 2003). Current microscopy tools are not capable of generating high spatial and temporal resolution 3D images, and to date, this has limited studies of 3D mechanotransduction. Traditional confocal microscopes have poor axial resolution, which can be significantly degraded by imaging into thick samples. Moreover, such systems suffer from poor temporal resolution and excessive photodamage, which limits their applicability to live cell studies. Recent developments in light sheet microscopy promise to overcome these limitations (Keller, Schmidt et al. 2008; Planchon, Gao et al. 2011; Shao, Kner et al. 2011; Truong, Supatto et al. 2011). Future studies combining high-end 3D imaging with 3D TFM will greatly enhance our understanding of how 3D cytoskeletal and FA organization gives rise to cell-generated tractions in 3D.

8.2.2 Measuring 3D traction profiles within organotypic models of tissue morphogenesis

Much of the work to date in the field of mechanotransduction has investigated how mechanical stresses contributed to changes in the behavior of individual cells. While these studies have been instrumental in advancing our understanding of how cells sense and respond to forces, the vast majority of the cells in our bodies do not exist in isolation. Recent work has been performed to measure the stresses generated by multicellular monolayers of epithelial cells (Trepat, Wasserman et al. 2009; Tambe, Hardin et al. 2011). Interestingly, these studies reveal

that tractions can propagate through the ECM and within the monolayer to affect cells many hundreds of microns away. Moreover, they reveal characteristic push-pull patterns of cell-ECM tractions that emerge from the collective action of all cells within the monolayer. It would be relatively straightforward to adapt our 2.5D TFM method to measure the normal and shear forces present in this setting.

Perhaps more interesting would be to apply our fully 3D TFM method to organotypic models of tissue morphogenesis. Several models exist in which multicellular structures undergo dramatic morphogenetic movements when encapsulated within a 3D ECM. Epithelial cells within 3D Matrigel cultures proliferate to form hollow cysts. When treated with appropriate soluble factors, cells within these cysts sprout away from the core and form hollow tubules in a process similar to what occurs during the formation of ductile organs such as within the salivary glands, breast, and lungs (Campbell and Watson 2009). Similarly, endothelial cells can be cultured either as spheroids or on the surface of micron-scale beads and embedded within a 3D matrix. In the presence of VEGF, these cells sprout and form lumen-containing blood vessel structures in a model of angiogenesis (Nehls and Drenckhahn 1995). However, it is unknown how these morphogenetic movements are driven. Do cells within the stalk proliferate, expand and push the leading cells into the surrounding matrix? Or to cells at the tips of these sprouts actively pull the stalk cells forward? Or, are both of these mechanisms occurring within different sprouts at different times? These very basic questions could be answered by combining 3D TFM with 3D organotypic systems.

8.2.3 Utilizing uTUGs as a platform to study both healthy and diseased tissue models

Our initial studies with the uTUGs utilized NIH 3T3 cells as a model. These cells are an immortalized mouse fibroblast line and are commonly used in studies of migration and mechanotransduction due to their availability and ease of culture. However, the uTUG system can be expanded to many different cell and matrix types to generate models of both healthy and diseased tissues. Motivated by the fact that ischemic heart disease is a leading cause of death in developed countries (Mathers, Bernard et al. 2008), we recently combined the uTUG platform with neonatal rat cardiomyocytes to generate hundreds of microscale heart tissues on a chip (Boudou, Legant et al. 2012). Carbon electrodes were incorporated at the periphery of the chip to permit electrical stimulation and pacing, and both static (diastolic) and stimulated (systolic) forces were measured by monitoring post deflections. Most importantly, this system provides reproducible contractile phenotyping that is virtually absent in 2D culture models and permits

quantitative 3D imaging of cardiac maturation and organization. These same attributes will likely provide valuable opportunities to elucidate how biomechanical, electrical, biochemical, and genetic/epigenetic cues modulate the differentiation and maturation of stem cells into cardiac tissues. Future studies that combine stem cell differentiation and microtissue engineering could pave the way to the production of high-quality functional myocardium from stem cells, opening an exciting avenue for the treatment of damaged heart tissue.

8.2.4 uTUGs for high-throughput combinatorial screens of mechanical and soluble factors

Studies of cell mechanics and mechanotransduction have emerged as an exciting avenue for investigation, and it is now well appreciated that mechanical inputs contribute to a vast array of biochemical functions. Many of these findings have been drawn from experiments that permit careful and independent modulation of mechanical factors including substrate rigidity, topology, and dimensionality. However, while such systems are essential for teasing out specific effects within a complex system, one must also keep in mind that ultimately, our findings must occur within the context of the human body. While mechanical factors are ever present in biology, understanding the extent to which such factors are dominant or secondary to the plethora of other inputs cells experience will be essential for translating our findings into clinically relevant therapies. Numerous studies have identified the ability of either soluble or mechanical factors to modulate cell phenotypes such as proliferation, matrix synthesis and differentiation (Gospodarowicz 1974; Chen, Mrksich et al. 1997; Leask and Abraham 2004; Engler, Sen et al. 2006; Gupta and Grande-Allen 2006). Traditionally, these two inputs have been studied independently by altering substrate mechanics while keeping soluble stimuli constant or vice versa. While these studies have been critical in identifying the *potential* for a given input to modulate cell behavior, the interplay between soluble and mechanical factors has not been closely investigated. It is currently unclear to what extent mechanical or soluble inputs will dominate when opposing signals are presented or to what extent they may synergize with complementary signals. Combining microfluidic networks with uTUG arrays could permit combinatorial modulation of soluble and mechanical factors and provide an approach to address such questions. Such a platform would likely be widely applicable to study the combinatorial effects of both soluble and mechanical factors within many different tissue models.

8.2.5 Future tool developments

While the extensions listed above have focused primarily on applying the tools developed as part of this dissertation for studies of cell biology, many exciting studies could also be enabled by improvements or modifications to our current methods. For example, our implementation of 3D TFM required that cells be cultured within a continuous elastic 3D matrix. However, the topology of the ECM surrounding many cells within our body is not continuous, but rather fibrillar. While natural matrices such as collagen or fibrin mimic this fibrillar architecture, the mechanics of such matrices are too complex to permit high resolution measurements of cell-generated tractions. Synthetic electrospun matrices may offer an alternative. These systems permit both careful control over the fiber diameter and spacing as well as fiber mechanics. In theory, it should be possible to adapt the discretized Green's function approach that we utilized to measure 3D tractions within continuous matrices in order to measure the tractions exerted by cells within fibrillar electrospun matrices.

8.3 FINAL REMARKS

A few months ago, I was proposing some of these future projects as part of an interview and was asked an intriguing question. "At what stage in this project will you be done? When will you be able to say 'now we fully understand mechanotransduction'?" After several perplexing seconds, the only response that jumped to my mind was "well, of course the answer is never." This doesn't mean that our exertions are hopeless, but rather that we are working within a biological realm in which the vast majority of factors are unknown. Each small step we take in understanding how a specific cell type responds to a specific mechanical input under a given combination of soluble conditions fills in a piece of that puzzle, but the total number of pieces is unknown. Some pieces are larger and more important than others, but generally once we place a given piece, we realize that the picture we are building is bigger than we previously thought. However, within our pursuit, there will exist milestones at which we can begin to apply our primitive understanding to develop devices, therapies, and treatments capable of improving human health and quality of life. As engineers (and even as scientists in general) our responsibility is to recognize these opportunities when they arise.

BIBLIOGRAPHY

Abercrombie, M., J. E. Heaysman, et al. (1971). "The locomotion of fibroblasts in culture. IV. Electron microscopy of the leading lamella." Exp Cell Res **67**(2): 359-67.

Adachi, Y., T. Mio, et al. (1998). "Fibronectin production by cultured human lung fibroblasts in three-dimensional collagen gel culture." In Vitro Cell Dev Biol Anim **34**(3): 203-10.

Alexandrova, A. Y., K. Arnold, et al. (2008). "Comparative dynamics of retrograde actin flow and focal adhesions: formation of nascent adhesions triggers transition from fast to slow flow." PLoS One **3**(9): e3234.

Antia, M., G. Baneyx, et al. (2008). "Fibronectin in aging extracellular matrix fibrils is progressively unfolded by cells and elicits an enhanced rigidity response." Faraday Discuss **139**: 229-49; discussion 309-25, 419-20.

Aratyn-Schaus, Y. and M. L. Gardel (2010). "Transient frictional slip between integrin and the ECM in focal adhesions under myosin II tension." Curr Biol **20**(13): 1145-53.

Asnes, C. F., J. P. Marquez, et al. (2006). "Reconstitution of the Frank-Starling mechanism in engineered heart tissues." Biophys J **91**(5): 1800-10.

Balaban, N. Q., U. S. Schwarz, et al. (2001). "Force and focal adhesion assembly: a close relationship studied using elastic micropatterned substrates." Nat Cell Biol **3**(5): 466-72.

Baneyx, G., L. Baugh, et al. (2002). "Fibronectin extension and unfolding within cell matrix fibrils controlled by cytoskeletal tension." Proc Natl Acad Sci U S A **99**(8): 5139-43.

Barnhart, E. L., K. C. Lee, et al. (2011). "An adhesion-dependent switch between mechanisms that determine motile cell shape." PLoS Biol **9**(5): e1001059.

Baugh, L. and V. Vogel (2004). "Structural changes of fibronectin adsorbed to model surfaces probed by fluorescence resonance energy transfer." J Biomed Mater Res A **69**(3): 525-34.

Bazen, A. M. and S. H. Gerez (2002). "Systematic methods for the computation of the directional fields and singular points of fingerprints." IEEE Trans Pattern Anal Mach Intell: 905–919.

Bell, E., B. Ivarsson, et al. (1979). "Production of a tissue-like structure by contraction of collagen lattices by human fibroblasts of different proliferative potential in vitro." Proc Natl Acad Sci U S A **76**(3): 1274-8.

Beloussov, L. V., J. G. Dorfman, et al. (1975). "Mechanical stresses and morphological patterns in amphibian embryos." J Embryol Exp Morphol **34**(3): 559-74.

Beningo, K. A., M. Dembo, et al. (2001). "Nascent focal adhesions are responsible for the generation of strong propulsive forces in migrating fibroblasts." J Cell Biol **153**(4): 881-8.

Berk, B. C., K. Fujiwara, et al. (2007). "ECM remodeling in hypertensive heart disease." J Clin Invest **117**(3): 568-75.

Bershadsky, A., M. Kozlov, et al. (2006). "Adhesion-mediated mechanosensitivity: a time to experiment, and a time to theorize." Curr Opin Cell Biol **18**(5): 472-81.

Boucaut, J. C. and T. Darribere (1983). "Presence of fibronectin during early embryogenesis in amphibian Pleurodeles waltlii." Cell Differ **12**(2): 77-83.

Boudou, T., W. R. Legant, et al. (2012). "A Microfabricated Platform to Measure and Manipulate the Mechanics of Engineered Cardiac Microtissues." Tissue Eng Part A.

Boussinesq, J. (1885). Application des potentiels à l'étude de l'équilibre et du mouvement des solides élastiques. Paris, Gauthier-Villars.

Bower, A. F. (2009). Applied Mechanics of Solids. Boca Raton, CRC Press.

Burridge, K. and M. Chrzanowska-Wodnicka (1996). "Focal adhesions, contractility, and signaling." Annu Rev Cell Dev Biol **12**: 463-518.

Butler, J. P., I. M. Tolic-Norrelykke, et al. (2002). "Traction fields, moments, and strain energy that cells exert on their surroundings." Am J Physiol Cell Physiol **282**(3): C595-605.

Cai, Y., O. Rossier, et al. (2010). "Cytoskeletal coherence requires myosin-IIA contractility." J Cell Sci **123**(Pt 3): 413-23.

Campbell, J. J. and C. J. Watson (2009). "Three-dimensional culture models of mammary gland." Organogenesis **5**(2): 43-9.

Carlsson, A. E. and D. Sept (2008). "Mathematical modeling of cell migration." Methods Cell Biol **84**: 911-37.

Cerruti, V. (1882). Acc. lincei mem.fis. mat. Roma.

Chabria, M., S. Hertig, et al. (2010). "Stretching fibronectin fibres disrupts binding of bacterial adhesins by physically destroying an epitope." Nat Commun **1**: 135.

Chan, C. E. and D. J. Odde (2008). "Traction dynamics of filopodia on compliant substrates." Science **322**(5908): 1687-91.

Chen, C. S. (2008). "Mechanotransduction - a field pulling together?" J Cell Sci **121**(Pt 20): 3285-92.

Chen, C. S. and D. E. Ingber (1999). "Tensegrity and mechanoregulation: from skeleton to cytoskeleton." Osteoarthritis Cartilage **7**(1): 81-94.

Chen, C. S., M. Mrksich, et al. (1997). "Geometric control of cell life and death." Science **276**(5317): 1425-8.

Chiquet-Ehrismann, R., M. Tannheimer, et al. (1994). "Tenascin-C expression by fibroblasts is elevated in stressed collagen gels." J Cell Biol **127**(6 Pt 2): 2093-101.

Choi, C. K., M. Vicente-Manzanares, et al. (2008). "Actin and alpha-actinin orchestrate the assembly and maturation of nascent adhesions in a myosin II motor-independent manner." Nat Cell Biol **10**(9): 1039-50.

Choquet, D., D. P. Felsenfeld, et al. (1997). "Extracellular matrix rigidity causes strengthening of integrin-cytoskeleton linkages." Cell **88**(1): 39-48.

Chrzanowska-Wodnicka, M. and K. Burridge (1996). "Rho-stimulated contractility drives the formation of stress fibers and focal adhesions." J Cell Biol **133**(6): 1403-15.

Cukierman, E., R. Pankov, et al. (2001). "Taking cell-matrix adhesions to the third dimension." Science **294**(5547): 1708-12.

Davenport, E. A. and P. Nettesheim (1996). "Type I collagen gel modulates extracellular matrix synthesis and deposition by tracheal epithelial cells." Exp Cell Res **223**(1): 155-62.

Deakin, N. O. and C. E. Turner (2008). "Paxillin comes of age." J Cell Sci **121**(Pt 15): 2435-44.

Debnath, J. and J. S. Brugge (2005). "Modelling glandular epithelial cancers in three-dimensional cultures." Nat Rev Cancer **5**(9): 675-88.

Delanoe-Ayari, H., J. P. Rieu, et al. (2010). "4D traction force microscopy reveals asymmetric cortical forces in migrating Dictyostelium cells." Phys Rev Lett **105**(24): 248103.

Dembo, M., T. Oliver, et al. (1996). "Imaging the traction stresses exerted by locomoting cells with the elastic substratum method." Biophys J **70**(4): 2008-22.

Dembo, M. and Y. L. Wang (1999). "Stresses at the cell-to-substrate interface during locomotion of fibroblasts." Biophys J **76**(4): 2307-16.

Deshpande, V. S., R. M. McMeeking, et al. (2006). "A bio-chemo-mechanical model for cell contractility." Proc Natl Acad Sci U S A **103**(38): 14015-20.

Discher, D. E., P. Janmey, et al. (2005). "Tissue cells feel and respond to the stiffness of their substrate." Science **310**(5751): 1139-43.

du Roure, O., A. Saez, et al. (2005). "Force mapping in epithelial cell migration." Proc Natl Acad Sci U S A **102**(7): 2390-5.

Dubin-Thaler, B. J., G. Giannone, et al. (2004). "Nanometer analysis of cell spreading on matrix-coated surfaces reveals two distinct cell states and STEPs." Biophys J **86**(3): 1794-806.

Dzamba, B. J., K. R. Jakab, et al. (2009). "Cadherin adhesion, tissue tension, and noncanonical Wnt signaling regulate fibronectin matrix organization." Dev Cell **16**(3): 421-32.

Edwards, K. A. and D. P. Kiehart (1996). "Drosophila nonmuscle myosin II has multiple essential roles in imaginal disc and egg chamber morphogenesis." Development **122**(5): 1499-511.

Elbert, D. L. and J. A. Hubbell (2001). "Conjugate addition reactions combined with free-radical cross-linking for the design of materials for tissue engineering." Biomacromolecules **2**(2): 430-41.

Engler, A. J., C. Carag-Krieger, et al. (2008). "Embryonic cardiomyocytes beat best on a matrix with heart-like elasticity: scar-like rigidity inhibits beating." J Cell Sci **121**(Pt 22): 3794-802.

Engler, A. J., S. Sen, et al. (2006). "Matrix elasticity directs stem cell lineage specification." Cell **126**(4): 677-89.

Eschenhagen, T., C. Fink, et al. (1997). "Three-dimensional reconstitution of embryonic cardiomyocytes in a collagen matrix: a new heart muscle model system." Faseb J **11**(8): 683-94.

Farge, E. (2003). "Mechanical induction of Twist in the Drosophila foregut/stomodeal primordium." Curr Biol **13**(16): 1365-77.

Foulds IG, P. M. (2006). "A planar self-sacrificial multilayer SU-8-based MEMS process utilizing a UV-blocking layer for the creation of freely moving parts." Journal of Micromechanics and Microengineering **16**: 2109.

Fournier, M. F., R. Sauser, et al. (2010). "Force transmission in migrating cells." J Cell Biol **188**(2): 287-97.

Fraley, S. I., Y. Feng, et al. (2010). "A distinctive role for focal adhesion proteins in three-dimensional cell motility." Nat Cell Biol **12**(6): 598-604.

Franck, C., S. A. Maskarinec, et al. (2011). "Three-dimensional traction force microscopy: a new tool for quantifying cell-matrix interactions." PLoS One **6**(3): e17833.

Friedl, P. and D. Gilmour (2009). "Collective cell migration in morphogenesis, regeneration and cancer." Nat Rev Mol Cell Biol **10**(7): 445-57.

Fu, J., Y. K. Wang, et al. (2010). "Mechanical regulation of cell function with geometrically modulated elastomeric substrates." Nat Methods **7**(9): 733-6.

Fung, Y. C. (1967). "Elasticity of soft tissues in simple elongation." Am J Physiol **213**(6): 1532-44.

Furchgott, R. F. and P. M. Vanhoutte (1989). "Endothelium-derived relaxing and contracting factors." Faseb J **3**(9): 2007-18.

Gao, L., R. McBeath, et al. (2010). "Stem cell shape regulates a chondrogenic versus myogenic fate through Rac1 and N-cadherin." Stem Cells **28**(3): 564-72.

Gao, Y. X. and M. L. Kilfoil (2009). "Accurate detection and complete tracking of large populations of features in three dimensions." Optics Express **17**(6): 4685-4704.

Garcia, A. J., M. D. Vega, et al. (1999). "Modulation of cell proliferation and differentiation through substrate-dependent changes in fibronectin conformation." Mol Biol Cell **10**(3): 785-98.

Gardel, M. L., B. Sabass, et al. (2008). "Traction stress in focal adhesions correlates biphasically with actin retrograde flow speed." J Cell Biol **183**(6): 999-1005.

Gardel, M. L., I. C. Schneider, et al. (2010). "Mechanical Integration of Actin and Adhesion Dynamics in Cell Migration." Annu Rev Cell Dev Biol.

Geiger, B., J. P. Spatz, et al. (2009). "Environmental sensing through focal adhesions." Nat Rev Mol Cell Biol **10**(1): 21-33.

George, E. L., E. N. Georges-Labouesse, et al. (1993). "Defects in mesoderm, neural tube and vascular development in mouse embryos lacking fibronectin." Development **119**(4): 1079-91.

Georges, P. C., J. J. Hui, et al. (2007). "Increased stiffness of the rat liver precedes matrix deposition: implications for fibrosis." Am J Physiol Gastrointest Liver Physiol **293**(6): G1147-54.

Giannone, G., B. J. Dubin-Thaler, et al. (2007). "Lamellipodial actin mechanically links myosin activity with adhesion-site formation." Cell **128**(3): 561-75.

Gilbert, P. M., K. L. Havenstrite, et al. (2010). "Substrate elasticity regulates skeletal muscle stem cell self-renewal in culture." Science **329**(5995): 1078-81.

Gobin, A. S. and J. L. West (2002). "Cell migration through defined, synthetic ECM analogs." Faseb J **16**(7): 751-3.

Gospodarowicz, D. (1974). "Localisation of a fibroblast growth factor and its effect alone and with hydrocortisone on 3T3 cell growth." Nature **249**(453): 123-7.

Grashoff, C., B. D. Hoffman, et al. (2010). "Measuring mechanical tension across vinculin reveals regulation of focal adhesion dynamics." Nature **466**(7303): 263-6.

Griffith, L. G. and M. A. Swartz (2006). "Capturing complex 3D tissue physiology in vitro." Nat Rev Mol Cell Biol **7**(3): 211-24.

Grinnell, F. (1994). "Fibroblasts, myofibroblasts, and wound contraction." J Cell Biol **124**(4): 401-4.

Grinnell, F. (2003). "Fibroblast biology in three-dimensional collagen matrices." Trends Cell Biol **13**(5): 264-9.

Grinnell, F., R. E. Billingham, et al. (1981). "Distribution of fibronectin during wound healing in vivo." J Invest Dermatol **76**(3): 181-9.

Grinnell, F. and W. M. Petroll (2010). "Cell motility and mechanics in three-dimensional collagen matrices." Annu Rev Cell Dev Biol **26**: 335-61.

Gumbiner, B. M. (1996). "Cell adhesion: the molecular basis of tissue architecture and morphogenesis." Cell **84**(3): 345-57.

Gupta, V. and K. J. Grande-Allen (2006). "Effects of static and cyclic loading in regulating extracellular matrix synthesis by cardiovascular cells." Cardiovasc Res **72**(3): 375-83.

Halliday, N. L. and J. J. Tomasek (1995). "Mechanical properties of the extracellular matrix influence fibronectin fibril assembly in vitro." Exp Cell Res **217**(1): 109-17.

Hansen, P. C. (2001). The L-Curve and its use in the numerical treatment of inverse problems. Computational Inverse Problems in electrocardiography (Advances in Computational Bioengineering). P. R. Johnston. Southampton, WIT Press. **5:** 119-142.

Hansen, P. C. (2007). "Regularization Tools Version 4.0 for Matlab 7.3." Numerical Algorithms **46**(2): 189-194.

Harris, A. K., P. Wild, et al. (1980). "Silicone rubber substrata: a new wrinkle in the study of cell locomotion." Science **208**(4440): 177-9.
Hersen, P. and B. Ladoux (2011). "Biophysics: Push it, pull it." Nature **470**(7334): 340-1.
Hill, A. (1938). "The heat of shortening and the dynamic constants of muscle." Proceedings of the Royal Society of London. Series B, Biological Sciences **126**(843): 136-195.
Hill, A. V. (1922). "The maximum work and mechanical efficiency of human muscles, and their most economical speed." J Physiol **56**(1-2): 19-41.
Hinz, B., D. Mastrangelo, et al. (2001). "Mechanical tension controls granulation tissue contractile activity and myofibroblast differentiation." Am J Pathol **159**(3): 1009-20.
Hocking, D. C., J. Sottile, et al. (2000). "Stimulation of integrin-mediated cell contractility by fibronectin polymerization." J Biol Chem **275**(14): 10673-82.
Hoffman, B. D., C. Grashoff, et al. (2011). "Dynamic molecular processes mediate cellular mechanotransduction." Nature **475**(7356): 316-23.
Huang, S., C. S. Chen, et al. (1998). "Control of cyclin D1, p27(Kip1), and cell cycle progression in human capillary endothelial cells by cell shape and cytoskeletal tension." Mol Biol Cell **9**(11): 3179-93.
Huebsch, N., P. R. Arany, et al. (2010). "Harnessing traction-mediated manipulation of the cell/matrix interface to control stem-cell fate." Nat Mater **9**(6): 518-26.
Hur, S. S., Y. Zhao, et al. (2009). "Live Cells Exert 3-Dimensional Traction Forces on Their Substrata." Cell Mol Bioeng **2**(3): 425-436.
Hutson, M. S., Y. Tokutake, et al. (2003). "Forces for morphogenesis investigated with laser microsurgery and quantitative modeling." Science **300**(5616): 145-9.
Huxley, H. E. (1969). "The mechanism of muscular contraction." Science **164**(3886): 1356-65.
Hwang, N. S., S. Varghese, et al. (2011). "Regulation of osteogenic and chondrogenic differentiation of mesenchymal stem cells in PEG-ECM hydrogels." Cell Tissue Res **344**(3): 499-509.
Hynes, R. O. (1992). "Integrins: versatility, modulation, and signaling in cell adhesion." Cell **69**(1): 11-25.
Hynes, R. O. (2002). "Integrins: bidirectional, allosteric signaling machines." Cell **110**(6): 673-87.
Ingber, D. (1991). "Integrins as mechanochemical transducers." Curr Opin Cell Biol **3**(5): 841-8.
Ingber, D. E. (2003). "Mechanobiology and diseases of mechanotransduction." Ann Med **35**(8): 564-77.
Isenberg, G., P. C. Rathke, et al. (1976). "Cytoplasmic actomyosin fibrils in tissue culture cells: direct proof of contractility by visualization of ATP-induced contraction in fibrils isolated by laser micro-beam dissection." Cell Tissue Res **166**(4): 427-43.
Jaalouk, D. E. and J. Lammerding (2009). "Mechanotransduction gone awry." Nat Rev Mol Cell Biol **10**(1): 63-73.
Jannat, R. A., M. Dembo, et al. (2011). "Traction forces of neutrophils migrating on compliant substrates." Biophys J **101**(3): 575-84.
Kadler, K. E., A. Hill, et al. (2008). "Collagen fibrillogenesis: fibronectin, integrins, and minor collagens as organizers and nucleators." Curr Opin Cell Biol **20**(5): 495-501.
Kanchanawong, P., G. Shtengel, et al. (2010). "Nanoscale architecture of integrin-based cell adhesions." Nature **468**(7323): 580-4.
Keller, P. J., A. D. Schmidt, et al. (2008). "Reconstruction of zebrafish early embryonic development by scanned light sheet microscopy." Science **322**(5904): 1065-9.

Keller, R., L. A. Davidson, et al. (2003). "How we are shaped: the biomechanics of gastrulation." Differentiation **71**(3): 171-205.

Kelley, C., P. D'Amore, et al. (1987). "Microvascular pericyte contractility in vitro: comparison with other cells of the vascular wall." J Cell Biol **104**(3): 483-90.

Khan, Z. A., B. M. Chan, et al. (2005). "EDB fibronectin and angiogenesis -- a novel mechanistic pathway." Angiogenesis **8**(3): 183-96.

Klein, E. A., Y. Yung, et al. (2007). "Cell adhesion, cellular tension, and cell cycle control." Methods Enzymol **426**: 155-75.

Klotzsch, E., M. L. Smith, et al. (2009). "Fibronectin forms the most extensible biological fibers displaying switchable force-exposed cryptic binding sites." Proc Natl Acad Sci U S A **106**(43): 18267-72.

Kolodney, M. S. and E. L. Elson (1993). "Correlation of myosin light chain phosphorylation with isometric contraction of fibroblasts." J Biol Chem **268**(32): 23850-5.

Kolodney, M. S. and E. L. Elson (1995). "Contraction due to microtubule disruption is associated with increased phosphorylation of myosin regulatory light chain." Proc Natl Acad Sci U S A **92**(22): 10252-6.

Kolodney, M. S. and R. B. Wysolmerski (1992). "Isometric contraction by fibroblasts and endothelial cells in tissue culture: a quantitative study." J Cell Biol **117**(1): 73-82.

Kong, F., A. J. Garcia, et al. (2009). "Demonstration of catch bonds between an integrin and its ligand." J Cell Biol **185**(7): 1275-84.

Kong, H. J., T. R. Polte, et al. (2005). "FRET measurements of cell-traction forces and nano-scale clustering of adhesion ligands varied by substrate stiffness." Proc Natl Acad Sci U S A **102**(12): 4300-5.

Krieg, M., Y. Arboleda-Estudillo, et al. (2008). "Tensile forces govern germ-layer organization in zebrafish." Nat Cell Biol **10**(4): 429-36.

Kubow, K. E. and A. R. Horwitz (2010). "Reducing background fluorescence reveals adhesions in 3D matrices." Nat Cell Biol **13**(1): 3-5; author reply 5-7.

Kubow, K. E., E. Klotzsch, et al. (2009). "Crosslinking of cell-derived 3D scaffolds up-regulates the stretching and unfolding of new extracellular matrix assembled by reseeded cells." Integr Biol (Camb) **1**(11-12): 635-48.

Kumar, S., I. Z. Maxwell, et al. (2006). "Viscoelastic retraction of single living stress fibers and its impact on cell shape, cytoskeletal organization, and extracellular matrix mechanics." Biophys J **90**(10): 3762-73.

Kuo, J. C., X. Han, et al. (2010). "Analysis of the myosin-II-responsive focal adhesion proteome reveals a role for beta-Pix in negative regulation of focal adhesion maturation." Nat Cell Biol **13**(4): 383-93.

Laevsky, G. and D. A. Knecht (2003). "Cross-linking of actin filaments by myosin II is a major contributor to cortical integrity and cell motility in restrictive environments." J Cell Sci **116**(Pt 18): 3761-70.

Lan, M. A., C. A. Gersbach, et al. (2005). "Myoblast proliferation and differentiation on fibronectin-coated self assembled monolayers presenting different surface chemistries." Biomaterials **26**(22): 4523-31.

Lauffenburger, D. A. and A. F. Horwitz (1996). "Cell migration: a physically integrated molecular process." Cell **84**(3): 359-69.

Leask, A. and D. J. Abraham (2004). "TGF-beta signaling and the fibrotic response." Faseb J **18**(7): 816-27.

Lee, J. Y. and B. Goldstein (2003). "Mechanisms of cell positioning during C. elegans gastrulation." Development **130**(2): 307-20.
Lee, K. M., K. Y. Tsai, et al. (1998). "Extracellular matrix and pulmonary hypertension: control of vascular smooth muscle cell contractility." Am J Physiol **274**(1 Pt 2): H76-82.
Lee, S. E., R. D. Kamm, et al. (2007). "Force-induced activation of talin and its possible role in focal adhesion mechanotransduction." J Biomech **40**(9): 2096-106.
Legant, W. R., J. S. Miller, et al. (2010). "Measurement of mechanical tractions exerted by cells in three-dimensional matrices." Nat Methods **7**(12): 969-71.
Legant, W. R., A. Pathak, et al. (2009). "Microfabricated tissue gauges to measure and manipulate forces from 3D microtissues." Proc Natl Acad Sci U S A **106**(25): 10097-102.
Lemmon, C. A., C. S. Chen, et al. (2009). "Cell traction forces direct fibronectin matrix assembly." Biophys J **96**(2): 729-38.
Levental, K. R., H. Yu, et al. (2009). "Matrix crosslinking forces tumor progression by enhancing integrin signaling." Cell **139**(5): 891-906.
Little, W. C., R. Schwartlander, et al. (2009). "Stretched extracellular matrix proteins turn fouling and are functionally rescued by the chaperones albumin and casein." Nano Lett **9**(12): 4158-67.
Liu, Y., R. Yanai, et al. (2006). "Promotion by fibronectin of collagen gel contraction mediated by human corneal fibroblasts." Exp Eye Res **83**(5): 1196-204.
Lo, C. M., H. B. Wang, et al. (2000). "Cell movement is guided by the rigidity of the substrate." Biophys J **79**(1): 144-52.
Lu, L., S. J. Oswald, et al. (2008). "Mechanical properties of actin stress fibers in living cells." Biophys J **95**(12): 6060-71.
Lutolf, M. P. and J. A. Hubbell (2005). "Synthetic biomaterials as instructive extracellular microenvironments for morphogenesis in tissue engineering." Nat Biotechnol **23**(1): 47-55.
Mao, Y. and J. E. Schwarzbauer (2005). "Fibronectin fibrillogenesis, a cell-mediated matrix assembly process." Matrix Biol **24**(6): 389-99.
Marquez, J. P., G. M. Genin, et al. (2005). "The relationship between cell and tissue strain in three-dimensional bio-artificial tissues." Biophys J **88**(2): 778-89.
Maskarinec, S. A., C. Franck, et al. (2009). "Quantifying cellular traction forces in three dimensions." Proc Natl Acad Sci U S A **106**(52): 22108-13.
Mathers, C. D., C. Bernard, et al. (2008). Global Burden of Disease: Data Sources, Methods and Results. Geneva, Switzerland, World Health Organization.
McBeath, R., D. M. Pirone, et al. (2004). "Cell shape, cytoskeletal tension, and RhoA regulate stem cell lineage commitment." Dev Cell **6**(4): 483-95.
Midwood, K. S., L. V. Williams, et al. (2004). "Tissue repair and the dynamics of the extracellular matrix." Int J Biochem Cell Biol **36**(6): 1031-7.
Miller, J. S., C. J. Shen, et al. (2010). "Bioactive hydrogels made from step-growth derived PEG-peptide macromers." Biomaterials **31**(13): 3736-43.
Mitra, S. K., D. A. Hanson, et al. (2005). "Focal adhesion kinase: in command and control of cell motility." Nat Rev Mol Cell Biol **6**(1): 56-68.
Montesano, R., L. Orci, et al. (1983). "In vitro rapid organization of endothelial cells into capillary-like networks is promoted by collagen matrices." J Cell Biol **97**(5 Pt 1): 1648-52.
Mosher, D. F., F. J. Fogerty, et al. (1991). "Assembly of fibronectin into extracellular matrix." Ann N Y Acad Sci **614**: 167-80.

Munevar, S., Y. Wang, et al. (2001). "Traction force microscopy of migrating normal and H-ras transformed 3T3 fibroblasts." Biophys J **80**(4): 1744-57.

Nakagawa, S., P. Pawelek, et al. (1989). "Extracellular matrix organization modulates fibroblast growth and growth factor responsiveness." Exp Cell Res **182**(2): 572-82.

Nehls, V. and D. Drenckhahn (1995). "A novel, microcarrier-based in vitro assay for rapid and reliable quantification of three-dimensional cell migration and angiogenesis." Microvasc Res **50**(3): 311-22.

Nelson, C. M., R. P. Jean, et al. (2005). "Emergent patterns of growth controlled by multicellular form and mechanics." Proc Natl Acad Sci U S A **102**(33): 11594-9.

O'Brien, L. E., M. M. Zegers, et al. (2002). "Opinion: Building epithelial architecture: insights from three-dimensional culture models." Nat Rev Mol Cell Biol **3**(7): 531-7.

Olberding, J. E., M. D. Thouless, et al. (2010). "The non-equilibrium thermodynamics and kinetics of focal adhesion dynamics." PLoS One **5**(8): e12043.

Pampaloni, F., E. G. Reynaud, et al. (2007). "The third dimension bridges the gap between cell culture and live tissue." Nat Rev Mol Cell Biol **8**(10): 839-45.

Parsons, J. T., A. R. Horwitz, et al. (2010). "Cell adhesion: integrating cytoskeletal dynamics and cellular tension." Nat Rev Mol Cell Biol **11**(9): 633-43.

Paszek, M. J., N. Zahir, et al. (2005). "Tensional homeostasis and the malignant phenotype." Cancer Cell **8**(3): 241-54.

Patel, P. N., A. S. Gobin, et al. (2005). "Poly(ethylene glycol) hydrogel system supports preadipocyte viability, adhesion, and proliferation." Tissue Eng **11**(9-10): 1498-505.

Pathak, A., V. S. Deshpande, et al. (2008). "The simulation of stress fibre and focal adhesion development in cells on patterned substrates." J R Soc Interface **5**(22): 507-24.

Pathak, A. and S. Kumar (2011). "Biophysical regulation of tumor cell invasion: moving beyond matrix stiffness." Integr Biol (Camb) **3**(4): 267-78.

Pelham, R. J., Jr. and Y. Wang (1997). "Cell locomotion and focal adhesions are regulated by substrate flexibility." Proc Natl Acad Sci U S A **94**(25): 13661-5.

Pelham, R. J., Jr. and Y. Wang (1999). "High resolution detection of mechanical forces exerted by locomoting fibroblasts on the substrate." Mol Biol Cell **10**(4): 935-45.

Planchon, T. A., L. Gao, et al. (2011). "Rapid three-dimensional isotropic imaging of living cells using Bessel beam plane illumination." Nat Methods **8**(5): 417-23.

Ponti, A., M. Machacek, et al. (2004). "Two distinct actin networks drive the protrusion of migrating cells." Science **305**(5691): 1782-6.

Raeber, G. P., M. P. Lutolf, et al. (2005). "Molecularly engineered PEG hydrogels: a novel model system for proteolytically mediated cell migration." Biophys J **89**(2): 1374-88.

Ramanujan, S., A. Pluen, et al. (2002). "Diffusion and convection in collagen gels: implications for transport in the tumor interstitium." Biophys J **83**(3): 1650-60.

Rayment, I., H. M. Holden, et al. (1993). "Structure of the actin-myosin complex and its implications for muscle contraction." Science **261**(5117): 58-65.

Raz-Ben Aroush, D., R. Zaidel-Bar, et al. (2008). "Temporal evolution of cell focal adhesions: experimental observations and shear stress profiles." Soft Matter **4**(12): 2410-2417.

Rozario, T., B. Dzamba, et al. (2009). "The physical state of fibronectin matrix differentially regulates morphogenetic movements in vivo." Dev Biol **327**(2): 386-98.

Sabass, B., M. L. Gardel, et al. (2008). "High resolution traction force microscopy based on experimental and computational advances." Biophys J **94**(1): 207-20.

Saez, A., A. Buguin, et al. (2005). "Is the mechanical activity of epithelial cells controlled by deformations or forces?" Biophys J **89**(6): L52-4.

Salmeron-Sanchez, M., P. Rico, et al. (2011). "Role of material-driven fibronectin fibrillogenesis in cell differentiation." Biomaterials **32**(8): 2099-105.

Sawada, Y., M. Tamada, et al. (2006). "Force sensing by mechanical extension of the Src family kinase substrate p130Cas." Cell **127**(5): 1015-26.

Schwartz, M. A. (2010). "Integrins and extracellular matrix in mechanotransduction." Cold Spring Harb Perspect Biol **2**(12): a005066.

Schwarz, U. S., N. Q. Balaban, et al. (2002). "Calculation of forces at focal adhesions from elastic substrate data: the effect of localized force and the need for regularization." Biophys J **83**(3): 1380-94.

Schwarzbauer, J. E., R. S. Patel, et al. (1987). "Multiple sites of alternative splicing of the rat fibronectin gene transcript." Embo J **6**(9): 2573-80.

Sechler, J. L. and J. E. Schwarzbauer (1997). "Coordinated regulation of fibronectin fibril assembly and actin stress fiber formation." Cell Adhes Commun **4**(6): 413-24.

Sellers, J. R. (1991). "Regulation of cytoplasmic and smooth muscle myosin." Curr Opin Cell Biol **3**(1): 98-104.

Shao, L., P. Kner, et al. (2011). "Super-resolution 3D microscopy of live whole cells using structured illumination." Nat Methods **8**(12): 1044-6.

Shen, N., D. Datta, et al. (2005). "Ablation of cytoskeletal filaments and mitochondria in live cells using a femtosecond laser nanoscissor." Mech Chem Biosyst **2**(1): 17-25.

Shroff, H., C. G. Galbraith, et al. (2007). "Dual-color superresolution imaging of genetically expressed probes within individual adhesion complexes." Proc Natl Acad Sci U S A **104**(51): 20308-13.

Sieminski, A. L., R. P. Hebbel, et al. (2004). "The relative magnitudes of endothelial force generation and matrix stiffness modulate capillary morphogenesis in vitro." Exp Cell Res **297**(2): 574-84.

Smith, M. L., D. Gourdon, et al. (2007). "Force-induced unfolding of fibronectin in the extracellular matrix of living cells." PLoS Biol **5**(10): e268.

Somogyi, K. and P. Rorth (2004). "Evidence for tension-based regulation of Drosophila MAL and SRF during invasive cell migration." Dev Cell **7**(1): 85-93.

Sottile, J. and D. C. Hocking (2002). "Fibronectin polymerization regulates the composition and stability of extracellular matrix fibrils and cell-matrix adhesions." Mol Biol Cell **13**(10): 3546-59.

Sottile, J., F. Shi, et al. (2007). "Fibronectin-dependent collagen I deposition modulates the cell response to fibronectin." Am J Physiol Cell Physiol **293**(6): C1934-46.

Stopak, D. and A. K. Harris (1982). "Connective tissue morphogenesis by fibroblast traction. I. Tissue culture observations." Dev Biol **90**(2): 383-98.

Stopak, D., N. K. Wessells, et al. (1985). "Morphogenetic rearrangement of injected collagen in developing chicken limb buds." Proc Natl Acad Sci U S A **82**(9): 2804-8.

Svitkina, T. (2007). "Electron microscopic analysis of the leading edge in migrating cells." Methods Cell Biol **79**: 295-319.

Taber, L. A. (1995). "Biomechanics of growth, remodeling, and morphogenesis." Appl Mech Rev **48**: 487-545.

Tambe, D. T., C. C. Hardin, et al. (2011). "Collective cell guidance by cooperative intercellular forces." Nat Mater **10**(6): 469-75.

Tan, J. L., S. Ravid, et al. (1992). "Control of nonmuscle myosins by phosphorylation." Annu Rev Biochem **61**: 721-59.
Tan, J. L., J. Tien, et al. (2003). "Cells lying on a bed of microneedles: an approach to isolate mechanical force." Proc Natl Acad Sci U S A **100**(4): 1484-9.
Theriot, J. A. and T. J. Mitchison (1991). "Actin microfilament dynamics in locomoting cells." Nature **352**(6331): 126-31.
Thiery, J. P., J. L. Duband, et al. (1985). "Cell migration in the vertebrate embryo: role of cell adhesion and tissue environment in pattern formation." Annu Rev Cell Biol **1**: 91-113.
Thompson, W. L. K. (1848). "Note on the integration of the equations of equilibrium of an elastic solid " The Cambridge and Dublin mathematical journal **3**: 87–88.
Tomasek, J. J., G. Gabbiani, et al. (2002). "Myofibroblasts and mechano-regulation of connective tissue remodelling." Nat Rev Mol Cell Biol **3**(5): 349-63.
Trepat, X., M. R. Wasserman, et al. (2009). "Physical forces during collective cell migration." Nature Physics **5**: 426-430.
Truong, T. V., W. Supatto, et al. (2011). "Deep and fast live imaging with two-photon scanned light-sheet microscopy." Nat Methods **8**(9): 757-60.
Urban, E., S. Jacob, et al. (2010). "Electron tomography reveals unbranched networks of actin filaments in lamellipodia." Nat Cell Biol **12**(5): 429-35.
Vicente-Manzanares, M., X. Ma, et al. (2009). "Non-muscle myosin II takes centre stage in cell adhesion and migration." Nat Rev Mol Cell Biol **10**(11): 778-90.
Vogel, V. (2006). "Mechanotransduction involving multimodular proteins: converting force into biochemical signals." Annu Rev Biophys Biomol Struct **35**: 459-88.
Vogel, V. and M. Sheetz (2006). "Local force and geometry sensing regulate cell functions." Nat Rev Mol Cell Biol **7**(4): 265-75.
Wakatsuki, T., M. S. Kolodney, et al. (2000). "Cell mechanics studied by a reconstituted model tissue." Biophys J **79**(5): 2353-68.
Wallace, D. G. and J. Rosenblatt (2003). "Collagen gel systems for sustained delivery and tissue engineering." Adv Drug Deliv Rev **55**(12): 1631-49.
Wang, J. H. and J. S. Lin (2007). "Cell traction force and measurement methods." Biomech Model Mechanobiol **6**(6): 361-71.
Wilson, C. A., M. A. Tsuchida, et al. (2010). "Myosin II contributes to cell-scale actin network treadmilling through network disassembly." Nature **465**(7296): 373-7.
Wipff, P. J., D. B. Rifkin, et al. (2007). "Myofibroblast contraction activates latent TGF-beta1 from the extracellular matrix." J Cell Biol **179**(6): 1311-23.
Wirtz, D., K. Konstantopoulos, et al. (2011). "The physics of cancer: the role of physical interactions and mechanical forces in metastasis." Nat Rev Cancer **11**(7): 512-22.
Wolff, J. (1892). Das gesetz der transformation der knochen, Kirschwald. Berlin, Springer.
Wozniak, M. A. and C. S. Chen (2009). "Mechanotransduction in development: a growing role for contractility." Nat Rev Mol Cell Biol **10**(1): 34-43.
Wozniak, M. A., R. Desai, et al. (2003). "ROCK-generated contractility regulates breast epithelial cell differentiation in response to the physical properties of a three-dimensional collagen matrix." J Cell Biol **163**(3): 583-95.
Wozniak, M. A., K. Modzelewska, et al. (2004). "Focal adhesion regulation of cell behavior." Biochim Biophys Acta **1692**(2-3): 103-19.
Xu, K., H. P. Babcock, et al. (2012). "Dual-objective STORM reveals three-dimensional filament organization in the actin cytoskeleton." Nat Meth **advance online publication**.

Yamada, K. M. and E. Cukierman (2007). "Modeling tissue morphogenesis and cancer in 3D." Cell **130**(4): 601-10.

Yang, Z., J. S. Lin, et al. (2006). "Determining substrate displacement and cell traction fields--a new approach." J Theor Biol **242**(3): 607-16.

Zahalak, G. I., J. E. Wagenseil, et al. (2000). "A cell-based constitutive relation for bio-artificial tissues." Biophys J **79**(5): 2369-81.

Zaidel-Bar, R., S. Itzkovitz, et al. (2007). "Functional atlas of the integrin adhesome." Nat Cell Biol **9**(8): 858-67.

Zamir, E., M. Katz, et al. (2000). "Dynamics and segregation of cell-matrix adhesions in cultured fibroblasts." Nat Cell Biol **2**(4): 191-6.

Zhong, C., M. Chrzanowska-Wodnicka, et al. (1998). "Rho-mediated contractility exposes a cryptic site in fibronectin and induces fibronectin matrix assembly." J Cell Biol **141**(2): 539-51.

Zimmermann, W. H., I. Melnychenko, et al. (2006). "Engineered heart tissue grafts improve systolic and diastolic function in infarcted rat hearts." Nat Med **12**(4): 452-8.